CALIFORNIA INSTITUTE OF TECHNOLOGY

EARTHQUAKE ENGINEERING RESEARCH LABORATORY

ACCELEROGRAM PROCESSING USING RELIABILITY BOUNDS AND OPTIMAL CORRECTION METHODS

by

Marie–Bernard P. Levine

Report No. EERL 90–02

A Report on Research Supported by Grants from the
United States National Science Foundation
and the Earthquake Research Affiliates Program
of the California Institute of Technology

Pasadena, California

1990

ACCELEROGRAM PROCESSING USING RELIABILITY BOUNDS AND OPTIMAL CORRECTION METHODS

Thesis by

Marie-Bernard P. Levine

In Partial Fulfillment of the Requirements

for the Degree of

Doctor of Philosophy

California Institute of Technology

Pasadena, California

1990

(Submitted May 7, 1990)

ACKNOWLEDGEMENTS

I would like to express my sincere gratitude and appreciation to my thesis advisor, Professor James L. Beck, for the guidance and encouragement he has given me during the course of my research. I am also grateful to Professor Ronald F. Scott for the many valuable suggestions and enjoyable discussions. I further extend my appreciations to Professor Hiroo Kanamori for his help.

Special thanks to my friend Crista Potter and to Sharon Beckenbach for their skillful word processing and their cheerful cooperation, and to Cecilia Lin for her patience and her expert help with the illustrations.

My thanks also go to all my friends and colleagues who made my life so full and happy by their warm friendship and pleasant company. I am especially grateful to my extended family, Bernie Miller and Blandine Damaskin, for making Pasadena my home away from home, and for always being there during the best and the worst of times.

Finally, I wish to dedicate this thesis to my mother and father. Without their love, support and understanding, the achievement of my goal would not have been possible.

ABSTRACT

This study addresses the problem of obtaining reliable velocities and displacements from accelerograms, a concern which often arises in earthquake engineering. A closed-form acceleration expression with random parameters is developed to test any strong-motion accelerogram processing method. Integration of this analytical time history yields the exact velocities, displacements and Fourier spectra. Noise and truncation can also be added. A two-step testing procedure is proposed and the original Volume II routine is used as an illustration. The main sources of error are identified and discussed. Although these errors may be reduced, it is impossible to extract the true time histories from an analog or digital accelerogram because of the uncertain noise level and missing data. Based on these uncertainties, a probabilistic approach is proposed as a new accelerogram processing method. A most probable record is presented as well as a reliability interval which reflects the level of error-uncertainty introduced by the recording and digitization process. The data is processed in the frequency domain, under assumptions governing either the initial value or the temporal mean of the time histories. This new processing approach is tested on synthetic records. It induces little error and the digitization noise is adequately bounded. Filtering is intended to be kept to a minimum and two optimal error-reduction methods are proposed. The "noise filters" reduce the noise level at each harmonic of the spectrum as a function of the signal-to-noise ratio. However, the correction at low frequencies is not sufficient to significantly reduce the drifts in the integrated time histories. The "spectral substitution method" uses optimization techniques to fit spectral models of near-field, far-field or structural motions to the amplitude spectrum of the measured data. The extremes of the spectrum of the recorded data where noise and error prevail are then partly altered, but not removed, and statistical criteria provide the choice of the appropriate cut-off frequencies. This correction method has been applied to existing strong-motion far-field, near-field and structural data with promising results. Since this correction method maintains the whole frequency range of the record, it should prove to be very useful in studying the long-period dynamics of local geology and structures.

TABLE OF CONTENTS

Chapter 1

INTRODUCTION

Strong-motion accelerograph records are an important source of data in earthquake engineering, be it for research or design. It is crucial that the information retrieved from these records be as faithful as possible to the actual motions occurring at the site during the seismic event. The transducer in a strong-motion accelerograph can usually be modelled as a single-degree-of-freedom oscillator which records the relative displacement, due to the acceleration at the site, between the transducer and the instrument housing. Typically these motions are recorded on an analog photographic film trace, which means that the data must be digitized and interpolated at equal time intervals before any processing can be done. This process gives rise to errors and it is desirable to correct for these. In recent years strong-motion accelerographs with digital recorders have been developed. But as yet, there are far less digitally recorded earthquake data available compared to the extensive number of analog records. The nature of the problems involved with processing the two types of data are mathematically quite similar, arising from digitization noise and error in the baseline of the signals. The processing methodology proposed herein can be applied to both analog and digital accelerograph records. However, for analog records the problems are more acute because of larger error levels. They should provide a better test for the validity of the proposed processing technique. Thus, the following discussion will emphasize analog earthquake records, although most of the theory presented applies equally well to data from digital accelerographs.

Over the years, many signal processing methods have been proposed for analog earthquake records, the most popular one being the one developed by Trifunac & Lee at Caltech [1973]. The Volume II routine within this method performs all the processing in the time domain, integrates the acceleration data with the

trapezoidal rule, and uses the Ormsby filter as its main tool to correct for both high-frequency and low-frequency errors. However, the original Volume II processing routine has been shown to have certain deficiencies, which have been corrected for in various ways. This has yielded many versions, such as those used by the California Division of Mines and Geology (*CDMG*) [Porter, 1982], and by the U.S. Geological Survey (*USGS*) [Converse *et al.*, 1984]. Other processing methods have also been developed. The one proposed by Sunder & Connor [1982], which also corrects the signal in the time domain, uses the Schuessler-Ibler integration rule and an elliptic high-pass filter with an infinite impulse response and nonlinear phase distortion. Khemici & Chiang [1984] suggested a method which is very similar to the Volume II processing routine, except that all the operations are done in the frequency domain, thus replacing the equivalent convolution integral operation by a simple multiplication. However, since the original Volume II routine remains the one that has been the most widely used and studied, it is chosen in Ch. 2 as an example for applying a procedure for testing of earthquake accelerogram correction and integration methods. Also, a discussion of how the other methods, as well as the improvements made on the original Volume II routine, change the processed data is included at the end of the chapter.

Up to now, most methods have been tested by either processing a given earthquake signal, such as El Centro 1940, or a digitized straight line [Trifunac *et al.*, 1973]. Neither of these is completely satisfactory since in the first case the actual velocity and displacement are not known accurately, and in the second case the processing routine may behave differently when used for an earthquake signal, which has the appearance of a highly erratic time series. Some methods are even tested by comparing the obtained results with those of another processing routine, which may itself have some flaws [Khemici & Chiang, 1984]. It is the purpose of Ch. 2 to suggest a systematic and unbiased method to study processing-induced errors by proposing an analytical expression for the acceleration, which has the main characteristics expected from an earthquake, and which can be integrated exactly to yield a closed-form expression for the velocity and displacement. The exact signals are then compared to those obtained through the earthquake processing methods to test their reliability in certain situations such as when noise is included to simulate

recording and digitization errors, or when the start of the record is truncated to model the trigger and start-up time of an analog accelerograph. Another effect that can be studied is the way the processing routine deals with cases where final displacements are expected, as along a fault or in a partially collapsed structure. It is shown that errors imparted by the processing techniques may in some ways be improved by careful inspection of their corresponding mathematical representation, for example, continuous filters which must be discretized to be used in computer codes. It is also shown that the errors found in the time histories are mostly due to digitization and processing noise and uncertainties in the acceleration baseline because of trigger cut-offs. These errors contaminate the whole spectrum of the signals, and not just the lower and upper frequencies.

Because these errors are uncertain, it is impossible to retrieve the exact motions at the time of the event from the contaminated signal. So, regardless of the level of sophistication of the processing method, the corrected signal will still contain errors. Also, the degree of inaccuracy of the corrected data, especially the displacements which are obtained after double integration, and other data massaging methods, may not be well understood by users unfamiliar with the limitations of digital signal processing. In view of these arguments, a novel approach to accelerogram processing is presented in Ch. 3, in which the integration is performed in the frequency domain without the use of any filters. The measured and recorded acceleration is treated as a signal contaminated with random noise and which has a random number of points removed. These random sources of error are modelled by probabilistic laws which can be incorporated into the integration scheme to produce the most probable acceleration, velocity and displacement. So that the user is aware of the margin of confidence with which these signals can be used, the corrected time histories, which are also the most probable ones, are presented with their respective standard deviations. Accounting for uncertainties in records of either ground or structural motions should prove to be particularly useful for future research.

As is shown in the results presented in Ch. 3, the range in which the unfiltered acceleration and velocity may depart from the most probable value is very small;

meaning that the time history presented as the best estimate is indeed a good representation of the motion at the site. The unfiltered displacements, however, show a very large degree of uncertainty. This implies that the true displacement is very difficult to recover, as is well known, and that the proposed displacement record may not be an adequate representation of the actual motion, although mathematically it is the most probable on the basis of the information used. Hence, the processed displacement data turns out to be of little use for analysis of structures or for extraction of seismic information. In general, the expected value of the displacements exhibits a parabolic drift due to low-frequency errors. The traditional method of dealing with this problem is to completely remove the low-frequency end of the signal, below some frequency cut-off value, through the use of filters. As demonstrated in Ch. 2, one of the inconveniencies of this approach lies in the fact that digital filters do not always remove frequency contributions properly within the rejection band, sometimes even increasing the amplitude at the cut-off. Two other frequently-voiced complaints against this approach are the arbitrary way the cut-off frequency is chosen, and the possibility that important structural and seismic information is lost within the rejection band.

Ch. 4 investigates two new approaches to error correction that reduces these three previously mentioned sources of error arising in a band-pass filtering approach. The first method is one that was initially suggested by Wiener [1950]. It uses a probabilistic approach and prior information on the true signal and the noise level, to produce the optimal noise filter for the measured signal. Although this method seems promising, and can be applied to the probabilistic description of the noisy signal given in Ch. 3, it assumes that the necessary prior information is known and available. Unfortunately, this is not often the case when processing earthquake records. Applying Wiener's mathematical derivation to compute a noise filter, based on the measured data and prior information about the noise level, results in a transfer function equal to unity (thus proving that the optimal way of removing noise from the accelerogram is not to use a filter at all!). However, some hybrid versions of the optimal noise filter Wiener originally intended are used on the synthetic records. It will be shown that these filters are effective on signals which have a low signal-to-noise ratio, but do not remove enough noise within the spectrum

of signals with large signal-to-noise ratios to make a significant improvement on the corrupted record.

Traditional digital filtering methods (i.e., infinite and finite impulse response filters) and optimal methods (i.e., Wiener) treat the recorded and digitized accelerogram as it would any other signal. The second approach, studied in Ch. 4, uses the particular characteristics that make up the signature of an earthquake accelerogram to correct, but not completely remove, the noise-contaminated portions of the record. Using the Bayesian formulation applied to system identification techniques [Beck, 1989], a model for the seismic source or structural spectrum is fitted to the recorded data to obtain the model parameters. One of these parameters is the *d.c.* value of the velocity spectrum, which, if properly identified, can capture any possible final displacement offset.

The general methodology and analytical derivation used to perform accelerogram processing, inferred by the spectral minimization of the source and structural parameters, is presented in detail in Sec. 4.3.1. The data are replaced by the best fit model in the upper and lower ranges of the spectrum, where the signal-to-noise ratio appears to be small. The probability density function of the error between the data and the model is used to define the proper cut-off frequencies at which the substitution occurs. Hence, this new approach to accelerogram processing offers the extra advantages of incorporating the whole spectral range of the corrected signal, as well as a systematic criterion for choosing the appropriate cut-off frequencies for correction.

Within the last twenty years, substantial advances have been made in earthquake source modelling of body wave spectra. These waves provide the main contribution to the signals recorded by the strong-motion accelerograph. There is still heated debate among seismologists about the proper seismic source spectrum, especially regarding the high-frequency decay for near-field and far-field records [Joyner & Boore, 1988]. However, most agree on the behavior of the displacement spectra at low frequencies. A general review of the existing models is presented in Sec. 4.3.2; the first one of which was initially suggested by Brune [1970]. So that an appropriate model characterization is available for both free-field and structural

records, two different types of model spectrum are chosen for the identification of the parameters from the accelerogram. One is meant to be a general representation of strong ground motion, and the other models structural response.

In Secs. 4.3.4 and 4.3.5 , the spectral substitution method is applied to ground motion and structural response records obtained during the 1979 Imperial Valley earthquake. The records from the severely damaged Imperial County Services Building ($ICSB$), and the strong ground motion array which crosses the Imperial fault, prove to be a good test for the validity of both the proposed correction method and the spectral models used for the system identification.

A case study is presented in Ch. 5. Trace 3 of the $ICSB$ records obtained during the October 15, 1979 Imperial Valley earthquake is taken as an example of complete processing with this new probabilistic method. This particular record measured the northern component of motion at the west end of the roof of the $ICSB$. The results which are presented show the most probable value of the acceleration, velocity and displacement, with and without spectral corrections, as well as their respective levels of uncertainty, as described in Chs. 3 and 4. The results of the probabilistically processed record are then compared to those provided by *CDMG* in Volume II.

Finally, a general analysis of the advantages and disadvantages of the new correction and integration method is presented in Ch. 6, as well as recommendations for future research to improve the present version of the processing method.

Chapter 2

TESTING OF EARTHQUAKE ACCELEROGRAM PROCESSING AND INTEGRATION METHODS WITH SYNTHETIC RECORDS

2.1 Errors in Data Processing of Analog Accelerograms

When acceleration data recorded on a photographic film is to be analyzed, the first step that is performed is digitization of the signal. This leads to both high-frequency errors from digitizing a point not exactly at the center of the actual signal trace and from interpolation of the data at equally spaced time intervals, and low-frequency errors which occur when the baseline of the signal is shifted. These digitization errors have been extensively studied by Trifunac *et al.* [1973], Hudson [1979], Shakal & Ragsdale [1984], and others. The contribution from the high-frequency digitization noise decreases with integration, so that the velocity and the displacement data obtained by integrating the acceleration will not be affected much by this type of noise. However, velocities and especially displacements are sensitive to low-frequency errors in the acceleration.

It has been shown that the noise spectrum of such errors can be modelled for accelerograms as a constant over a wide frequency range and corresponds to stationary white noise with standard deviation of the order of a thousandth of a g. When a strong-motion accelerograph is triggered, it not only records the earthquake signal but also a straight line which is used as a reference for the digitization, so that it can be assumed that the baseline of the digitized acceleration is only off by a constant amount. However, a constant mean error of only 0.001 g in the acceleration, after double integration over a 20 sec time span, leads to a parabolically increasing error of 198 cm in the displacement, which is clearly unacceptable and makes it difficult to determine the final displacement that can be expected in certain cases.

For this reason, most processing methods focus mainly on ways to filter out longer-period errors in the acceleration. How well these filters perform can be studied using the analytical earthquake formulation proposed in this chapter.

The signal that is digitized is that of the relative displacement, $x(t)$, of the transducer with respect to the instrument housing, but which is calibrated as an acceleration. The accelerometer can usually be modelled as a single-degree-of-freedom oscillator, whose characteristic frequency and damping are found from calibration tests. The absolute ground acceleration, $a(t)$, can be obtained from the application of the equation of motion of the transducer:

$$\ddot{x}(t) + 2\zeta\omega_0\dot{x}(t) + \omega_0^2 x(t) = -a(t) \ , \tag{2.1.1}$$

where the relative velocity, $\dot{x}(t)$, and relative acceleration, $\ddot{x}(t)$, could be found by numerical differentiation of $x(t)$. Also, since the accelerometer only gives reliable records up to frequencies of the order of the natural frequency, the data must be low-pass filtered; typically for the standard analog strong-motion instrument in the U.S., the cut-off frequency is chosen near 25 Hz. The above process is called instrument or transducer correction. Because this step of the earthquake processing uses a well-defined equation, it is assumed that little error is introduced in the record, except maybe for some high-frequency noise introduced by the low-pass filter and the numerical differentiation, to which the integrated velocity and displacement are not very sensitive. However, filter errors can be studied in other steps of the processing method. Thus, the analytical earthquake equation proposed in this report is assumed to represent the absolute instrument-corrected acceleration. In future work, small modifications to the testing procedures can be made to study the effects of instrument corrections on the data.

Another problem that arises in the integration of the earthquake signal is that of the unknown initial conditions to use for the velocity and displacement. Typically, an accelerometer triggers for signals higher than a hundredth of a g, by which time the initial velocity and displacement are no longer exactly zero, even though they should still be very small. The Volume II processing routine treats this problem by performing least square fitting of straight lines to the acceleration, velocity and

displacement, from which it indirectly assigns initial values to the integrated data. The original Volume II processing method is explained in more detail in Sec. 2.3, and how well it estimates these initial quantities is discussed in Sec. 2.4.

In Sec. 2.4, a new method of studying the errors induced in accelerograms is presented. This method uses synthetic accelerograms generated by closed-form expressions for the accelerations, which can be exactly integrated to produce the corresponding velocities and displacements, and spectra. The derived analytical expression of the acceleration does not attempt to reproduce exactly the motion of any specific earthquake, but is intended to be general enough to capture the features common to most strong-motion accelerograms. The equation for the synthetic acceleration calls for parameters that are randomly chosen within specified bounds. This allows the generation of a multitude of different sorts of earthquake-like acceleration signals. The accelerogram processing and integration methods can then be tested with the synthetic records, and comparison of the differences between the processed and analytical solutions can help detect and confirm the source of the processing-induced errors.

2.2 Synthetic Earthquake Accelerograms

2.2.1 Earthquake Characteristics

As is illustrated in Fig. 2.1 [Hudson, 1979], earthquake ground accelerations come in all shapes and sizes, and further differences occur when the records are those from vibrating structures. Some are of short duration, such as the M =5.3 San Francisco earthquake of 1957, or the M =5.4 Lytle Creek earthquake of 1970. Others are longer in duration with uniform acceleration levels such as the M =6.7 El Centro earthquake of 1940. Some records have sharp peaks such as the M =4.6 Stone Canyon earthquake of 1972, or have very strong shaking levels and fast decay as the M =6.4 San Fernando earthquake of 1971. The frequency content of the earthquakes also varies; the M =6.5 Koyna earthquake of 1967 has a very high-frequency content, but the near-field records from the 1966 M =5.6 Parkfield earthquake shows a low-frequency component, and of course earthquake acceleration responses of tall buildings are predominantly composed of long-period harmonics. Even though these accelerograms all have distinct features, they do

have some common characteristics: they start initially at zero, and decay down to zero after a certain amount of time, they can be represented as a sum of sinusoidal functions with various frequencies and phases, and they have zero temporal mean since the corresponding velocity end conditions are zero. The analytical expression for the accelerogram must also take into account the fact that the integrated velocity and displacement start at zero and the velocity must also decay to zero when the earthquake is over. If the constraint of having zero mean velocity is added then this automatically assures that the final displacement is zero. In some cases however, when the instrument is located along a fault or in a damaged structure for instance, some final offset is expected, thus making the final displacement non-zero.

2.2.2 Existing Earthquake Accelerogram Models

Synthetic accelerograms can be generated by using a time series representation. For instance, a Fourier series with an exponential decay could be constructed to simulate the accelerations such that:

$$\ddot{x}(t) = Cte^{-\alpha t} \sum_{k=1}^{n} a_k \cos(\omega_k t + \phi_k) \ , \tag{2.2.1}$$

where ω_k and ϕ_k are the discrete frequency and phase of the n harmonics of the model. C is a scaling factor. The amplitudes a_k could be computed to represent the spectral amplitude model of the seismic source. One such model is proposed by Brune [1970], and is of the form:

$$a_k = \frac{\omega_k^2}{\omega_c^2 + \omega_k^2} e^{-\beta R \omega_k} \ , \tag{2.2.2}$$

where β is the shear wave velocity, ω_c is the corner frequency and R is the wave attenuation factor. It should be noted that the envelope function in Eq. 2.2.1 does alter the low-frequency content somewhat from that given in Eq. 2.2.2. Trifunac [1974] proposed a spectral model where the amplitude of the k^{th} harmonic is given by:

$$a_k = \Delta\sigma \ \exp\left(-\frac{\omega_k D}{2\beta R}\right) \ , \tag{2.2.3}$$

and where $\Delta\sigma$ is the stress drop along the fault and D the distance from the source.

These previous models may be suitable to reproduce the ground acceleration near the earthquake epicenter. However, to test accelerogram processing methods, the analytical expression does not have to specifically simulate the source mechanism. For example, a more general model has already been proposed by Brady & Mork [1984], who suggested a displacement equation of the form:

$$x(t) = \sum_{k=1}^{n} a_k t^2 e^{-\alpha_k t^2} \sin(\omega_k t) \tag{2.2.4}$$

where the amplitudes a_k and frequencies ω_k are chosen arbitrarily, and the envelope parameters α_k assigned for each of the harmonics are a function of the time at which the peak value occurs. Expressions for the velocity and acceleration are obtained by differentiating Eq. 2.2.4. Such an approach is not completely satisfactory since it assumes a shape for the displacement signal, of which, in fact, less is known. It is preferable to assume an expression for the acceleration, and derive the velocity and displacement equations by integration assuming zero initial conditions. The model proposed by Brady & Mork forces the displacement to decay to zero, which physically is not always the case, as was mentioned above. Their model also allows for phase shifts in the harmonics by selecting different start times for each of the frequency components, and by using trial and error to generate earthquake-like motions. This makes it tedious to generate many signals at a time.

Schiff & Bogdanoff [1967] suggested an analytical expression for the acceleration of the form:

$$\ddot{x}(t) = \sum_{k=1}^{n} t e^{-\alpha_k t} \cos(\omega_k t + \phi_k) \,, \tag{2.2.5}$$

where the amplitude of the signal is constant and equal to 1, α_k are positive arbitrary constants in the range 0.35 to 0.50, ω_k are the equally spaced angular frequencies chosen between the bounds 6 to 40 rad/sec (1.9 to 12.7 Hz), ϕ_k are the independent random phase variables uniformly distributed over the interval 0 to 2π, and the number of harmonics is arbitrarily set to 40. The analytic expression for the acceleration given by Eq. 2.2.5 can be integrated to obtain closed-form solutions for the velocity and displacement in which the constants of integration are set to obtain zero initial conditions. The acceleration time history that is generated by

such a procedure does not generally have zero temporal mean. This implies that the integrated time histories may not behave as expected from earthquake motions. The same is also true for the formulation in Eq. 2.2.1.

In the following, a formulation and methodology is proposed which automatically generates time histories without using trial and error methods, and which have most of the features expected from earthquake motions.

2.2.3 Proposed Analytical Earthquake Accelerogram Model

Any of the above models could have been chosen for the synthetic accelerograms, but the following form is based on the Schiff & Bogdanoff model. The analytical expression for the acceleration is very similar to the one in Eq. 2.2.5, with the exception that each harmonic is allowed to have a different amplitude a_k, and the envelope α_k is chosen such that it follows the decay expected in accelerograms. The parameters are now chosen randomly in such a way that certain characteristics required for an earthquake are respected, as explained below. Hence, this approach is different from all those mentioned previously in that the parameters are not computed using seismic source properties, or are not selected using trial-and-error. It is stressed that the intent is to generate analytical time histories which have similar general characteristics to real earthquake motions, and not to model any particular event.

Eq. 2.2.5 can be rewritten as the sum of n acceleration harmonics $\ddot{x}_k(t)$ such that:

$$\ddot{x}(t) = \sum_{k=1}^{n} \ddot{x}_k(t) \,, \tag{2.2.6}$$

and,

$$\ddot{x}_k(t) = a_k t e^{-\alpha_k t} \cos(\omega_k t + \phi_k) \,. \tag{2.2.7}$$

The acceleration boundary conditions are satisfied since $\ddot{x}_k(0)$ is equal to zero, and $\ddot{x}_k(t)$ decays to zero as t goes to infinity. Each harmonic k is assigned an individual amplitude a_k which is randomly chosen in the range 0 to 1, as is the phase ϕ_k between $-\frac{\pi}{2}$ and $+\frac{\pi}{2}$. The frequencies ω_k are equally spaced between any prescribed bounds for any given number of harmonics n. The added condition

that the mean acceleration is zero selects what values to choose for the harmonic envelope parameters α_k. Indeed, assuming zero mean acceleration is equivalent to forcing the *d.c.* component of the acceleration Fourier transform $\ddot{X}(\omega{=}0)$ to also be zero. The expression for the acceleration Fourier transform can also be put in closed form:

$$\ddot{X}_k(\omega) = \int_0^\infty a_k t e^{-\alpha_k t} \cos(\omega_k t + \phi_k) e^{-i\omega t} dt \,, \tag{2.2.8}$$

which reduces to,

$$\ddot{X}_k(\omega) = \frac{a_k}{\left[(\alpha_k + i\omega)^2 + \omega_k^2\right]^2} \left\{ \left[(\alpha_k + i\omega)^2 - \omega_k^2\right] \cos\phi_k - 2(\alpha_k + i\omega)\omega_k \sin\phi_k \right\} . \tag{2.2.9}$$

Applying the condition that $\ddot{X}_k(0) = 0$, leads to

$$\alpha_k = \omega_k \frac{\sin\phi_k + 1}{\cos\phi_k} \,, \tag{2.2.10}$$

where α_k must always be positive for the envelope to decay. From physical considerations of earthquakes, other conditions must be applied to determine the bounds for α_k. The envelope function of the k^{th} harmonic, $t\exp(-\alpha_k t)$, reaches its maximum value at time $t = \frac{1}{\alpha_k}$. Typically these peak values are reached after at least 1 sec of excitation, so that α_k should be less than or equal to 1. For harmonics to decay fast enough the lower bound for α_k is arbitrarily set to 0.4. This constraint forces the records to be of short duration, to limit the amount of data to be stored. Synthetic records of longer duration could easily be generated by allowing α_k to become smaller. Also, to limit the effects of very high or very low frequencies, the following bounds are used for α_k instead of 0.4 and 1.0:

$$\omega_k \leq 0.25 \text{ Hz} \,, \qquad 0.4 \times \frac{0.25}{\omega_k} \leq \alpha_k \leq 1.0 \times \frac{0.25}{\omega_k}$$

$$\omega_k \geq 10.0 \text{ Hz} \,, \qquad 0.4 \times \frac{\omega_k}{10} \leq \alpha_k \leq 1.0 \times \frac{\omega_k}{10} \,.$$

Analytical formulations for the velocity and displacement are obtained by integration of Eq. 2.2.7 where the integration constants are found by setting the initial

conditions to be zero. Thus,

$$\dot{x}(t) = \sum_{k=0}^{n} \dot{x}_k(t) = \sum_{k=0}^{n} \int_0^t \ddot{x}_k(t)dt \ , \tag{2.2.11}$$

where,

$$\dot{x}_k(t) = -V_k + a_k \frac{e^{-\alpha_k t}}{\beta_k^2} \Big[(\omega_k \beta_k t + 2\alpha_k \omega_k) \ \sin(\omega_k t + \phi_k) - (\alpha_k \beta_k t + \gamma_k) \ \cos(\omega_k t + \phi_k) \Big] \ , \tag{2.2.12}$$

$$V_k = -\frac{a_k}{\beta_k^2} (2\alpha_k \omega_k \ \sin\phi_k + \gamma_k \ \cos\phi_k) \ , \tag{2.2.13}$$

and β_k and γ_k are defined below in Eq. 2.2.17 and Eq. 2.2.18 respectively. Also,

$$x(t) = \sum_{k=0}^{n} x_k(t) = \sum_{k=0}^{n} \int_0^t \dot{x}_k(t)dt \ , \tag{2.2.14}$$

where,

$$x_k(t) = -a_k \ \frac{e^{-\alpha_k t}}{\beta_k^3} \Big\{ (2\alpha_k \omega_k t \beta_k + 2\gamma_k \omega_k + 4\alpha_k^2 \omega_k) \ \sin(\omega_k t + \phi_k) - (\alpha_k^2 t \beta_k + 2\gamma_k \alpha_k - \omega_k^2 \beta_k t - 4\alpha_k \omega_k^2) \cos(\omega_k t + \phi_k) \Big\} - V_k t - D_k \ , \tag{2.2.15}$$

and,

$$D_k = -\frac{2a_k}{\beta_k^3} \left\{ (\gamma_k \omega_k + 2\alpha_k^2 \omega_k) \sin\phi_k + (2\alpha_k \omega_k^2 - \gamma_k \alpha_k) \cos\phi_k \right\} \ , \tag{2.2.16}$$

$$\beta_k = \alpha_k^2 + \omega_k^2 \ , \tag{2.2.17}$$

$$\gamma_k = \alpha_k^2 - \omega_k^2 \ . \tag{2.2.18}$$

The program which generates the synthetic accelerograms (Fig. 2.2) automatically computes the values of the equally spaced frequencies according to the number of harmonics and bounds prescribed. Then it randomly selects the amplitude and

phase for each of the components, and computes the corresponding envelope parameter. If the latter does not fall within the bounds defined above, then other values for the phase ϕ_k are randomly chosen until a proper α_k is found. The algorithm then computes the acceleration, velocity and displacement by summing up all the harmonics for each time step using the appropriate analytic expression, as given in Eqs. 2.2.6, 2.2.7 and 2.2.11 through 2.2.18. It is also possible to obtain the analytically generated Fourier amplitude spectrum of the acceleration to check the frequency content of the signal.

The analytic velocity, given by Eqs. 2.2.11 through 2.2.13, does not assume that the velocity has mean zero, so the displacement time history obtained from Eqs. 2.2.14 through 2.2.16 is expected to have a final offset. However, if required, a corrective term can be added to the velocity equation to remove the mean and impose the final displacement to be zero. This is done by fitting a sinusoidal function to the velocity. Define $\ddot{x}(t)$ and $\dot{x}(t)$ as the quantities obtained with no correction for the mean velocity, and $\ddot{y}(t)$ and $\dot{y}(t)$ as the mean corrected signal, such that:

$$\dot{y}(t) = \dot{x}(t) + pte^{-\alpha_0 t} \sin \omega_0 t \,, \tag{2.2.19}$$

where the frequency ω_0 is a function of the total duration t_d of the record at which no more excitation is occurring, such that:

$$\omega_0 = \frac{2\pi}{t_d} \,. \tag{2.2.20}$$

In practice, t_d is selected as the time at which the digitized synthetic accelerograms are zero within the data storage precision. As will be seen in Ch. 3, this causes errors in the temporal mean of the acceleration of the order of the data precision. The envelope parameter α_0 is associated with ω_0 and a phase angle of $\pi/2$, and the constant p is a function of the final displacement $C = x(t_d)$ and is given by:

$$p = \frac{C}{\int_0^\infty te^{-\alpha_0 t} \sin \omega_0 dt} \,, \tag{2.2.21}$$

which reduces to:

$$p = \frac{C(\alpha_0^2 + \omega_0^2)^2}{2\alpha_0 \omega_0} \,. \tag{2.2.22}$$

This added corrective term changes the analytical expression for each of the quantities in the following way:

$$\ddot{y}(t) = \ddot{x}(t) + pe^{-\alpha_0 t}\Big(\sin\omega_0 t - \alpha_0 t\,\sin\omega_0 t + t\omega_0\cos(\omega_0 t)\Big)\,, \tag{2.2.23}$$

and,

$$y(t) = x(t) - p\,\frac{e^{-\alpha_0 t}}{\beta_0^2}\Big\{\Big(\alpha_0 t + \frac{\alpha_0}{\beta_0}\Big)\sin(\omega_0 t) + \Big(\omega_0 t + \frac{2\alpha_0\omega_0}{\beta_0}\Big)\cos(\omega_0 t)\Big\} + C\,, \tag{2.2.24}$$

and,

$$Y_k(\omega) = X_k(\omega) + i\,\frac{2p\omega\omega_0(\alpha_0 + i\omega)}{\left[(\alpha_0 + i\omega)^2 + \omega_0^2\right]^2}\,, \tag{2.2.25}$$

where β_0 and γ_0 are given by Eqs. 2.2.17 and 2.2.18 for frequency ω_0 and constant α_0 .

The process for generating earthquake signals is summarized in Fig. 2.2. Examples of the type of records generated by this model are given in Figs. 2.3 through 2.8. Fig. 2.3 illustrates one of the analytically obtained earthquake signals, *Q1U*, for the acceleration, velocity, displacement and acceleration Fourier amplitude spectrum. *Q1U* was generated by randomly choosing α_k, a_k and ϕ_k for 200 frequencies equally spaced within the range 0.05 Hz to 25.0 Hz. The main characteristics sought in an earthquake record are respected: initial conditions are zero, acceleration and velocity decay down to zero after 20 sec (within the three decimal points of the storage precision), the frequency content of the acceleration is mainly within the range 0.1 Hz to 10 Hz, and the final displacement is nonzero. The signal can be scaled to any size. For instance in Fig. 2.3, *Q1U* has a peak acceleration of about 5.0, which can be interpreted as 5 m/sec^2 (approximately 50% g) for a large earthquake, and thus the peak velocity is 0.40 m/sec and the peak displacement is 0.35 m with a final offset of 0.20 m. However, *Q1U* can also be scaled down to a small earthquake level, in which case the peak acceleration is 0.5 m/sec^2 (approximately 5% g), the peak velocity is 0.040 m/sec, with a peak displacement of 0.035 m and a final offset of 0.02 m. The concept of earthquake size is important in defining

signal-to-noise ratios and instrument trigger levels; this will be discussed in more detail in Sec. 2.2.4.

Fig. 2.4 represents the analytically generated earthquake *Q1C*, which has the same characteristics as *Q1U* (Fig. 2.3), except that the mean is removed from the velocity, forcing the final displacement to be zero. The overall form of the signal is unaltered, which implies that the corrective term has little effect other than removing the final displacement offset. However slight changes can be observed, such as small variations in the amplitudes of the peak velocity and displacement. Also, the *Q1C* acceleration spectrum has a slightly higher peak at 0.05 Hz, which corresponds to the frequency of the corrective term for the 20 sec record. In the following discussion the letter "*U*" will always refer to an uncorrected signal (i.e., nonzero final displacement), and the letter "*C*" will always stand for a mean-velocity corrected signal (i.e., zero final displacement).

Figs. 2.5 and 2.6 show the uncorrected and mean-velocity corrected signals of another analytically simulated earthquake, *Q2U* and *Q2C*. Even though both *Q1* and *Q2* have been generated using the same number of frequencies over the same frequency range, they do not have the same characteristics because ϕ_k, α_k and a_k are chosen randomly. The simulated earthquake *Q2* (Figs. 2.5 and 2.6) decays faster than *Q1* (Figs. 2.3 and 2.4), however *Q2* has a very pronounced peak in the acceleration record, and has higher peak velocities and displacements than *Q1*. This type of behavior can be expected in an earthquake, as can be seen in the 1972 Stone Canyon ground acceleration in Fig. 2.1.

The simulated earthquake signal *Q8C*, illustrated in Fig. 2.7, is composed of 200 harmonics within the frequency range 0.4 Hz and 25.0 Hz. Hence, it differs from the two previous signals *Q1* and *Q2* since it does not have harmonics between 0.05 Hz and 0.4 Hz. The velocity and displacement have a very pronounced 2.5 sec period, which could be expected in the response of a tall building. Thus, the analytical approach that is proposed in this report to simulate earthquakes is general enough to generate a wide range of signals, yet the formulation still complies with most of the important features common to seismic records. This is useful to test the effects of processing methods on a large number of different accelerograms.

Also, to study the effect of the processing routine on each individual harmonic of the earthquake, a signal is created which contains a modulated harmonic at frequency 1 Hz, and which still has the required characteristics. This signal, *SIN1C*, illustrated in Fig. 2.8, will be very useful in detecting how each harmonic is modified or affected by the correction and integration method.

2.2.4 Simulation of Noise and Instrument Trigger

Trifunac & Lee [1973] studied the noise due to digitization of straight lines and concluded that it could be modelled as Gaussian distributed white noise, with zero mean and standard deviation of about a thousandth of a g. Thus, to simulate the noise obtained after digitization of a true earthquake accelerogram, Gaussian distributed white noise, with zero mean and standard deviation of a thousandth of a g is added to the synthetic accelerogram. The signal-to-noise ratio of the record will depend on the size of the seismic event. As mentioned above, two earthquake sizes are considered here. If on the acceleration scale of Figs. 2.3 through 2.7, the value 5 represents 5 m/sec^2, or approximately 50% g, then the signal is said to represent that of a large earthquake, however if 5 represents 0.5 m/sec^2, or approximately 5% g, then the record is said to be that of a small earthquake. The synthetic signal, modelled both as a small and large record, is contaminated with the same noise sample which is scaled to the simulation size. Hence, there will be 10 times larger noise-to-signal in the accelerogram of a small event than that of a large one, as can be observed in the plots of the acceleration noise and in the tail-portion of the acceleration time histories (Fig. 2.9). Also, the approximate noise-to-signal ratio for this particular example is 0.4% for large event simulations, and 4% for small event simulations.

Typical strong motion analog accelerographs will trigger at levels of a hundredth of a g. To reproduce the effect of the transducer start-up time, the analytically generated accelerogram is truncated at the beginning of the record until the trigger level is reached, so that for small events a longer portion of the record will be missing than for a larger earthquake. Typically results from the synthetic records show that instruments are triggered for large events at the very first data point, whereas for small events over 10 points may go by unrecorded. Hence, it can

be assumed that for large events, the instruments are modelled to trigger at the first arrival of the P waves.

The type and amount of recording and digitization errors suggested above apply primarily to records obtained from analog accelerographs. Synthetic accelerograms can also be corrupted to simulate errors commonly found in records obtained from digital accelerographs. In this latter case however, data missing due to trigger truncation does not apply because of the pre-event memory, and the amount of quantization noise will depend on the digitization precision.

These analytical records, in which noise is added and the first few data points are truncated, will be used to study how well the processing methods remove noise and estimate initial conditions. Since the noise-to-signal ratio and the truncation are larger in the small level earthquakes, it is expected that they will be harder to correct and integrate accurately than larger level accelerograms. Thus, the small analytic earthquakes will be very useful in determining the types of errors that are induced by the processing routines.

It should be noted that the errors modelled above are those that are most commonly found in earthquake accelerograms. Other sources of errors that may occur, such as loosening of the instrument housing during the event, or instrument malfunction are not considered here.

2.3 The Original Volume II Processing Routine

Before testing any earthquake accelerogram correction and integration technique, it is very important to understand how the processing changes the signal and at which steps errors might be introduced. In the following, the original Volume II routine developed at Caltech by Trifunac & Lee [1973] is used as an example of how processing methods can be tested with the use of the synthetic accelerograms developed in Sec. 2.2. This processing method was chosen because it has been the most extensively used and studied, and also because its computer code was readily available, but the methodology applied hereafter can be used on any other kind of digital processing and correction method.

Some of the sources of the Volume II processing errors have already been reported in several papers [Fletcher *et al.*, 1980; Converse *et al.*, 1984; Joyner & Boore, 1988; and others] and improvements have already been proposed to reduce the level of these errors. However, the purpose of the following chapter is to show how it is theoretically possible, but tedious, to investigate the errors in each processing step by an equivalent mathematical formulation, and how, on the other hand, these same processing-induced errors can be identified by simple visual inspection through the use of the synthetic accelograms, using only a limited knowledge of digital signal processing techniques. The artificial record testing method has the added advantage that it can also be used to study how the correction routine handles uncertainties such as trigger truncation and digitization noise, which cannot be described by a deterministic equation.

The original Caltech processing routine is separated into four different parts. The first one, refered to as Volume I, performs the interpolation to equal time steps and the instrument calibration of the raw, or uncorrected, acceleration data as digitized from the photographic film. In Volume II the raw data is first instrument corrected, and then filtered and integrated, to produce the corrected acceleration, velocity and displacement. This is the section of the Caltech routine that is studied in depth within this chapter. The response spectra and the Fourier spectra are computed in Volume III and Volume IV, respectively. All the operations within the processing program are performed in the time domain.

Volume II, the part of the original Caltech processing routine which performs the high-pass filtering and integration of the raw acceleration, is schematically represented in Fig. 2.10 [Hudson, 1979]. Each of the steps are numbered. It is assumed that the data has already been digitized, interpolated at 0.02 sec intervals, instrument corrected, and that the high frequencies have been filtered out. Each step is explained in the following sections.

2.3.1 Linear Trend Removal

In step 1, the acceleration, $a(t)$, is least square fitted to a straight line to remove the mean and any linear trend that might be in the signal. The linearly corrected acceleration $a_1(t)$ is then integrated using the trapezoidal rule to obtain

the velocity $v_1(t)$, assuming zero initial conditions. The velocity $v_1(t)$ is in turn least square fitted to a straight line in step 3. This will impose the final displacement to be zero, if the initial displacement is also zero. Thus, this step makes it impossible to obtain any final offset in the displacement record. The linear velocity corrective term a_1, is then added in step 4 to the linearly corrected acceleration $a_1(t)$ to yield a new acceleration signal a_2(t).

2.3.2 Low-Pass Running-Mean Filter and Decimation

The baseline-corrected acceleration data, a_2(t), is then low-pass filtered in the time domain using convolution, which implies that the data must be extended both at the beginning and at the end of the record by the width of the filter window, as is done in step 5. To reduce the computational effort, Volume II decimates the data in step 7 by saving every tenth point, so that the new time increment is increased from 0.02 sec to 0.2 sec, and the Nyquist frequency is thus reduced from 25 Hz to 2.5 Hz. Because of the change in the Nyquist frequency, decimation of the data creates aliasing, and all the frequencies in the signal between 2.5 Hz and 25 Hz are wrapped around, and appear as frequencies between 0 Hz and 2.5 Hz, thus changing the low-frequency content of the signal. To minimize the aliasing effect of the decimation, the data must first be low-pass filtered to remove any frequencies beyond 2.5 Hz. In Volume II this is done in step 6 with an equal-weight running-mean filter $h_1(t)$ of width T_w equal to 0.4 sec which has the transfer function $H_1(f)$ illustrated in Fig. 2.11. Up to 0.1 Hz this filter has an amplitude equal approximately to 1, leaving the signal unaltered in that range, but it decreases in amplitude between 0.1 Hz and 2.5 Hz, thus changing the low-frequency content of the record. Also, it does not remove all the frequencies beyond 2.5 Hz, so that some aliasing still occurs when the data is decimated. It should be noted that the remaining frequency content between 2.5 Hz and 5 Hz, 7.5 Hz and 10 Hz, and so on, will have a 180^o phase shift relative to the unfiltered data.

2.3.3 Low-Pass Ormsby Filter

To high-pass filter the accelerogram, the Volume II processing routine first subjects the data to a low-pass filter, and then substracts the long-period components of the earthquake record from the unfiltered data. The ideal low-pass

filter is the boxcar filter illustrated as a dashed line in Fig. 2.12.b. It should remove from the data all frequencies beyond a specified cut-off value f_c. In the time domain, this nonrecursive filter is defined by:

$$y_n = \sum_{k=-\infty}^{+\infty} h_k x_{n-k} \ , \tag{2.3.1}$$

where x_k and y_k are, respectively, the unfiltered and filtered data array, and h_k are the discrete symmetric filter weights (Fig. 2.12.a). Equivalently, the boxcar function is described exactly in the frequency domain by the discrete infinite Fourier series:

$$H(f) = \sum_{k=-\infty}^{+\infty} h_k \exp\left(\frac{i\pi k f}{f_N}\right) \ , \tag{2.3.2}$$

where f_N is the Nyquist frequency of the digitized signal. Because of numerical limitations however, this filter cannot be represented as an infinite sum in the time domain, and hence the series must be truncated and the discontinuity of the transfer function at the cut-off frequency cannot be captured properly. The failure of the truncated series to converge at the discontinuity produces a ringing effect both before and after the cut-off frequency. This effect is also known as the Gibbs phenomenon, and is illustrated in Fig. 2.12.b. Increasing the number of weights in the filter will decrease the width of the ringing in the transfer function, however the amplitude of the error does not decrease by the same proportions. Hence, as the number of terms in the series, given by Eq. 2.3.2, goes to infinity, the Gibbs phenomenon appears as a sharp overshoot above and below the discontinuity.

One way to reduce the error due to the Gibbs phenomenon is to decrease the order of the discontinuity at the cut-off frequency. One such filter is the Ormsby filter, which is used in the Volume II processing routine to indirectly remove low-frequency errors from the data. The low-pass Ormsby filter transfer function, $H_2(f)$, has a linear ramp between its roll-off and cut-off frequencies, f_r and f_c, as illustrated in Fig. 2.13.a. As is the case for the ideal filter, the Ormsby filter is a nonrecursive filter, and it is given in its ideal form by:

$$y_n = \sum_{k=-\infty}^{+\infty} h_{2k} x_{n-k} \ , \tag{2.3.3}$$

where h_{2k} are the discrete symmetric filter weights defined as:

$$h_{2k} = h_{-2k} = \frac{\cos(2\pi f_c k\Delta t) - \cos(2\pi f_r k\Delta t)}{2\pi^2 k^2 \Delta t^2(\omega_r - \omega_c)} \,. \tag{2.3.4}$$

The equivalent transfer function for the ideal Ormsby filter with an infinite number of weights is illustrated in Fig. 2.13.a. However, because of numerical limitations, only a finite number of filter weights can be used to define the Ormsby filter in the time domain. Thus, the digital filter will exhibit the Gibbs phenomenon both before and after the discontinuity (Fig. 2.13.a). For this type of filter the overshoot or ripple error is not only a function of the number of weights, M, but also of the steepness of the slope between the cut-off and roll-off frequencies. As the slope becomes steeper, the discontinuities at f_r and f_c become sharper, and the amplitudes of the Gibbs overshoot increase. Ormsby suggests that the upper-bound error in the digital filter transfer function is [Trifunac, 1970]:

$$\epsilon = \frac{0.012}{\lambda_r M} \,, \tag{2.3.5}$$

where the size of the transition region, represented by constant λ_r, is given by:

$$\lambda_r = (f_r - f_c)\Delta t \,. \tag{2.3.6}$$

The Volume II method chooses the number of weights M to be equal to:

$$M = \lambda_r^{-1} = \frac{1}{(f_r - f_c)\Delta t} \,. \tag{2.3.7}$$

Hence, whatever the order of decimation, or the roll-off to cut-off frequency interval, the program chooses the number of weights such that the error in the discontinuity is constant and bounded above by 1.2%. Therefore, for the same number of filter weights the amount of expected error remains less than that of the boxcar filter mentioned previously. As the number of Ormsby filter weights are increased, the errors are concentrated over a narrower frequency range, but this also requires more computation time for the convolution. This is why the data is decimated before it is filtered, so that larger time steps Δt can be used. Nevertheless, the Ormsby filter remains appropriate for the Volume II earthquake processing method since it does not change the phase of the signal. This is a property of all nonrecursive

symmetric filters. To remove long-period errors due to uncertainties in the velocity and displacement initial values, these integrated time histories must also be filtered, and it is important that the phase difference between the acceleration, velocity and displacement be respected.

2.3.4 Interpolation

Once the acceleration is low-pass filtered as part of the high-pass filtering steps 5 through 10 (Fig. 2.10), it is interpolated back to the original time interval (Δt =0.02 sec), from the decimated time interval ($\Delta T = 0.2$ sec). Hence, the order of the decimation p is 10, with $\Delta T = p\Delta t$, and $M = p\,N$, where $m = 0, 1, \ldots, M$ is the index of the data points for the record interpolated at $\Delta t = 0.02$ sec, and $n = 0, 1, \ldots, N$ is the index for the decimated signal at $\Delta T = 0.2$ sec. The linearly interpolated data, y_m, can be reconstructed from the decimated data, x_n, using the following equation:

$$y_m = x_n + \frac{x_{n+1} - x_n}{p} K \,, \tag{2.3.8}$$

where K is an integer which takes values between 0 and $(p-1)$, and relates the indices m and n such that:

$$m = np + K \,. \tag{2.3.9}$$

For discrete band-limited waveforms and for even values of p, the transfer function of this interpolation filter can be shown to be expressed by:

$$H_{3k} = H_3(\omega_k) = \frac{1}{p^2}\left[p + \sum_{K=1}^{p-1} 2(p-K)\,\cos\left(\frac{2\pi K k}{M}\right)\right] \,. \tag{2.3.10}$$

This tranfer function is illustrated in Fig. 2.14 for order of decimation p equal to 10. This filter unfolds the decimated signal over p times its Nyquist frequency with decreasing amplitudes, thus creating spurious frequency components into the signal.

2.3.5 Numerical Example of Low-Pass Filter Errors

In effect the original acceleration signal has been low-pass filtered four times, once through the running-mean filter in step 6, once through the decimation in step 7, once through the Ormsby filter in step 8, and finally once through the interpolation in step 9. Each of these steps changes the low-frequency content of the

data, and in extreme cases can alter it to a point where it is considerably different from the original input signal.

The changes in the input signal as it is processed by each of these steps can be worked out analytically. As an illustration of this, consider a signal composed of 4 harmonics, at 0.05 Hz and 0.1 Hz with amplitude 0.1, and at 5.05 Hz and 5.10 Hz with amplitude 10.0. The time domain equivalent of this signal is composed of 4 pure sine functions with no decay term, and thus cannot be compared directly to an earthquake signal. However, it can still be used as a first approximation to locate the problems in the processing method. The input is assumed to be interpolated at a 0.02 sec interval, over a 20 sec time span. The running-mean filter has a time window of width T_w equal to 0.4 sec. The Ormsby low-pass filter uses 250 weights, has a cut-off frequency of 0.05 Hz and a roll-off frequency of 0.1 Hz. The decimation order p is equal to 10. These correspond to the typical values used when processing earthquake data with the Volume II routine. The numerical results are summarized in Table 2.1.

The running-mean filter has little effect on the long-period end of the spectrum, yet it reduces the amplitudes of the higher frequencies by one to two orders of magnitude. Ideally, the magnitudes of these high-frequency components, at 5.05 Hz and 5.10 Hz, should have been zero, but after application of the running-mean filter are now comparable in size to the 0.1 Hz and 0.05 Hz harmonics.

In the next step, because of aliasing due to decimation, the 5.05 Hz component will appear to have a frequency of 0.05 Hz, and the 5.1 Hz harmonic will wrap around as a 0.1 Hz signal, since the Nyquist frequency has gone down from 25 Hz to 2.5 Hz. At this point of the processing, which corresponds to step 7 of the Volume II routine, both high-frequency components have disappeared from the signal, but the low-frequency harmonic 0.05 Hz has doubled in amplitude, whereas the 0.1 Hz harmonic has nearly tripled.

These two components are now used as input to the Ormsby low-pass filter. It is assumed that because of the Gibbs phenomenon, the amplitude error at the cut-off frequency, 0.05 Hz, and at the roll-off frequency, 0.1 Hz, are about 1.2% of the input (this evaluation of the error percentage comes from Eq. 2.3.5, and

from numerical tests performed on the filter). Thus, after step 8, the signal is now composed of a 0.05 Hz harmonic with twice the amplitude of the original one, and a 0.1 Hz component for which the amplitude is reduced by two orders of magnitude but with reverse sign, meaning that this component is now 180^0 out-of-phase with the original input.

Finally in step 9, the data is interpolated back to its original time interval. It has been shown above, that in the frequency domain the harmonics must be "unwrapped" from the 2.5 Hz, to the 25 Hz Nyquist frequency, by applying the transfer function given in Eq. 2.3.10. Numerically, the 0.05 Hz component is reproduced into 4.95 Hz, 5.05 Hz, 9.95 Hz,... harmonics, and the 0.1 Hz component is periodically extended into 4.9 Hz, 5.1 Hz, 9.9 Hz,... harmonics, as shown in Table 2.1. Applying the interpolation transfer function does not have much effect on the low-frequency components, however it generates noise at the aliased frequencies which did not exist in the original input signal. In this particular example, the aliased frequencies were close to the zeroes of the interpolation transfer function, which for a time interval of 0.2 sec are located at 5 Hz, 10 Hz, 15 Hz, 20 Hz and 25 Hz. The noise level would have been much higher had the aliased frequencies coincided with the maxima of the function.

Thus, the final low-passed signal no longer has much in common with the input acceleration data, since the amplitude of the 0.05 Hz harmonic has doubled, the amplitude of the 0.1 Hz component is reduced to 3.5% of its original value, but with a 180^0 phase shift, and the new low-passed data now contains higher frequency noise generated by the interpolation.

2.3.6 High-Pass Ormsby Filter

After the interpolation back to the original time interval is performed, the data is high-pass filtered by subtracting out the low-frequency content obtained in step 9, from the unfiltered signal in step 4. Using the low-pass Ormsby filter and substraction to get a high-passed acceleration, is equivalent to using a filter for which the transfer function is equal to $(1 - H_2(f))$, as is illustrated in Fig. 2.13.b. Because of the Gibbs phenomenon, the amplitude at the roll-off frequency f_r is

increased by 1.2% with respect to the original input data. Hence, this filter amplifies the content of the record at that frequency, in the same way as the low-pass Ormsby filter described previously. Thus conceivably, the Volume II processing method may disproportionatly amplify a low-frequency component within the signal, which, after applying step 10 and obtaining the "high-passed" acceleration, could be misinterpreted as a true phenomenon at the recording site.

Returning to the example in Table 2.2, the 0.05 Hz component, which corresponds to the cut-off frequency of the Ormsby filter, is still present in the data but with a small amplitude and a 180^o phase shift. The amplitude of the signal at the low-pass Ormsby filter roll-off frequency of 0.1 Hz, has increased by 3.5%. However the higher frequencies remain almost unchanged except for the aliased noise introduced by the interpolation step. The errors in the low-frequency content will become even more important when the acceleration data is integrated to obtain the velocity and displacement.

2.3.7 Velocity and Displacement Corrections

After integration of the high-passed acceleration obtained in step 10, the velocity may no longer have zero mean. To avoid the velocity from drifting off, the process applied in steps 1 through 3 is used a second time in steps 10 through 13, which will force the integrated displacement to have zero final displacement, since zero initial conditions are assumed. Again this step makes it impossible to detect any final offset that may have occured after the earthquake.

In step 11 the acceleration signal is integrated using the trapezoidal rule, which can be considered as the convolution with a digital filter defined by the finite-impulse response equation:

$$y_n = y_{n-1} + \frac{\Delta t}{2}(x_{n-1} + x_n) \; . \tag{2.3.11}$$

In the frequency domain, this digital filter has transfer function, H_4:

$$\left|H_{4k}\right| = \frac{\dfrac{\Delta t}{2}}{\tan\left(\dfrac{\pi k}{N}\right)} \; . \tag{2.3.12}$$

The exact integration transfer function, H_e is:

$$|H_{ek}| = \frac{\frac{\Delta t}{2}}{\left(\frac{\pi k}{N}\right)} . \qquad (2.3.13)$$

Comparison of Eqs. 2.3.12 and 2.3.13 shows that the trapezoidal rule integrates data digitized at 0.02 sec accurately to about 10 Hz, after that the error grows rapidly up to the Nyquist frequency. However, the high-frequency errors introduced by the trapezoidal rule integration scheme into the velocity and displacement output signals remain small compared to those due to any pre-existing low-frequency error in the acceleration. Indeed, after exact integration, low-frequency errors in the acceleration are increased as ω^{-1} in the velocity, and as ω^{-2} in the displacement. To decrease the effect of long-period errors after integration of the acceleration - which errors it must be noted are either due to the digitization process or added in by the "high-pass" filtering steps of the processing routine - the velocity is also high-pass filtered using the equivalent low-pass Ormsby filter in steps 14 and 17. As was the case for the acceleration in step 8, this filter spuriously enhances the component of the roll-off frequency yet another time.

To make the velocity signal exactly obtainable by integration of the acceleration, the low-frequency error removed from the velocity is also removed from the acceleration. Even though differentiation reduces the effect of long-period components, step 15 will still add more low-frequency error from the Ormsby filtered velocity into the acceleration signal. Continuing the example of Table 2.1, the final "corrected" acceleration signal, as would be obtained in step 16, has a 0.1 Hz component whose amplitude is 4.8% higher than expected. Because the low-frequency errors of the velocity are also removed from the acceleration in steps 14 and 15 this signal has a very small, but negative, amplitude at the 0.05 Hz component. Hence, the high-passed acceleration still contains low-frequency information with negative phase, and high-frequency noise has been introduced by the process.

The amplitudes for each of the harmonics for both the exact and the filtered velocity and displacement signals could also be worked out numerically. In the Volume II routine the displacements are obtained from the integration of the high-passed

velocity, and are in turn also high-passed using the equivalent low-pass Ormsby filter with the same characteristics as for the acceleration and velocity filtering. Thus, the error due to the high-pass Ormsby filter is entered twice into the processing of the velocity data, and three times for the displacement data which also includes error due to double integration of the acceleration using the trapezoidal rule. Finally the "corrected" velocity has approximately a +5% amplitude error compared to the exact value for the 0.1 Hz harmonic, and the displacement has about a +5.8% amplitude error at that frequency.

When using the Volume II routine, the velocity and displacement traces are also decimated before being Ormsby low-pass filtered, as was the acceleration. After the low-pass filter is applied, the integrated signals are also interpolated, which, as in step 9, generates high-frequency noise at the aliased frequencies. This effect is expected to be minimal for the velocity and displacement, since integration greatly decreases the energy of the high-frequency components. However, this will have an effect on the acceleration, since the velocity high-frequency noise is differentiated in step 15, thus increasing the noise proportionally to the aliased frequency value before being injected back into the acceleration data, in step 16. Hence, the Volume II processing routine adds high-frequency noise in the acceleration at two different steps.

2.3.8 Limitations of Analytical Testing Methods

Theoretically, missing data at the beginning and at the end of the accelerogram changes the mean of the signal. The estimate of the initial values after triggering depend on how this uncertain value of the mean is treated. In the case of Volume II, it is impossible to estimate how well the routine evaluates the initial conditions, since the mean of the signal is removed and altered in several steps, by adding or subtracting out constants and low-frequency components of the data in the acceleration, velocity and displacement signals. Thus the initial values, which are estimated in an indirect way, depend more on the nature of the input accelerogram, and the amount of missing data, than on the processing method itself. The only way to judge how well the Volume II routine evaluates the initial conditions is

to test it with data for which the initial conditions are known. This is one of the applications of the synthetic accelerogram to test earthquake correction procedures.

The example worked out above illustrates how some errors introduced by the Volume II processing method can be identified and measured. The example case was a relatively simple one, with only four frequency components and no modulation, yet the testing procedure was somewhat long and tedious, involving mathematical derivations of the transfer functions, and careful bookkeeping of the changes occurring at each of the frequencies. Such an analytical approach would become very difficult to implement in practice for cases where many harmonics with exponential decays are summed up to simulate earthquake motions. Also, the analytical testing method is not suitable to study how well random noise (which does not have a deterministic representation) is removed from the original signal, and how it affects the integrated velocity and displacement, since, in those cases, errors due to the modelled digitization noise and those induced by the processing routine become indistinguishable.

The simplified transfer function testing approach described above is useful in providing a better understanding of how the accelerogram processing routine works, and where problems are to be expected. Thus, it should be used as a quick preliminary step to a more detailed investigation of the processing method, in which the synthetic test signal used now contains most of the features expected in an accelerogram, as will be done in the next section.

2.4 Analysis of the Original Volume II Method using Synthetic Signals

2.4.1 Analysis Procedure

The synthetic accelerograms developed in Sec. 2.2 can also be used to test problems expected to occur in processing and integration methods for either analog or digital records. The methodology described below is intended to be general enough to be applicable to a wide variety of processing methods. The original Volume II routine is used as an example for testing procedures.

A processing method may be judged through two different criteria. The first question is: how much distortion or error does the correction method add into

the input signal and its integrals, when the continuous, time-limited, and complete signal is quantized and sampled at Δt? This can be defined as a measure of the "*internal performance*" of the method, and can be studied either analytically as in Sec. 2.3, or numerically with the synthetic signals as described below. The second question is: how well does the processing method correct the errors of the input signal, which errors are often of an uncertain nature (i.e., digitization noise, missing data, etc)? Or equivalently, how well does the processing algorithm extract a continuous signal and its integrals from a sampled, noise-corrupted and truncated version? This is a measure of the "*correction effectiveness*" of the method, and it can only be studied by applying the processing method to signals containing accelerogram-like features. It should be noted that, *a priori*, there is no reason why a method could not have poor correction effectiveness but good internal performance, or *vice versa.*

When synthetic signals are used, the answer to the first question (i.e., what is the internal performance of the routine?) requires only a basic understanding of how the processing method works, and where problems may be expected to occur, as opposed to the analytical approach described in Sec. 2.3, which required lengthy derivation of the equivalent transfer functions and careful numerical bookkeeping. In the case of Volume II, as is shown in the flowchart Fig. 2.10, the processing can be separated into two main subroutines. The first one, BAS (steps 1-10), performs the linear correction, decimation and filtering for the acceleration. The second one, HYPSVD (steps 11-20), performs the integration to obtain the velocity and displacement, and also uses BAS for filtering and correction. Each of the functions of the subroutine can be isolated and tested, either by altering the program to monitor the signals before and after the step that is being studied, or by adjusting the processing parameters to activate only one of the steps at a time. The second alternative is easier to implement since it does not require an in-depth understanding of the way the program is written.

The next step is to choose a set of reference values for the variables of the processing method which are to be used for the correction of the synthetic signals. These processing parameters are then altered one at a time, and the change in the

output result is monitored. This part of the analysis identifies the errors added into the original input signal after recording and digitization by the correction scheme, and therefore evaluates the internal performance of the processing method. Testing should be performed on a reference signal, that is, one of the analytically generated accelerograms which has zero final displacement, no noise, and no trigger truncation. The results of this part of the analysis are of the same type as those arrived at analytically in Sec. 2.3.

In the case of the Volume II method, the steps that are expected to create errors within the processing routine are the decimation, interpolation, and integration schemes, and the application of the running-mean and the Ormsby filters. The effect of each of these steps on the signal can be studied independently. The parameter describing the decimation and interpolation steps is the order p. When p is set equal to one, the input signal is kept at its original time increment, and so there is no decimation or interpolation error in the output signal. However, when p is varied, and all other variables are kept at the reference values, the change in the amount of error in the output result can be attributed to the decimation step. In the same manner, the effect of the running-mean filter can be studied by varying the width T_w of the window, and that of the Ormsby filter by changing the number of filter weights, and the values of the cut-off and roll-off frequencies. The errors due to the repeated BAS subroutine corrections of the acceleration and the integrated velocity and displacement, can be separated out, either by skipping BAS (steps 1-10, Fig. 2.10) and using the "uncorrected" acceleration as input to HYPSVD(steps 11-20), or by bypassing BAS within the integration steps of HYPSVD.

It is advisable to first test the method with a simple synthetic "accelerogram," such as *SIN1C* (Fig. 2.8), which is composed of a modulated harmonic at 1 Hz. Any change in the modulated 1 Hz component or any other existing components outside of the modulation bandwidth obtained after "correction" must then be attributed to one of the steps of the processing method. The errors imparted to each of the steps can then be identified by the procedure described above. Narrow-band signals, such as *SIN1C*, are useful in studying which of the steps of the processing routine introduce errors, and by what amount. These types of signals are certainly the

best to use in the study of the internal performance of the processing method, but accelerogram-like data remains useful to observe how each type of error combines in a multi-harmonic signal.

Signals which have all the features of a digitized accelerogram must be used to answer the second question, that is, how does the processing method correct the errors that exist within the input signal, or alternatively how correction-effective is it? This is where the synthetic accelerogram with added noise to model digitization, with missing data to simulate instrument trigger, and with or without any final displacement offset, becomes particularly useful. The synthetic accelerogram is then put through the processing routine. The correction is judged to be effective if it significantly reduces the amount of noise, and estimates other parameters properly, such as the initial conditions and the final displacement. Because the method in which earthquake motions are modelled, as described in Sec. 2.2, is very flexible, a multitude of signals can be created. The uncertain features of the accelerogram can then be added separately to the original synthetic signal to study how well the processing routine corrects for each source of error.

The testing of the internal performance and the correction effectiveness of the processing routine is accomplished by comparing the "corrected" signal at the output of the program, to its corresponding exact analytical representation. Hence, the quantities of interest for the study are the errors between the processed and analytical acceleration, velocity, and displacement at each step. The Fourier transform of these errors can also be used to identify the specific frequencies where errors are introduced.

Both internal performance and correction effectiveness have been extensively studied on many test cases. The results from only a few significant examples will be presented below in Secs. 2.4.2 and 2.4.3.

2.4.2 Internal Performance of the Original Volume II Method

Only the two main sources of error induced by the original Volume II processing method will be analyzed below. These are the aliasing introduced by the decimation-interpolation process, and the effect of the Ormsby filter. The other

errors such as those introduced by the trapezoidal integration rule, the repeated removal of the mean in the signal, and digit truncation of the stored data will be pointed out in some of the figures, but will not be analyzed in detail.

2.4.2.1 Aliasing

A preliminary analysis of the Volume II processing method would show that aliased frequency components are introduced by the steps involving the running-mean filter, the decimation and the interpolation (steps 5, 6, 7 and 9 in Fig. 2.10). As mentioned earlier, each of these steps are described by different parameters: the width T_w, the decimation step size, and the interpolation step size, respectively. It is theoretically possible to study the effect on the output signal of each of these parameters taken individually. However, in the original Volume II routine, these three steps form a whole, and cannot be separated. That is, the running-mean filter width is chosen as a function of the new Nyquist period after decimation, which is itself a function of the decimation step size. Then, the interpolation step restores the decimated data back to its original time step. This reduces the analysis of the aliasing effect to the variation of a single parameter: the decimation step size.

To study the aliasing problem due to decimation, the synthetic signal *SIN1C* (Fig. 2.8), which is composed of a single modulated harmonic with frequency 1 Hz, is subjected to the Volume II routine. The program normally sets the decimation order to be 10 throughout the whole processing routine. However, it has been altered to allow for specified decimation orders in the acceleration (variable NSKIPA), in the velocity (variable NSKIPV), and in the displacement (variable NSKIPD). Also, the subroutine BAS, which performs the acceleration corrections in steps 1 through 10 (Fig. 2.10), can be bypassed in order to study the effect of the velocity and displacement correction separately. When subroutine BAS of the program is not used, the acceleration that is input at steps 11 and 13 is that of the exact synthetic signal in which no correction has been made.

In the following figures, the titles AN, VN, DN refer to the Volume II-corrected acceleration, velocity and displacement signals; ERA, ERV, ERD are the error between the exact and Volume II-corrected accelerations, velocities and displacements;

FFT ERA, FFT ERV, FFT ERD refer to the plots of the fast Fourier transform of the acceleration, velocity and displacement errors. These will help locate at which frequencies the processing adds errors into the signal. Note that for each of the following figures, the scales are altered as to permit the best observation of the errors. In the figures, the captions also indicate how many Ormsby filter weights are used, and what the cut-off frequency, f_c, and roll-off frequency, f_r, of the filter are.

The effects of the decimation aliasing are shown in the four cases illustrated in Figs. 2.15 through 2.18. Each figure represents the Volume II-corrected output (AN, VN, DN), the error (ERA, ERV, ERD), and the frequency content of the error (FFT ERA, FFT ERV, FFT ERD) for the acceleration, velocity and displacement signals respectively. The Ormsby filter characteristics are kept constant for all four cases, so that only the differences due to the decimation are observed. All the synthetic records used in the study of Volume II are stored with a precision of six decimal digits and at constant time increments of 0.02 sec, with the exception of *Q1C* which is stored with a precision of three decimal points to duplicate accelerogram-like conditions.

The reference test, Case 1, is that of *SIN1C* subjected to the Volume II processing method in its usual operating mode: the acceleration correction step, BAS, is not bypassed and all three decimation orders are equal to 10. This increases the time increment between two data points from 0.02 sec to 0.2 sec, or alternatively decreases the Nyquist frequency from 25 Hz to 2.5 Hz, in all three of the quantities - acceleration, velocity and displacement. Fig. 2.15, which represents plots of the acceleration quantities AN, ERA, and FFT ERA, for Case 1, show that the error ERA induced by the Volume II routine is about a thousandth of the maximum acceleration AN. Thus, it is well within the expected noise level of a real accelerogram. However, *SIN1C* is only composed of one harmonic; in an earthquake-like signal the acceleration is made up of many harmonics, at each of which errors are introduced by the program, thus making the error level larger as will be seen later in Fig. 2.19, when the effect of processing realistic synthetic seismic records is discussed. In the FFT ERA plot (Fig. 2.15) the aliasing error due to the decimation really stands

out. In this plot, the first peak is located at about 0.12 Hz, which coincides with the roll-off frequency of the Ormsby filter, this effect will be discussed in Sec. 2.4.2.2. The other peaks are at frequencies 1 Hz, 4 Hz, 6 Hz, 9 Hz, 11 Hz, 14 Hz, 16 Hz, 19 Hz, 21 Hz, and 24 Hz. These correspond to the original and aliased frequencies of 1 Hz for a signal that has a 2.5 Hz Nyquist frequency, which is the case here since NSKIPA is equal to 10. The errors introduced by the aliased 1 Hz frequency is apparent in ERA (Fig. 2.15) where the error signal exhibits contributions from higher frequencies. As has been studied in the example of Sec. 2.3, a dominant error is located at the signal harmonic frequency, which is 1 Hz for *SIN1C*, and the error at the corresponding aliased components decreases as the value of the frequency increases. Also as expected, the corresponding error at the aliased frequencies in the velocity, FFT ERV, and in the displacement, FFT ERD, have almost disappeared. The aliasing error in the acceleration is a mirror image of the signal AN, as seen in the time domain ERA plot. This effect is still apparent in ERV, but has completely disappeared in ERD. The main source of error in these integrated signals arises from the low-pass Ormsby filter. The errors found in the velocity, ERV, are mainly that of the Ormsby filter at 0.125 Hz which are twice as large as the decimation error at 1 Hz. Also, the predominant error in the displacement signal, ERD, is by far due to the Ormsby filter, which gives some insight as to how this filter can alter the signal, and how it could become difficult to distinguish this type of error from the signal itself.

In Case 2, illustrated in Fig. 2.16, no decimation is required for the velocity and displacement corrections (NSKIPV = 1, NSKIPD = 1), however NSKIPA remains equal to 10. The case shows what happens to the signals when decimation is only applied to the acceleration, and no such error can be introduced by the velocity or displacement correction back into the acceleration (step 15, Fig. 2.10). The final corrected acceleration still displays proof of aliasing, but beyond 4 Hz the frequency content of the error is negligible compared to the error at 1 Hz (ERA, Fig. 2.16), which is almost two times greater than for the previous case (ERA, Fig. 2.15). The error in the velocity (ERV, Fig. 2.16) and in the displacement (ERD, Fig. 2.16) are again mainly due to the Ormsby filter, with some contribution from the 1 Hz component which comes from the integration of the acceleration

error. Also, the velocity signal in this case contains no directly aliased frequencies (FFT ERV, Fig. 2.16) since no decimation is performed.

In Case 3, illustrated in Fig. 2.17 the acceleration used to produce the velocity and the displacement is not corrected, since the BAS subroutine is bypassed (i.e., NSKIPA = 0), and the velocity and displacement are decimated with order 10 (i.e., NSKIPV = 10, NSKIPD = 10). This case can be viewed as the complement of Case 2 to Case 1, the reference test case. Even though the acceleration is not corrected initially, some changes are made in that signal through the velocity correction terms in step 15 (Fig. 2.10); thus the acceleration errors apparent in Fig. 2.17 come from the velocity processing only. The two main errors are at 1 Hz and 4 Hz, with almost no error due to the Ormsby filter at 0.125 Hz. In the ERA plot (Fig. 2.17), the error has a step function appearance which can be attributed to quantization error when the velocity corrective term is added into the acceleration. This step is also responsible for the 1 Hz aliasing error, and could be investigated in more detail. In Case 4 no decimation is used, but BAS is implemented (i.e., NSKIPA = 1, NSKIPV = 1, NSKIPD = 1) (Fig. 2.18). The aliasing error arising from decimation has disappeared, and the dominant source of error in the processed and integrated time histories are induced by the Ormsby filter. Thus, it can be concluded that the predominant acceleration aliasing seen in Fig. 2.15 is produced by the decimation of the acceleration and by the differentiation of the decimated velocity, which is added into the acceleration trace in step 15 of the processing. Proof of this statement can be further confirmed by studying other cases where the decimation steps are varied.

Studying the effect of aliasing on *SIN1C*, which is composed of only one modulated harmonic, helps in better understanding and separating the errors observed in an earthquake-like synthetic signal such as *Q1C* which is made up of a combination of 200 frequencies between 0.05 Hz and 25 Hz. In Fig. 2.19, *Q1C* is subjected to the Volume II routine with the same parameters as *SIN1C* in Case 1 (Fig. 2.15): the decimation orders are set at 10 for all quantities, the acceleration is filtered in BAS, and the Ormsby filter characteristics are the same. In Fig. 2.19, the ERA plot of the acceleration for *Q1C* shows that the error is of the order the noise level expected in accelerograms of large events (Fig. 2.9), and that most of it comes from

the Ormsby filter roll-off frequency, with evidence of some high-frequency noise and aliasing from the velocity decimation superimposed over it. In this case, the step-like error at the end of the signal must be attributed to digit truncation of the stored data. In the ERV plot (Fig. 2.19), the error is again mainly due to the Ormsby filter, and represents about 5% of the velocity signal maximum amplitude. The high-frequency velocity error which is superimposed on the long-period error is due to the trapezoidal rule, as will be explained later on in this section. The long-period error becomes very predominant in the displacement (25% of the maximum), since integration diminishes the contribution of high-frequency components, and because the Ormsby filter error is added into the signal at three different steps before the displacement is obtained.

In the results for *SIN1C* signal processing, the corrected acceleration, velocity and displacement contain errors, but these are very small and the aliased frequencies are well separated without having any influence on other existing harmonics. Thus the overall shape of the new signals are practically unchanged from their original form. However, when many harmonics are used to model the signal as in *Q1C*, the processing method, through the filtering and decimation steps, completely change the content at each of the components which correspond to an aliased frequency, thus altering the overall appearance of the "corrected" signal. Indeed, the differences between the exact integrated signals (Fig. 2.4) and the processed integrated signals (Fig. 2.19) are apparent to the "naked eye." In the velocity and displacement signals, the long-period drift is clearly visible, the initial values have substantial errors (they should be zero), and the peak values are slightly different. These same remarks hold for a wide range of synthetic accelerograms tested on the original Volume II processing method.

2.4.2.2 The Ormsby Filter

Comparison of various plots and cases shows that the main source of the processing-induced error comes from the Ormsby low-pass filter. To help identify more clearly the key sources of errors, preliminary analysis is performed of the errors induced by the Ormsby filter on a narrow-banded signal such as *SIN1C*.

More complex earthquake-like signals can subsequently be used to investigate the combined effect of filter errors on the accelerograms.

As discussed in Sec. 2.3, the largest source of error is induced by the rippling of the Ormsby filter at the cut-off and roll-off frequencies, due to the Gibbs phenomenon (i.e., the inability of a truncated Fourier series to represent a discontinuity in the frequency domain). The nature and size of the rippling is controlled by the order of the discontinuity and by the number of filter weights taken to compute the time series. When applied to the Ormsby filter, this translates into a study of the changes in the ripples due to variations in the roll-off to cut-off frequency interval, and the number of weights used to describe the filter in the time domain. These changes can be directly observed by plotting the transfer function of the filter as it is actually implemented within Volume II. The following concern is then to inspect what effect the changes in the ripples have on the output signal.

In the examples discussed previously, Cases 1 through 4 of *SIN1C*, the roll-off and cut-off frequencies of the filter have been kept the same for all cases. The number of weights were computed as a function of the difference between these two frequencies and the order of decimation, and is meant to give a maximum overshoot of the Ormsby filter due to the Gibbs phenomenon of 1.2% at the cut-off and roll-off frequencies (Eq. 2.3.5). Thus, for $f_c = 0.105$ Hz and $f_r = 0.125$ Hz, the filter is computed with 250 weights if the order of decimation p is equal to 10 ($\Delta t = 0.2$ sec), or with 2500 weights if the p is equal to 1 ($\Delta t = 0.02$ sec). Comparison of the plots FFT ERA for $p = 10$ (Fig. 2.15), and for $p = 1$ (Fig. 2.18), shows that the error in the acceleration that occurs at the filter roll-off frequency is approximately the same. This proves that the way the number of weights is computed does keep the ripple error within the same order of magnitude, when the number of filter weights are modified to comply with the decimation step.

But why does the error show up at the roll-off frequency f_r of the low-pass Ormsby filter (Fig. 2.13)? There is further evidence of this behavior when *SIN1C* is tested for other values of the cut-off frequency. In the following two cases, Case 6, $f_c = 0.23$ Hz, and Case 8, $f_c = 0.15$ Hz, the data is decimated with order $p = 10$, the roll-off frequency f_r is kept at 0.25 Hz, and the number of filter weights are estimated

as to conserve a 1.2 % Gibbs's phenomenon overshoot at the discontinuities of the Ormsby filter. The respective Fourier transforms of the error in the output records, FFT ERA, FFT ERV, and FFT ERD, are shown in Figs. 2.20 and 2.21. All the plots consistently indicate a sharp peak at frequency 0.25 Hz, which coincides exactly with the chosen roll-off frequency, regardless of the value of the cut-off frequency.

Insight into this observation can be gained by considering not just the transfer function of the Ormsby filter, but that of the complete input-to-output relationship. Indeed, as was described in Sec. 2.3, each time-domain operation of the Volume II processing method can be represented by a transfer function. These steps are the application of the running-mean filter, the decimation, the low-pass Ormsby filter, the interpolation and the removal of this low-passed signal from the original input to obtain a high-pass filtered record. In the frequency domain, this succession of steps is analytically represented by the combined product of each of the corresponding transfer functions. In particular, one must consider the product of the running-mean filter transfer function $H_1(f)$ for $T_w = 0.4$ sec (Fig. 2.11), and that of the Ormsby filter $H_2(f)$, for $f_c = 0.23$ Hz and $f_r = 0.25$ Hz (Fig. 2.13.a). Fig. 2.22 shows $H_2(f)$, as well as the blown-up views of the behavior of the resulting transfer function $H_1(f) * H_2(F)$ at the cut-off and roll-off frequencies. These figures illustrate the transfer functions governing the output signals obtained in Case 6. The runnning-mean filter transfer function (Fig. 2.11) decreases by about 1.5%, from 1 at *d.c.*, to 0.985 at 0.25 Hz, and the amount of error induced by the Gibbs phenomenon at f_r and f_c in the Ormsby filter is approximately 1.2%. When both filters are multiplied, the resulting transfer function (Fig. 2.22) is always less than 1, except at *d.c.*. In particular, the ripples at the cut-off frequency are always below 1, with a maximum overshoot error close to 1, and after the roll-off frequency the ripples oscillate about the zero axis and are either negative or positive, with a maximum overshoot error of about -1.1%. When this resulting low-pass filter is tranformed into a high-pass filter, by subtracting 1 from the product of the transfer functions (Fig. 2.13.b), the amplitude at the cut-off frequency f_c is nearly zero, hence no error is introduced, but that at the roll-off frequency is now equal to 1.011, which increases the contribution of the aliased frequencies by 1.1%. Similar conclusions can be reached from the study of the transfer function for Case 8 (Fig. 2.23) for

$f_c = 0.15$ Hz with 50 filter weights. In Case 8, it can also be seen that the value of the combined transfer function $H_1 * H_2$ is slightly greater than 1 at f_c. When the high-pass filtering step is implemented (i.e., $1 - H_1 * H_2$), Volume II will generate an error at f_c with negative phase. Hence, in general the original Volume II routine will spuriously increase the component at the roll-off frequency regardless of the cut-off frequency f_c, and, for low enough values of f_c, components with negative phase can be generated. The resulting errors in the output signal are a function of the Gibbs overshoot and the value of the running-mean filter's transfer function at the roll-off and cut-off frequencies.

In Case 6 and 8 (Figs. 2.20 and 2.21) the interval between the roll-off and cut-off frequencies have been increased from 0.02 Hz to 0.10 Hz, thus decreasing the number of weights from 250 to 50, to maintain a maximum ripple overshoot of 1.2 % in the Ormsby filter transfer function. However, these plots show that the errors in the acceleration, velocity and displacement are decreased as the width of the ramp is increased. The error in the acceleration, FFT ERA, at the roll-off frequency is 0.0038 when $\Delta f = 0.02$ Hz (Case 6, Fig. 2.20), and .0017 when $\Delta f = 0.1$ Hz (Case 8, Fig. 2.21).

The latter phenomenon can be partly explained by the fact the amplitude of the transfer function for the running-mean filter $H_1(f)$ becomes closer to 1 as f_c becomes smaller. Comparison of the behavior of the combined transfer functions $H_1(f) * H_2(f)$ near the cut-off and roll-off frequencies for each of the cases (Figs. 2.22 and 2.23) shows that the amplitude of the overshoots at f_r and f_c are reduced, although the maximum errors in the Ormsby filter at both f_r and f_c are still of the order of 1.2%. Also, the ripple interval of the Gibbs phenomenon at the roll-off frequency increases in almost the same proportions as the number of filter weights and the width of the filter ramp. For large transition bands, the ripples at the cut-off frequency have virtually disappeared and have been replaced by a slowly increasing ramp with a smooth transition at f_c (Fig. 2.23). Although Eq. 2.3.7 appears to provide an adequate estimate of the amplitude of the maximum overshoot error at the discontinuity of the Ormsby filter $H_2(f)$, it does not reflect how spread out

the rippling of the error is, what frequency range is affected by it, and what the amplitude of the error of the combined filter $H_1(f) * H_2(f)$ is.

Another source of error which has been studied is the repeated filtering of the acceleration, velocity and displacement, to produce the "corrected" signals. It was concluded that the errors in the velocity time history increase with the number of times the Ormsby filter is implemented in the routine. Such a conclusion could not be made for the displacement signals. It appeared that the main source of error arises from the correction in the temporal means. As will be seen in Sec. 4.3, forcing the unknown temporal mean of a truncated accelerogram to be zero creates a discontinuity at the ends of the time histories. This appears as a $\frac{\sin f}{f}$-type error in the spectrum, which is centered at *d.c.* This error in the *d.c.* of the spectrum increases as the discontinuity becomes larger.

Using the narrow-banded signal *SIN1C* has helped to pinpoint the sources of errors within the processing method by comparing the spurious frequencies as a function of the characteristics of the Ormsby filter. It is also possible to use a synthetic signal such as *Q8C* (Fig. 2.7) to study the errors induced by the Ormsby filter. Recall that this signal was generated by combining 200 harmonics between 0.4 Hz and 25.0 Hz. As an example, this synthetic accelerogram is processed with Volume II, in its normal operating mode, for two different locations of the low-pass filter ramp. The output displacement results, as well as the error with the exact analytical displacement signal, are illustrated in Fig. 2.24. In the first case, shown on the left of the figure, the roll-off frequency of the Ormsby filter $f_r = 0.125$ Hz and the cut-off frequency $f_c = 0.105$ Hz. In the second case, shown on the right of of the figure, $f_c = 0.18$ Hz and $f_r = 0.20$ Hz. Since the cut-off ramps, which are of equal width, are located far below the smallest modulated harmonic present in *Q8C* at 0.4 Hz, there should be very little difference in the signal after processing. However, as can be seen in Fig. 2.24, this is not the case. The error in the displacement varies between 8% to 11% of the maximum, depending on the location of the cut-off ramp and the amount of aliasing induced by the decimation steps at that location. In both examples, the source of the error is clearly a sine-like function, with a period in the range of the selected Ormsby filter transition band. This is also a good

illustration of how a spurious harmonic can be added without altering the "look" of a signal, and how it might result in misleading conclusions. In the example on the left of Fig. 2.24, it is rather obvious that the behavior at the end of the record is not physically possible, and that it must be due to some error induced by the processing method. But in the example on the right, the displacement record decays properly, even though the filter added an erroneous component at the roll-off frequency with an amplitude equivalent to about 10% of the maximum. An engineer, not familiar with processing-induced errors in the accelerations, might be tempted to conclude that this strong component may be due to the response of a structure or of the underlying soil at resonance.

Separating the true harmonic composition of a record from the error added in by the Ormsby filter becomes even more difficult when the cut-off ramp coincides with frequencies existing within the signal. Synthetic record *Q1C*, represented in Fig. 2.4, is used to illustrate this case. *Q1C* is composed of 200 harmonic components between 0.05 Hz and 25 Hz. It is subjected to the original Volume II routine, in its normal operating mode. The Ormsby filter roll-off frequency is equal to 0.125 Hz, and the ramp is 0.02 Hz wide for the high-pass filtering. The results, presented in Fig. 2.19, show the output acceleration, velocity and displacement, as well as the error with the corresponding exact analytical signals. The error in the processed acceleration represents less than 0.5% of the maximum and is mainly composed of a combination of the filter error and digital storage truncation error. Most of the synthetic signals processed with Volume II showed that the method-induced errors in the acceleration were comparable or below the normal noise level found in real analog accelerograms. Hence, the corrected accelerations obtained with the original version of Volume II can be used with confidence.

This is not always the case with the processed velocity and displacement. The difference between the processed and the exact signals are clearly visible, and the error plots for the velocity and the displacement confirm that the difference is a sine-like function that has a period which coincides with the Ormsby filter transition band. In real accelerograms, the processed signal could be misinterpreted as having a predominant resonant frequency in that range.

The values of the peak velocity and displacement of the "corrected" signal are inaccurate. This results from the uncertain manner in which the processing errors and the uncorrected accelerogram combine, and depends on the frequency content of the seismic event. For instance in Fig. 2.19, the error in the acceleration of *Q1C* represents about 0.5% of the maximum, the error in the velocity about 5%, and in the displacement about 25%. These numbers were more or less consistent for a large number of tested cases with signals that did not simulate digitizing noise, trigger truncation or expected final offsets in the displacements. The latter sources of uncertainties are expected to increase the errors in the final output, as will be shown when the processing method is tested for its correction effectiveness in Sec. 2.4.3. Hence, as has been speculated previously, the amount of processing error increases as the signal becomes more complex, but the amount of error that is added into an input accelerogram by the processing method varies from one case to the next, and cannot be exactly quantified. However, application of many analytically generated accelerograms to the processing routine can help get a better feel for the internal performance of the method.

The way the processing-induced errors contaminate the input signal may also have significant implications on the choice of the high-pass filter cut-off frequency. Earthquake engineers traditionally emphasize the contamination of accelerogram by long-period noise. Their emphasis is motivated by the observations of many processed velocity and displacement records which exhibit long-period drifts. They rely on high-pass filters to remove these errors, and they choose the cut-off in such a way that the long-period behavior is no longer apparent in the processed records. In view of the previous discussions, this can compound the problem. Indeed, as shown, the largest source of long-period error when using the original Volume II method may not be the one contained in the recorded accelerogram, but that introduced by the Ormsby filter at the cut-off and roll-off frequencies. In the process, actual low-frequency information of significant scientific importance may also have been removed.

Another source of error that can be observed in the velocity (Fig. 2.19) is high-frequency noise, which is strongest at the beginning of the signal, but decays rapidly. This high-frequency error is almost nonexistent in the displacement record, compared to the level of the filter-induced error. This processing noise is produced by the trapezoidal integration rule, which cannot integrate properly at high frequencies, as is shown in the comparison of its transfer function to the exact integration (Eqs. 2.3.12 and 2.3.13). Because of the initial arrival of the P waves in the accelerogram, or because of the faster decay of the high-frequency harmonics in the synthetic records, the acceleration usually exhibits high-frequency motions mostly at the beginning. Hence, after using the trapezoidal rule to integrate the acceleration into the velocity, the error is expected to be greatest at the beginning of the signal, as is shown in Fig. 2.19. Integration emphasizes the contribution of the lower frequency components over the higher frequencies. Hence, integration from velocity to displacement with the trapezoidal rule creates a lesser amount of error, as shown in Fig. 2.19.

In summary, this section illustrated the versatility of the synthetic records in identifying the errors induced by a processing method and in evaluating its internal performance. This approach can be used on any processing method, without requiring expertise in digital signal processing, to pinpoint the exact source of the error, as well as the added amount it contributes to the input signal. The synthetic signals also prove to be quite useful in showing how the procesing errors and the input signals could combine to produce errors in the output signal which could have gone by unnoticed, had it not been for the comparison with the exact analytical counterpart. Synthetic signals are next shown to be even more useful in evaluating the correction effectiveness of a processing method.

2.4.3 Correction Effectiveness of the Original Volume II Method

A processing method is defined to have perfect correction effectiveness if it is capable of reproducing the exact acceleration, velocity and displacement at the recording site. This implies that the method can remove all the digitizing noise from the raw data, identify the missing initial conditions due to instrument trigger, and cope with the final displacements that may occur along a fault or within a

damaged structure. Although this ideal can never be achieved, it is possible for one processing method to correct better than others the errors in the input signal.

Some aspects of the correction effectiveness of a method have been tested by monitoring both the acceleration and the displacement produced on a shaking table, and comparing the measured displacement with the one obtained after processing and integration of the acceleration [Trifunac *et al.*, 1973; Khemici & Chiang, 1984]. These tests can only provide information on the processing method's capacity to identify final displacements, and possibly initial conditions, but are not flexible enough to measure and vary the noise level within the acceleration. This manner of testing a processing method's correction effectiveness is not only very time-consuming, but it also requires an elaborate and expensive laboratory setup. It is the purpose of this section to show how the correction effectiveness can be tested very simply and thoroughly with the synthetic accelerograms.

In Sec. 2.3 an analytic expression was derived to describe an earthquake accelerogram with or without final displacements. Methods to simulate the missing initial points due to trigger and added digitizing noise, for various earthquake sizes, were also presented. Each of these features: final displacement, initial truncation of the data, and digitizing noise, can be incorporated one at a time into the exact synthetic acceleration. These can model accelerogram records for either large events (e.g., 0.5 g maximum acceleration) or small events (e.g., 0.05 g maximum acceleration). Separating the sources of error in the input will help to evaluate the correction effectiveness of the processing method in each of the cases. The correction effectiveness of the processing method can also be studied on the synthetic records contaminated with combined sources of error. Also, because of the ease with which the synthetic signals can be generated, the processing method can be tested with many different accelerograms.

The following conclusions of the analysis are illustrated through the results obtained for only one of the synthetic signals, *Q1*. In the previous section, this same synthetic signal was used in its "simplest" form to study the internal performance of the Volume II method: it contained no noise to simulate the digitization process, it did not have missing initial points to model trigger truncation, and the final

displacement was zero. This signal is refered to as *Q1C*. To distinguish it from the other forms of the signal the following notation convention is used. The added letter "*N*" means that the signal has added noise, "*T*" means that the initial points have been removed to simulate trigger effects, "*U*" means that the final displacement is nonzero, as opposed to "*C*" which corresponds to the case where there is no offset in the final displacement. The levels at which these effects are incorporated into the synthetic signal are denoted by letter "*L*" for a large earthquake and "*S*" for a small earthquake. For example *Q1UNTS* is the synthetic signal *Q1*, which has nonzero final displacement, with added noise and initial trigger truncation to simulate small seismic events.

Figs. 2.25 through 2.28 show the output acceleration, velocity and displacement, as well as their respective errors based on the exact "uncontaminated" analytical values. All the signals are processed with the original Volume II method, in its normal operating mode. Unless it is mentioned otherwise, the low-pass Ormsby filter that is used in the high-pass filtering stages has a cut-off frequency $f_c = 0.105$ Hz and a roll-off frequency $f_r = 0.125$ Hz. The input signals used to illustrate this study of the Volume II method are, in the same order as the figures, *Q1U*, *Q1CNL*, *Q1CNS*, *Q1UNTS*. The conclusions obtained from each of these tests are described below.

2.4.3.1 Effects of Final Displacement Offsets

The way Volume II processes a record, which exhibits a final displacement offset, is illustrated by the processing of synthetic signal *Q1U* (Fig. 2.25); the exact analytical data is shown in Fig. 2.3. As expected, because of the multiple linear correction steps within Volume II, the final offset cannot be recovered. Comparisons with the processing results of *Q1C* (Fig. 2.19), also show that the two signals produce very similar output records, providing no clue as to the possibility of a final offset. This could have been predicted since the only difference between a signal that has an offset in the displacement and one that does not, lies in the difference in the mean of the velocity. It is a nonzero mean in the velocity that produces a final offset in the displacement, when the initial value is equal to zero. Hence, removing the mean in the velocity, as is done in Volume II, regardless of

whether a final offset is expected or not, should indeed produce approximately the same displacement after integration. Consequently, this processing method cannot be used to study possible final displacement offsets, such as would be expected for motions recorded along a fault or within a damaged structure.

The inability of Volume II to cope with permanent offsets can create other very large errors within the displacement signals. Comparison of the exact displacement *Q1U* (Fig. 2.3), and its processed and integrated counterpart (Fig. 2.25), shows how much the processing has altered the signal. The most noticeable error occurs at the maximum of the record, which is decreased from its true value of 0.35, down to 0.16. This is an error of over 90% at the peak. This is a particularly good example of how a processing method can significantly alter a signal to such an extent that it is no longer even an approximate representation of the actual motions.

The large error in the displacement, due to the method's inability to recover permanent offsets, also produces additional errors in the processed acceleration and velocity. This is due to the steps within Volume II which adjust the velocity by a constant obtained from the least squares fit of the displacement, and subsequently to the equivalent steps which correct the acceleration from the velocity, as shown steps 11, 12 and 13 of Fig. 2.10. Compare the results obtained after processing of *Q1C* (Fig. 2.19) and *Q1U* (Fig. 2.25). The error in the velocity, which in both cases is a maximum at the initial value, has more than tripled from *Q1C* to *Q1U*, increasing from 0.020 which represents 5% of the peak value, to 0.070 which is 18% of the peak. The high-frequency error at the beginning of the record, due to the trapezoidal integration rule, is still noticeable in the error of *Q1U*. In *Q1C*, the integration-induced error is of the same order as that resulting from the Ormsby filter (i.e., 5%). However, in *Q1U*, the trapezoidal rule error in the velocity is still 5%, and contributes much less to the overall 18% error than does the long-period oscillation about the Ormsby filter transition frequency band. Similarly, comparison of the acceleration errors show that the level has more than doubled from *Q1C* to *Q1U*. This trend is noticeable in other synthetic traces. This is due to the way the signal must adjust itself to comply with the zero mean velocity requirement, in combination with the added filter error due to the Gibbs phenomenon.

It must then be concluded that, as expected, the original Volume II method is very ineffective in correcting signals which have a nonzero final offset in the displacement, since these cannot be identified or reproduced. It has also been shown that the error levels in the processed acceleration, velocity, and displacement are greatly increased in recorded signals which yield final displacement offsets. This could be particularly troublesome as it is often impossible to predict whether an actual accelerogram should exhibit a final displacement offset or not. Also the records from which an offset is expected are often those that are produced by very large levels of shaking, and hence of greatest scientific interest, and yet they turn out to be those in which the processing method generates large amount of error.

2.4.3.2 Effects of Digitizing Noise

To simulate the digitization process on an accelerogram, white noise is added onto synthetic signal *Q1C*, as described in Sec. 2.2.4. *Q1CNL* models the digitization noise level of a large event with peak acceleration of approximately 50% g, with a signal-to-noise ratio equal to 500. *Q1CNS* models the digitization noise level of a small event with peak accelerations of about 5% g, with a signal-to-noise ratio equal to 50. Hence, *Q1CNS* is the synthetic signal *Q1C* which is contaminated by 10 times more noise than *Q1CNL*. The results of the processing by the original Volume II method on the noise-free synthetic signal *Q1C* (Fig. 2.19), and on the noise-contaminated signals *Q1CNL* (Fig. 2.26) and *Q1CNS* (Fig. 2.27) are compared to study how the increasing noise levels alter the corrected acceleration, velocity and displacement.

Adding noise in the acceleration changes its mean, and hence creates a linear drift in the velocity and a parabolic drift in the displacement. The only feature within Volume II which corrects this aspect of noise-induced errors are the repeated linear-trend corrections, which remove the mean in the acceleration, velocity and displacement. This, however, also makes it impossible to recover any possible final offset in the displacement, and can produce significant errors in the output signals, as was discussed in the previous section. Also, because laboratory tests have shown that the digitization process can be modelled as white noise, the error level due to this type of noise is equally shared on the average among all the frequencies of

the signal's spectrum. Volume II only removes the digitization noise outside the band-pass filter's roll-offs, but does not alter it, let alone decrease or remove it, within the frequency range defined by the the band-pass.

A preliminary analysis has shown that the simulated digitization noise is still present in the processed accelerations. To examine more thoroughly how much of the noise is removed from the acceleration, and to identify the underlying errors, the ERA plots shown in Figs. 2.26 to 2.28 represent the errors between the noisy input acceleration and the noisy processed acceleration. The ERV and ERD plots in those figures represent the errors between the exact noise-free synthetic velocities and displacements and the noise-contaminated processed and integrated counterparts. Comparison of the plots of the corrected accelerations show that there is very little perceptible difference between the processed results of *Q1C* (ERA, Fig. 2.19) and *Q1CNL* (ERA, Fig. 2.26). Since the ERA plots in these two figures are almost identical, it can be concluded that the simulated digitization noise affected the noise-contaminated acceleration in an identical manner before and after processing. The same remarks and conclusion apply for the noise-contaminated simulation of a small event such as *Q1CNS* (ERA, Fig. 2.27). Hence, Volume II does not alter the nature and the level noise present in the signal, and has very poor correction effectiveness with regard to digitization noise.

For large event simulations, the noise level is of the order of 10^{-2} (Fig. 2.9), and is comparable in magnitude to the processing-induced errors. The underlying error (i.e., without the digitization noise) in the acceleration after processing is greater by 1% when noise is added to simulate conditions for large events, than when there is no noise at all (ERA, Figs. 2.19 and 2.26). The errors in the velocity and the displacement are also of that same order. In the processed velocity, the digitization noise is still present, but it produces errors which are of the same magnitude as the trapezoidal integration rule, and are smaller than the filter-induced error. The same comments that were made on the processing errors due to Volume II on *Q1C* still hold for *Q1CNL*, namely that a dominant source of error is the Ormsby filter, even after noise is added into the signal. This could have been predicted, since the error in the acceleration due to the filter internal performance is of the same order

as the noise level for large event simulations. Thus, for large events, the internal performance error due to the processing is of the same order of magnitude as the error due to digitization noise.

The additional digitization noise would be expected to produce linear and parabolic drifts in the integrated records, due to the change in the mean acceleration. These differences are not apparent in *Q1CNL* (ERV and ERD, Fig. 2.26) since Volume II performs multiple linear-trend corrections to remove the temporal means of the acceleration, velocity and displacement, and the errors in the temporal means are an order of magnitude lower than the filter-induced error. Therefore, the processing method is correction effective in removing the errors in the mean due to the noise for untruncated large events, but the errors due to the poor internal performance of the filter overshadow the possible differences in the processing results between the clean and noise-contaminated signals.

When the noise level is increased to simulate small events, as in *Q1CNS* (Fig. 2.27), the differences in the processing errors of a clean and a noise-contaminated signal are more apparent. This is especially true in the plot of the processed and filtered acceleration (AN), which still exhibits high-frequency noise throughout the signal of the order of 10^{-1}. This is a clear indication that Volume II does not remove digitization noise properly. For small event simulations, the errors in the corrected acceleration due to the digitization noise are one order of magnitude larger than the errors attributed to the processing method. Nevertheless, after processing of *Q1CNS* (Fig. 2.27), the errors in the velocity and displacement are comparable in magnitude to the errors found after processing of *Q1C* (Fig. 2.19). The largest difference between digitization noise simulation of large and small accelerograms is noticeable in the output error of the processed velocity. It appears to be a combination of the filter-induced effects, and the high-frequency digitization noise, which for small events significantly contributes to a change in the mean acceleration, and hence alters the way the velocity must adjust itself to comply with the zero mean velocity criteria imposed by the processing method. Because integration greatly reduces the contribution of the higher frequencies, the error in the displacement is still mainly that of the low-pass Ormsby filter used in the high-pass filtering stages. The errors

due to the change in the mean acceleration by the digitization noise are properly corrected for in this case since neither the velocity or the displacement drift away.

One of the most noticeable features of the study of noise effects on the Volume II method is that, regardless of the noise level, the processing produces very similar accelerations, velocities and displacements, as can be seen in the comparisons of *Q1C*, *Q1CNL*, *Q1CNS*. Hence, although the original Volume II method exhibits poor internal performance, because of its use of the Ormsby filter, and is relatively ineffective in removing the noise within the data, it is nevertheless consistent in producing similar signals over a wide range of noise levels.

2.4.3.3 Effects of Initial Trigger Truncation

The original Volume II processing method does not explicitly try to obtain the true value of the signal at the time of trigger. Indeed, the initial value comes up indirectly as a result of the removal of the linear trend in the acceleration, velocity and displacement, after the filtering and integration steps have been performed. It may have been presumed that the initial values obtained by the processing method are a close representation of the actual quantities. The synthetic accelerograms are used to show that, in fact, this is not always the case.

There was no simulation of trigger effects in any of the previously studied cases (i.e., *Q1C*, *Q1CNL*, *Q1CNS* and *Q1U*), and the true initial acceleration, velocity and displacement are equal to zero for all of them. However, after processing with Volume II, the results show a great disparity in the evaluation of the initial conditions. For *Q1C* (Fig. 2.19), the initial acceleration is estimated to be equal to 0.02, which is the largest error in the signal at 0.5% of the peak; the initial velocity is -0.02, which is also the largest error in the record at 5% of the peak, and the same holds for the initial displacement at 0.05, which is equivalent to 25% of the peak. Thus, the relative error in the estimate of the initial data point is increased by about one order of magnitude for each successive integration step within Volume II. The error in the initial acceleration is very small, the error in the initial velocity is significant enough to be noticeable and could be easily misinterpreted as an actual truncation effect, but the error in the initial displacement is too large to be representative of any kind of earthquake-induced motion. Indeed, physically,

the first arrival of the high-frequency waves at the time of trigger is not expected to generate such large displacements. On the contrary, the displacements at the beginning of the event should be close to zero, and they should pick up with the arrival of the longer period waves. The error in the initial acceleration estimate increases to accomodate the additional digitizing-induced error when noise is added to the signal to simulate either a large or a small event, as is shown in the plotted results of *Q1CNL* (Fig. 2.26) and of *Q1CNS* (Fig. 2.27). However, the initial estimate of the velocity and the displacement do not change much when noise is added. For *Q1U*, the relative error in the initial conditions change slighty because of the improper handling of the final displacement offset. This causes the error in the initial velocity to be greatly increased from 5% to 20% of the peak, even though the errors in the initial acceleration and displacement do not vary much. The variations in the estimate of the initial values can be attributed to changes in the temporal means of the time histories induced by the digitization noise and the removal of the final displacement offset.

The test cases show that the errors in the estimates of the initial conditions are usually the largest errors to be found within the processed signals. However, there is no definite pattern between the error of the initial estimate at the time of trigger, and the amount of missing data. Comparison of the processing-induced errors on many different synthetic accelerograms modelled for trigger truncation shows that the estimate of the initial acceleration is fairly reliable (0.5% error relative to the peak), the estimate of the initial velocity is often questionable (about 5% of the peak), but the estimate of the initial displacement is very uncertain (up to 50% of the peak). Again, the errors in the estimate of the first data point after trigger increases by about one order of magnitude for each integration step. This significant increase in the relative amount of error is due to the combination of the triple filtering and correction of the signal, and the increase in the long-period error due to integration.

It is interesting to note that the error level of the untruncated synthetic signals, with or without added noise modelled for small and large events, are approximately the same. The study of the correction effectiveness of Volume II with truncated

synthetic signals also produced very similar output results for any amount of trigger truncation. This implies that, as for the case of the noise-contaminated signals, the processing method handles trigger truncation in a consistent manner regardless of the extent of the missing data, and that it is the poor internal performance of the high-pass filter steps that largely dominate the errors.

2.4.3.4 Effects of Combined Error Sources

Noise, truncation and final displacement offsets can also be combined in synthetic signals, and processed with the original Volume II method. An extensive study showed that regardless of the amount or nature of the input error, and regardless of the true temporal mean value of the signal, Volume II will always make the means of the acceleration, velocity and displacement zero. This in turn implies that, for any type of input error added to a particular synthetic record, the output signal will always be approximately the same, and the error in the output signal will usually be of the same order of magnitude. Thus, it is not the level of recording and digitization noise, but rather the poor internal performance of the processing method that governs the amount of error measured in the output records.

The highest degree of combined input error is found in synthetic signals such as *Q1UNTS*, which model digitization noise, start-up truncation (11 initial data points are dropped) and nonzero final displacement offsets for small events. Though a small earthquake is physically not expected to generate significant final offsets in the displacement, *Q1UNTS* can be used as the more severe test case to study the correction effectiveness of the processing method. In that respect, *Q1C* is the most favorable case to test the correction effectiveness of the processing method, since it contains none of the recording and digitization-induced input errors.

The output acceleration, velocity and displacement obtained for *Q1UNTS* with Volume II, as well as the respective errors are shown in Fig. 2.28. Disregarding the digitization error, the output error in the acceleration for *Q1UNTS* is very similar to the results obtained for *Q1U*, the corresponding synthetic signal which contains no noise or no truncation (Fig. 2.3). The maximum acceleration error relative to the peak is of the order of 0.5% in both cases. The main difference lies in the digitization noise which is still apparent in the processed and corrected output

acceleration of the noisy signal AN, indicating once again that Volume II is not correction effective in removing noise within the usable frequency band of the filter, as expected. There is still some evidence of digitization noise within the output velocity record VN, but the greatest share of the error comes from the long periods induced by the overshoot at the Orsmby filter cut-off and roll-off frequencies, and by the way the noise-corrupted velocity must comply to the zero mean criteria of the Volume II processing routine. In this case of course, the true mean velocity is not zero, since final displacement offsets are expected, which implies that the processing method induces even more error when making the temporal mean velocity zero. This explains why the relative error in the output velocity has gone up from about 5% for *Q1C*, to about 20% for both *Q1U* and *Q1UNTS*. Hence, the error due to the non-identified final displacement offset seems to overshadow the errors that could have been induced by the digitization and recording processes.

Once again, however, the output records of *Q1UNTS* produced by the Volume II processing method are very similar to the output records of any of the other related signals generated by *Q1*, regardless of the sources or sizes of the input errors, for the same reasons that were explained before. In agreement with the previously studied signals, the error in the initial estimates is disparate and follows no specific trend. It is off by a factor of 50 in the acceleration, which represents however an error of only 0.1% of the peak value. The initial velocity is off by about a factor of 20, at a level comparable to 5% of the peak, and similarly the initial displacement is off by a factor of 40 which represents about a 6% error relative to the peak.

2.4.4 Concluding Remarks

In the study of the correction effectiveness of the processing method, it has been shown that there is very little variation in the results of the output records between *Q1UNTS* (Fig. 2.28), the worst scenario case, and *Q1C* (Fig. 2.19), the most favorable case. It was shown that the original Volume II processing method is ineffective in removing the digitization noise within the acceleration, in estimating initial values at the time of trigger, especially in the displacement, and it is completely incapable of recovering final displacement offsets, as may occur along a

fault or within a damaged structure. However, because the major effect of each of these sources of errors is to alter the mean of the signal, and because the processing method repeatedly removes the *d.c.* of the acceleration, velocity and displacement, the output signals will always be approximately the same regardless of the input errors, or the true value of the mean of the signals. In that respect, Volume II can be said to be consistent.

It was also shown that Volume II is insensitive to digitization noise and truncation because it is the internal performance of the method which dominates the error in the output signal. The error level is about 0.5% in the acceleration, 5% to 10% in the velocity and 25% or more in the displacement. When the true record is one which should produce a nonzero final offset, the error in the processed velocity may increase up to 20%, and may exceed 75% in the displacement.

In the case of the Volume II method, it was concluded that the poor internal performance is a result of the multiple use of the low-pass Ormsby filter used in the high-pass filtering stages, and the decimation and the mean removal from the acceleration, velocity and displacement. Also, Volume II did not have good correction effectiveness since it did not remove the digitization noise, nor did it properly estimate the true value of the signals at the time of trigger or recover existing final displacement offsets. Some of these sources of errors have been identified in the past, as will be discussed further in the next section; however, the testing procedure proposed in this chapter presents a thorough and systematic way to quantify the amount of error induced by a correction method, as well as the amount of noise removed from an accelerogram-like signal.

The purpose of Sec. 2.4 is to demonstrate the testing procedure rather than showing the specific problems of the original Volume II method. The latter was used because its computer code was readily available. It was widely distributed and used for accelerogram processing in the seventies. We stress that some of the sources of errors have been detected and corrected by various researchers in the 1980's. In the United States, at least, this version of the Volume II routine is no longer in use, and has been replaced by various corrected versions. It must be noted nevertheless, that

when it was first proposed in the early seventies, the original Volume II method was by far the best accelerogram processing method available at the time.

2.5 Discussion of Other Processing Methods

The previous analyses have shown how the versatility of the synthetic signal proved to be a valuable tool which permitted an in-depth study of the internal performance and the correction effectiveness of the original Volume II method. Though some of the conclusions that resulted from the study have already been published by other researchers, the novelty of this approach lies in the systematic way any source of error can be measured and identified. The methodology that was used to study the original Volume II method is general enough to be applied to any other of the existing accelerogram processing methods, be it records from analog or digital accelerographs.

In the last several years, many attempts have been made to improve what is defined herein as the internal performance and correction effectiveness of the original Volume II processing method. The aliasing error induced by the decimation step has been identified by Fletcher, *et al.* [1980], and this step is no longer implemented in most current processing methods. Because of the development of better digitization techniques, accelerograms are now routinely discretized at 0.01 sec, thus increasing the Nyquist frequency up to 50 Hz, and reducing the effects of high-frequency aliasing. To limit the errors induced by the Ormsby filter, guidelines are now used to choose the high-pass cut-off frequency and ramp; these are selected on the basis of the low-frequency noise limitations of the instrument, the record length, and the faulting duration [Basili & Brady, 1978; Shakal & Ragsdale, 1984]. Nonetheless, errors due to the Ormsby filter are still expected to contaminate the processed accelerograms. The U.S. Geological Survey has substituted the nonrecursive Ormsby filter by the recursive Butterworth filter to decrease the amount of error induced at the low-frequency cut-off [Converse, *et al.* 1984]. However, recursive filters distort the phase of the original signal, and an extra correction step is necessary to reestablish the proper phase of the accelerogram. Similarly, Shyam Sunder & Connor [1982] have proposed a recursive elliptical band-pass filter, which

will also induce some phase distortion. They also suggest the use of the Schuessler-Ibler integration rule to decrease the errors induced by the trapezoidal integration rule. Khemici & Chiang [1984] propose a frequency-domain approach in which instrument correction, integration, and filtering with the Ormsby filter is performed in a single step. However, they assume that the temporal mean of the acceleration, velocity and displacement are zero, thus making it impossible to recover any final displacement offsets, and creating errors at and about *d.c.* Sunder & Connor [1982] suggest that the integration of the acceleration in the time domain should be performed under the assumptions that the initial velocity and displacement are zero; this may also alter the temporal mean of the velocity and displacement if baseline correction is done by a simple offset. Converse, *et al.* [1984] propose to correct the error in the temporal mean of the acceleration by fitting a straight line through the final portion of the velocity. This assumes that the data has a relatively high signal-to-noise ratio, and that no sources of error other than a shift in the acceleration baseline is responsible for the drift in the integrated velocity.

Although all the changes suggested above are expected to improve somewhat the internal performance of the original Volume II processing method, these have not been thoroughly tested on earthquake-like signals for their effectiveness in decreasing the recording and processing errors, and in reproducing the exact motions of the event. Such an investigation can be easily accomplished by using the synthetic accelerograms developed in Sec. 2.2, and the testing procedure described in Sec. 2.4, on any of the aforementioned accelerogram processing methods, as was done in this chapter for the original Volume II method.

It would appear from such investigations that an ideal filter and integration scheme cannot be implemented in the time domain. Regardless of the amount of sophistication of the processing method, the internal performance of time-domain approaches will always be limited by the internal performance of the filters. These limitations can be reduced for methods that perform the filtering and the integration in the frequency domain. Also, a frequency-domain approach should require less computing time, since all of the correction steps can be performed through

multiplication by a single transfer function incorporating instrument correction, filtering and integration, instead of the multiple convolution operations required by the time-domain approach. A frequency-domain accelerogram processing method is proposed in Sec. 3.3.

Testing of the correction effectiveness of these processing methods would also show that, because of the uncertainties involved in the recording and digitization processes (i.e., missing data, added noise), it is impossible to retrieve the exact signal from the measured accelerogram. In other words, a deterministic solution for this problem does not exist; however, a most probable solution and its level of reliability can be found by describing the errors statistically, as will be seen in Ch. 3. Such a probabilistic approach to accelerogram processing would prevent engineers from being mislead in their studies about the degree of accuracy of the "corrected" records, particularly in the displacement histories.

Freq.	Input Signal Ampl.	Running-Mean Filter (H_1) $T_w = 0.4$ sec	Decimation and Aliasing	Ormsby Low-Pass (H_2) (0.05–0.1 Hz)	Periodic Extension	Interpolation ($p = 10$) Low-Pass Output	High-Pass Output (step 10)
0.05	0.10	0.099934	0.19888	0.20127	0.20127	0.20127	−0.10127
0.10	0.10	0.099737	0.29530	−0.00354	−0.00354	−0.00353	0.10353
4.90	—	—	—	—	−0.00354	$-1.52\ 10^{-6}$	$1.52\ 10^{-6}$
4.95	—	—	—	—	0.20127	$2.09\ 10^{-5}$	$-2.09\ 10^{-5}$
5.05	10.0	0.098945	0	—	0.20127	$2.01\ 10^{-5}$	9.99998
5.10	10.0	0.195563	0	—	−0.00354	$-1.41\ 10^{-6}$	10.00000
9.90	—	—	—	—	−0.00354	$-4.11\ 10^{-7}$	$4.11\ 10^{-6}$
9.95	—	—	—	—	0.20127	$5.73\ 10^{-6}$	$-5.73\ 10^{-6}$
10.05	—	—	—	—	0.20127	$5.63\ 10^{-6}$	$-5.63\ 10^{-6}$
10.01	—	—	—	—	−0.00354	$-3.97\ 10^{-7}$	$3.97\ 10^{-7}$
14.90	—	—	—	—	−0.00354	$-2.15\ 10^{-7}$	$2.15\ 10^{-7}$
14.95	—	—	—	—	0.20127	$3.01\ 10^{-6}$	$-3.01\ 10^{-6}$

Table 2-1. Numerical analysis of the errors in a simple signal due to the high-pass filtering process in Volume II.

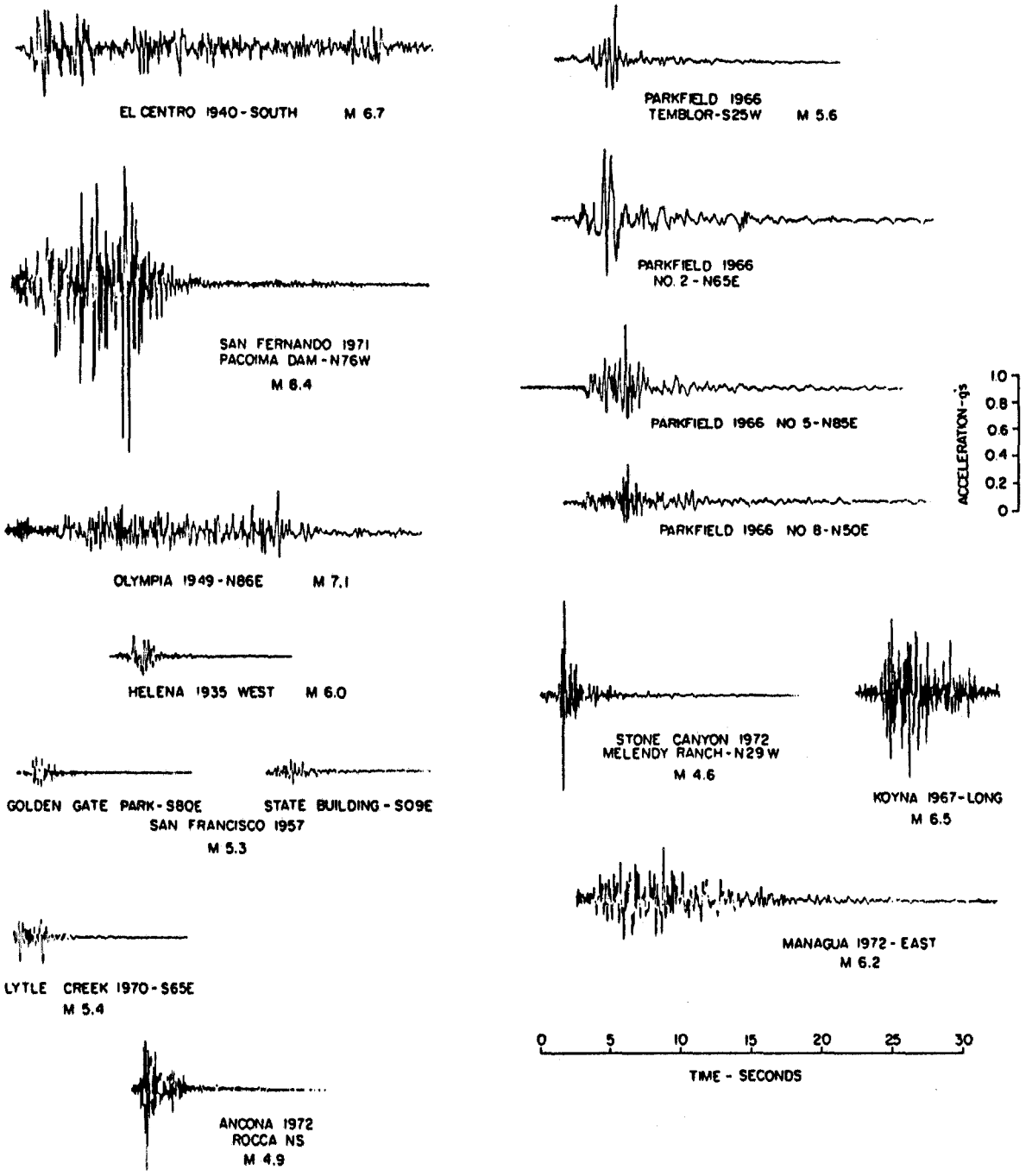

Figure 2-1. Earthquake Ground Accelerations in Epicentral Regions [Hudson, 1979].

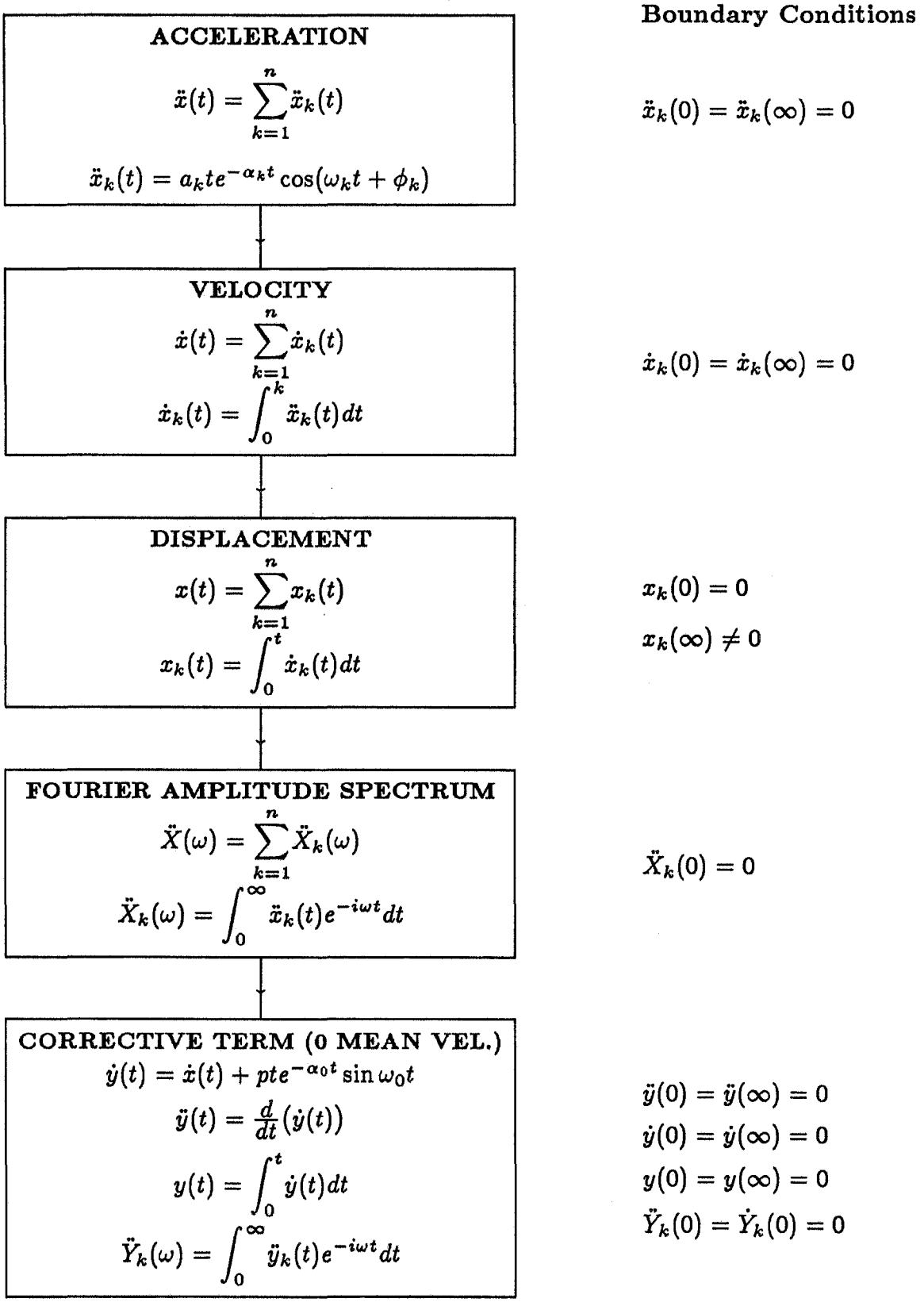

Figure 2.2. Process for generating analytic earthquake signals.

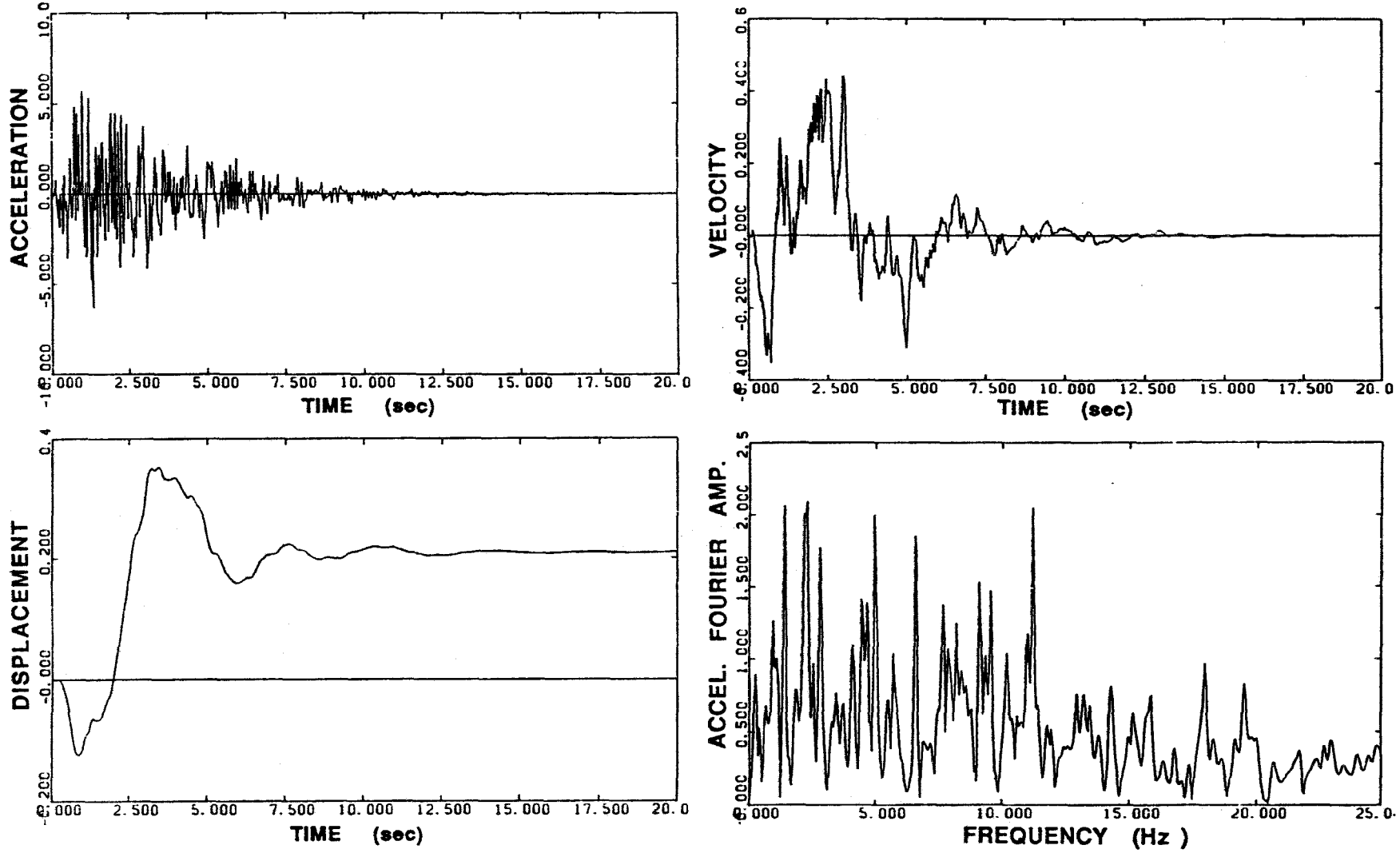

Figure 2-3. Analytically generated earthquake Q1U
(200 frequencies: 0.05 Hz–25.0 Hz).

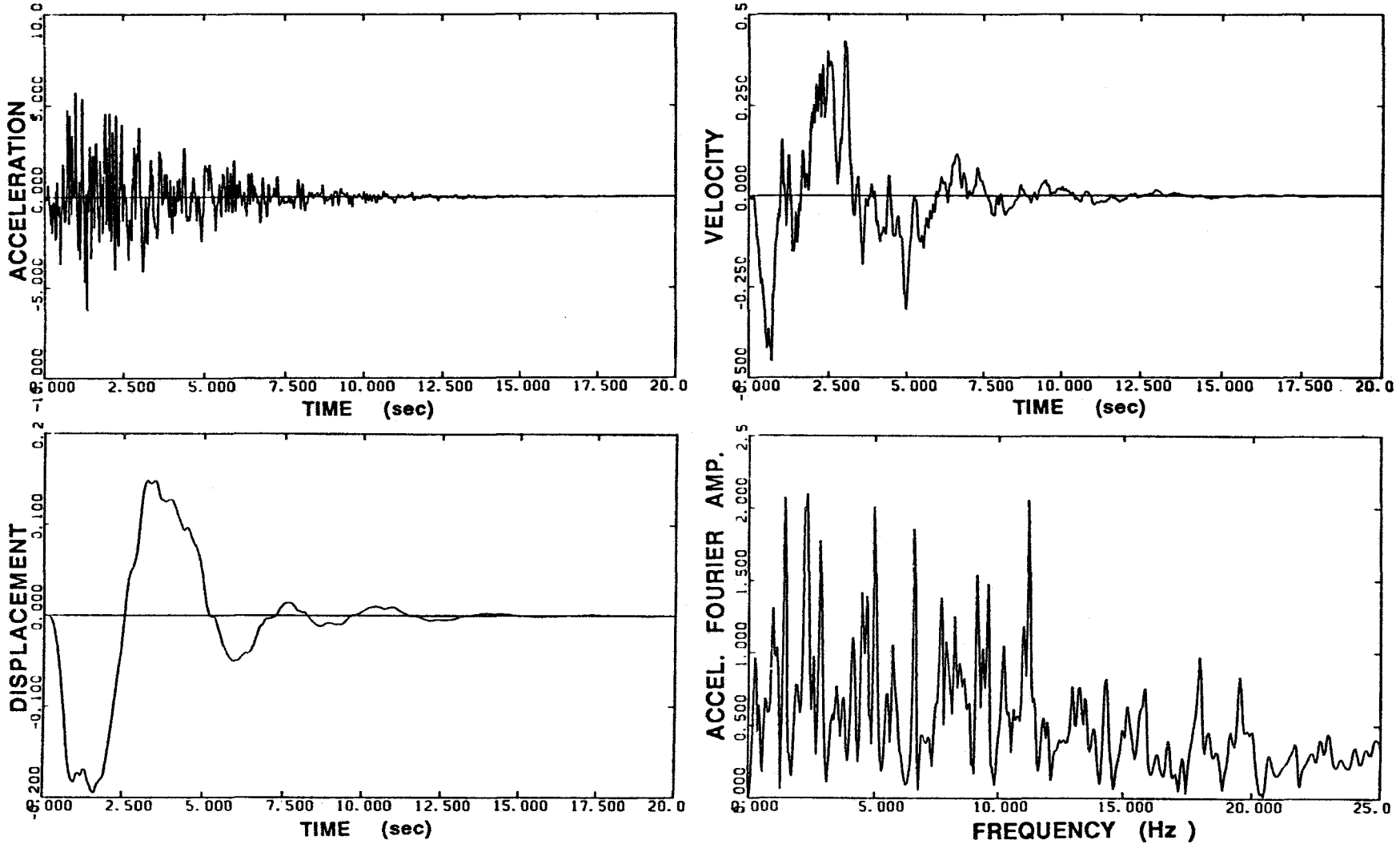

Figure 2-4. Analytically generated earthquake Q1C (200 frequencies: 0.05 Hz–25.0 Hz).

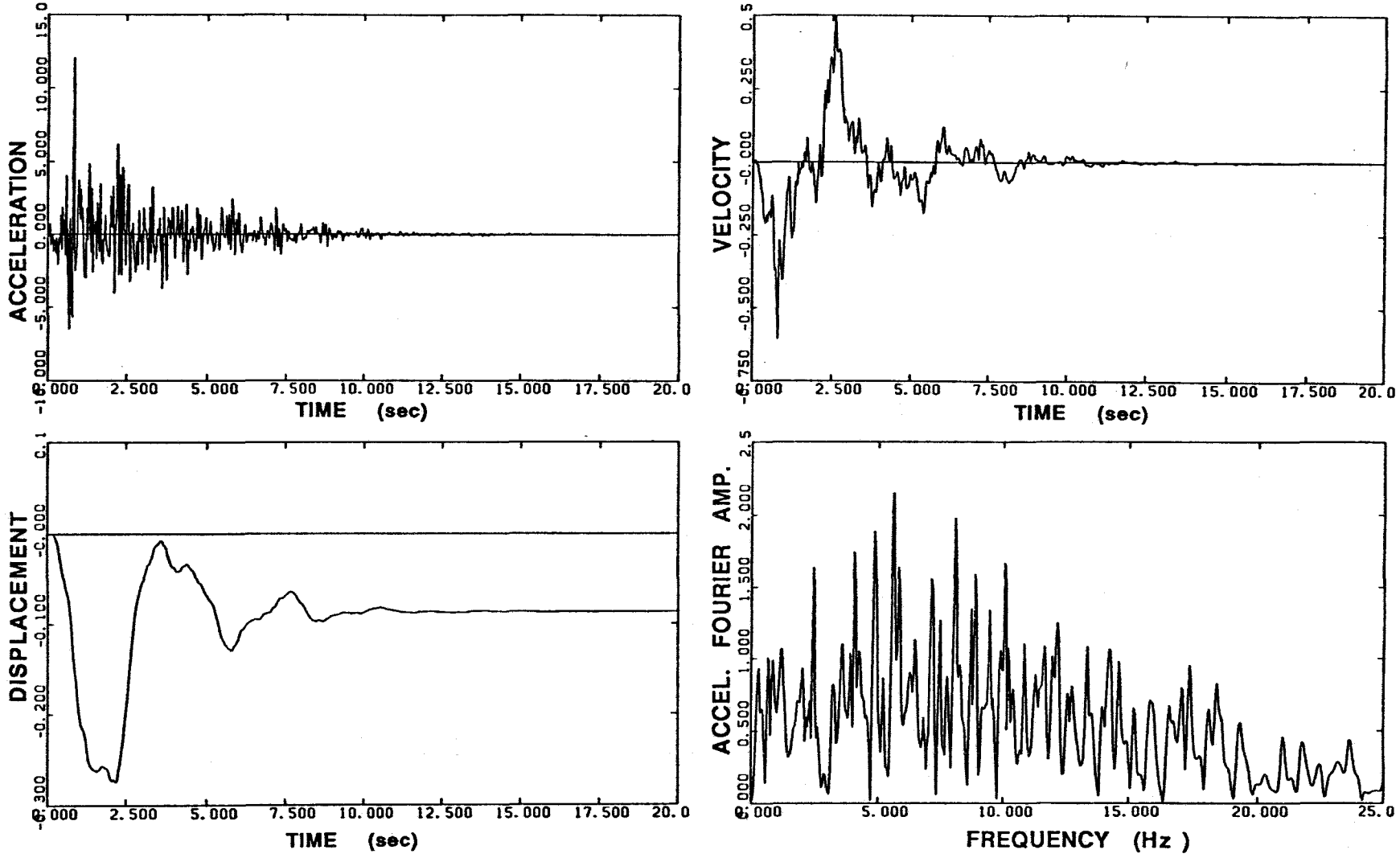

Figure 2-5. Analytically generated earthquake Q2U (200 frequencies: 0.05 Hz–25.0 Hz).

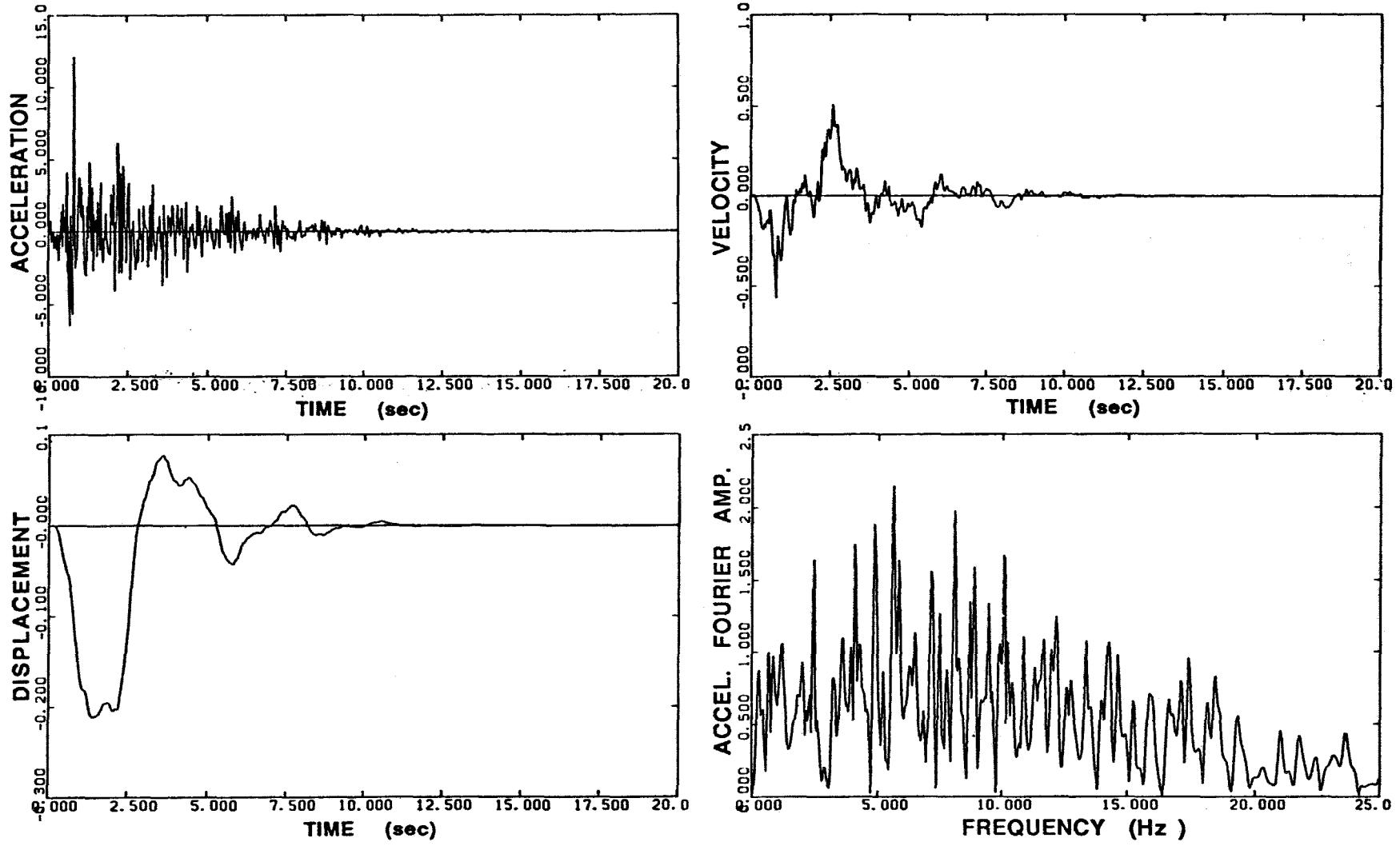

Figure 2-6. Analytically generated earthquake Q2C (200 frequencies: 0.05 Hz–25.0 Hz).

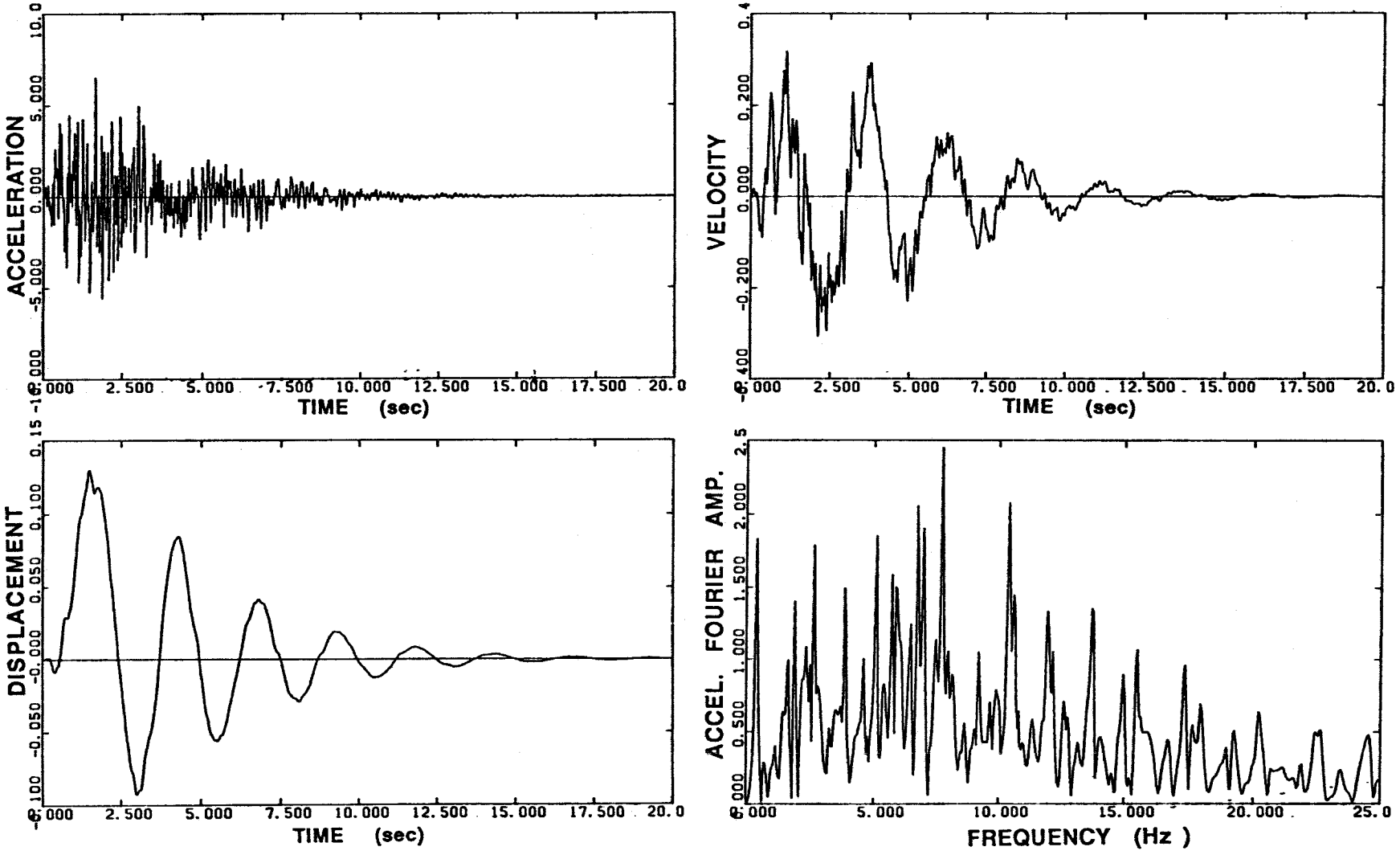

Figure 2-7. Analytically generated earthquake Q8C (200 frequencies: 0.4 Hz–25.0 Hz).

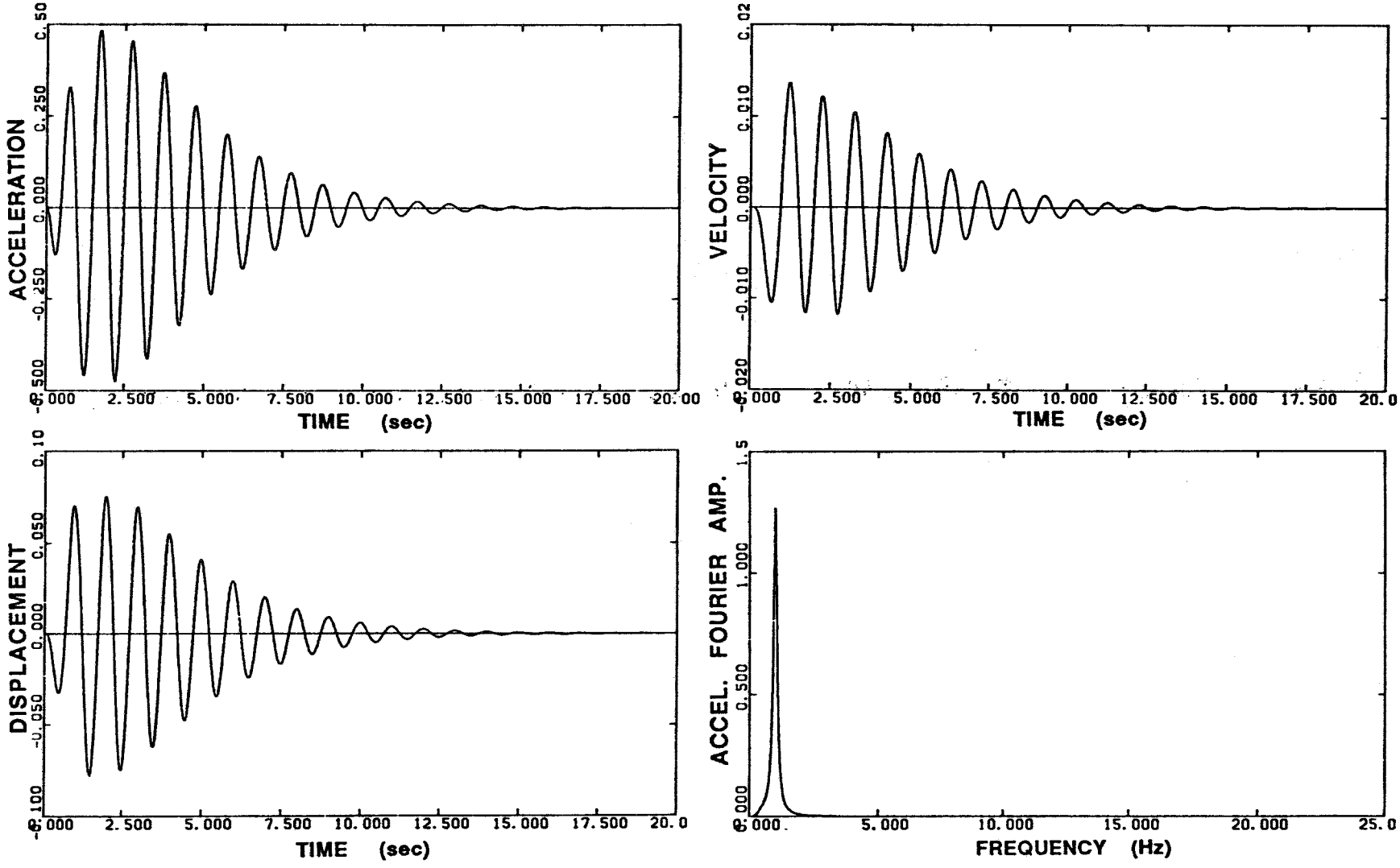

Figure 2-8. Analytically generated earthquake SIN1C (1 frequency: 1 Hz).

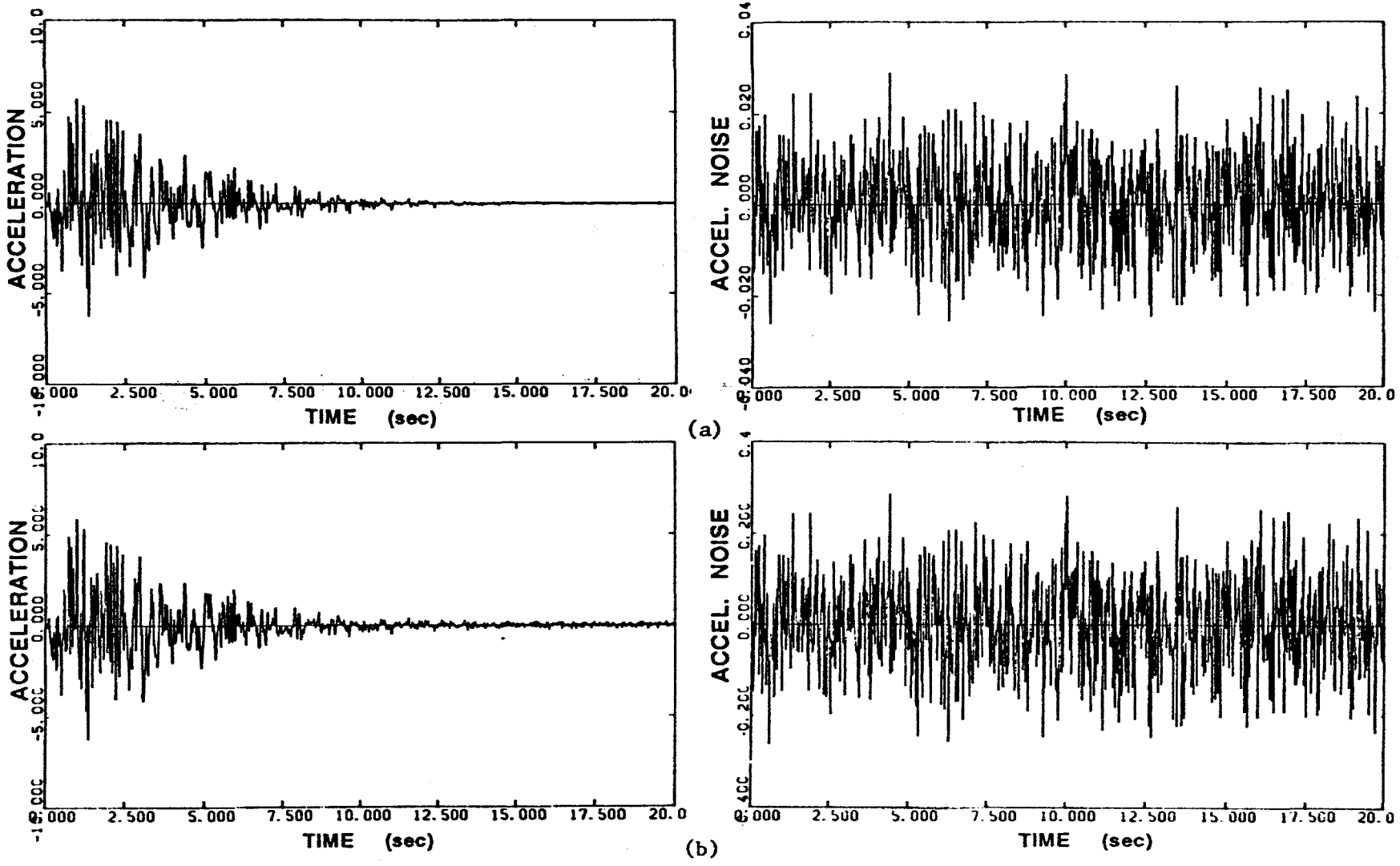

Figure 2-9. Noise-contaminated synthetic accelerogram and errors for large and small earthquakes.
(a) large earthquake accelerogram
(b) small earthquake accelerogram

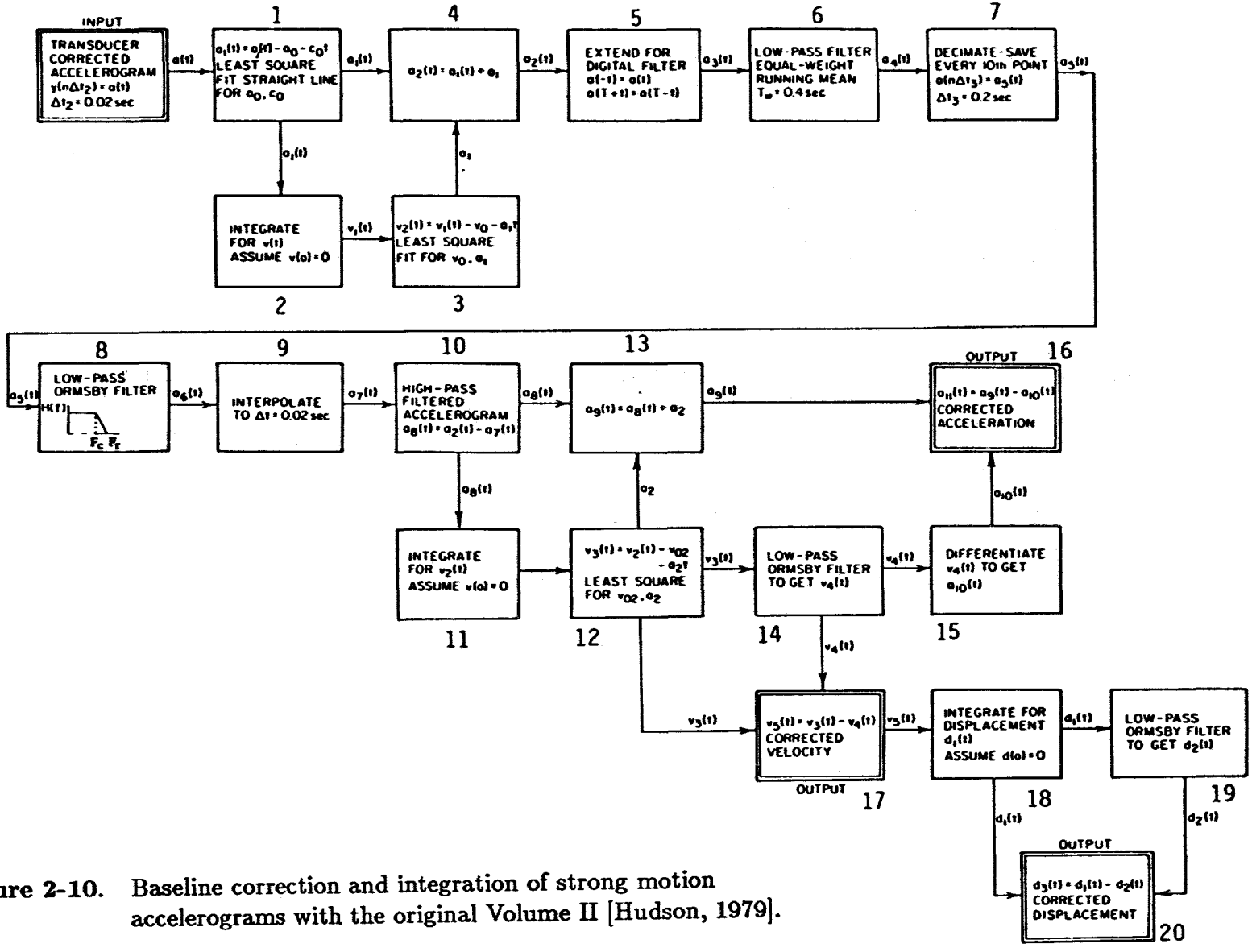

Figure 2-10. Baseline correction and integration of strong motion accelerograms with the original Volume II [Hudson, 1979].

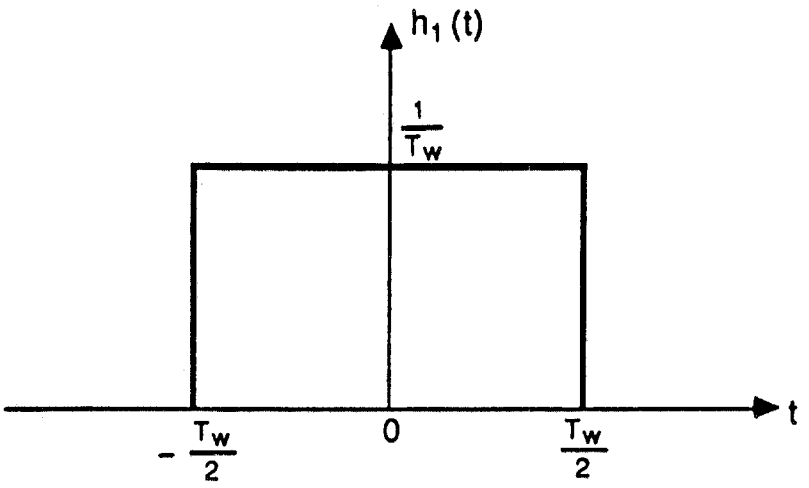

(a) Time domain

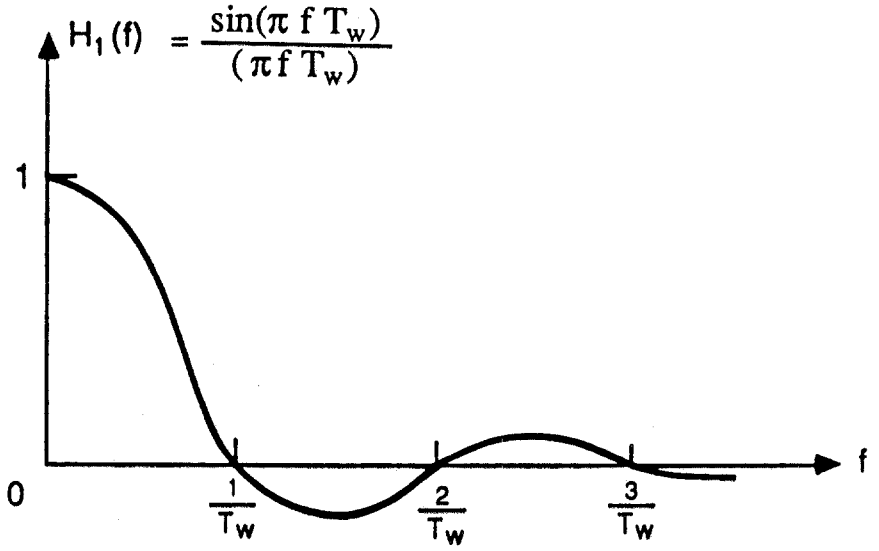

(b) Frequency domain

Figure 2-11. Equal weight running-mean filter.

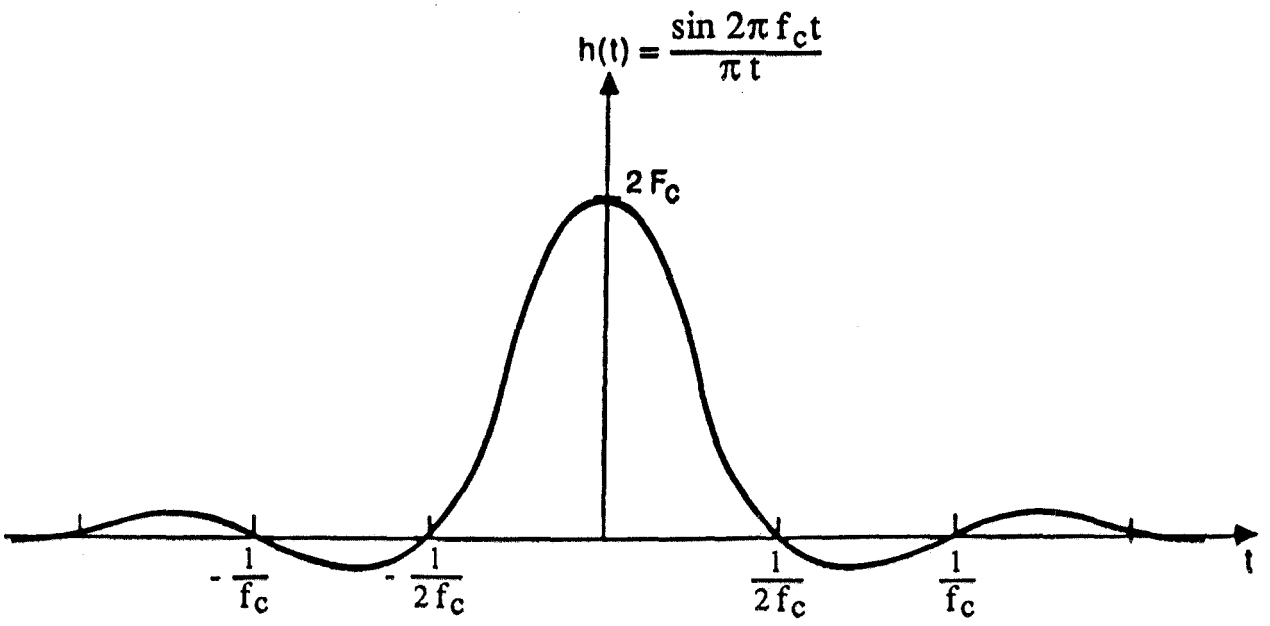

(a) Time domain

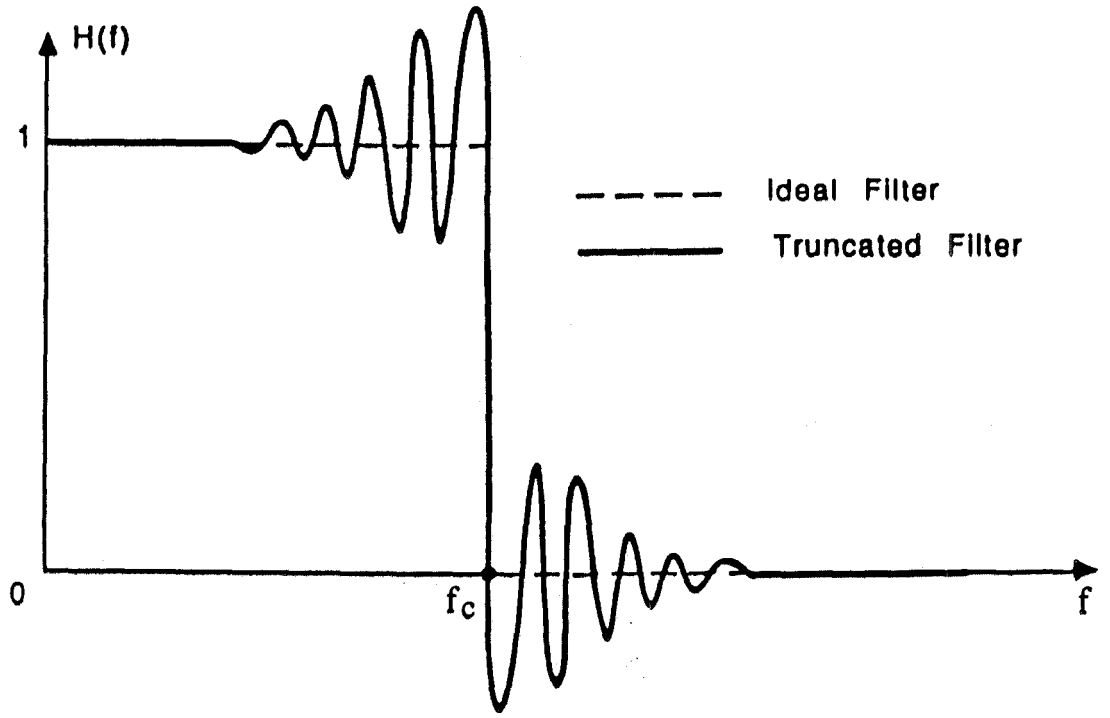

(b) Frequency domain

Figure 2-12. Low-pass boxcar filter.

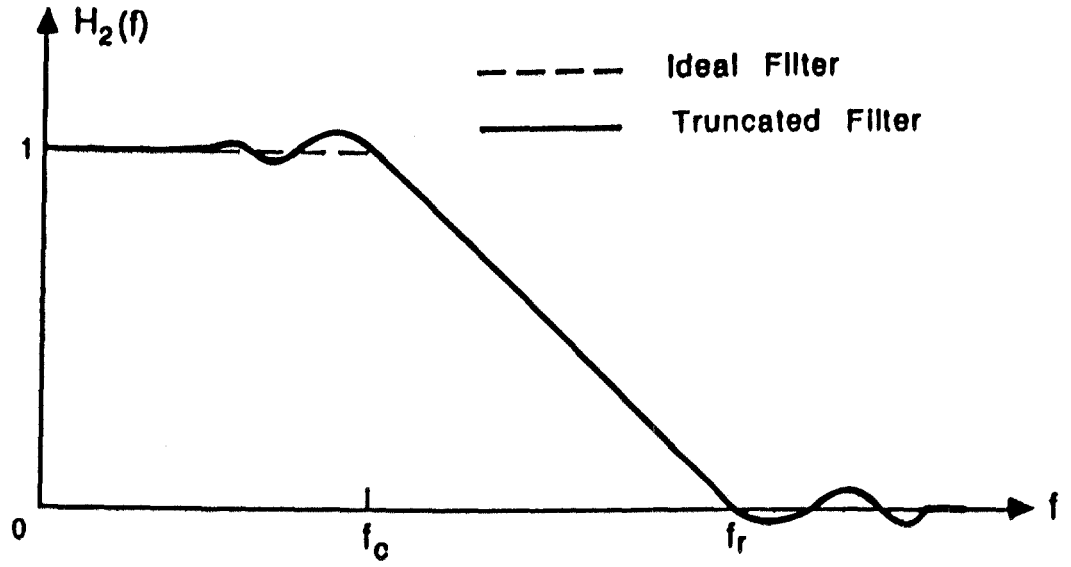

(a)

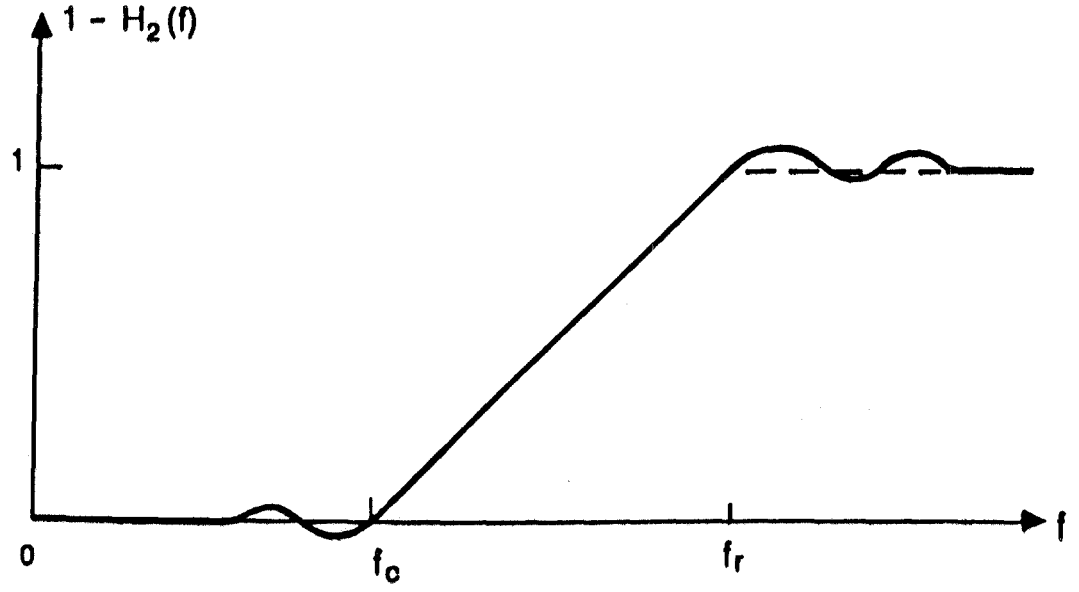

(b)

Figure 2-13. Ormsby filter transfer function with cut-off f_c and roll-off f_r.
(a) low-pass filter
(b) equivalent high-pass filter

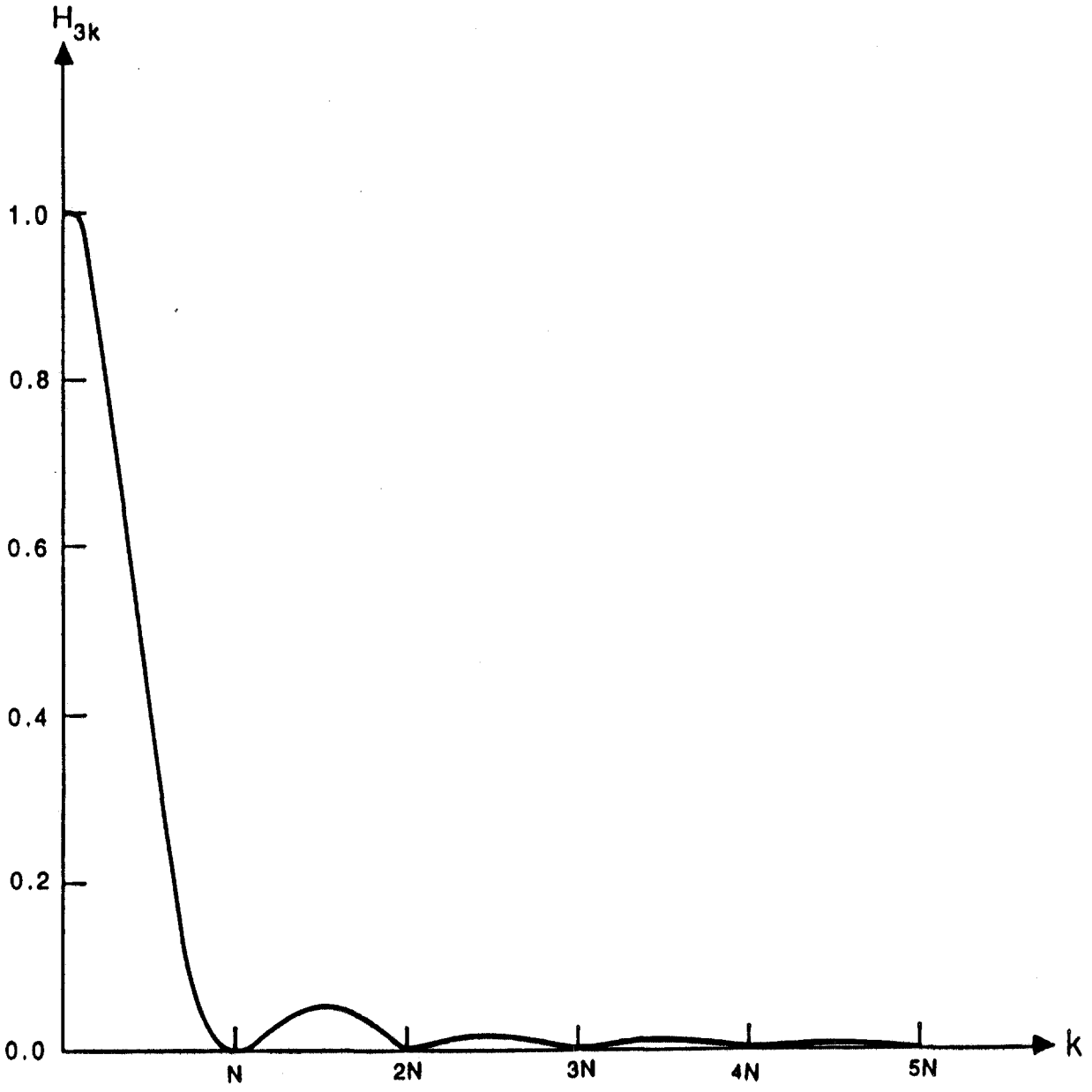

Figure 2-14. Transfer function of the interpolation filter for decimation order $P = 10 \quad (M = 10 \cdot N)$.

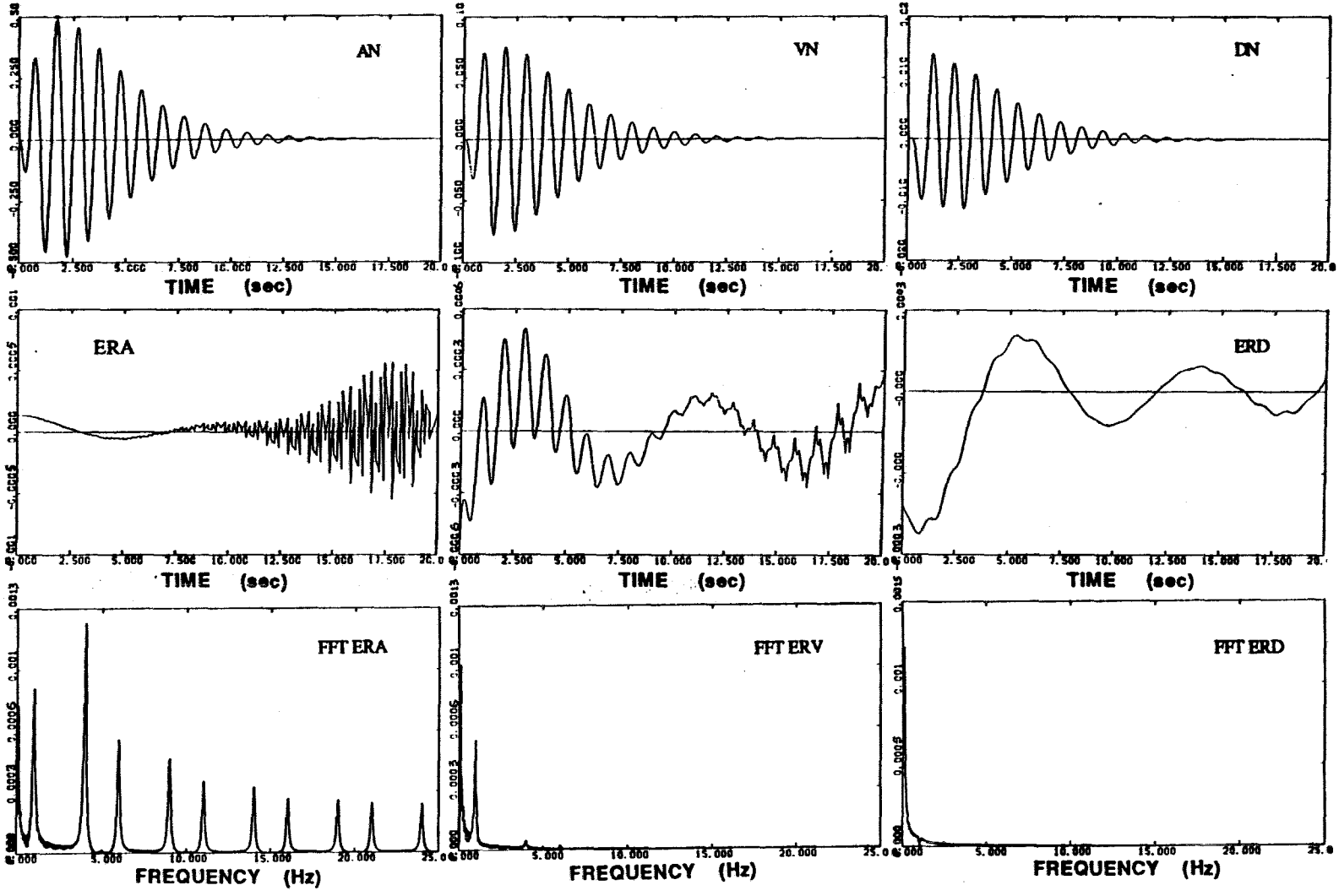

Figure 2-15. Synthetic signal SIN1C processed with Volume II.
Case 1: NSKIPA = 10, NSKIPV = 10, NSKIPD = 10
f_c = 0.105 Hz, f_r = 0.125 Hz 250 filter weights.

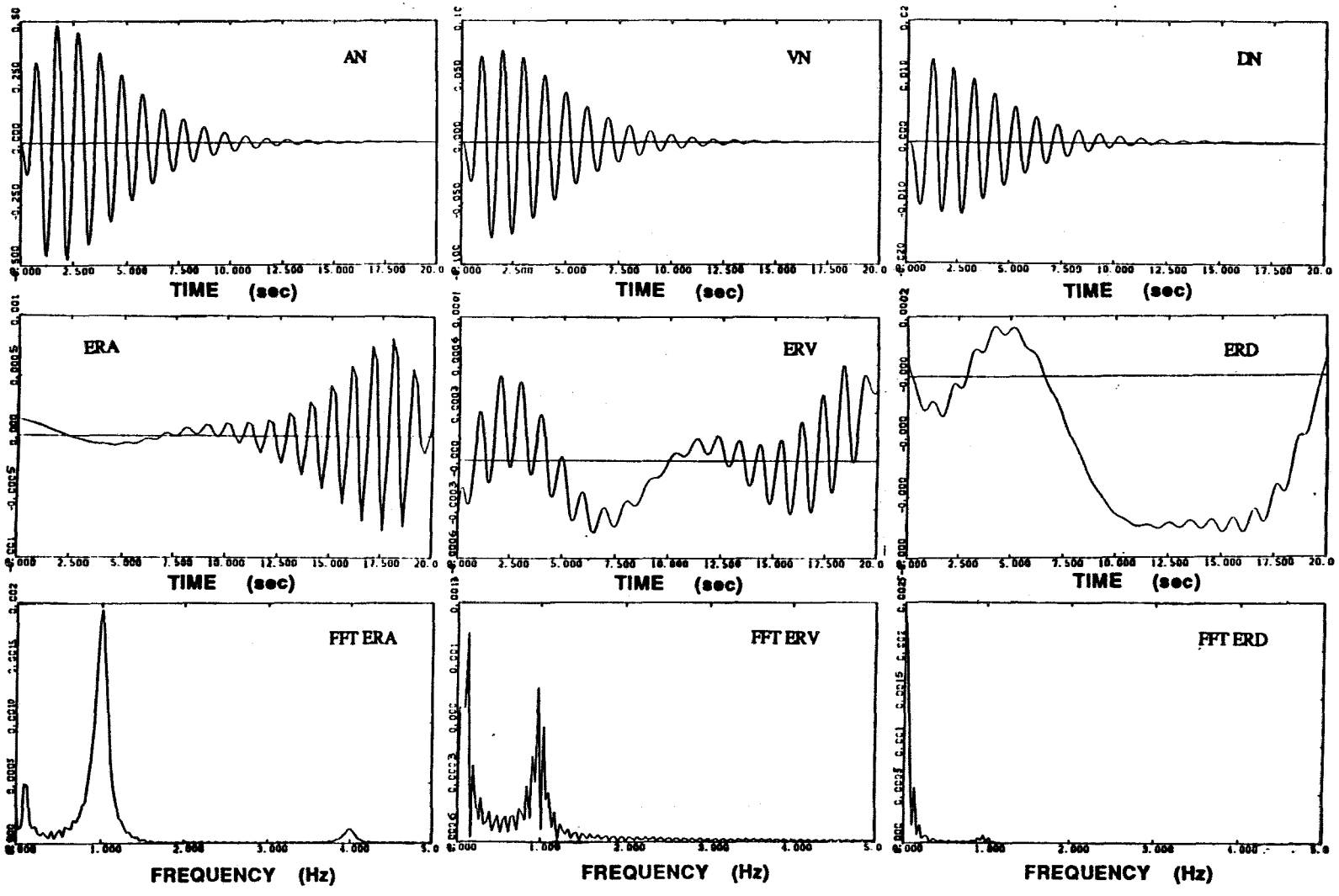

Figure 2-16. Synthetic signal SIN1C processed with Volume II.
Case 2: NSKIPA = 10, NSKIPV = 1, NSKIPD = 1
$f_c = 0.105$ Hz, $f_r = 0.125$ Hz 250 filter weights.

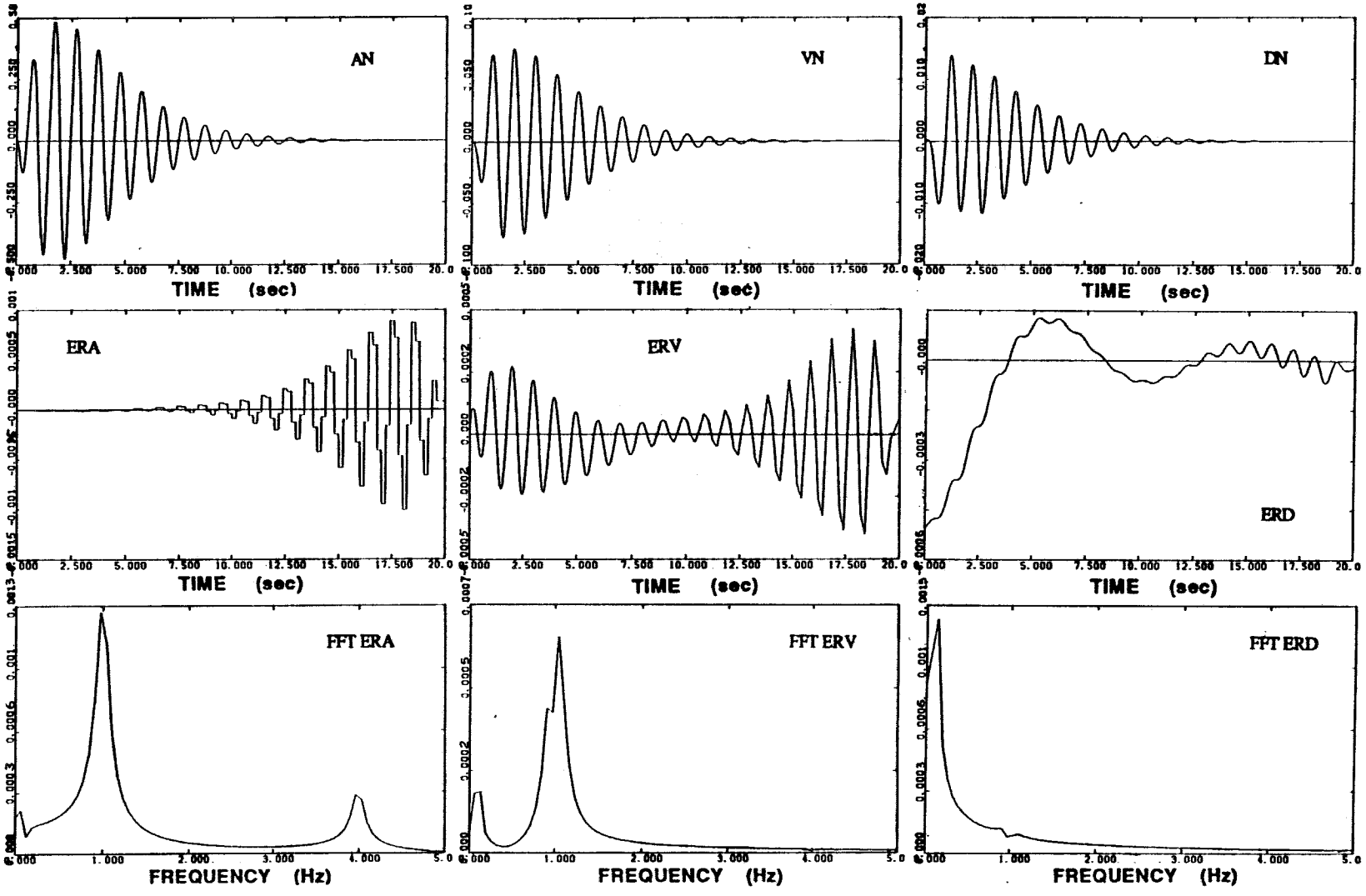

Figure 2-17. Synthetic signal SIN1C processed with Volume II.
Case 3: NSKIPA = 0, NSKIPV = 10, NSKIPD = 10
$f_c = 0.105$ Hz, $f_r = 0.125$ Hz 250 filter weights.

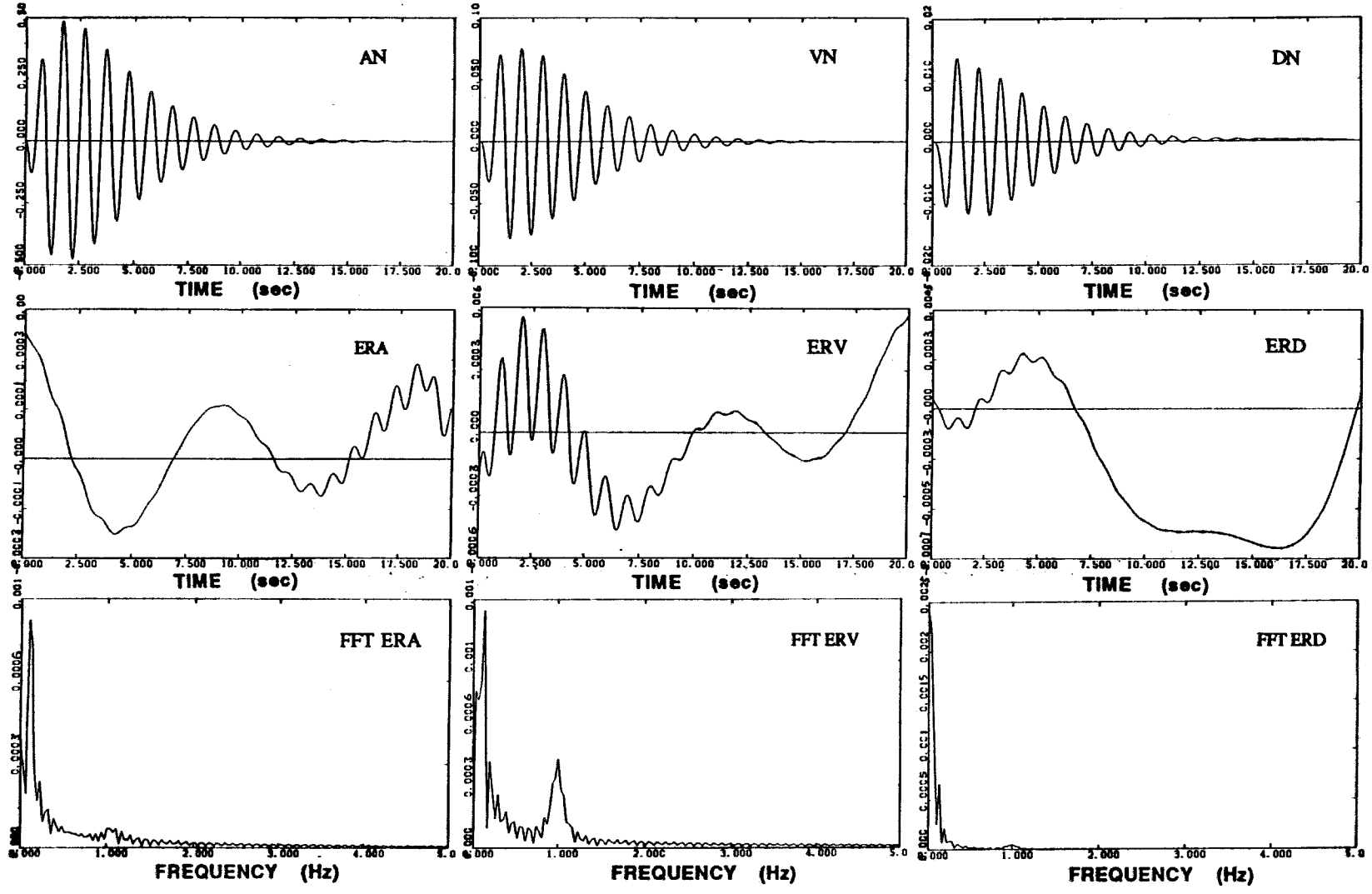

Figure 2-18. Synthetic signal SIN1C processed with Volume II.
Case 4: NSKIPA = 1, NSKIPV = 1, NSKIPD = 1
$f_c = 0.105$ Hz, $f_r = 0.125$ Hz 2500 filter weights.

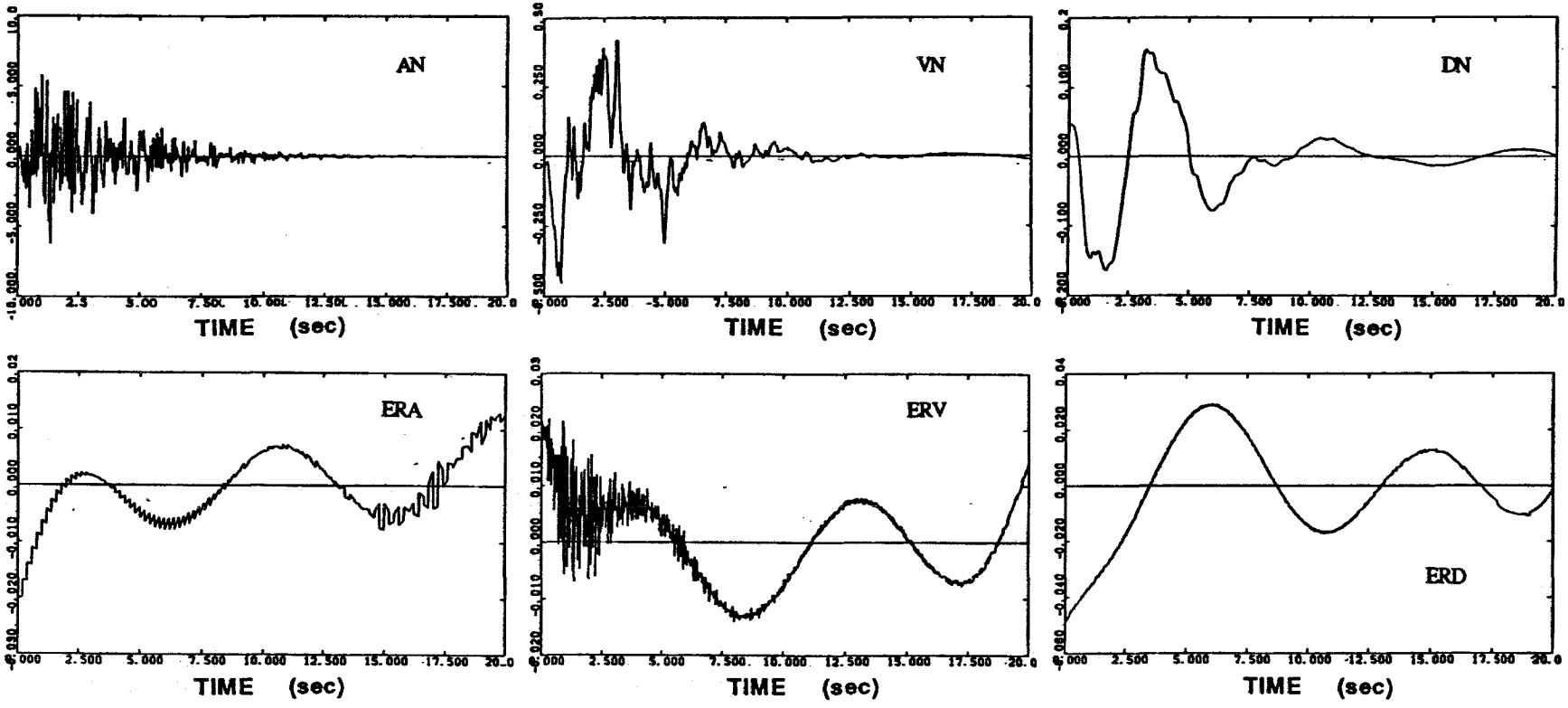

Figure 2-19. Synthetic signal Q1C processed with Volume II.
NSKIPA = 10, NSKIPV = 10, NSKIPD = 10
$f_c = 0.105$ Hz, $f_r = 0.125$ Hz, 250 filter weights.

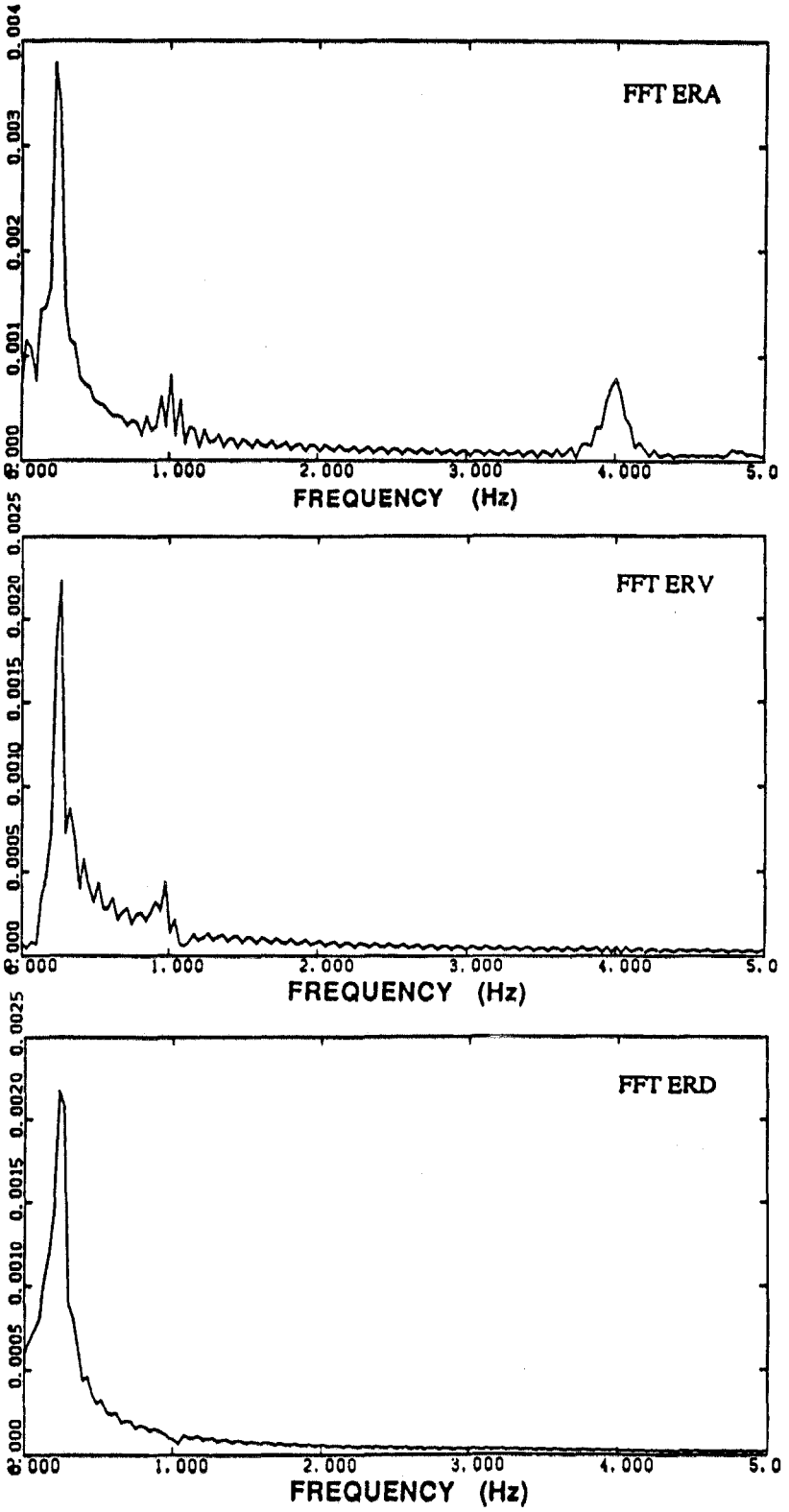

Figure 2-20. Synthetic signal SIN1C processed with Volume II (Fourier transform of the error).
Case 6: NSKIPA = 10, NSKIPV = 10, NSKIPD = 10
f_c = 0.23 Hz, f_r = 0.25 Hz, 250 filter weights.

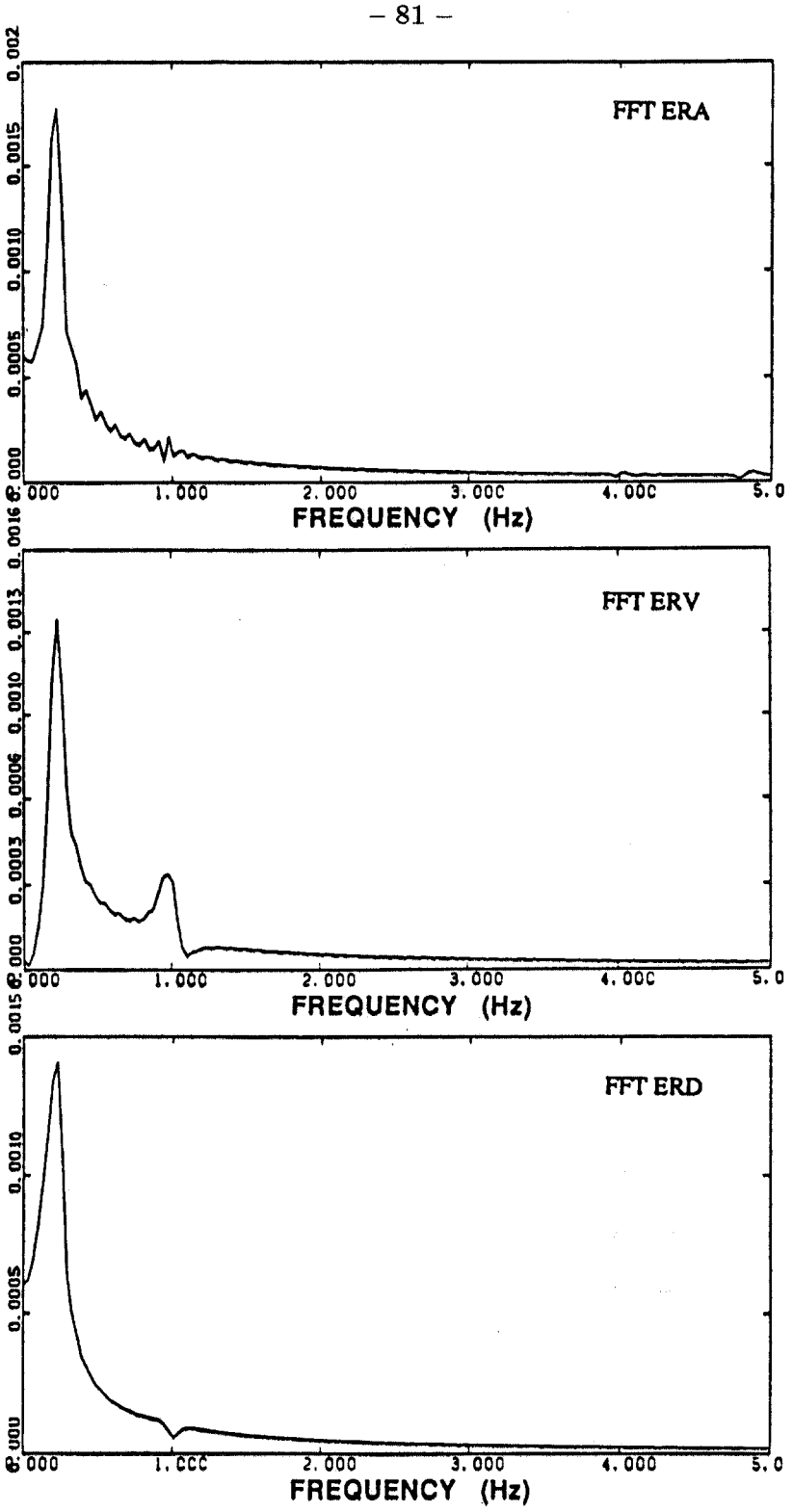

Figure 2-21. Synthetic signal SIN1C processed with Volume II (Fourier transform of the error).
Case 8: NSKIPA = 10, NSKIPV = 10, NSKIPD = 10
f_c = 0.15 Hz, f_r = 0.25 Hz, 50 filter weights.

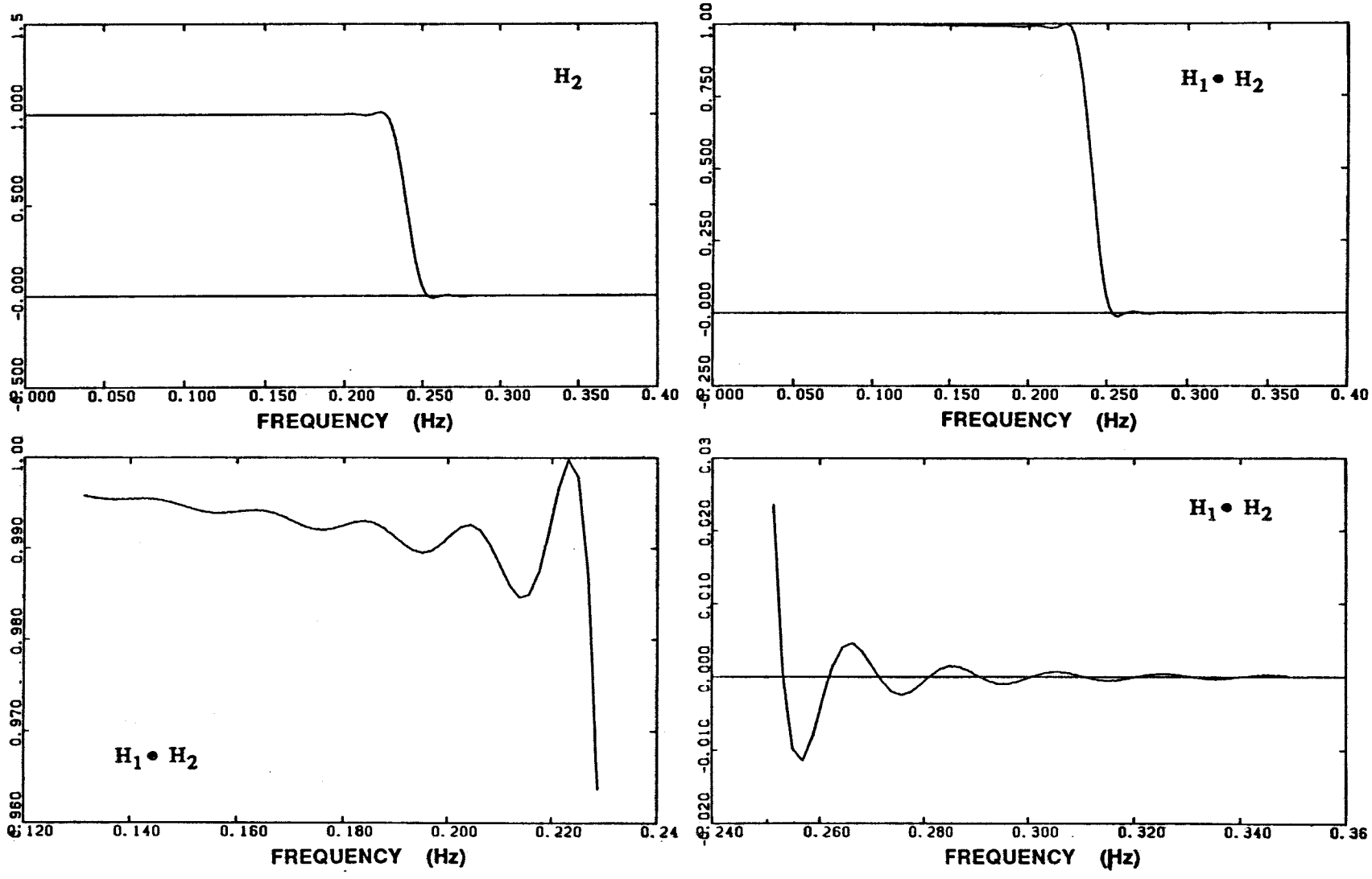

Figure 2-22. Transfer functions of Ormsby low-pass filter (H_2) and $(H_1 \cdot H_2)$.
Case 6: $f_c = 0.23$ Hz, $f_r = 0.25$ Hz, 250 filter weights.

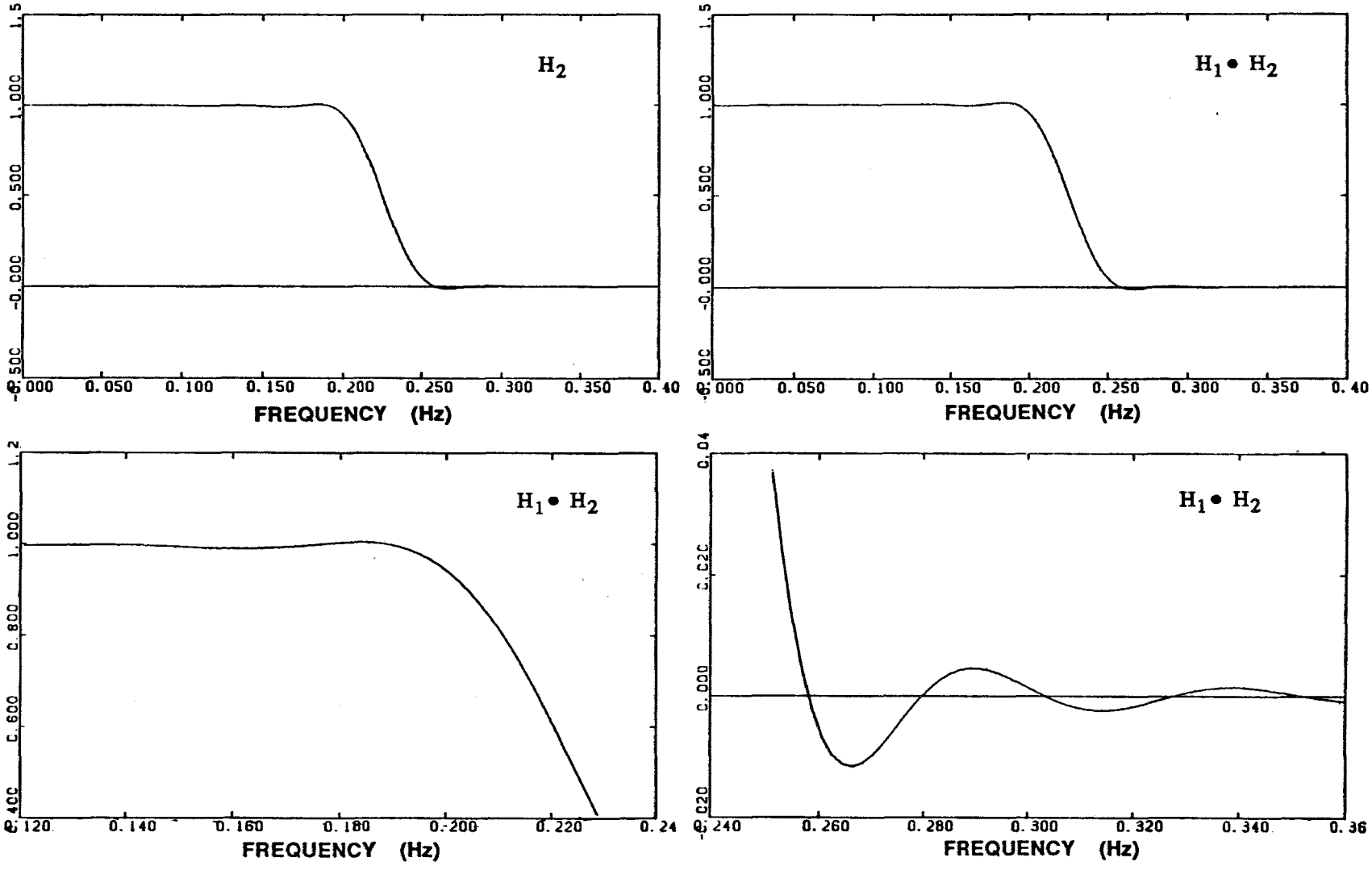

Figure 2-23. Transfer functions of Ormsby low-pass filter (H_2) and $(H_1 \cdot H_2)$.
Case 8: $f_c = 0.15$ Hz, $f_r = 0.25$ Hz, 50 filter weights.

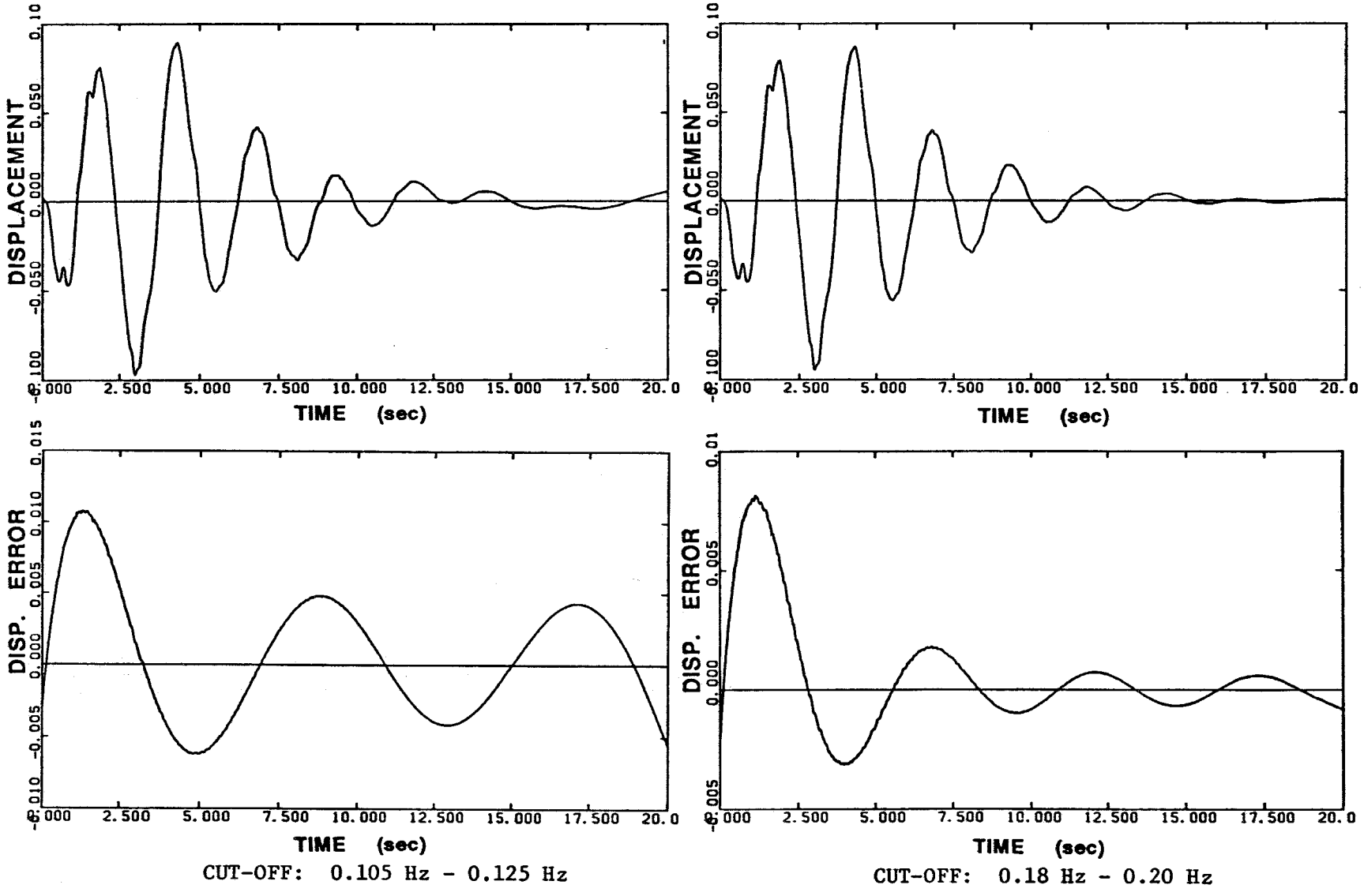

Figure 2-24. Synthetic signal Q8C processed with Volume II (frequency content of signal: 0.4 Hz–25 Hz).

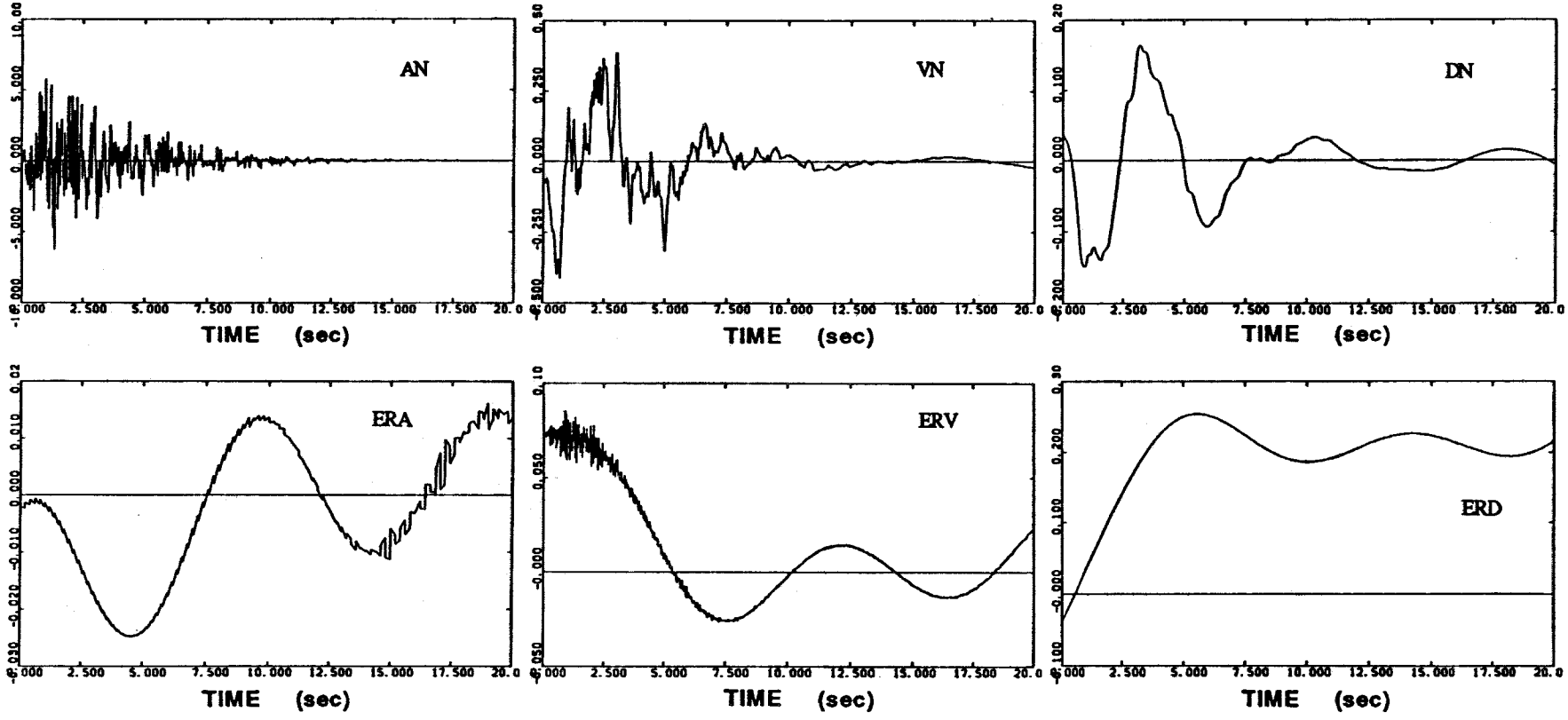

Figure 2-25. Synthetic signal Q1U processed with Volume II.
NSKIPA = 10, NSKIPV = 10, NSKIPD = 10
f_c = 0.105 Hz, f_r = 0.125 Hz, 250 filter weights.

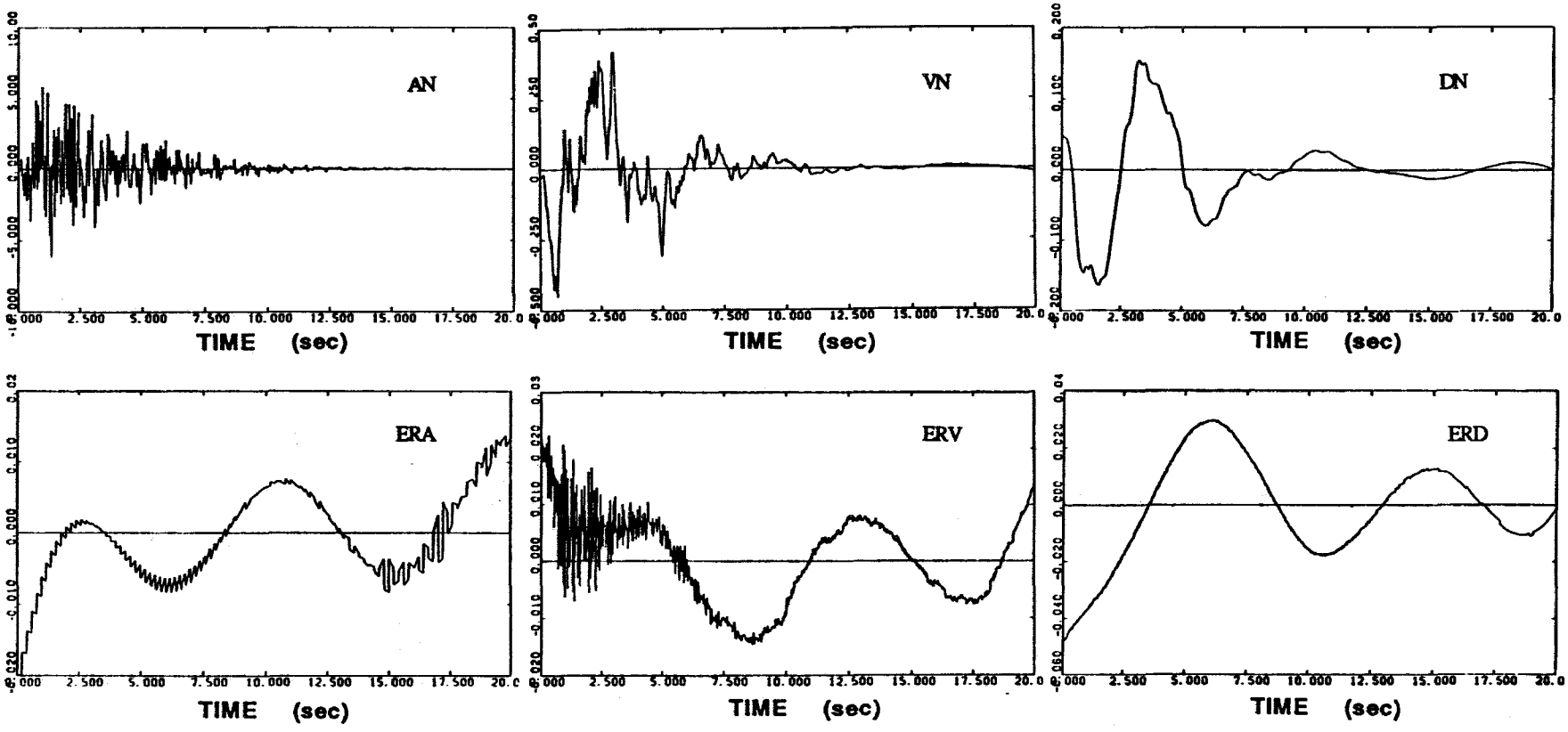

Figure 2-26. Synthetic signal Q1CNL processed with Volume II.
NSKIPA = 10, NSKIPV = 10, NSKIPD = 10
$f_c = 0.105$ Hz, $f_r = 0.125$ Hz, 250 filter weights.

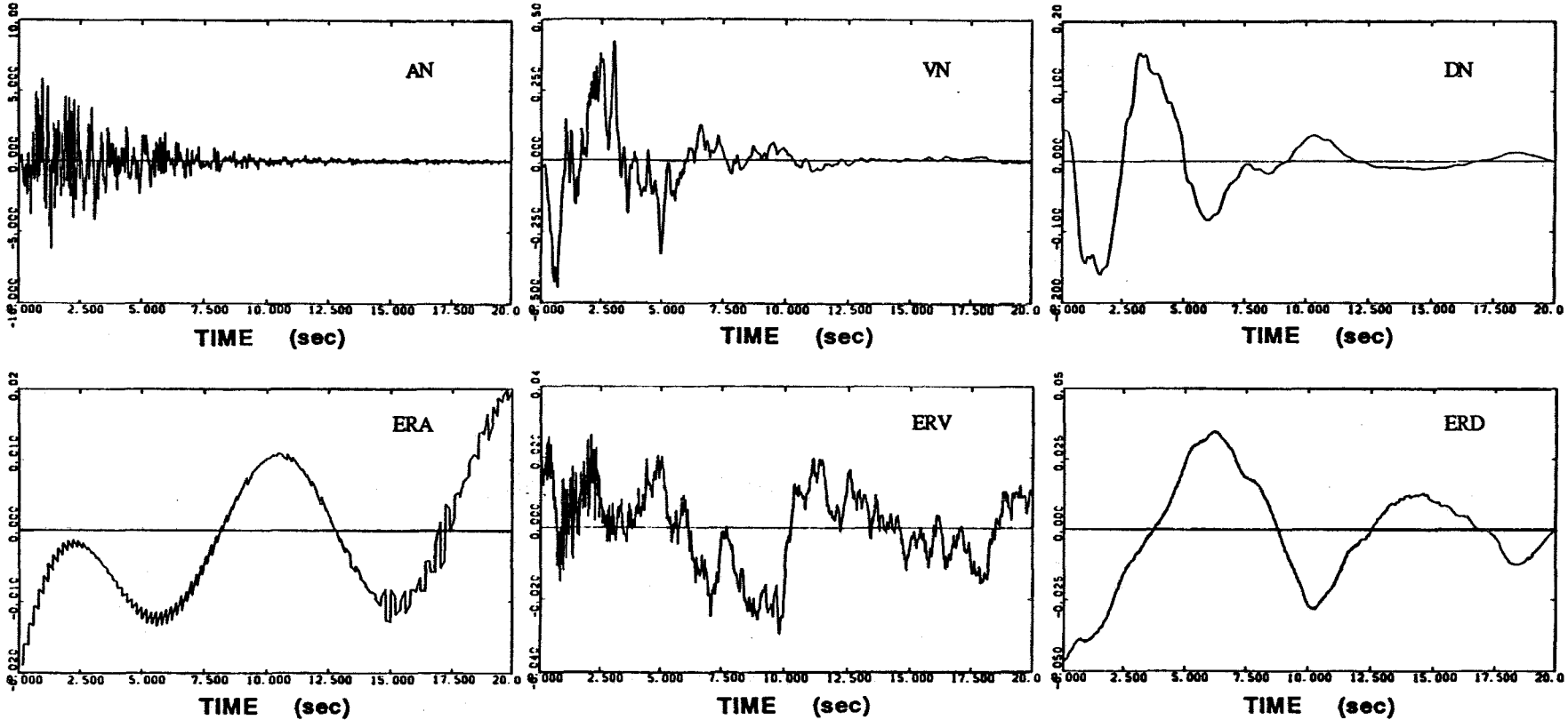

Figure 2-27. Synthetic signal Q1CNS processed with Volume II.
NSKIPA = 10, NSKIPV = 10, NSKIPD = 10
$f_c = 0.105$ Hz, $f_r = 0.125$ Hz, 250 filter weights.

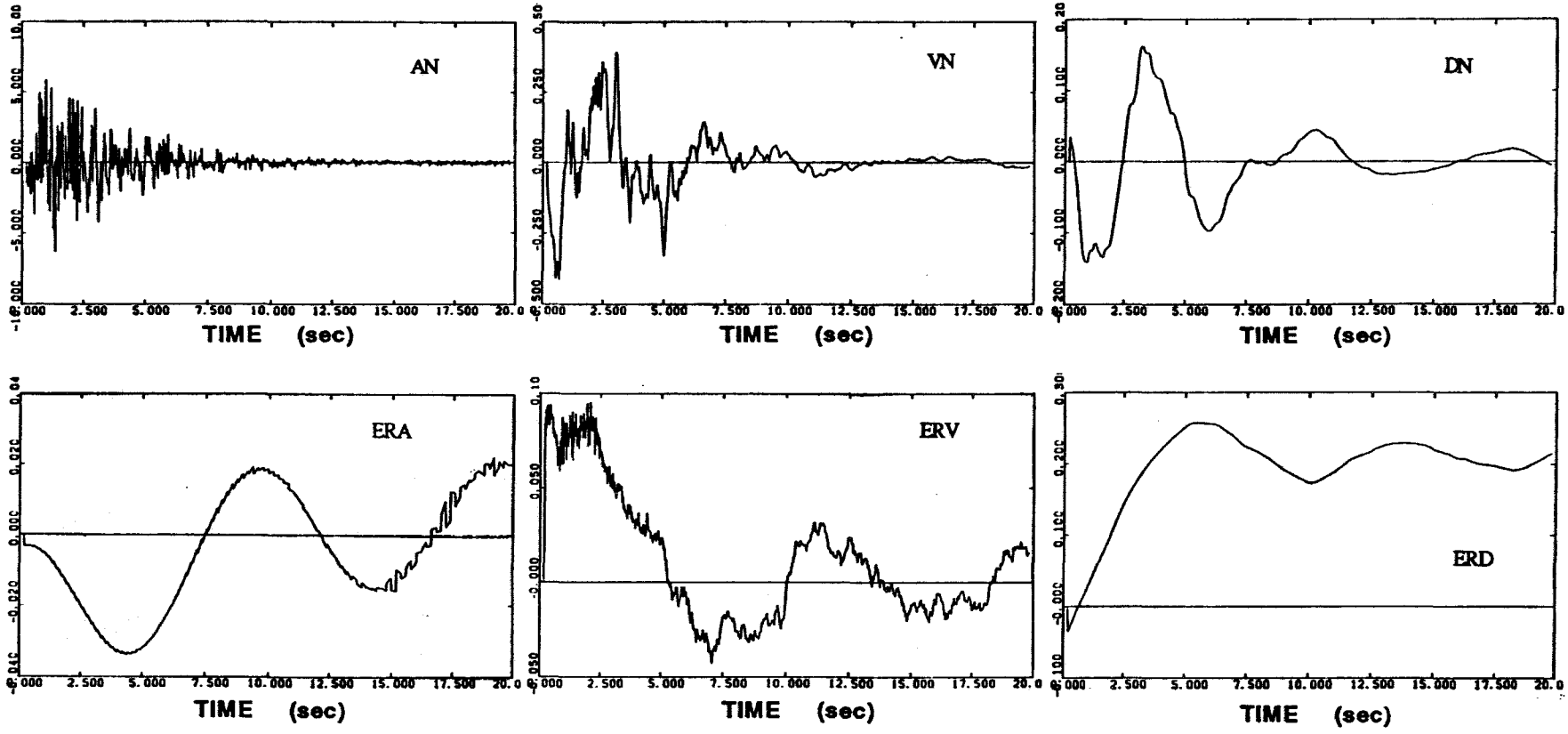

Figure 2-28. Synthetic signal Q1UNTS processed with Volume II.
NSKIPA = 10, NSKIPV = 10, NSKIPD = 10
$f_c = 0.105$ Hz, $f_r = 0.125$ Hz, 250 filter weights.

Chapter 3

PROCESSING OF ACCELEROGRAMS USING RELIABILITY BOUNDS

3.1 Motivation and Methodology

In view of the results obtained from the analyses of accelerogram filtering and integration methods performed on synthetic records, it is the purpose of this chapter to propose a novel, and possibly more appropriate, approach to processing of seismic data.

As has been hinted by some of the new accelerogram processing methods, the advent of faster computers now makes it possible to perform all the processing and corrections in the frequency domain, without having to resort to convolution with finite sums and decimation in the time domain which are two of the largest sources of error in the Volume II method. In the frequency domain, the instrument correction, integration and possible high-pass filtering steps, which involve lengthy and separate convolution operations when a time domain procedure is adopted, can be replaced by a single multiplication representing the combined transfer function of each step. This also has the advantage of giving a much better internal performance, although there still are errors involved in computing the Fourier transforms of the accelerograms, as will be explained in more detail within this chapter. Moreover, it is common practice in most accelerogram processing methods to compute and plot the Fourier transform of the record. In standard processing methods this is done in the section called Volume IV. Thus, since the Fourier transform of the signal is to be computed anyway, there is not much more work involved in using a frequency domain approach. Actually, it may even prove to be more time efficient although it is necessary to obtain the inverse transform. Hence, in view of the preceding comments, it appears that a frequency domain procedure for integrating and correcting earthquake accelerograms is the better approach.

It has been shown that high-pass filters are a major source of error within the processed output records, because they alter certain frequency components by changing the amplitude (i.e., the Gibbs phenomenon in nonrecursive filters) or by changing the phase (i.e., recursive filters). So why are high-pass filters implemented? Mostly to remove the linear drift in the velocity and the parabolic drift in the displacement due to a false estimate of the mean acceleration, and to remove the noise-contaminated long-period components of the acceleration which are substantially increased after double integration. The analysis of the internal performance of the original Volume II method has proved that the errors induced by the filters were often greater than those due to digitization noise and trigger truncation of the original accelerogram. Moreover, these latter errors are still present in the "corrected" output records, indicating that the filters cannot properly perform the tasks they were intended to do. High-pass filters only partially remove the noise, and delete low-frequency information which could be of scientific interest. It has also been seen in Ch. 2 that the choice of the high-pass filter cut-off and roll-off frequencies made significant changes in the processed signals, and that to date there are no satisfactory physically-based criteria for the selection of these filter parameters. Since high-pass filters are a major source of internal processing error, and do not contribute much to the overall correction effectiveness of the method, the new processing procedure described within this chapter does not recommend the use of any high-pass filter. However, they can be easily incorporated and implemented within the program's structure if filtering is wanted. Also, filters can be used that do not change the phase or delete complete bands of the spectrum, and do not require an arbitrary choice of the filter parameters. These are the optimal filters, described in Ch. 4. If it is decided to use a filter to process the data, the procedure should be performed only once, as opposed to the multiple filtering which occurs within the Volume II routine for example. In effect, viewed from the perspective of the frequency domain, and after the integration process is completed, the derivation of the velocity and the displacement have involved the square and the cube respectively of the transfer function. As was seen in Ch. 2, multiple filtering of records increases the internal performance error in the processed signal, without significantly decreasing the error found in the input accelerogram.

Most processing methods make the temporal mean of the accelerogram zero. This is based on the fact that the mean of the total acceleration produced by an earthquake is indeed zero, since the velocity must start and end at zero. The missing data and digitizing noise alter the true temporal mean however, and there is no reason for this contaminated accelerogram to actually have zero mean. Thus, the drifts in the velocity and displacement in most processing methods are in part created by the method itself when it forces the accelerogram to have zero temporal mean. On the other hand, it is not possible to identify the exact mean of the recorded signal because of the unknown missing data and the uncertain amount of noise. Some methods also force zero mean both in the velocity and the displacement, but this does not help to solve the problem since it may spuriously alter the lower frequencies, which in turn may increase the need to implement a high-pass filter. Systematically forcing the temporal mean in the velocity and displacement to be zero also makes it impossible to retrieve possible final displacement offsets. Although there may be some physical justification in forcing a zero temporal mean acceleration, as well as a zero mean velocity in certain cases, there is none regarding a zero mean displacement. Some exceptions in the velocity are for earthquakes that produce small levels of shaking, or for far-field records, since they are not expected to display final displacement offsets. In these cases, removing the temporal mean from the velocity is justifiable if data truncation effects are not substantial. The processing method proposed hereafter only forces the acceleration mean to be zero, without altering that of the integrated velocity or displacement, except in certain cases involving small seismic events and far-field records, and which are specified by the user of the method.

In fact, because the original errors in the accelerogram (i.e., digitization noise and start-up truncation) are uncertain, there is no deterministic solution to this problem, contrary to what most processing methods seem to imply. However, it is feasible to determine from laboratory experiments the range of possible values these uncertain parameters can take, and assign a probability distribution to each of them. Therefore, it appears to be more suitable to produce the most probable acceleration, velocity and displacement, as well as their respective intervals of

confidence, computed on the assumption of probability distributions for the uncertain parameters. Such an approach will make it possible to obtain accelerations, velocities and displacements which are the most likely to have occured during the seismic event based on the measured accelerogram and the most probable trigger truncation and digitization noise levels.

In summary, this new approach to earthquake accelerogram processing proposes to treat explicitly the uncertainty in the mean acceleration and in the recording and digitization noise. The signal is then integrated twice, assuming probability distributions for the initial velocity and displacement. The standard deviations of the acceleration, velocity and displacement are computed separately as a function of the digitization noise and the trigger level uncertainties, using the probability distributions assumed for the mean acceleration, initial velocity and initial displacement. Finally, the procedure produces plots which represent the most probable value of the processed signal, along with the corresponding standard deviations. In this chapter, filters are not implemented to process the data. However, alternatives to traditional high-pass filtering methods are discussed in detail in Ch. 4. In this chapter, it is also assumed that the accelerogram that is being processed is the one obtained directly from the transducer without instrument correction. This assumption is reasonable since most transducers are calibrated for accelerations. For analog records digitized at 0.02 sec and obtained from instruments which have a 25 Hz natural frequency (i.e., SMA's), or for analog and digital records digitized at 0.01 sec and obtained from instruments which have a 50 Hz natural frequency (i.e., FBA's), the errors at the higher frequencies due to noninstrument correction are small and can be neglected. Instrument correction can always be done as an initial step of the procedure if necessary.

The acceleration mean-correction and integration, as well as the computation of the standard deviation levels for the acceleration, velocity and displacement will first be derived in the time domain (Sec. 3.2). This processing method is then tested using the synthetic signal approach presented in Ch. 2. The equivalent formulation of the processing method is then derived in the frequency domain (Sec. 3.3) and is also tested for its correction effectiveness and internal performance. All of the

following theoretical derivations apply equally well to analog and digital records. Differences only arise in the value of certain parameters, as will be pointed out in the next section.

3.2 Time Domain Formulation and Applications

3.2.1 Assumptions and Definitions

If $\ddot{x}_n$ is the quantized sampled instrument signal at time $t_n = n\Delta t$ (i.e., measured signal), $\ddot{y}_n$ is the true instrument signal at time t_n (i.e., true acceleration at the site altered by the transfer function of the instrument), and $\ddot{e}_n$ are the errors introduced in measuring and digitizing the signal $\ddot{y}_n$, then:

$$\ddot{x}_n = \ddot{y}_n + \ddot{e}_n \ , \qquad n = 1, \ldots, N \ . \tag{3.1}$$

The $\ddot{e}_n$ arise from the quantization due to finite precision storage, from electrical noise for digital accelerographs or from uncertainty in the exact center of the optical trace for analog accelerographs, and from the unknown offset in the baseline. Some researchers have assumed in the past that the offset error is a linear drift. However, for analog accelerograph a straight trace is usually recorded along with the signal, and for digital accelerographs the drift is very nearly constant over the duration of the recording. Thus, the offset can be assumed to be constant in both cases. Define:

$$\ddot{z}_n = \ddot{x}_n - \frac{1}{N}\sum_{k=1}^{N} \ddot{x}_k \ , \qquad n = 1, \ldots, N \ , \tag{3.2}$$

where $\ddot{z}_n$ is the baseline-corrected measured signal at time t_n and,

$$\ddot{\delta}_n = -(\ddot{e}_n - \frac{1}{N}\sum_{k=1}^{N} \ddot{e}_k) \ , \qquad n = 1, \ldots, N \ . \tag{3.3}$$

Then, Eq. 3.2 can be rewritten using Eqs. 3.1 and 3.3:

$$\ddot{y}_n = \ddot{z}_n + \ddot{\delta}_n + M \ , \qquad n = 1, \ldots, N \ , \tag{3.4}$$

where,

$$M = \frac{1}{N}\sum_{k=1}^{N}(\ddot{x}_k - \ddot{e}_k) = \frac{1}{N}\sum_{k=1}^{N} \ddot{y}_k \ . \tag{3.5}$$

Thus, in Eq. 3.4, M is the unknown constant temporal mean of the signal $\ddot{y}_n$, $n = 1, \ldots, N$, $\ddot{z}_n$ is the zero-mean corrected data, and $\ddot{\delta}_n$ is an uncertain error with a zero temporal mean.

The goal is to estimate the unknown $\ddot{y}_n$ from the known $\ddot{z}_n$. The estimated $\ddot{y}_n$ can then be instrument-corrected by deconvolution to get an estimate of the actual acceleration at the location of the instrument, if instrument correction was felt necessary. Since M and the $\ddot{\delta}_n$ are uncertain, they are described by probability laws which allow the uncertainty in the $\ddot{y}_n$ to be analyzed. For this purpose, $\ddot{e}_n$ and M are modelled as independent Gaussian random variables with most probable value zero and variance $\frac{N}{N-1}a^2$ and d^2 respectively. Also, $\ddot{e}_n$ and $\ddot{e}_m$, for $n \neq m$, are modelled as independent random variables. It follows from Eq. 3.3 that the $\ddot{\delta}_n$'s are Gaussian variables with most probable value zero and variance a^2, independent of M. Also, it will always be assumed that N is large, so the $\ddot{\delta}_n$'s can be treated as independent since for $n \neq m$, $E[\ddot{\delta}_n \ddot{\delta}_m] = -\frac{a^2}{N-1}$ is almost zero. Hence, from Eq. 3.4, given the data $\ddot{z}_n$, $n = 1, \ldots, N$, the true accelerations are described by a Gaussian distribution such that:

$$E(\ddot{y}_n) = \ddot{z}_n \qquad \sigma^2(\ddot{y}_n) = a^2 + d^2 \qquad , n = 1, \ldots, N \; . \tag{3.6}$$

A rationale for the choice of probability laws starts as follows. According to Eq. 3.5, M represents the temporal mean of the true signal $\ddot{y}_n$, for the recorded points $n = 1, \ldots, N$. The temporal mean of the entire and true acceleration time history, from the beginning of the event up to its very end, is identically zero. Thus, $-M$ represents the temporal mean of the missing and unrecorded signal. The error due to missing data can itself be separated into two categories: that missing at the beginning due to instrument trigger being induced by the shaking (i.e., analog instruments), and also possibly that missing at the end of the record due to premature instrument shut-off or lack of complete digitization. The truncated data at the beginning affects both the estimate of the true mean acceleration and the initial conditions for integration, whereas that at the end only changes the mean of the acceleration. To avoid complications due to cross-correlated terms in

the standard deviations of the integrated signal, the missing data at the beginning and at the end must be seperated in the expression of the temporal mean.

Trigger truncation mainly applies to analog instruments, since digital recorders have a pre-event memory. Simulations on the truncated synthetic records suggest that whatever the earthquake size, the initial velocity and displacement are small. Thus, it will be assumed for integration purposes that the instrument triggered within the time span $2\Delta t$ prior to the first recorded point and that there is at the most one point, $\ddot{y}_0$, missing at the beginning of the record (Fig. 3.1). If there is more than one point missing due to instrument trigger, it should not be of great consequence for the estimate of the initial velocity and displacement, and the error that it causes in the total mean acceleration can be absorbed within the temporal mean error due to missing data at the end. Hence, the temporal mean of the recorded portion of the event, M, can be defined as a function of the missing initial point, $\ddot{y}_0$, and the sum T of the P missing end points defined by:

$$T = \sum_{p=N+1}^{N+P} \ddot{y}_p \ , \tag{3.7}$$

such that:

$$M = \frac{1}{N} \sum_{k=1}^{N} \ddot{y}_k = -(\frac{\ddot{y}_0}{N} + \frac{T}{N}) \ . \tag{3.8}$$

In terms of these new variables, the true and uncertain acceleration can be written as:

$$\ddot{y}_n = \ddot{z}_n + \ddot{\delta}_n - \frac{1}{N}(\ddot{y}_0 + T) \ , \qquad n = 1, \ldots, N \ . \tag{3.9}$$

These equations imply that the uncertain acceleration $\ddot{y}_n$ is statistically described by three random variables: $\ddot{\delta}_n$ for the digitization noise, $\ddot{y}_0$ for the trigger truncation, and T for the shut-off truncation. As will be justified in Sec. 3.2.2, all three of these random variables can be assumed to be independent stationary processes described by a zero-mean Gaussian distribution, with respective variance a^2, b^2, c^2, or equivalently:

$$\begin{aligned} E(\ddot{\delta}_n) &= 0 \qquad \sigma^2(\ddot{\delta}_n) = a^2 \qquad , n = 1, ..., N \\ E(\ddot{y}_0) &= 0 \qquad \sigma^2(\ddot{y}_0) = b^2 \\ E(T) &= 0 \qquad \sigma^2(T) = c^2 \ . \end{aligned} \tag{3.10}$$

Others have shown that the above Gaussian model is appropriate for digitization noise in analog accelerograms [Trifunac *et al.*, 1973]. Figs. 3.8 and 3.10 show that M is described by a Gaussian distribution such that:

$$E(M) = 0 \qquad \sigma^2(M) = \frac{b^2}{N^2} + \frac{c^2}{N^2} = d^2 \; . \tag{3.11}$$

Hence, the only parameters necessary to define the Gaussian distribution of the true acceleration $\ddot{y}_n$ are a^2, b^2 and c^2, as described in Fig. 3.1, and as given by:

$$E(\ddot{y}_n) = \ddot{z}_n \qquad \sigma^2(\ddot{y}_n) = a^2 + \frac{b^2}{N^2} + \frac{c^2}{N^2} \; . \tag{3.12}$$

Integration of the discrete acceleration is performed with the trapezoidal rule. The uncertain velocity $\dot{y}_n$ is given by the following equation:

$$\dot{y}_n = \ddot{y}_0 \Delta t + \Delta t \sum_{k=1}^{n-1} \ddot{y}_k + \frac{1}{2} \ddot{y}_n \Delta t \; , \qquad n = 1, \ldots, N \; . \tag{3.13}$$

It is found to have a Gaussian distribution with most probable value,

$$E(\dot{y}_n) = \Delta t \sum_{k=1}^{n-1} \ddot{z}_k + \frac{\Delta t}{2} \ddot{z}_n \; , \tag{3.14}$$

and variance,

$$\sigma^2(\dot{y}_n) = \Delta t^2 \left[\left(\frac{2N - 2n + 1}{2N} \right)^2 b^2 + \left(n - \frac{3}{4} \right) a^2 + \left(\frac{2n - 1}{2N} \right)^2 c^2 \right] \; . \tag{3.15}$$

These results are obtained by factoring out each term in Eq. 3.13 as a function of the independent variables $\ddot{y}_0$, $\ddot{\delta}_n$ and T, which have the distributions given in Eq. 3.10.

Similarly, double integration of the acceleration with the trapezoidal rule yields the following equation for the uncertain displacement y_n:

$$y_n = \ddot{y}_0 n \Delta t^2 + \Delta t^2 \sum_{k=1}^{n-1} [(n-k) \ddot{y}_k] + \frac{\Delta t^2}{4} \ddot{y}_n \; , \qquad n = 1, \ldots, N \; . \tag{3.16}$$

The probability distribution of the displacement is also Gaussian, with most probable value,

$$E(y_n) = \Delta t^2 \sum_{k=1}^{n-1} (n-k)\ddot{z}_k + \frac{\Delta t^2}{4}\ddot{z}_n \,, \tag{3.17}$$

and variance,

$$\begin{aligned}\sigma^2(y_n) =& \Delta t^4 \left[\left(n - \frac{2n^2-2n+1}{4N} \right)^2 b^2 + \left(\frac{n^3}{3} - \frac{n^2}{2} + \frac{n}{6} + \frac{1}{16} \right) a^2 \right. \\ & \left. + \left(\frac{2n^2-2n+1}{4N} \right)^2 c^2 \right]\end{aligned} \,. \tag{3.18}$$

The variances of the acceleration, velocity and displacement given in Eqs. 3.12, 3.15, and 3.18, could be simplified under the assumption that N and n are large. Therefore,

$$\sigma^2(\ddot{y}_n) \simeq a^2 \tag{3.19}$$

$$\sigma^2(\dot{y}_n) \simeq \Delta t^2 \left[\left(1 - \frac{n}{N} \right)^2 b^2 + na^2 + \left(\frac{n}{N} \right)^2 c^2 \right] \tag{3.20}$$

$$\sigma^2(y_n) \simeq \Delta t^4 \left[n^2 \left(1 - \frac{n}{2N} \right)^2 b^2 + \frac{n^3}{3} a^2 + \frac{n^4}{4N^2} c^2 \right] \tag{3.21}$$

Hence, the error in the acceleration is very small, and is a constant approximately equal to the standard deviation of the digitizing noise a, which is small (Eq. 3.19). This implies that the most probable value of the acceleration as given by removing the mean from the recorded portion of the seismic event is a fairly good estimate. The standard deviation of the velocity (Eq. 3.20) increases as $\sqrt{n}$ for the digitization noise and as $\frac{n}{N}$ for the end truncation, but decreases as $1 - \frac{n}{N}$ for the missing initial point. In this latter contribution, it can be shown that b^2 contributes both as a constant for the uncertainty in the initial velocity $\dot{y}_0$, and as $(\frac{n}{N})^2$ (also a coefficient for c^2) for the uncertainty in the temporal mean M. The cross-product $-2\frac{n}{N}$ in the first term of Eq. 3.20 describes the correlation between the missing initial data and the uncertain temporal mean. Therefore, near the beginning of the record, it is the trigger truncation that dominates the error in the velocity; however,

this error is small since it is of the order of $b\Delta t$. But as n approaches N, the error is mostly induced by the digitization noise and the mean of the missing end points. The relative importance of these last two terms depends on how the product Na^2 compares to c^2. However, it can be concluded that in the limit for very large N, the uncertainty in the velocity is mainly due to the noise and increases as the square root of time.

The standard deviation of the displacement (Eq. 3.21) increases as n for the trigger effect, which is also the dominant source of error near the beginning of the record, although small. However, as n approaches N the uncertainty becomes dominated by both the digitization noise, as $\sqrt{n^3}$, and the unknown temporal mean, as $\frac{n^2}{N}$. Again the relative contribution of these terms depends on how a^2 and N compare to b^2 and c^2. But in the limit for very large N, the uncertainty due to the noise will be quite large since it increases approximately as $\sqrt{n^3}$. Hence, for the acceleration, velocity and displacement, the error in the signal is dominated by the noise, and the assumption on the missing initial point. Also, the standard deviations are independent of the integrated time histories and only depend on the time, and the noise and truncation levels as defined by a, b, and c. Thus, for a set of records obtained under similar conditions, the standard deviations of the time histories need only be computed once.

It is also possible to assign probability laws to the missing initial velocity and displacement. These laws will depend on the assumptions made on the missing initial acceleration, and can be generally assumed to be Gaussian, with certain means and variances: $E(\dot{y}_0)$, $\sigma^2(\dot{y}_0)$, $E(y_0)$, $\sigma^2(y_0)$. It was assumed earlier in this section that the instrument triggered within the time $2\Delta t$ prior to the the first recorded point; thus, the missing initial velocity and displacement are given by the trapezoidal rule:

$$\dot{y}_0 = \ddot{y}_0 \frac{\Delta t}{2} , \tag{3.22}$$

and,

$$y_0 = \ddot{y}_0 \frac{\Delta t^2}{4} . \tag{3.23}$$

Thus, according to Eq. 3.10, they are described by a Gaussian distribution such that:

$$E(\dot{y}_0) = 0 \qquad \sigma^2(\dot{y}_0) = \frac{\Delta t^2}{4} b^2 \tag{3.24}$$

for the initial velocity, and

$$E(y_0) = 0 \qquad \sigma^2(y_0) = \frac{\Delta t^4}{16} b^2 \tag{3.25}$$

for the initial displacement. The variances obtained for $\ddot{y}_0$, $\dot{y}_0$, and y_0 show that with each integration, the error in assuming zero initial conditions becomes smaller by $\frac{\Delta t}{2}$. This confirms the remarks that were made in Ch. 2 regarding the low probability of having large initial displacements such as those produced by the Volume II processing method.

From tests performed on analog and digital instruments located side by side, it would appear that triggering of the analog instruments for strong shaking often occurs within the time span Δt prior to the first recorded point [Iwan *et al.*, 1984], and for such cases the "missing" initial acceleration, velocity and displacement are exactly zero. This is a less conservative condition than the one adopted in the previous analysis, for which it was assumed that the instrument triggered within the time span $2\Delta t$ prior to the first recorded point. For small events it could be possible for more than one point to be unrecorded initially. In such cases the error in the acceleration temporal mean due to the missing initial points can be incorporated into the error in the temporal mean due to the missing end points without significantly affecting the reliability bounds of the time histories.

An approach similar to the one used to compute Eqs. 3.12 to 3.18 could be used to obtain the most probable time histories and standard deviations for instrument-corrected accelerograms. In this case, the measured, discretized and baseline corrected $\ddot{y}_n$ (Eq. 3.9) must be convolved with the impulse response function of the instrument. The probabililistic description of the acceleration, velocity and displacement corresponding to Eqs. 3.11 to 3.18 must be recomputed accordingly. These derivations can become intricate and messy. In the expressions for the standard deviations, they are only expected to alter the uncertainties arising from errors at the higher frequencies of the recorded accelerogram, which affect the acceleration

time history to a small extent, but have little influence on the velocity and displacement. Hence, the effect of instrument correction on the standard deviations can be neglected, and Eqs. 3.12, 3.15 and 3.18 can be used as a close approximation for the uncertainties in the instrument-corrected acceleration, velocity and displacement as well.

The most probable values and the uncertainties for the integrated velocity and displacement in Eqs. 3.13 and 3.18 were computed under the zero initial velocity assumption. As will be seen in the Sec. 3.2.3, to avoid unrealistic drifts in the displacement time histories of small or far-field events due to noise and truncation, the velocity could be assumed to have zero temporal mean. For such cases, the temporal mean velocity term, $\frac{1}{N}\sum_{i=1}^{N}\dot{y}_i$, should be removed from Eq. 3.13, and the integrations and uncertainties computed accordingly. It is expected that the resulting displacement standard deviation initially behaves as in Eq. 3.18, but approaches zero near the end of the event mainly as a function of the P missing and uncertain end points. Unfortunately, because little is known about the missing end data, as will be explained in Sec. 3.2.2, a reasonable estimate of the standard deviations computed under the zero temporal mean velocity condition cannot be obtained. Hence, Eqs. 3.15 and 3.18 will be used although they may be too conservative.

Eqs. 3.9 to 3.25 describe the probabilistic behavior of the acceleration, velocity and displacement in its most general form, as a function of only three variables: a, b, and c, representing the standard deviations of the sources of error. In the following section numerical values for a, b and c are suggested which are appropriate for some analog accelerographs, and their effect on the standard deviations of the acceleration, velocity and displacement are discussed.

3.2.2 Description of the Uncertainties

The variances of the digitization noise, a^2, and of the initial missing point due to trigger b^2, can be easily quantified. Laboratory tests on several analog accelerograms have shown that the digitization noise can indeed be modelled as Gaussian white noise with a most probable value of zero, and standard deviation a =0.001 g (Ch. 2). The value of b can be obtained by considering the trigger mechanism of analog accelerographs. Since the instrument starts recording as soon

as an acceleration greater than approximately 0.01 g is detected, according to the assumptions the event must have occured within only one Δt prior to the first point, or equivalently somewhere between $\ddot{y}_0$ and $\ddot{y}_1$. Hence, the missing initial point of the record, $\ddot{y}_0$, should be less than approximately 0.01 g. Assuming that b is equal to one-third of the nominal trigger level, or 0.0033 g, for a Gaussian distribution, implies that there is a 99.8% probability that the missing data point is below 0.01 g. This is consistent with the expected behavior of the trigger mechanism. If these two values are adopted for the standard deviations of both the digitizing noise and the trigger truncation error, then the following ratio is established:

$$b = \frac{10}{3} a \, . \tag{3.26}$$

On the other hand, assigning a value for the standard deviation, c, to the unknown end mean, T, is a much more subjective problem. It should be theoretically possible to perform many experiments in which earthquake-like signals are recorded with standard analog accelerographs which shut off automatically, and then measure the error induced by the missing end portion of the motion. Based on the results of these experiments, a probability distribution could then be defined for T. Unfortunately, no such experiments have been performed to date, and it will be necessary to rely on judgement to evaluate c.

The standard deviation c depends on the standard deviations of each of the P missing end points $\ddot{y}_p$, for $p = N+1, \ldots, N+P$, which have a nonstationary behavior as the signal decays down to rest. Nevertheless, it may be possible to assign bounds to the combined uncertainty c arising from the missing end points. In the most favorable case, it can be assumed that the data missing at the end is so small that its trace on the film would have been a straight line, and thus it would have a constant standard deviation $\sigma(\ddot{y}_p)$ equal to that of the digitizing noise a. So under this assumption, the lower-bound estimate of the variance of T is :

$$c^2 = Pa^2 \, . \tag{3.27}$$

According to the shut-off mechanism, analog instruments stop recording several seconds after the passage of the last acceleration greater than approximately 0.01

g. So, if the recorded data has been digitized to the end, there is a very low probability that the missing portion of the signal contains data greater than 0.01 g. Hence, even though the signal comes down to rest at the end of the event, the least favorable case is to assume that the missing end data is stationary with a constant variance equal to one third of the nominal shut-off level, or 0.0033 g. This is also the value assigned to b to describe the error due to instrument trigger. Hence, from Eq. 3.26 the upper-bound estimate of the variance of T is:

$$c^2 \simeq 10Pa^2 \,. \tag{3.28}$$

However, a more realistic description of the problem is to assume that on the average, after instrument shut-off, the level of the signal decays linearly down to rest. This implies that the variance of T is:

$$c^2 \simeq 3.33Pa^2 \,. \tag{3.29}$$

It remains nevertheless, that these expressions for c^2 are given as a function of the number of missing end points P, which is itself an unknown. It might be possible to avoid dealing with the estimate of c^2 altogether, if it can be proved that in certain cases the missing end data does not contribute much to the total error. This involves studying the range that P can take in the expressions for $\sigma^2(\dot{y}_n)$ (Eq. 3.15) and $\sigma^2(y_n)$ (Eq. 3.18) so that the terms containing c are small and can be neglected with respect to the terms describing the uncertainty of the digitization noise, a, and the trigger truncation, b. As n approaches N, the c terms in those equations would in practice remain negligible as long as they are one order of magnitude smaller than the leading term in a, or equivalently as long as the following condition is met:

$$c^2 \leq \frac{N}{10}a^2 \,. \tag{3.30}$$

Hence, for c^2 to satisfy the condition in Eq. 3.30, there must be a trade-off between the number of missing end points and the level of uncertainty assigned to each of them. Or in other words, the more data points are missing, the smaller the level of the missing signal must be. However, the above condition would be easier to satisfy if the number of digitized points, N, is large.

According to the condition in Eq. 3.30 and under the most favorable assumption that the missing end data produces the same level of error as the digitization noise, as expressed in Eq. 3.27, up to 10% of the earthquake could be unrecorded or undigitized without significantly affecting the confidence intervals of the acceleration, velocity and displacement. Similarly, under the worst case (Eq. 3.28), if less than 1% of the data is missing then the effect of the missing end data can be neglected. Most realistically however, according to Eq. 3.29, this number can be safely increased to 3%. Such an assumption can be acceptable, under the condition that the recorded data has been fully digitized up to the very end of the record. This can be easily accomplished with modern digitizers, and digital recorders, and should become common practice. If portions of the recorded data are not digitized, then values that must be assigned to the variance of T will have to be larger than b because the instrument had not yet been automatically shut-off. This in turn implies that the number of missing points P would represent an even larger proportion of the total record, and thus according to Eqs. 3.15 and 3.18, would unnecessarily and significantly increase the level of error in the velocity and in the displacement.

For digital accelerographs the value of the uncertainties are typically smaller than those suggested above for analog instruments. Because of the pre-event memory, there are no missing points in the initial portion of the record. Hence, for accelerograms obtained from digital recorders, the first data point $\ddot{y}_0$ is at rest with an "uncertainty" $b = 0$. Similarly there should be no error due to missing data at the end of the event, and according to the previous paragraphs the c terms can be neglected in the equations describing the standard deviations of the acceleration, velocity and displacement. The uncertainty due to the noise, a, is primarily governed by the quantization of data at 12 bits or 16 bits, and may be smaller than for analog accelerographs.

The errors that are modelled above in the treatment of the uncertainties are those that are the most commonly found in records obtained from analog and digital accelerographs. Rare errors such as instrument malfunction and loosening of the instrument housing are not considered here. It would be difficult to explicitely

treat the uncertainties of such errors, since it is hard to assign probabilities to their existence within the records.

In the following section, the time domain approach using the probabilistic description of the uncertainties for digitization noise and signal truncation is tested on the synthetic records. It will be assumed that the contribution of the end truncation can be neglected under the conditions described by Eq. 3.30.

3.2.3 Application to Synthetic Records

The internal performance and the correction effectiveness of the time domain processing method with treatment of the uncertainties have been tested with three different synthetic signals with and without final displacement offset, and with various levels and combination of noise and trigger truncation. The following analyses and conclusions apply for all the tested cases, but are illustrated with the results obtained for synthetic signal *Q11* only.

From the nomenclature convention used in Ch. 2, recall that the initial "*C*" stands for a signal whose displacement decays down to zero, "*U*" is for one that has a nonzero final offset, "*T*" is a record that is truncated at the beginning to simulate instrument start-up, "*N*" is for a signal that contains digitizing noise. These uncertainties are modelled for two levels of shaking; "*L*" is for a large event which has a maximum acceleration of the order of 50% g, and "*S*" is for a small event which has a maximum acceleration of the order of 5% g. Each of these versions of the record, *Q11C*, *Q11CNL*, *Q11CNS*, *Q11CTL*, *Q11CTS*, *Q11U*, *Q11CNTL*, *Q11CNTS*, *Q11UNTL* and *Q11UNTS* are shown in Figs. 3.2 through 3.11 respectively. In all of the plots for large events ("*L*") 1 unit on the y-axis of the acceleration velocity and displacement represents 1m/sec^2, 1m/sec, and 1m respectively. For small events ("*S*"), 1 unit on the y-axis represents 0.1m/sec^2, 0.1m/sec, and 0.1m respectively. These plots show on the left-hand side the processed and most probable acceleration, velocity and displacement (solid line) as well as their exact analytic counterparts (dotted line). On the right-hand side is shown the error between the exact and processed signals for each of the output records.

Signal *Q11* is composed of 250 frequencies between 0.05 Hz and 25 Hz, and is generated at time intervals of 0.01 sec, as described in Sec. 2.2. The synthetic acceleration time history is assumed to be nearly zero after 20 sec, and is stored at a precision of six decimal points. As explained in Ch. 2, errors in the acceleration temporal mean of 10^{-6} are thus expected, as well as quantization errors of the order of 10^{-7}.

3.2.3.1 Assessment of the Internal Performance

The internal performance of the time domain processing method only depends on the trapezoidal-rule integration method, which is the only step within the program that could generate error in computing the most probable velocity and displacement. The trapezoidal rule is simply tested by integrating the noise-free and untruncated signal *Q11C*, and by comparing the error between the processed and the exact record, as shown in Fig. 3.2. With this method the processed signals are the most probable ones, and are computed with the assumption that the most probable temporal mean of the acceleration is zero. There is no visible difference between the exact and the processed records on the left of Fig. 3.2, but the error plots on the right help in better identifying the errors induced by the processing method. The acceleration error plot, shows that there is a constant error in the mean equal to -2.6 10^{-6}. This error comes from the step within the routine which removes the temporal mean in the acceleration to produce the most probable value of the signal. The difference between the processed and the exact signal reflects the change in the mean due to the record truncation at 20 sec and the quantization accuracy. This error is very small and is barely noticeable in the velocity error, but it is partly responsible for the parabolic drift in the displacement, although it remains quite small.

The error in the velocity is predominantly that of the trapezoidal rule, which cannot properly integrate signals with high-frequency content. As was mentioned in Ch. 2, the error is greatest at the beginning of the synthetic signal because the high frequencies have not significantly decayed. In real accelerograms, the same error would also exist because of the first arrival of the P waves. The maximum error it creates is small however, and represents less than 1% of the maximum velocity.

The trapezoidal-rule error at high frequencies is still apparent at the beginning of the displacement record, at levels equivalent to less than 0.1% of the maximum. The drifting problem in the displacement is due to truncation of *Q11C* at 20 sec and to quantization accuracy of the acceleration data, and shows up at the end as a parabolic function. The combined sources of error represent about 0.1% of the maximum displacement.

The processing method is also capable of capturing a nonzero final displacement in a signal which contains no digitizing noise or instrument start-up simulations, as illustrated with *Q11U* in Fig. 3.7. The displacement record shows that there is no observable difference between the exact and the processed signals, and that the behavior of the record as it decays down to rest is properly replicated. As was discussed for *Q11C* (Fig. 3.2), the greatest source of error remains the change in the mean acceleration due to finite precision and truncation of *Q11U* at 20 sec, and is of the order of -2.4 10^{-6}. This produces an error in the displacement which is less than 0.1% of the exact maximum, and is negligible in practice.

Hence, it can be concluded that the internal performance of the time domain processing method is good since it adds relative errors of less than 1% to the output records, which are solely due to the trapezoidal integration rule. The other errors observed in the processed signals arise from errors in the temporal mean acceleration which existed before processing, and are not a reflection of the internal performance of the correction and integration method.

3.2.3.2 Assessment of the Correction Effectiveness

As for the original Volume II method described in Ch. 2, the correction effectiveness is tested by studying how well the processing method is capable of removing digitization noise and of coping with missing initial data. The effect of digitizing noise alone is shown in the plots of the processed results, for large and small event simulations, in Fig. 3.3 for *Q11CNL* and Fig. 3.4 for *Q11CNS* respectively. In each of these records, the same noise sample is used to contaminate the synthetic signal *Q11C*, but it is scaled for either small event or large event simulations.

The processing method presented in Sec. 3.2.1 does not attempt to remove the digitizing noise within the recorded data. The digitizing noise, modelled as white noise, affects the whole frequency range of the signal including the *d.c.* component. Since the data is processed with the assumption that the most probable temporal mean of the acceleration is zero, the error that appears as drifts after integration is due to the changes in the temporal mean of the acceleration induced by the added digitization noise. Furthermore, the error in the mean acceleration is larger as the relative noise level becomes more important. For the large event *Q11CNL* (Fig. 3.3) the maximum acceleration is of the order of 30% g, and the noise adds an error at each data point of about one thousandth of a g, which represents 0.3% of the peak. Similarly for the small event *Q11CNS* (Fig. 3.4), the maximum acceleration is approximately 3% g and the noise-to-signal level which is ten times larger corresponds to about 3% of the peak. This difference in the noise level between the large and small event simulations is observable in the tail end of the acceleration, where the digitizing noise is much more predominant in *Q11CNS* (Fig. 3.4) than it is in *Q11CNL* (Fig. 3.3). As a result of the digitization noise, the mean in the acceleration has increased by 0.0001 for *Q11CNL* and by 0.001 for *Q11CNS*.

The combination of having a noise-contaminated signal and of removing its temporal mean creates a shift in the acceleration which forces the velocity record to assume a parabolic shape with zero final value. This phenomenon is particularly noticeable in Fig. 3.4 for the small event simulation, in which the shift in the mean is greatest and is responsible for an error in the velocity equivalent to 12% of the exact maximum. For large events (Fig. 3.3), the error in the velocity due to the shift in the acceleration mean represents 1.2% of the maximum, and is at about the same level as the high-frequency error from the trapezoidal integration rule. Hence, when the digitizing noise in the acceleration is increased tenfold, so is the error it produces in the velocity, as expected. It is also interesting to note that, apart from the difference in scales, both the large event model (*Q11CNL*, Fig. 3.3) and the small event model (*Q11CNS*, Fig. 3.4) alter the velocity in very much the same way to conform to the assumptions, as is seen in the error plots.

The departure of the processed velocity from its true zero temporal mean value creates a drift in the displacement which is greater as the noise level is increased. The error in the displacement is a combination of a parabolic function due to the shift in the mean acceleration, and a linear function due to the change in the mean velocity imposed by the method. This is seen in both the displacement error plots for *Q11CNL* and *Q11CNS*, in which the error first appears as a linear slope, before tapering off at the end of the signal. Again, both event sizes exhibit exactly the same shape for the displacement error, except that the one for the small event is ten times larger than that of the large event, and represents a 250% difference relative to the maximum. Hence, the digitization and processing errors are treated as expected, since the noise sample for the small event is ten times larger than that for the large event. The processing method as presented so far does not try to correct for the displacement drifts created by uncertain sources such as digitization noise, but as will be discussed later the standard deviations will properly describe bounds for these errors.

The effect of simulated start-up truncation is discussed next. Figs. 3.5 and 3.6 show the processed results of synthetic signals *Q11CTL* for large events, and *Q11CTS* for small events, respectively. To comply with the model of the start-up mechanism, 3 data points, or 0.03 seconds, have been removed from the beginning of *Q11CTL*, and 29 data points, equivalent to 0.3 sec, have been truncated from the beginning of signal *Q11CTS*. These synthetic signals are not corrupted by digitization noise. Removing the initial points in the acceleration is expected to change its temporal mean, as is seen in the error plots of the acceleration. For large events the error is about -2.0 10^{-5}, and for small events it is about one hundred times larger than that at 1.2 10^{-3}. After integration, the error in the velocity appears as a linear drift, where the slope is equal to the error in the mean acceleration. For large events (*Q11CNL*, Fig. 3.5), the error in the velocity is very small compared to the trapezoidal-rule errors at high frequencies. The combination of these two errors represent a total of less than 1% of the maximum velocity, and are minute enough not to cause an observable difference between the processed most probable signal and its exact synthetic counterpart. However, in small events, the error in the velocity reaches up to 7% of the maximum and is predominantly induced

by the error in the mean acceleration due to trigger truncation. The difference between the exact and processed velocity for small event models is clearly visible (*Q11CTS*, Fig. 3.6). Nevertheless, it is the processed displacement record that is the most affected by the trigger truncation. For the same reasons as for the noise simulation, the errors in the temporal means of the acceleration creates a drift in the displacement error which is parabolic in shape. This produces only a small error at the end of the displacement for *Q11CTL* (2% of the exact maximum), but the error is more important for *Q11CTS*, and represents 200% of the peak displacement. However, the processing method takes these errors into account, as will be seen when reliability intervals are discussed.

The synthetic signals can also be used to study the evaluation of the first acceleration, velocity and displacement point after trigger. The processing method makes the assumption that the event started within the two time steps prior to the first recorded point. Hence, only one point is uncertain, since the first point is assumed to be exactly zero for integration purposes. Forcing the temporal mean of the signal to be zero affects the evaluation of the most probable initial acceleration, velocity and displacement. The error plots of *Q11CTL* (Fig. 3.5) and *Q11CTS* (Fig. 3.6) show that the inital estimates differ from the exact value by only a small amount. The largest error is found for the initial estimate of the velocity in *Q11CTS*, but represents only an error of 7% relative to the peak, even though a total of 29 points are missing because of trigger simulation. Nevertheless, the assumptions of the processing method produce excellent estimates for the most probable initial displacements regardless of the truncation level, as well as estimates for the most probable initial accelerations which only differ by the change in the temporal mean.

In summary, the truncation of the synthetic signal at 20 sec and quantization accuracy are responsible for an error of the order of 10^{-6} in the acceleration, while the trapezoidal-rule integration scheme produces errors of the order of 10^{-3} in the velocity. The combination of these two errors results in changes in the displacement of the order of 10^{-3}. For large event simulations, the digitizing noise alters the velocity by 10^{-3} and the displacement by 10^{-2}. For such events the instrument

start-up is responsible for changes in the temporal mean acceleration of 10^{-5}, which is one order of magnitude greater than the truncation after 20 sec and quantization effects. The velocity is still dominated by the trapezoidal integration rule errors at 10^{-3}, and combined with the start-up truncation effects amounts to an error of 10^{-3} in the displacement. Hence, for large events, it is the noise that is the predominant source of error. For small event simulations, the digitization noise creates an error of the order of 10^{-2} in the velocity, and 10^{-1} in the displacement. Initial instrument truncation changes the mean of the acceleration by 10^{-3}, producing an error of order 10^{-2} in the velocity and 10^{-1} in the displacement, but at only half the amount of that due to digitization noise. Hence, for small events, the digitization noise is also expected to be the dominant source of error in the processed signals, but the instrument start-up truncation effects are no longer negligible. The combination of these latter errors are several orders of magnitude larger than the errors induced by the trapezoidal integration rule. As will be seen in Sec. 3.3.3, these levels of errors will be significantly increased when the synthetic records are tested for end truncation effects.

The next four figures, Figs. 3.8 through 3.11, show how well the processing method handles cases where digitization noise, trigger truncation and final displacement offsets are combined together and modelled for both large and small seismic events. *Q11CNTL* (Fig. 3.8) is the synthetic signal which best models an accelerogram obtained from a large seismic event with no final displacement. As predicted in the previous paragraph, the error in the processed signal is predominantly due to the digitizing noise. Indeed, there are only slight differences between the error plots of *Q11CNL*, the signal with no instrument truncation effects (Fig. 3.3), and their respective counterparts in *Q11CNTL* (Fig. 3.8) which has 3 data points missing at the beginning. For small event simulations, as illustrated by *Q11CNTS* (Fig. 3.9), the output errors in the velocity and displacement have increased by 50% from the case where no instrument truncation effects are included (*Q11CNS*, Fig. 3.4), although there is little change in the shape of the error. This difference between the two cases corresponds almost exactly to the error introduced in the output signals by start-up truncation alone (*Q11CTS*, Fig. 3.6). Hence, this suggests that the uncertainties produce additive errors in the processed output records. This result also

follows mathematically from the fact that the noise and truncation lead to additive uncertainties in the mean acceleration, and noise in the acceleration is additive by definition.

The final displacement offsets are modelled along with digitization noise and instrument truncation in synthetic record *Q11UNTL* (Fig. 3.10) for large events, and in *Q11UNTS* (Fig. 3.11) for small events. It should be noted that it is very unlikely that a small earthquake produces a final offset in the displacement at the Earth's surface, and hence the synthetic signal *Q11UNTS* is unlikely to be representative of a seismic event. Nevertheless, it can be a good approximation of the worst kind of signal the processing method is expected to correct and represents a bound for the correction effectiveness. It turns out, however, that the errors in the acceleration, velocity and displacement after processing are nearly identical to those obtained previously for *Q11CNTL* and *Q11CNTS*. The remarks that were made in the previous paragraph then also apply to signals with final displacement offsets, and it is concluded that final displacement offsets do not affect the correction effectiveness of the processing method.

From the processing examples illustrated in the previous plots, it was shown that the largest errors were produced in the displacement time history of small event simulations by the relatively high levels of noise and truncation. The large drifts in the displacements result from the fact that the acceleration is assumed to have zero temporal mean, although the mean can be significantly altered by noise and missing data. Also, the initial velocity is assumed to be zero, which imposes the final velocity to be zero. This creates a spurious nonzero mean in the velocity time history which is reflected by drifts in the displacement time history with zero initial value.

When using this processing method on real accelerograms, the error in the displacement records can be reduced for small levels of shaking (i.e., far-field record or small event) by considering the physical constraint that such earthquakes do not produce nonzero final displacement offsets. This constraint is implemented by imposing that the temporal mean velocity is equal to zero, which reduces the drifts from the displacement signal by forcing the final displacement to be zero when the

initial displacement is assumed to be zero also. This correction step significantly reduces the error between the exact and the processed displacement records of small events, as is shown in Fig. 3.12 where *Q11CNTS* is processed using the zero mean velocity assumption. Removing the mean from the velocity creates an offset in that signal which can no longer start and decay about zero, as could be expected. The more data is missing due to truncation, the larger the shift in the velocity is expected to be. In extreme cases, forcing the temporal mean of the velocity to be zero could result in unrealistic initial velocities for far-field or small seismic events. In Ch. 4, optimal methods are used to correct the *d.c.* and low-frequency errors in accelerograms. It will be shown that the unrealistic shifts in the velocity temporal mean are significantly reduced when optimal correction methods are applied.

Even though the displacement corresponding to the zero mean velocity condition (Fig. 3.12) must now take an unrealistic parabolic shape to come to zero at the end of the record, the initial portion matches the exact motions much better than it does without the velocity mean correction (*Q11CNTS*, Fig. 3.9). Also, the maximum error for the displacement in Fig. 3.12 is reduced sevenfold from the one in Fig. 3.9. Hence, using the zero mean velocity criteria for small events improves the fit of the processed displacement at the beginning of the record, and significantly reduces the amount of processing error. It will be shown that these new sources of error can be bounded more properly by the standard deviations than the drifts in Fig. 3.9. The optimal methods used in Ch. 4 will also prove to be effective in reducing such parabolic errors in the displacements.

Hence, assuming that the final displacement is zero for small events considerably improves the correction effectiveness of the processing method. For large events,it was shown that the error introduced by the uncertain initial conditions and digitizing noise were relatively small, and did not affect the processed results much. Thus, the time domain method produces good estimates for the most probable acceleration, velocity and displacement for large seismic accelerograms, and could be made more correction effective for small events by taking into consideration certain physical constraints, as mentioned earlier.

3.2.3.3 Reliability Bounds for Signals

Contrary to most earthquake processing techniques, the errors induced by the uncertain initial conditions and the digitizing noise are not dealt with directly, in the sense that there are no steps within the program that remove or filter out the effects of these sources of error. Nevertheless, the processing method presents the most probable values of the processed records; these are the best estimate to the real event that can be achieved under the circumstances, unless additional information could be made available. The standard deviations, however, can help account for any source of error uncertainty by assigning reliability bounds within which the true motion is expected to have occurred. The variances of the acceleration, velocity and displacement as a function of the digitizing noise variance a^2, and the instrument trigger variance b^2 were derived in Eqs. 3.15, 3.21 and 3.27 respectively. The square root of these quantities define the standard deviations for each signal. Since the true, but uncertain acceleration, velocity and displacement are described by a Gaussian distribution, there is a probability of 84% that the true signal falls within one standard deviation of the most probable estimate, a probability of 97.7% for two standard deviations, and a probability of 99.9% for three standard deviations.

The smallest error between the most probable estimates and the exact records were shown to occur for signals of large events with or without final displacement offsets, such as *Q11CNTL* (Fig. 3.8). Fig. 3.13 shows the processed and most probable velocity and displacement (solid line) for signal *Q11CNTL*, bounded from top to bottom by one, two and three standard deviations (dashed line). In each figure the dotted line represents the exact value of the synthetic record. The velocity plots on the left of the figure show that the errors create very small levels of uncertainty about the most probable estimate, even at three standard deviations. The uncertainty bounds are much more spread out in the displacement plots, on the right of Fig. 3.13, and reflect the fact that the evaluation of reliable displacements from an error-contaminated accelerogram is a difficult task, as is well known. Nevertheless, the standard deviations about the most probable displacement do properly contain the exact signal. In this case, the true motion is completely bounded within the two

standard deviations of the most probable record. Fig. 3.14 shows the bounds for one, two and three standard deviations about the most probable acceleration. The uncertainties are extremely small, and there is little observable difference between the three cases. This is expected since the signal is a simulation of a large event for which the signal-to-noise ratio is very high. The noise-contaminated synthetic accelerograms will always be properly bounded by the standard deviations defined by Eq. 3.15, since by construction the noise is added onto the signals assuming a Gaussian distribution with most probable value zero, and variance a^2.

Simulations of large earthquakes with final displacement offsets are illustrated with *Q11UNTL* in Fig. 3.15. This figure shows the most probable velocity and displacement, as obtained by the processing method, which is bounded by one, two and three standard deviations, respectively, from top to bottom. It was shown that the time domain method could properly identify final displacement offsets. Also, the offset is not a parameter entering the description of the uncertainties. Hence, the reliability of such events are the same as those that exhibit zero final displacement for the same level of shaking. Thus, as for the previous case, the uncertainties in the processed velocities are very small, indicating that the most probable value is a good estimate. The estimate of the most probable displacement proves to be more uncertain, since the reliability interval is much larger than for the velocity. Nevertheless, the final displacement offset is properly captured by the standard deviation bounds as defined by the Gaussian distribution, and two standard deviations about the most probable estimate prove to be sufficient to include the complete signal.

Simulations of small events with no final displacements are illustrated with synthetic signal *Q11CNTS*, in Fig. 3.16. The reliability bounds about the most probable values are much wider in this case, since the signal-to-noise ratio is relatively small. The standard deviations about the most probable velocity remain small enough, however, to show that the processing method reproduces the exact velocity relatively well. On the other hand, the standard deviations about the most probable displacement are extremely large, indicating that it cannot be considered a reliable estimate of the exact motion. This confirms the fact that the error between

the processed and the exact displacement signal is expected to be very large for small seismic events, as was noted for Fig. 3.9. In particular, Fig. 3.16 shows that at the very beginning of the displacement record three standard deviations about the most probable are required to properly enclose the exact signal. This is a result of the large number of missing initial points, 29 in the case of *Q11CNTS*, for which the assumption of only one truncated point with variance b^2 is not fully satisfactory. The effect of having an uncertain number of points missing at the beginning on the variance of the initial point is equivalent to the problem discussed for the variance of the missing end data. Thus, when many points are missing, each with a variance lesser than b^2, the sum produces an error bound for the first recorded point which may be greater than b. Nevertheless, the error in the initial portion of the displacement time history is extremely small. Hence, the probabilistic description of the displacement bounds given by Eq. 3.24 remains acceptable since the digitization noise dominates the error in most cases, compared to the initial truncation effect. In practice, the results of *Q11CNTS* (Fig. 3.16) show that the assumption proposed in Sec. 3.2.1 is valid since three standard deviations about the most probable value of the displacement completely enclose the exact record.

A better description of the initial displacement behavior can be achieved by either increasing the value of b to account for the larger number of missing points due to instrument start-up, or by assuming that small earthquakes cannot produce nonzero final displacement offsets. The first option improves the description of the uncertainty, the second improves the estimate of the most probable value. When the mean is removed from the velocity, the initial portion of the signal fits the exact record well, and the standard deviations provide adequate bounds for the uncertainties. This is illustrated for the synthetic record *Q11CNTS* in Fig. 3.17. Although the most probable velocity no longer decays down to zero after the temporal mean is removed, the exact signal is still contained within one standard deviation. Hence, the velocity error is properly described by the probablistic assumptions. As for the displacement signal, its reliability is considerably increased by assuming that the velocity has zero temporal mean. Indeed, Fig. 3.17 shows that the processed displacement differs from the exact record by much less than one standard deviation. Hence, the processing of the synthetic signals have shown that for small events,

the estimates of the most probable velocities and displacement are considerably improved by assuming that the temporal mean of the velocity is zero. The errors induced by this assumption, namely nonzero final velocity and spurious parabolic shape in the displacement, are conservatively accounted for by the uncertainty prescribed by the probabilistic approach. As was mentioned previously, better reliability bounds for small events which are assumed to have no final displacement could be computed, but this requires information on the missing end points of which, in fact, little is known.

The reliability of the most probable acceleration for simulations of small seismic events, is illustrated with *Q11CNTS* in Fig. 3.18. Compared with the results for large events (Fig. 3.14) the scatter about the most probable value is greater. For the particular synthetic signal *Q11CNTS*, three standard deviations represents approximately 10% of the peak, which properly provides bounds to include the exact signal as seen more clearly from the acceleration error plot shown in Fig. 3.9.

As was mentioned previously, *Q11UNTS*, the synthetic signal which models small events with a nonzero final displacement, provides a bound for the testing of the correction effectiveness, since it represents a worst case that any accelerogram processing method should have to correct. The results of the most probable estimates of the velocity and displacement (Fig. 3.19) shows that even in this extreme case, and despite the optimistic assumption of only one missing initial point, the processing method has good internal performance, and the reliabilty bounds defined by three standard deviations about the most probable signal do include the exact time histories.

3.2.4 Concluding Remarks

In summary, the time domain processing method has good internal performance, in the sense that the only source of output error is introduced at high frequencies by the trapezoidal integration rule. These errors remain small and have been shown to be negligible compared to the effects of digitization noise, even for simulations of large events. The processing method does not have perfect correction effectiveness, since the noise is not removed, and the integrated velocities and displacements are allowed to drift due to various sources of errors affecting the

temporal means. However, the testing results suggest that the method provides reliabilty bounds about the most probable estimate of the signal which adequately describe the interval within which the exact signal should lie. This study has also shown that as the size of the earthquake increases, the relative amount of processing error decreases; implying that the most probable estimates of the motion, as provided by the processing method, also become more reliable. This is usually expected, but in Ch. 2 it was shown that for the original Volume II processing method such was not the case. Simulations of the processing of small accelerograms suggest that the accelerations and velocities are fairly accurate, but that the amount of error in the displacement is very large. The most probable estimate of the displacement could be made more accurate by assuming that small events have zero temporal mean in the velocity. It was shown, however, that even in the worst case, and without the implementation of the zero mean velocity criteria, the probabilistic formulation adequately assigns bounds to the estimates. Hence, the time domain processing method can be said to have both good correction effectiveness and internal performance.

The previous analysis of the correction effectiveness was based on synthetic signals corrupted for analog instrument trigger and digitization noise levels. A similar analysis could also have been performed for synthetic signals corrupted for digital instruments. In the latter case it is expected that truncation effects are negligible. The noise, however, is still present in the signal, although it is much smaller depending on 12-bit or 16-bit digitization. The analysis would show that because of the low error levels in the acceleration, there is very little difference between the processed and the exact signals. Nevertheless, as for the analog instrument study with *Q11CNL* and *Q11UNL*, the errors from the time domain processing method will depend on the noise level in the signal.

3.3 Frequency Domain Formulation and Results

In the previous section, the accelerogram processing method was derived in the time domain, and was shown to have good internal performance. But for reasons that were mentioned at the beginning of the chapter, performing the processing in the frequency domain remains the more logical choice. The assumptions and

the processing method for the frequency domain approach are presented below in Sec. 3.3.1, and the test results with the synthetic records are presented in Sec. 3.3.3.

3.3.1 Assumptions and Definitions

The assumptions that were made in Sec. 3.2.1 for the time domain approach are still valid for the frequency domain method, namely that each data point of the accelerogram is corrupted by white noise due to the digitization process, with most probable value zero and standard deviation a, that only one point is missing because of instrument trigger with most probable value zero and standard deviation b, and that the baseline of the accelerogram is offset by some constant, but uncertain, amount. Hence, Eq. 3.9 still holds, and $\ddot{z}_n$ represents the most probable value of the true acceleration time history $\ddot{y}_n$. The frequency domain is only used as a tool for processing $\ddot{z}_n$ to obtain the most probable acceleration, velocity and displacement, and does not affect the probabilistic description of the uncertainties in the final time histories. Thus, the standard deviations derived for the acceleration, velocity and displacement in Sec. 3.2 are still valid.

Actually, the probability distributions for the acceleration, velocity and displacement derived earlier, can also be derived in the frequency domain. When the N measured points of discrete data are used to estimate the true motions, the discrete Fourier transform pair is given by:

$$\ddot{Y}_m = \frac{1}{N} \sum_{n=0}^{N-1} \ddot{y}_n \exp\left(-i\frac{2\pi}{N}mn\right) , \qquad m = -\frac{N}{2}+1, \ldots, \frac{N}{2} \tag{3.31}$$

$$\ddot{y}_n = \sum_{m=-N/2+1}^{N/2} \ddot{Y}_m \exp\left(i\frac{2\pi}{N}mn\right) , \qquad n = 0, \ldots, N-1 . \tag{3.32}$$

In the frequency domain, Eq. 3.9 is thus given by:

$$\begin{cases} \ddot{Y}_0 = M \\ \ddot{Y}_m = \ddot{Z}_m + \ddot{\Delta}_m , \qquad m = 1, \ldots, \frac{N}{2} \end{cases} . \tag{3.33}$$

Eq. 3.33 provides the most general description of the problem in the frequency domain, where $\ddot{Y}_m$, $\ddot{Z}_m$, $\ddot{\Delta}_m$ are respectively the Fourier transforms of the uncertain but true acceleration $\ddot{y}_n$, of the measured acceleration from which the mean has been

removed $\ddot{z}_n$, and of the uncertain digitization noise $\ddot{\delta}_n$. Because the accelerogram is given by a real set of numbers of dimension N in the time domain, the spectrum is given by a complex set of numbers of dimension $\frac{N}{2}$ symmetric about zero in the frequency domain. In the time domain, the uncertain mean acceleration M of the N measured points of discrete data was shown to be due to a combination of missing points both at the beginning and at the end of the signal (Eq. 3.8), and was split up as such to provide an easier derivation of the probabilistic parameters. In the frequency domain, the error due to M only appears in the *d.c.* component of the spectrum, that is $\ddot{Y}_0$.

Using Eq. 3.31, it can be shown that since the noise $\ddot{\delta}_n$ is described by a Gaussian distribution with most probable value zero and variance a^2 in the time domain, then $\ddot{\Delta}_m$ is also described by a Gaussian distribution in the frequency domain such that:

$$E[\ddot{\Delta}_m] = 0 \qquad \text{and} \qquad \sigma^2[\ddot{\Delta}_m] = \frac{a^2}{N}\,, \qquad m = 1, \ldots, \frac{N}{2}\,. \tag{3.34}$$

The distribution for the *d.c.* component is also Gaussian as described by Eq. 3.11. Furthermore, it can be shown since $\ddot{\delta}_n$ and $\ddot{\delta}_k$, $n \neq k$, are independent for large N, so are $\ddot{\Delta}_m$ and $\ddot{\Delta}_p$, $m \neq p$, and therefore $\ddot{Y}_m$ and $\ddot{Y}_p$, $m \neq p$, are also independent, given $\ddot{Z}_m$ and $\ddot{Z}_p$.

Applying the above result to Eq. 3.33 leads to the conclusion that the Fourier transform of the true accelerogram is described by a Gaussian distribution such that:

$$E[\ddot{Y}_0] = 0 \qquad \text{and} \qquad \sigma^2[\ddot{Y}_0] = \frac{b^2 + c^2}{N^2}\,, \tag{3.35}$$

and,

$$E[\ddot{Y}_m] = \ddot{Z}_m \qquad \text{and} \qquad \sigma^2[\ddot{Y}_m] = \frac{a^2}{N}\,, \qquad m = 1, \ldots, \frac{N}{2}\,. \tag{3.36}$$

Hence, according to Eq. 3.36, the uncertainties in the Fourier coefficients of the true accelerogram are only a function of the digitization and processing noise, and are quite small. Thus, the Fourier transform of the N discrete points of measured data provides a good estimate of the true frequency content $\ddot{Y}_m$, $m \neq 0$. The largest

uncertainty appears in the estimate of the *d.c.* and is a function of the uncertainty associated with the missing data, both at the beginning and the end of the signal. It will be seen later that an error near *d.c.* is also induced by numerical limitations of the discrete Fourier transform, implemented with a fast Fourier transform algorithm for which zeroes must usually be added to the N discrete points of measured data.

Integration in the frequency domain from acceleration to velocity and displacement is simply achieved by dividing the Fourier coefficients respectively by $i\omega_m$ and $-\omega_m^2$, where ω_m is the corresponding frequency of the harmonic component. This can be proved by representing the original continuous time history by a harmonic series for which the coefficients are given by the discrete Fourier transform (to within the aliasing caused by the discrete time sampling). Hence,

$$\dot{Y}_m = \frac{\ddot{Y}_m}{i\omega_m} , \qquad m = 1, \ldots, \frac{N}{2} \tag{3.37}$$

and,

$$Y_m = -\frac{\ddot{Y}_m}{\omega_m^2} , \qquad m = 1, \ldots, \frac{N}{2} \tag{3.38}$$

where,

$$\omega_m = m\frac{2\pi}{N\Delta t} , \qquad m = 1, \ldots, \frac{N}{2} . \tag{3.39}$$

The *d.c.* is handled separately, as seen later. Hence, according to Eqs. 3.35 and 3.36, the spectral coefficients of the velocity and displacement are also described by Gaussian distributions such that:

$$E[\dot{Y}_m] = -i\frac{N\Delta t}{2\pi}\frac{\ddot{Z}_m}{m} \qquad \text{and} \qquad \sigma^2[\dot{Y}_m] = \frac{\Delta t^2}{4\pi^2}\frac{Na^2}{m^2} , \tag{3.40}$$

and,

$$E[Y_m] = -\left(\frac{N\Delta t}{2\pi}\right)^2\frac{\ddot{Z}_m}{m^2} \qquad \text{and} \qquad \sigma^2[Y_m] = \left(\frac{\Delta t^2}{4\pi^2}\right)^2\frac{N^3a^2}{m^4} . \tag{3.41}$$

These two last equations confirm that the most probable velocity and displacement spectra are computed directly from the most probable acceleration spectrum $\ddot{Z}_m$, which is itself obtained by forward transformation of the most probable acceleration time history $\ddot{z}_n$ with zero mean. These equations also imply that the uncertainties

$\sigma[\dot{Y}_m]$ and $\sigma[Y_m]$ in the estimate of the spectra are only a function of the digitization and processing noise a, and decrease inversely proportional to the frequency for the velocity, and to the square of the frequency for the displacement.

The frequency domain approach can be made consistent with the probabilistic description of the data which assumes that, at the most, one data point $\ddot{y}_0$ is missing due to trigger truncation with most probable value zero and variance b^2 (Fig. 3.1). This missing initial data point is accounted for in the Fourier transformation by adding an extra point, with value zero (i.e., $\ddot{z}_0 = 0$), at the beginning of the measured and discretized accelerogram $\ddot{z}_n$ with zero temporal mean.

The processing procedure for the frequency domain method is summarized in the flowchart of Fig. 3.20. The measured, digitized and baseline corrected accelerogram is described by the time history $\ddot{z}_n$ of dimension N. When using the fast Fourier transform (FFT) algorithm to compute the spectrum, in general zeroes have to be added at the end of $\ddot{z}_n$. In the implemented FFT algorithm [Hall, 1982], a total record length which is either a power of 2, or 3 times that, can be used. The spectral coefficients of the acceleration with zero *d.c.* can be adjusted for instrument correction and filtering, if desired, to obtain the most probable acceleration spectrum $\ddot{Z}_m$, for $m = 1, \ldots, \frac{N}{2}$. The most probable acceleration time history with zero temporal mean $\ddot{z}_{0n}$ is then obtained by inverse Fourier transformation of $\ddot{Z}_m$, with $\ddot{Z}_0 = 0$. The notation $\ddot{z}_{0n}$ is used for the acceleration time history with zero temporal mean obtained *after* inverse Fourier transformation, to distinguish it from the baseline-corrected discretized measured acceleration $\ddot{z}_n$ prior to processing. When no filtering is performed in the frequency domain $\ddot{z}_n$ and $\ddot{z}_{0n}$ are equal, within numerical round-off limitations.

The acceleration can be integrated by dividing $\ddot{Z}_m$ by $i\omega_m$ and $-\omega_m^2$ to produce the most probable velocity spectrum $\dot{Z}_m$ and displacement spectrum Z_m, where at *d.c.* $\dot{Z}_0 = 0$ and $Z_0 = 0$. Inverse transformation of these spectra generates the velocity time history v_n and displacement time history d_n which have zero temporal means and nonzero initial values v_0 and d_0 at trigger. From the arguments presented in the previous section, it was concluded that for small events or for far-field records, where no final displacement offset is expected, the most probable displacement has

zero initial and final value and corresponds to a zero temporal mean velocity. Thus, in this case, the most probable velocity with zero temporal mean $\dot{z}_{0n}$ is equal to v_n, and the most probable displacement z_{0n} is obtained by removing d_0 from all the d_n. For near-field records of large events, final displacement offsets can be expected. The most probable displacement must allow for this, and can only exist if the most probable velocity has nonzero temporal mean. Hence, in this case, the most probable velocity $\dot{z}_n$ is chosen to have zero initial value and is obtained by removing v_0 from all the v_n, and the most probable displacement z_n has a linear corrective term depending on v_0 and d_0. The assumptions and equations are summarized in Fig. 3.20.

Finally the standard deviations corresponding to the most probable acceleration, velocity and displacement are computed in the time domain using respectively Eqs. 3.12, 3.15 and 3.18.

3.3.2 Internal Performance of the Frequency Domain Method

The internal performance of this processing method is dependent on the internal performance of the discrete Fourier transform implemented with a fast Fourier transform algorithm. Along with the initial baseline correction of the signal, it is the only step within the procedure which can induce errors into the original signal. Indeed, the other steps, which include instrument correction and integration, are performed in the frequency domain using exact transfer functions.

The study of the errors created by the forward and inverse Fourier transformation of discrete signals is a topic which has been widely investigated. The main sources of error are summarized in Fig. 3.21, and are briefly explained in the next paragraphs. For more detail, the reader should consult text books on digital signal processing and Fourier transform techniques such as Oppenheim & Schaffer [1975], Rabiner & Gold [1975], Bendat & Piersol [1986], or Brigham [1974].

The two main sources of frequency domain errors induced by the processing of accelerograms are the result of sampling a continuous signal into a discrete form, and of truncating the record in the time domain. The first source of error leads to high-frequency aliasing which may contaminate the integrated time histories. The second

source of error leads to spectral rippling through out the whole frequency range, but this does not significantly affect the integrated time histories. However, baseline correction of a truncated acceleration signal forces zero temporal mean which can induce long-period errors in the time histories when zeroes are added to implement the FFT algorithm. Because errors arising from the uncertain acceleration *d.c.* can be separated from errors arising from aliasing and truncation (Eq. 3.33), the internal performance of the processing method for errors resulting from a nonzero temporal acceleration mean is studied separately at the end of this section.

The way the discrete Fourier transform generates and exhibits errors in signals with no baseline error can be decomposed into five steps, as shown in Fig. 3.21 [Brigham, 1974]. For each of the steps, the Fourier transform pair is shown, with the time domain representation to the left of the figure, and the frequency domain equivalent to the right. The signal used to illustrate this figure is that of a general waveform, which is neither periodic, time-limited or band-limited. As is the case for accelerograms, the time history is real, and hence the spectrum is symmetric about the origin.

Fig. 3.21(a) shows the exact Fourier transform pair for the continuous signals $h(t)$ and $H(f)$. When computing the discrete Fourier transform, the continuous time history must first be sampled at intervals of T ($= \Delta t$ used earlier) (Fig. 3.21(b)). This is equivalent to multiplying $h(t)$ with the time domain sampling function $\delta_0(t)$ such that:

$$\delta_0(t) = \sum_{k=-\infty}^{+\infty} \delta(t - kT) \; . \tag{3.52}$$

The time domain sampling function is equivalent in the frequency domain to another sampling function $\Delta_0(f)$ of interval $\frac{1}{T}$,as shown in Fig. 3.21(b), and such that:

$$\Delta_0(f) = \sum_{n=-\infty}^{+\infty} \delta\left(f - \frac{n}{T}\right) \; . \tag{3.53}$$

Because multiplication in the time domain is equivalent to convolution in the frequency domain, discretizing the continuous time history $h(t)$ at intervals of T is

equivalent to reproducing the continuous spectrum $|H(f)|$ at intervals of $\frac{1}{T}$, where $\frac{1}{2T}$ is the Nyquist frequency (Fig. 3.21(c)). Since the signal is not band-limited, aliasing will occur about frequencies $\pm\frac{1}{2T}$, $\pm\frac{3}{2T}$, $\pm\frac{5}{2T}$,..., where the duplicated spectra overlap. However, the effects of aliasing can be substantially reduced by choosing an interval T which is small enough to insure that the spectrum has significantly decreased in amplitude in the vicinity of the Nyquist frequency. Also, it can be proved by representing the original continuous acceleration time history by a harmonic series for which the coefficients are given by the discrete Fourier transform, that the acceleration aliasing error at each discrete $t_n = nT$ is zero, although it is nonzero in between these times. Spectra of earthquake accelerograms have little activity beyond 50 Hz. Hence, a discretization interval of $T = 0.01$ sec is usually sufficient to substantially limit the effects of high-frequency aliasing in the acceleration spectrum. Often after integration, most signs of the high-frequency aliasing have disappeared from the velocity and displacement spectra. However, it can be shown, by comparing the harmonic series described above and the Fourier series of a continuous acceleration signal, that aliasing errors due to discretization are expected to affect the integrated velocity and displacement time histories at each $t_n = nT$ to a small extent.

The second source of error is a direct result of truncating the infinite waveform. Although accelerograms are theoretically time-limited, they are nevertheless truncated either because of instrument trigger or shut-off mechanisms, or because of nondigitization of the final portion of the record. As is illustrated in Figs. 3.21(d) and (e), truncating a time history at time T_0 is equivalent to multiplying the infinite signal by a rectangular window $x(t)$ of width T_0. The Fourier transform of the unit boxcar function $x(t)$ is given by:

$$X(f) = \frac{\sin \pi T_0 f}{\pi f} \,. \tag{3.54}$$

Hence, in the frequency domain the truncation operation is equivalent to convolving $X(f)$ with the signal's spectrum. The result of this operation is called *leakage*. It can be shown that truncation does not induce leakage error in the discrete spectrum of periodic signals if the width of the rectangular window, T_0, is equal to exactly one complete cycle of the time history. Unfortunately, since earthquake motions are

not periodic in nature, leakage will occur in the spectra if the complete motion is not available. Because they introduce high frequencies, such leakage errors may also induce aliasing errors in the frequency domain for the sampled discrete time signal. These aliasing errors are expected to contaminate the integrated time histories after inverse transformation.

In Fig. 3.21(f), the final step of the discrete Fourier transform requires that the continuous spectrum be discretized at a frequency sampling which is the reciprocal of the truncation window width T_0. Hence, the spectrum is sampled at intervals which coincide exactly with the zeroes of $X(f)$, and the values of the spectrum given at the discrete frequencies will not be affected by the truncation process.

Unfortunately, when an FFT algorithm is used to compute the discrete Fourier transform, zeroes must often be appended at the end of the truncated signal, so that the total record length T_f which is used, is larger than T_0, the truncated duration. In effect, the spectrum is convolved by the window function which has zeroes at multiples of $\frac{1}{T_0}$, and is discretized at intervals of $\Delta f = \frac{1}{T_f}$. Hence, the values of the spectrum obtained at the discrete frequencies will reflect rippling from the leakage error due to the truncation of the time history. Although leakage is usually described as an error, this depends on the context. In this section, the frequency domain is used to carry out desired time domain operations, such as integration. It can be proved, by representing the original continuous acceleration time history by a harmonic series for which the coefficients are given by the discrete Fourier transform, that leakage does not produce errors in the processed and integrated time histories, except for possible aliasing of higher frequency noise. However in Sec. 4.3, the spectra are used for optimization purposes, and leakage errors should be considered.

Finally, as for step (b) of Fig. 3.21, discretizing in the frequency domain at intervals of $\frac{1}{T_0}$, is equivalent to reproducing periodically the time history at intervals of T_0 (Fig. 3.21(g)). Hence, the resulting time history is the discrete and truncated version of the continuous signal, which is periodically repeated at intervals of T_0 (T_f for signals with added zeroes), and is corrupted by aliasing. Although the truncation window width T_0 and the duration of the transformed signal with the

appended zeroes T_f may not coincide, the resulting discrete time history between 0 and T_0 is not corrupted by leakage error, other than high-frequency aliasing, as will be shown in the next section.

Before computing the Fourier transform, the processing method performs a baseline correction on the accelerogram. For infinite signals the shift in the temporal mean appears in the spectrum at *d.c.* only. However, because zeroes must usually be added at the end of the signal for the FFT, such an operation is equivalent to adding a boxcar function of amplitude equal to the shift in the mean over the entire record length T_0, and equal to zero between T_0 and T_f. Hence, in the frequency domain, the shift in the temporal mean creates an additive error which is proportional to the error at *d.c.* This error behaves as an $X(f)$ (Eq. 3.54) with zeroes at multiples of $\frac{1}{T_0}$ and will only appear in the discrete Fourier amplitude spectrum at multiples of $\Delta f = \frac{1}{T_f}$. Also, the errors are spread over the entire frequency domain, although they are largest at and near *d.c.* These errors significantly decrease beyond $\pm\frac{1}{T_0}$ because of the smaller side lobes of $X(f)$, but will still cause some aliasing because they are not strictly zero above the Nyquist frequency. Nevertheless, the low-frequency errors are amplified by integration, and greatly affect the resulting time histories, whereas the high-frequency errors are negligible in these integrated time histories.

In summary, truncation of accelerograms produces leakage, a convolutive error in the spectrum affecting the entire frequency range. However, the time histories obtained after inverse transformation should not be affected by leakage other than for some possible high-frequency aliasing. Baseline correction of the accelerogram creates an additive error in the spectrum which is dominant at lower frequencies. These long-period errors affect the time histories and are amplified by integration. The time domain processing of the synthetic accelerograms showed that shifts in the temporal mean, such as those resulting from missing data, are almost exclusively responsible for the long-period errors in the displacement time histories.

3.3.3 Application to Synthetic Records

The synthetic signals are used to test the internal performance of the frequency domain processing approach. In particular, the errors induced by the

FFT algorithm and the baseline correction are studied. Based on the previous paragraphs, the internal performance errors could arise mainly from the choice of the frequency sampling rate (which depends on the number of appended zeroes) and the truncation interval. The errors induced by the choice of the frequency sampling rate can be observed by processing an untruncated and noise-free synthetic accelerogram padded with zeroes of various durations. The synthetic signal used in the study of the internal performance of the frequency domain processing method is *Q11C*, the same as was used for the study of the internal performance of the time domain approach. This choice of the synthetic record allows direct comparison with the amount of error generated by each of the processing methods. In all of the following figures (Figs. 3.22 to 3.32), the Fourier amplitude spectra of the acceleration, velocity and displacement are shown with zero *d.c.* The correction to the temporal mean to obtain zero initial velocity and displacement is performed in the time domain after inverse Fourier transformation. The plots of the errors in the frequency domain reflect the initial value correction. Also, to produce the plots of the errors in the frequency domain it is necessary to have the same Δf for both the processed and the exact signal. Hence, in the time domain both signals must be of the same length, which is achieved by adding zeroes.

The complete synthetic signal *Q11C* is generated and discretized into 2001 points at intervals of 0.01 sec, for a total time span of 20 sec. Hence, the Nyquist frequency is 50 Hz. *Q11C* is generated for 250 harmonics at intervals of about 0.1 Hz between 0.05 and 25 Hz, which is far below the Nyquist frequency. Thus, the discrete Fourier transform should not induce high-frequency aliasing errors into the spectrum of *Q11C* (to within the accuracy of the quantization of the data). Also, any harmonic below 0.05 Hz apparent in the spectrum after processing, which has an amplitude larger than that expected from the exponential modulation of the synthetic accelerogram model, could be erroneous. Since the FFT algorithm which is used requires the total number of data points to be a power of 2, or 3 times that, zeroes must be added to the end of *Q11C*. The next highest number after 2001 (i.e., $T_0 = 20.0$ sec) that satisfies this condition is 2048 (i.e., $T_f = 20.48$ sec), and thus 47 zeroes are appended to *Q11C*. The frequency sampling interval is thus approximately 0.0488 Hz. The synthetic accelerogram is then processed according

to the frequency domain approach described in Sec. 3.2. In this case, the only difference between the two sets of results is that the "processed" acceleration is baseline corrected, and the "exact" acceleration is not. Hence, the errors can only be attributed to the baseline correction. Synthetic signal *Q11C* is analytically generated with zero temporal means for the acceleration and velocity over $[0, \infty)$. However, because of quantization and truncation of the signal to $[0, 20]$, the means may not be exactly zero, and so the "baseline correction" produces a slight offset in the acceleration.

The results are shown in Figs. 3.22 and 3.23. In Fig. 3.22, the time histories and the amplitude spectra of the processed and exact acceleration, velocity and displacement are overlaid on top of each other. The time histories are shown to the left of the figure, and the amplitude spectra are shown to the right. The solid line represents the processed data, and the dotted line represents the exact data. However, the difference between these two sets of data is indistinguishable in any of the plots. A more detailed analysis of the internal performance of the frequency domain approach can be achieved by studying the errors between the processed and the exact data for each of the quantities illustrated in Fig. 3.22. These errors are presented in Fig. 3.23, with a smaller frequency scale. The plots to the left represent the errors in the processed time histories, and the plots to the right represent the Fourier transform of the these time domain errors.

The only error present in the acceleration time history is a shift in the temporal mean of -2.7 10^{-6} induced by the quantization accuracy of the discrete data, which is stored to a precision of 6 decimal points, and the truncation of the synthetic signal at 20 sec. The error in the acceleration spectrum is only due to the shift in the mean and is composed of a spike at *d.c.*, and of a much smaller rippling error of an approximate period of 2 Hz (i.e., interval for which multiples of $\frac{1}{T_f}$ and $\frac{1}{T_0}$ coincide). The temporal-mean error in the acceleration appears in the final portion of the velocity-error plot as a line with slope -2.7 10^{-6}. A second error is observable in the initial portion of the velocity-error plot. According to the spectral-error plot, it arises from the integration of the ripples due to the shift in the temporal mean acceleration. In particular, the error at the first harmonic is larger than the error

at *d.c.* which incorporates the time domain correction for zero initial velocity. In the time domain, the error at the initial velocity is zero, although it is hard to see in the velocity-error plot. The high-frequency noise arises from digit truncation of the stored exact velocity; it is approximately 2 orders of magnitude less than the other errors, and can be neglected. The displacement errors are predominantly those induced by the shift in the temporal mean acceleration, and, as seen in the error plot of the displacement in the frequency domain in Fig. 3.23 (which shows only *d.c.* to 1 Hz), integration greatly increases the error in the low-frequency harmonics affected by the shift. Overall, these errors remain small, and represent only 10^{-4}% of the peak acceleration, 5x10^{-3}% of the peak velocity, and 0.1% of the peak displacement.

Figs. 3.24 and 3.25 show the processing errors in the time domain and in the frequency domain when the nominally untruncated and noise-free synthetic signal *Q11C* (i.e., $T_0 = 20.0$ sec) is appended with zeroes up to 3072 (i.e., $T_f = 30.72$ sec) and 4096 data points (i.e., $T_f = 40.96$ sec) respectively. Compared to the results in Fig. 3.23 for 2048 data points, it can be seen that the time domain errors are practically identical. In all three cases, these are due to the same shift in the temporal mean of the acceleration of -2.7 10^{-6} induced by the finite precision and end truncation of the stored data. The errors in the frequency domain appear to be different, but one must not forget that increasing the length of the data in the time domain also increases the frequency sampling rate by the same amount. The spectra of Figs. 3.23, 3.24. and 3.25 correspond to frequency intervals of 0.0488 Hz, 0.0325 Hz, and 0.0244 Hz respectively, and thus, increasing the number of zeroes at the end of the record, decreases the apparent period of the ripples due to the shift in the baseline. However, the harmonics that correspond to the same frequency have exactly the same spectral value in all of the above three cases, and the smaller sampling interval just provides a better description of the underlying spectrum at intermediate frequencies. Nonetheless, when tested on the synthetic record, decreasing the frequency sampling interval did not significantly affect the time histories, since the errors in the time domain are the same in all three cases. Thus, the errors induced by the frequency domain accelerogram processing method on a nominally untruncated signal are insensitive to the number of added zeroes, or equivalently, to the choice of the frequency sampling rate. The predominant

source of error remains the acceleration *d.c.* shift after baseline correction, arising from finite precision and end truncation of the stored data; this is not an internal performance error.

The frequency domain processed time histories of *Q11C* in Fig. 3.22, and the time-history error plots in Fig. 3.23, can be compared to the time domain processing results shown in Fig. 3.2. In both cases, the visual match between the processed and the exact time histories is excellent. The error in the estimate of the temporal mean acceleration is the same, but the error in the velocity for the time domain method is at least 2 orders of magnitude larger than for the frequency domain result, and is governed by the error induced by the trapezoidal rule for integration. There is no integration error in the frequency domain method, since an exact transfer function is used to compute the velocity and displacement. The errors in the displacement time history are almost identical for both processing methods, and are dominated by the effect of the acceleration *d.c.* shift. But the error in the displacement obtained with the time domain method still displays high-frequency errors due the trapezoidal rule. This comparison of the time and frequency domain processing methods shows that both produce almost exactly the same error from the shift in the temporal mean acceleration. However, the overall error level is lower for the frequency domain method since integration is exact. In particular, this is responsible for a decrease in the velocity error of 2 orders of magnitude. Hence, the frequency domain processing method has an even better internal performance than does the time domain method.

The correction effectiveness of the processing method for shifts in the temporal mean, resulting from substantial premature end truncation, is tested on synthetic signal *Q11C*. Errors due to shifts in the temporal mean alone can be separated from errors arising from adding zeroes for the FFT. An "exact" time history with nonzero temporal mean acceleration described by a number of points equal to a power of 2, or 3 times that, is compared to a "processed" time history of same length (i.e., $T_0 = T_f$). This condition is respected when synthetic signal *Q11C* is truncated at 1536 data points. In this case, the only difference between the exact and the processed signal arise from the shift in the baseline, and does not include zero-padding effects. The errors in the time domain and in the frequency domain

are illustrated in Fig. 3.26, in which the scale for the displacement-error spectrum is expanded. The error in the acceleration temporal mean is equal to 3.2 10^{-5}, and is an order of magnitude larger than that due to quantization error and truncation of *Q11C* to the first 20 sec (Fig. 3.23). The error in the velocity time history is almost perfectly linear with a slope equal to 3.2 10^{-5}, and that in the displacement time history is parabolic. Both these results are what is expected theoretically. Since $T_0 = T_f$, multiples of the frequency sampling Δf coincide with the zeroes of $X(f)$ (Eq. 3.54), and the side lobes due to shifting of the baseline and truncation (i.e., leakage) will not appear in the discretized Fourier amplitude spectrum. Indeed, the plots of the error in the frequency domain (Fig. 3.26) shows that the only error in the acceleration spectrum is at *d.c.* The spectrum of the errors in the velocity and the displacement represent the decomposition of a straight line and a parabola in the frequency domain, without any other sources of error, and are the largest at and near *d.c.*

Next, the unprocessed and nominally untruncated record *Q11C* padded with zeroes up to 2048 points is compared to the processed and truncated signal with 1536 points and padded with zeroes up to 2048 points (i.e., $T_0 = 15.36$ sec and $T_f = 20.48$ sec). In this case, the two signals differ by a shift in the temporal mean and by end truncation of the data. The errors are illustrated in Fig. 3.27 (note the change of frequency scale on the different spectra plots). The time domain errors are only due to the shift in the acceleration temporal mean, although the errors in the acceleration Fourier amplitude spectrum are strongly dominated by leakage errors. Recall that these leakage errors are produced by the convolution of the signal spectrum with $X(f)$ (Eq. 3.54). Hence, it is expected that the errors are the greatest in the frequency range where the signal is large, as illustrated in Fig. 3.27. A high-frequency error is superimposed over the leakage error, and is attributed to aliasing, as explained in Sec. 3.3.2. After integration, leakage errors still affect the velocity spectrum, but have virtually disappeared in the displacement spectrum; in both spectra, the errors near *d.c.* are dominated by effects of the acceleration baseline shift.

To investigate trends in the way the processing method treats errors due to end truncation, *Q11C* is truncated at T_0 equal to 15 sec, 12 sec, and 10 sec, and is processed with the frequency domain approach. In all 3 cases, the truncated signals are appended with zeroes to give 2048 data points (i.e., $T_f = 20.48$ sec). The time domain results are plotted out in Figs. 3.28, 3.29, and 3.30 respectively. In these figures, the plots to the left are the overlaid time histories, where the solid line represents the processed signal and the dotted line the exact signal. The plots to the right represent the error in the time histories between the exact and the processed signals. Comparison of these figures with those of the untruncated signal (Figs. 3.22 and 3.23) show that, as expected, end truncation affects the temporal mean of the acceleration, and the error in the baseline increases as more data is missing. Nevertheless, this may not always be necessarily so; it is possible for a signal to be truncated by a large amount but to have a temporal mean close to zero. In all of the tested cases, the error in the acceleration remains extremely small however, and represents no more than 0.01% of the peak. The linear error this induces on the velocity time histories is still acceptable, and does not exceed 1% of the peak. However, the parabolic error in the displacement time histories at the time of truncation represents up to 20% of the peak when the last half of the acceleration is missing, even though the missing acceleration data has very small amplitudes. This type of error may be important with real earthquake records, since it is common to find velocity levels at the time of end truncation that are higher than the ones shown in Fig. 3.30. Similarly, although there is very little motion left in the acceleration and velocity when the last quarter of the record is missing (Fig. 3.28), the error in the temporal mean due to end truncation is responsible for a drift in the displacement representing 10% of the peak. This stresses the importance of digitizing the earthquake accelerogram to its full extent up to the time of instrument shut-off. In any event, this drift in the displacement time histories can be properly bounded by the standard deviations if an appropriate estimate for the variance of the missing data, c^2 (Eq. 3.10), is used. Under this condition, the frequency domain method has good correction effectiveness.

The frequency domain errors in the acceleration and displacement of the truncated signal for T_0 equal to 15 sec, 12 sec, and 10 sec, corresponding to the above

three cases, are shown in Fig. 3.31 (note the change of scale). As was the case for $T_0 = 15.36$ sec (Fig. 3.27), the acceleration spectra are contaminated by leakage error, and the amplitudes of the errors increase as more of the data is missing. However, it is always restricted to the frequency range where the signal is the strongest. Although errors arising from data truncation are large in the frequency domain, they do not affect the time domain results (Figs. 3.28, 2.29, 3.30). After double integration, it is the baseline shift which dominates the error in the displacement Fourier amplitude spectrum, and so leakage is not a significant source of error even in the frequency domain. Shifting of the baseline creates an error which is largest at and near *d.c.* This is the source of the error observable in the time histories. As was explained in Sec. 3.3.2, in the frequency domain, the additive errors due to a shift in the baseline of a signal, truncated at time T_0, sharply decrease beyond $\frac{1}{T_0}$ because of the smaller side lobes of $X(f)$ (Eq. 3.54). This is apparent in the errors of the displacement spectra shown in Fig. 3.31. Hence, baseline errors are greatest in the displacement spectrum below $\frac{1}{T_0}$, but the remainder of the spectrum is relatively unaffected by truncation. Also, the error in the acceleration spectrum due to truncation is the greatest in the range where the signal-to-noise ratio is the smallest; it represents an error in the spectral amplitudes of less than 5% even in the worst of cases (Figs. 3.22 and 3.31). These facts will be particularly useful in Ch. 4, when system identification techniques are implemented to correct the spectrum near *d.c.* and to reduce the long-period errors in the time histories. Such methods can greatly improve the correction effectiveness of the processing method for truncated data.

The correction effectiveness of the frequency domain method could also be tested with the noise-corrupted and trigger-truncated synthetic records. Trigger truncation affects the temporal mean of the acceleration in the same way as end truncation, and has been investigated in detail in the preceeding paragraphs. The effects in the frequency domain of processing a truncated and noise-contaminated signal are illustrated in Fig. 3.32. In this figure, the frequency domain errors in the processed acceleration and displacement are represented in a log-log scale to emphasize the behavior near *d.c.* Fig 3.32(a) shows the spectral errors when *Q11C* is neither truncated or contaminated by noise. This is the reference case which is also illustrated in Figs. 3.22 and 3.23. As explained earlier, the errors arise from

the quantization of the data and the truncation of *Q11C* at 20 sec, and create a slight offset in the discretized version of the record. The errors are small, and behave as the $X(f)$ function with zeroes at frequencies where multiples of $\frac{1}{T_f}$ and $\frac{1}{T_0}$ coincide. This is the best the processing method can achieve. In Fig. 3.32(b), the synthetic signal modelled as a large event is contaminated with relatively small levels of white noise (i.e., *Q11CNL*). As expected, the error produced by the noise in the acceleration spectrum remains constant on the average, and in this case is nearly 3 orders of magnitude smaller than the spectral amplitude of the signal (Fig. 3.22). The corresponding effect in the displacement spectrum is dominated by a large error near *d.c.*, which represents approximately 100% of the signal's amplitude. When noise and end truncation are modelled in the synthetic signal (Fig. 3.32(c)), the noise dominates the error in the acceleration spectrum, although close inspection reveals some leakage error in the frequency range where the signal-to-noise ratio is large, between 1 Hz and 10 Hz. This leakage error remains negligible in the acceleration spectrum, and has very little effect on the displacement spectrum, which still has its largest errors near *d.c.* The level of these displacement errors remain about the same as in the case without truncation. Hence, in the acceleration spectrum, digitization and recording noise are much larger than leakage errors induced by truncation, and contaminate the whole frequency range. The noise error also affects the displacement spectrum more than the truncation error, but mostly in the very low frequency range, and presumably because the noise alters the temporal mean; the higher frequencies are not significantly perturbed by either of these sources of errors.

3.3.4 Concluding Remarks

The time histories obtained from the time domain and the frequency domain processing methods only differ in that the former uses the trapezoidal integration rule, whereas the latter relies on the discrete Fourier transform. As was shown in this section, the difference in the integration scheme alone is responsible for a decrease in the processing error of up to two orders of magnitude in the velocity when the frequency domain approach is used. Nonetheless, these differences

relate to the internal performance of the methods and not to their correction effectiveness. It has been shown in Secs. 3.2.1 and 3.3.1 that both approaches use the same assumptions to obtain the most probable estimates for the time histories. It is these assumptions which govern the correction effectiveness of the processing methods. Since both processing methods display good internal performance and induce errors into the accelerogram which are several orders of magnitude lower than the digitization and processing errors, they have equal correction effectiveness. Hence, the results and conclusions presented in Sec. 3.2.2 for the correction effectiveness of the time domain approach also apply to the correction effectiveness of the frequency domain method, and need not be reiterated.

In summary, adding zeroes to the end of a signal does not alter the time domain results, and provides a better description of the spectra by decreasing Δf. When the width of the truncation window is equal to the exact number of points required for the FFT, the only error that appears in the spectra are due to the baseline shift. Also, leakage errors, arising from data truncation and zero padding, do not affect the time histories. They are important in the acceleration spectrum through out most of the frequency range of motion and can lead to aliasing, but become much less important in the velocity and displacement spectra which are dominated by the baseline-shift error. The uncertain baseline errors which create large parabolic drifts in the displacement time histories, are mainly restricted to the harmonics in the displacement spectrum below the frequency corresponding to the truncation length, even in the presence of digitizing and processing noise. Theoretically, errors due to shifts in the uncertain baseline could be completely avoided if the exact value of the temporal mean of the signal at the time of truncation is known. In practice, this is impossible of course and setting the baseline of the recorded accelerogram to give zero temporal mean remains the best option. In Ch. 4, the results of this section are used with system identification techniques to decrease the long-period errors due to the uncertain baseline, and to decrease high-frequency noise arising from digitization and processing.

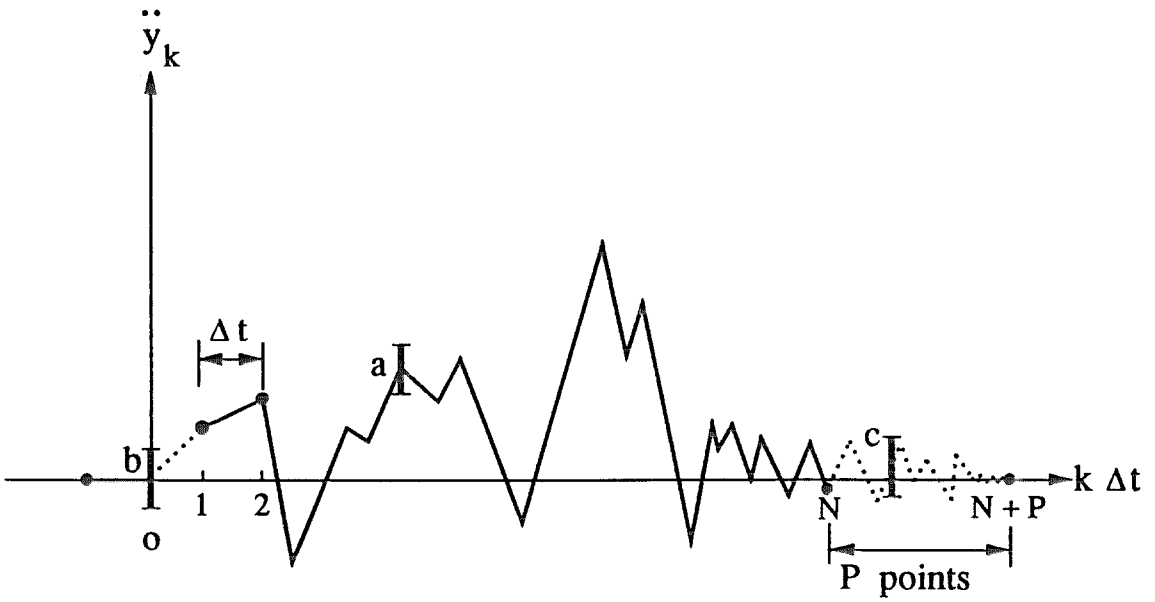

Figure 3-1. Representation of the assumptions used for the probabilistic processing of earthquake accelerograms.

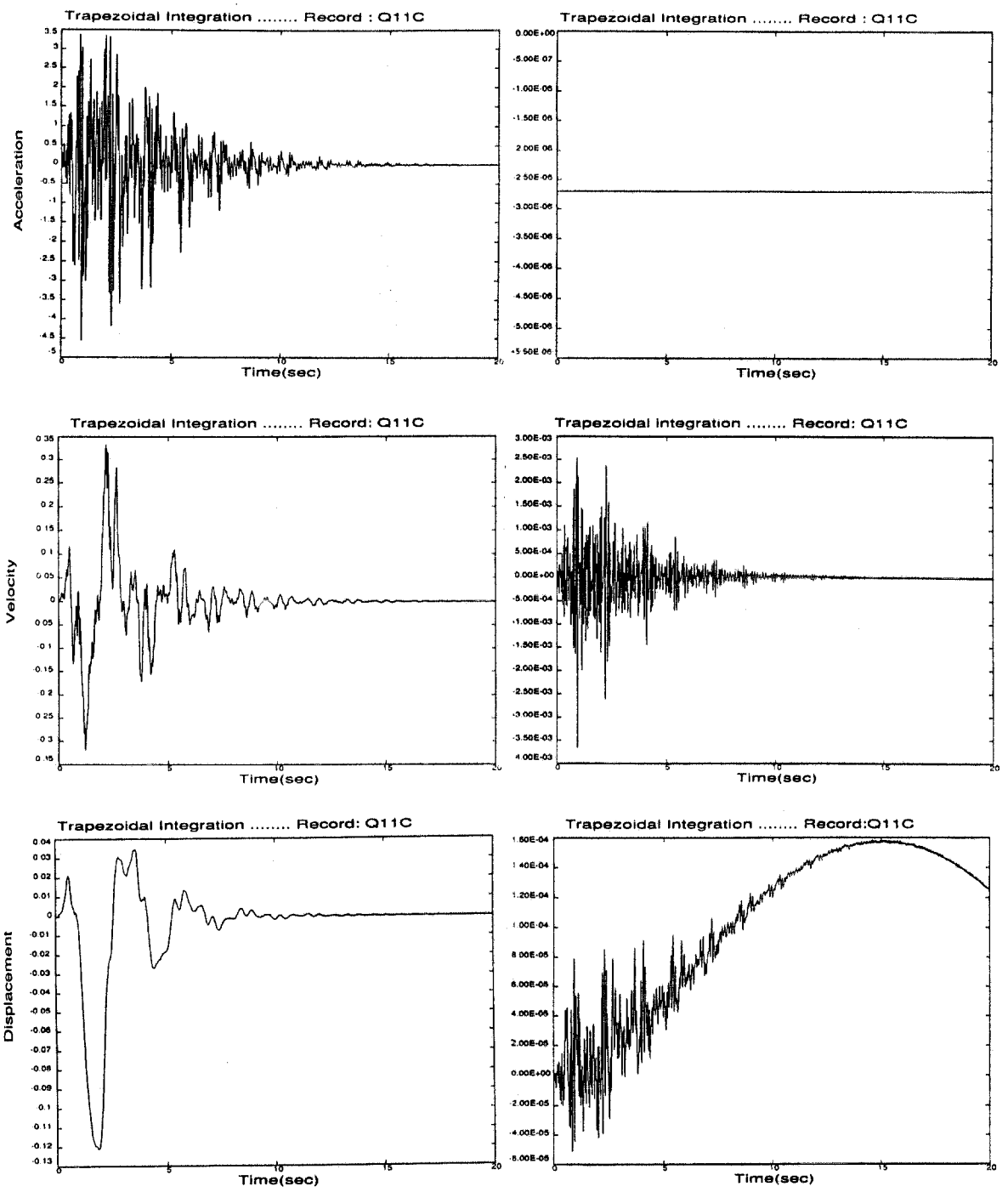

Figure 3-2. Time domain processing for synthetic record Q11C.

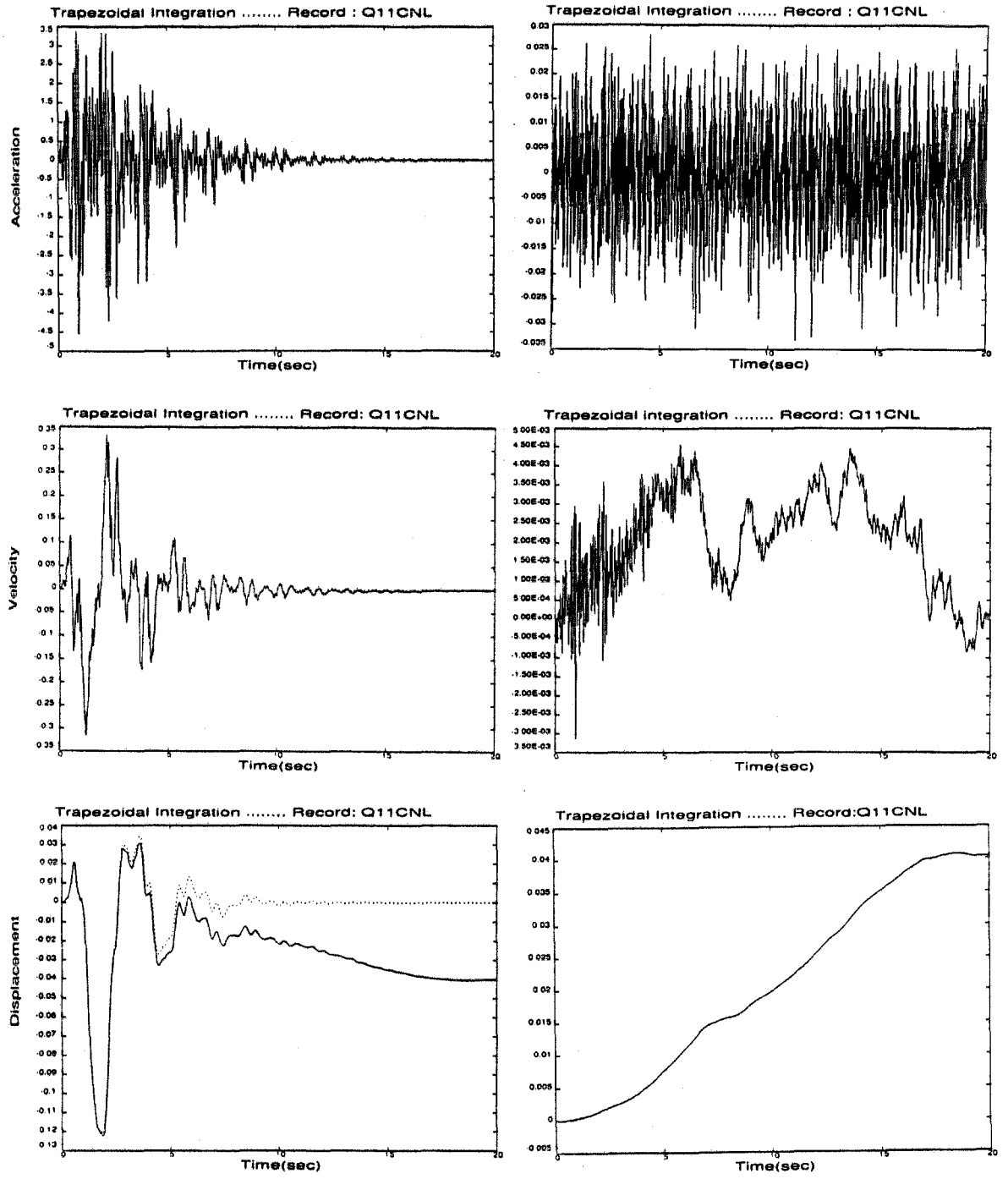

Figure 3-3. Time domain processing for synthetic record Q11CNL.

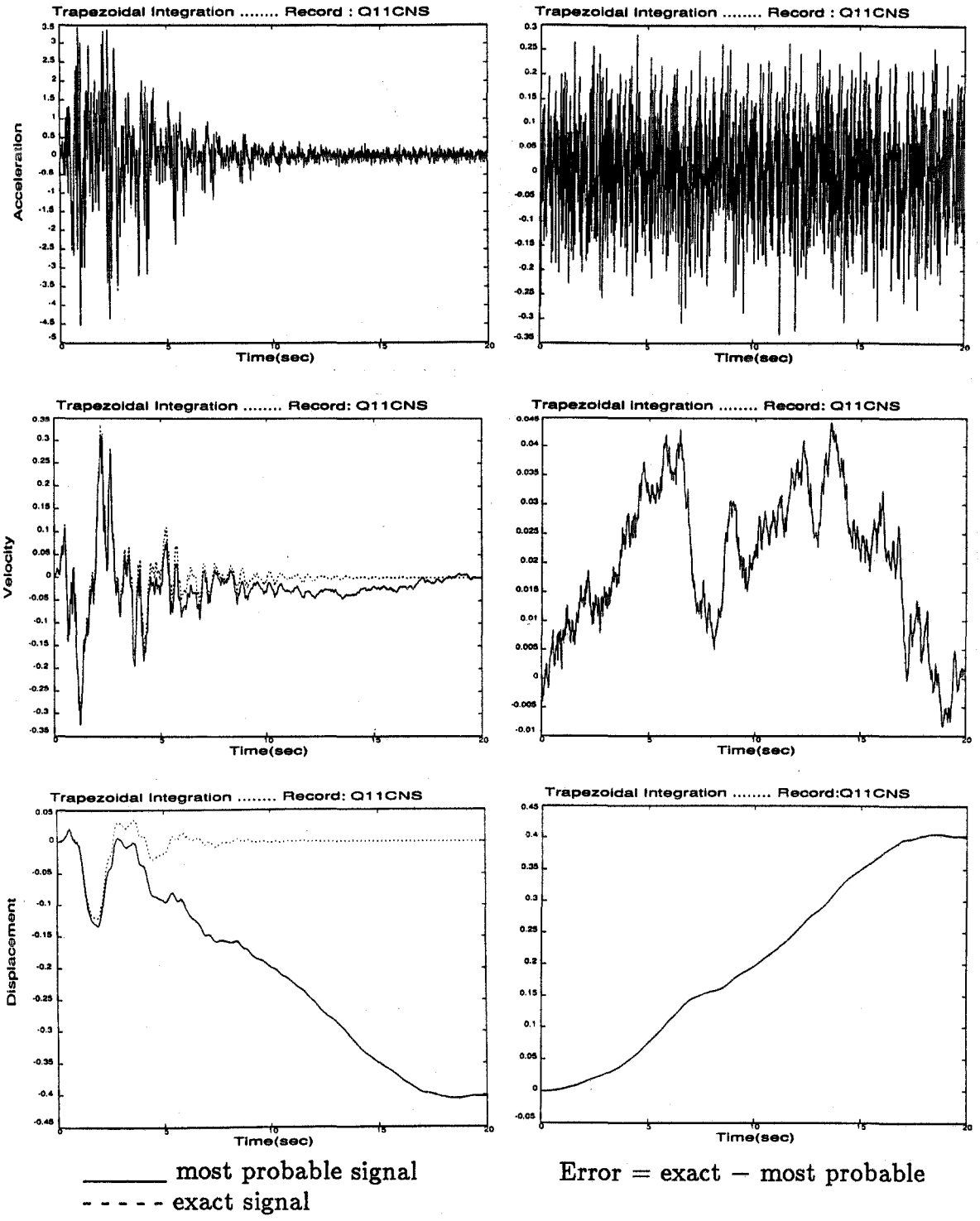

Figure 3-4. Time domain processing for synthetic record Q11CNS.

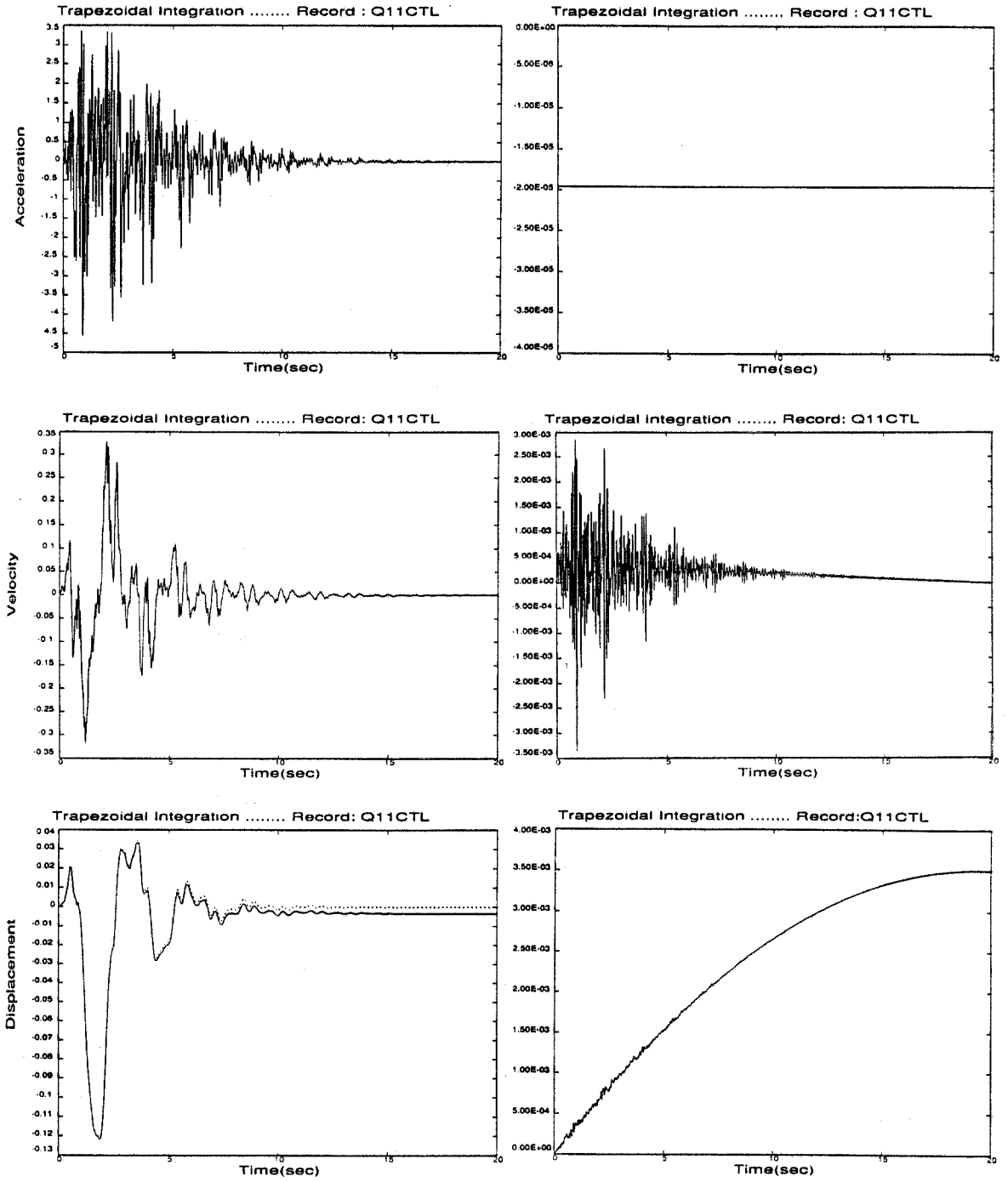

Figure 3-5. Time domain processing for synthetic record Q11CTL.

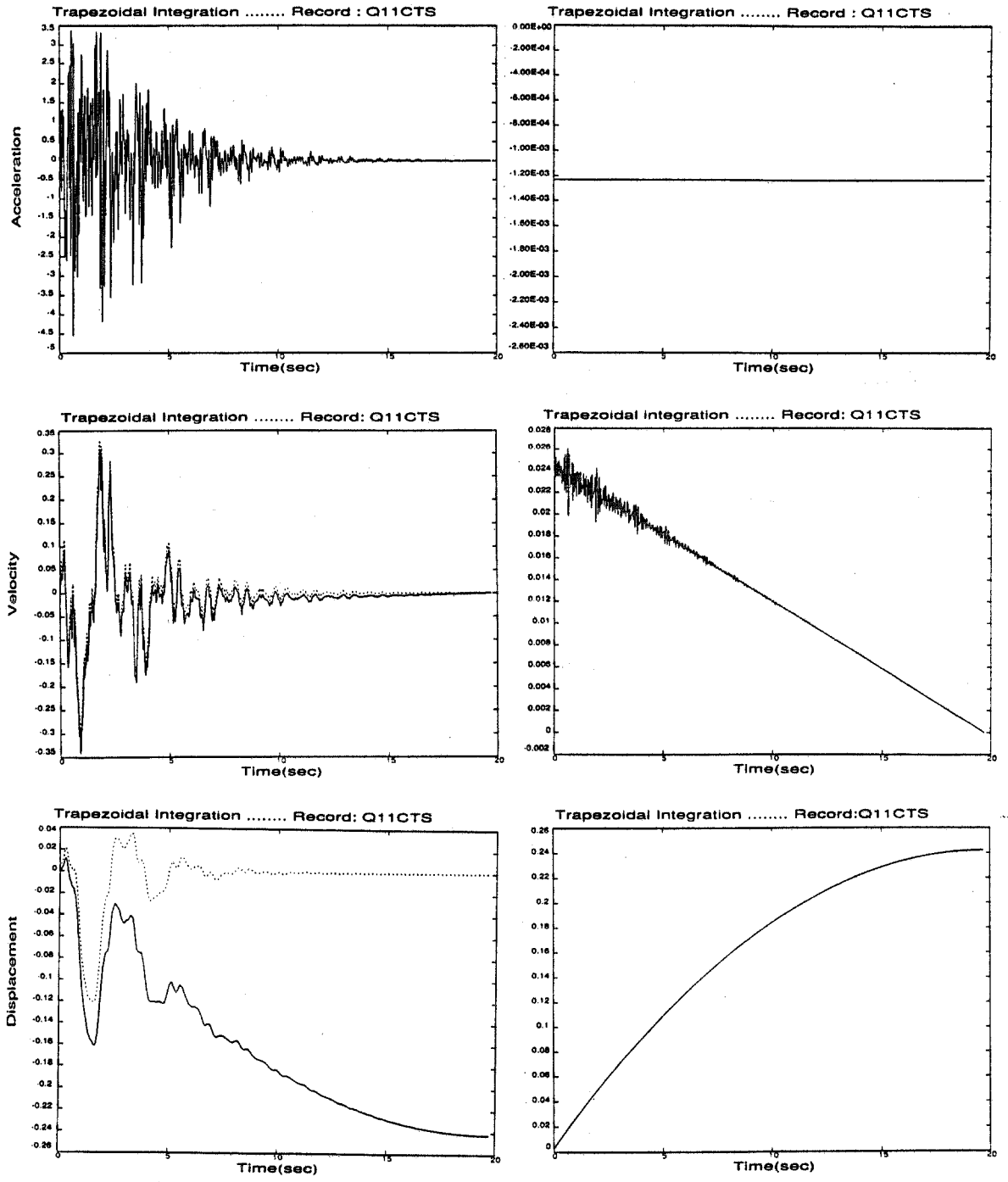

Figure 3-6. Time domain processing for synthetic record Q11CTS.

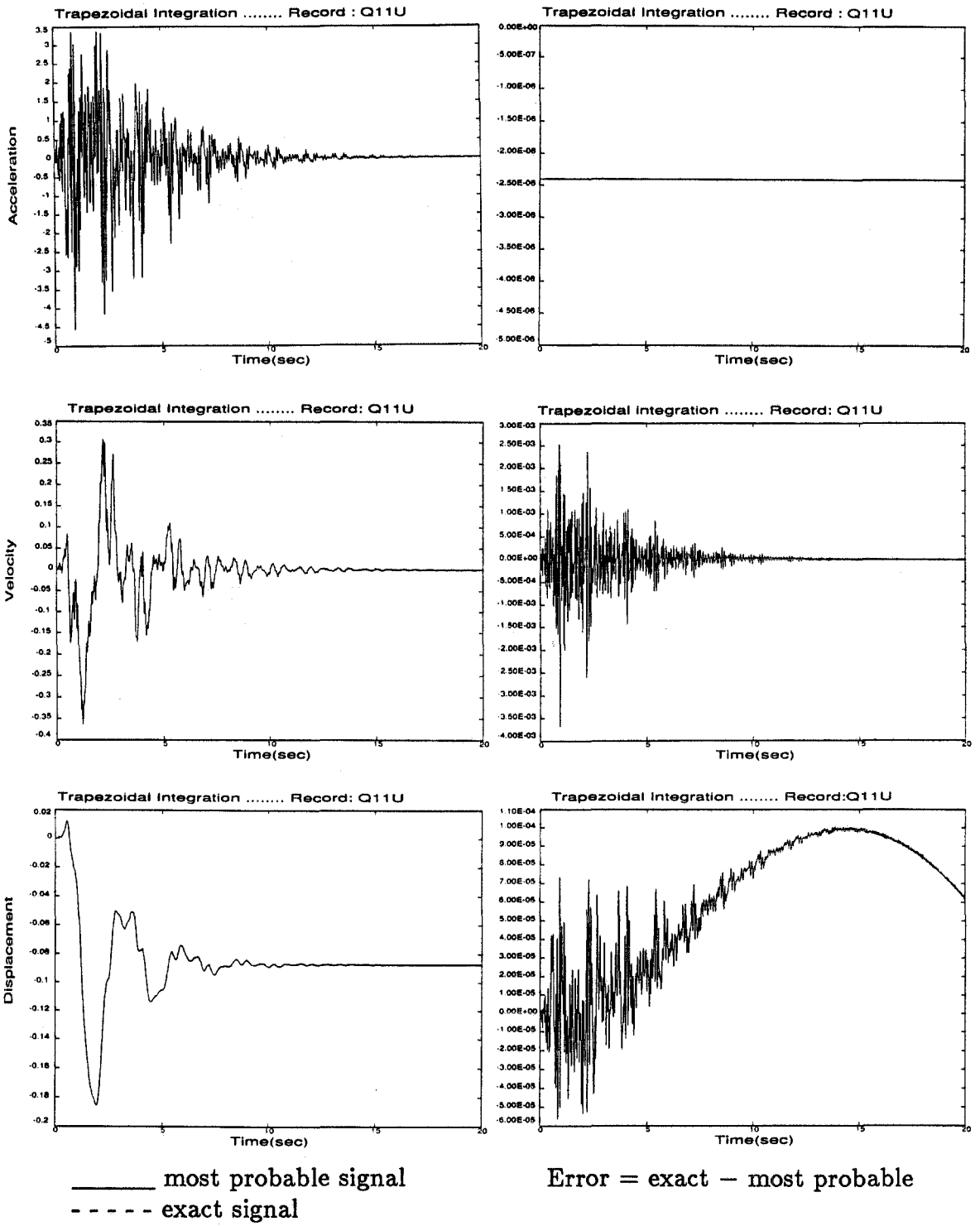

Figure 3-7. Time domain processing for synthetic record Q11U.

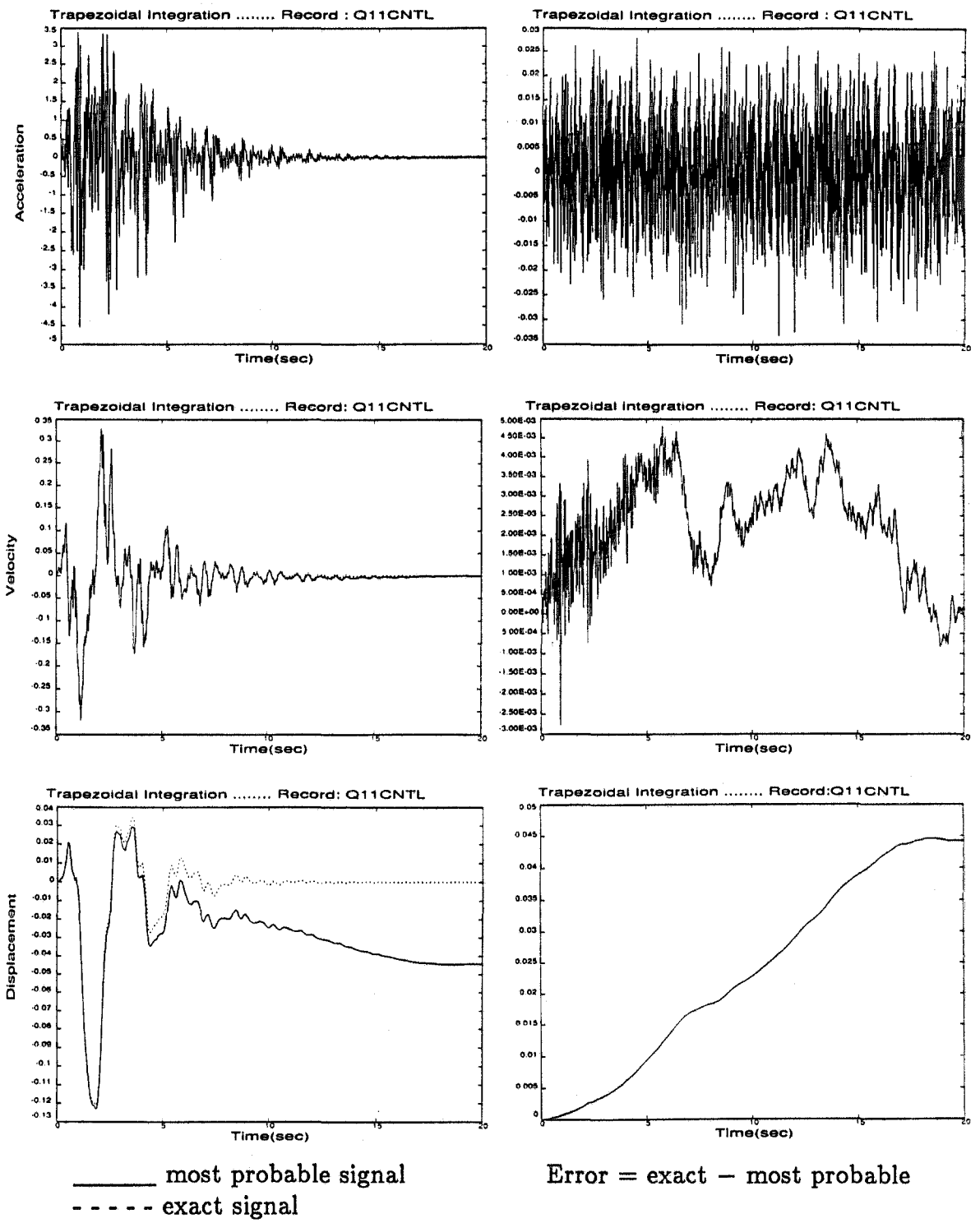

Figure 3-8. Time domain processing for synthetic record Q11CNTL.

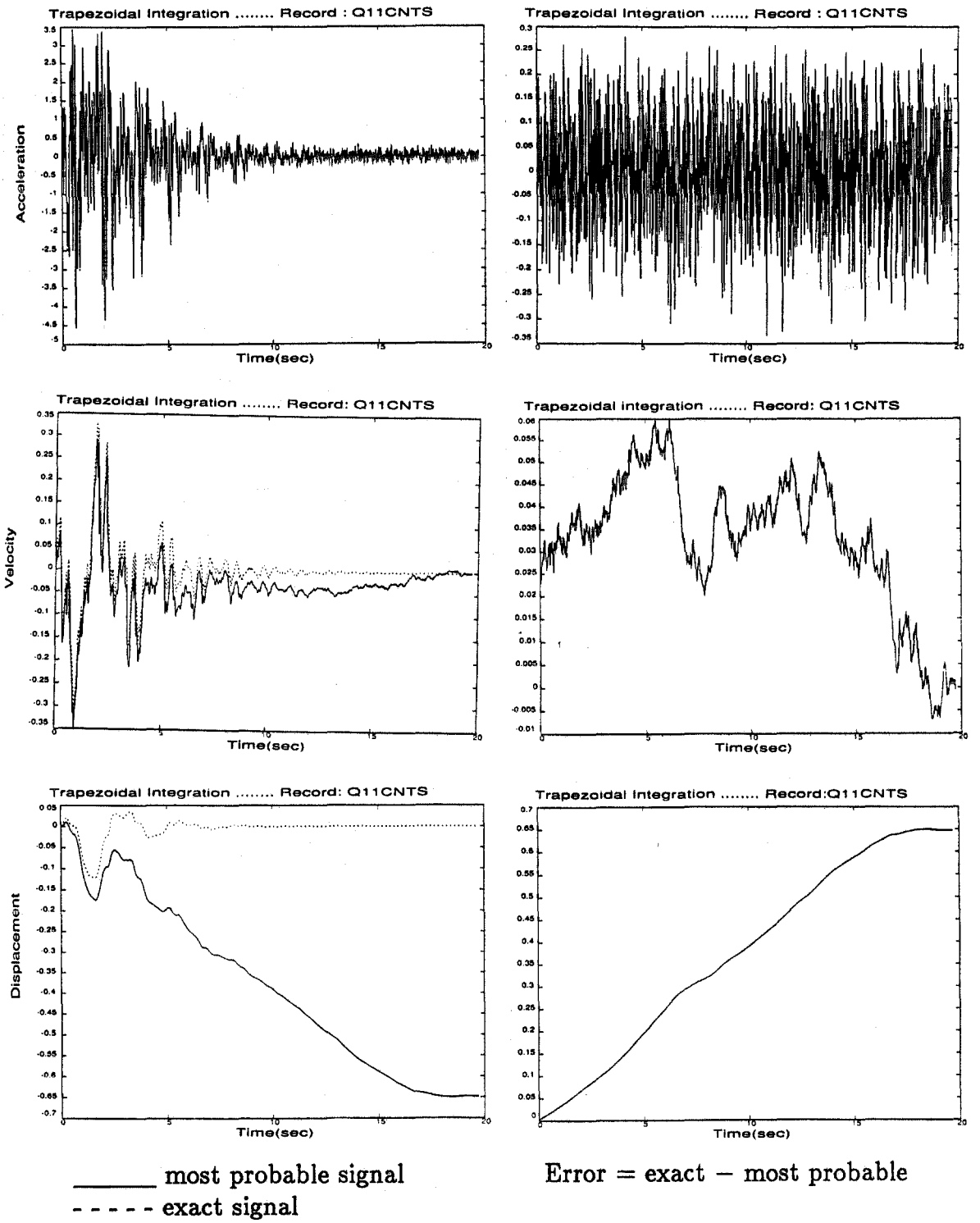

Figure 3-9. Time domain processing for synthetic record Q11CNTS.

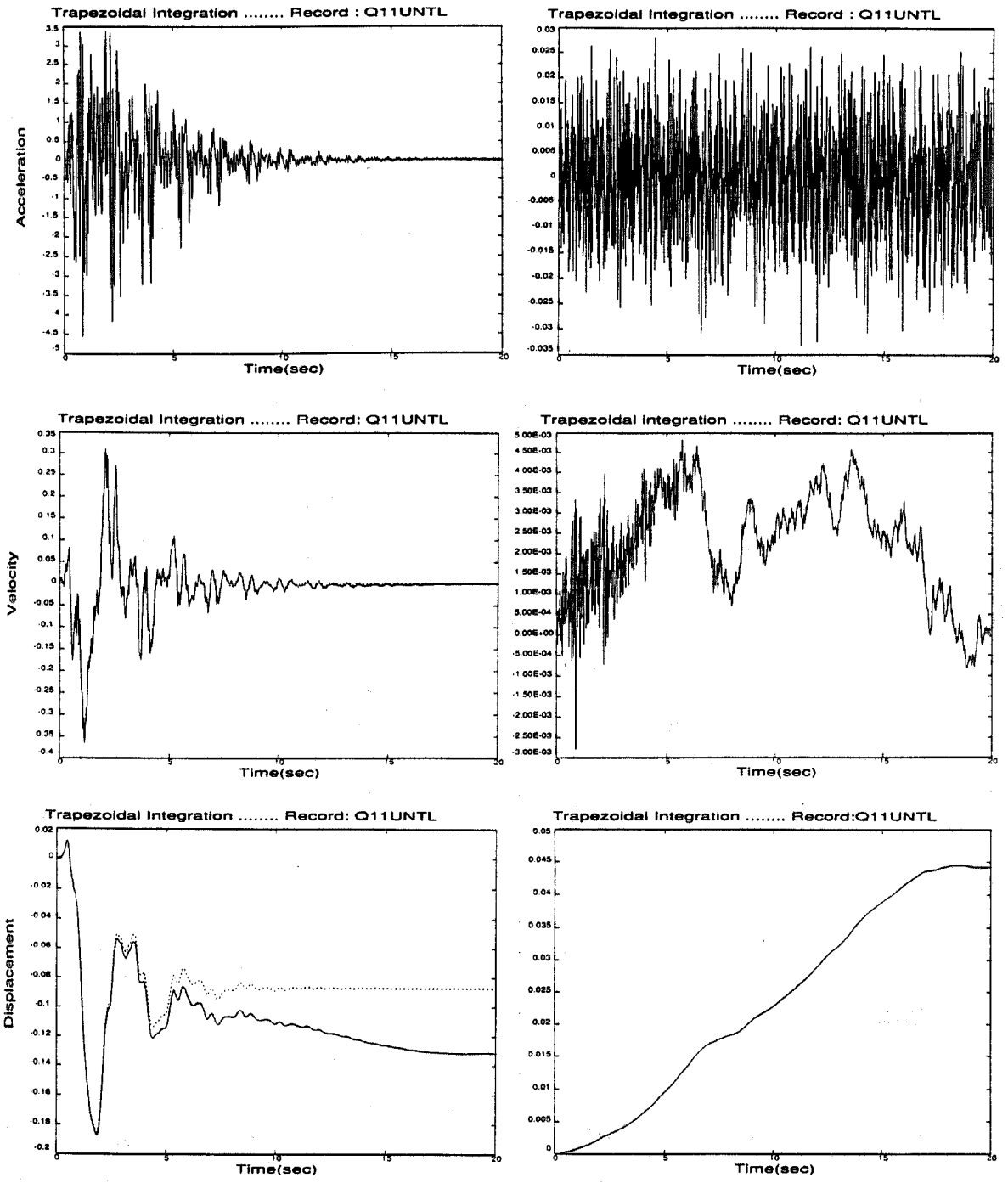

Figure 3-10. Time domain processing for synthetic record Q11UNTL.

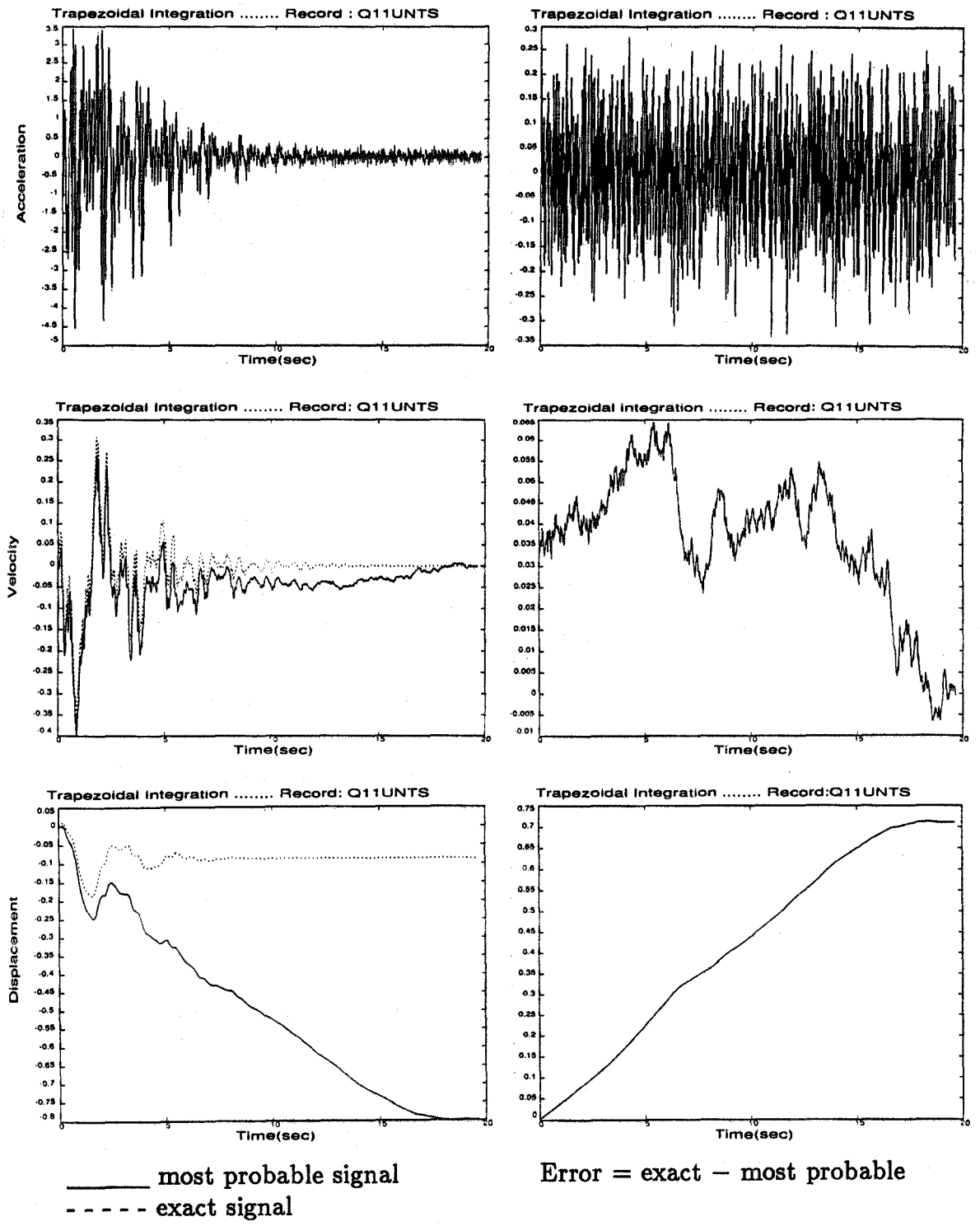

Figure 3-11. Time domain processing for synthetic record Q11UNTS.

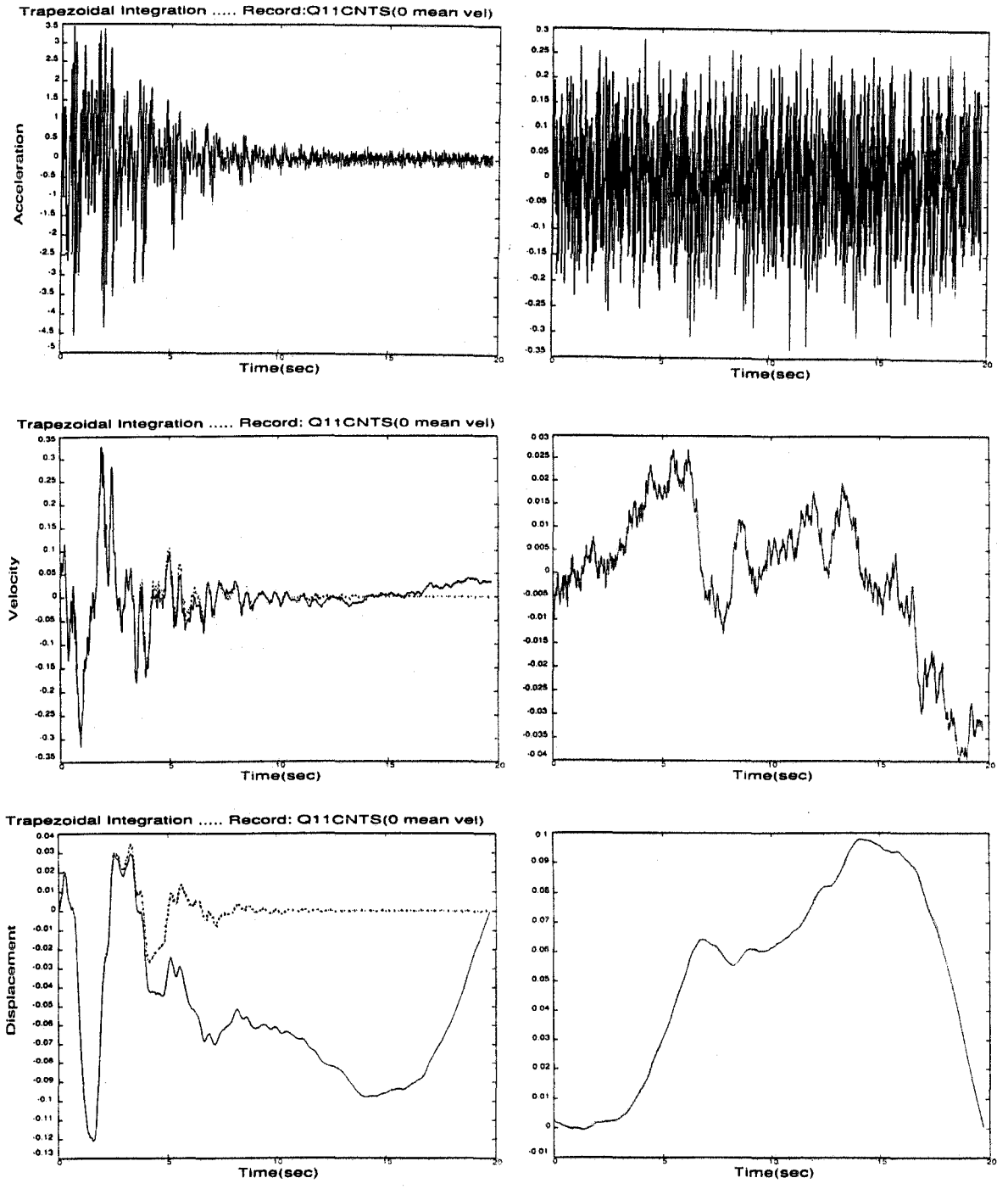

_____ most probable signal
- - - - - exact signal

Error = exact − most probable

Figure 3-12. Time domain processing for synthetic record Q11CNTS, with zero mean velocity.

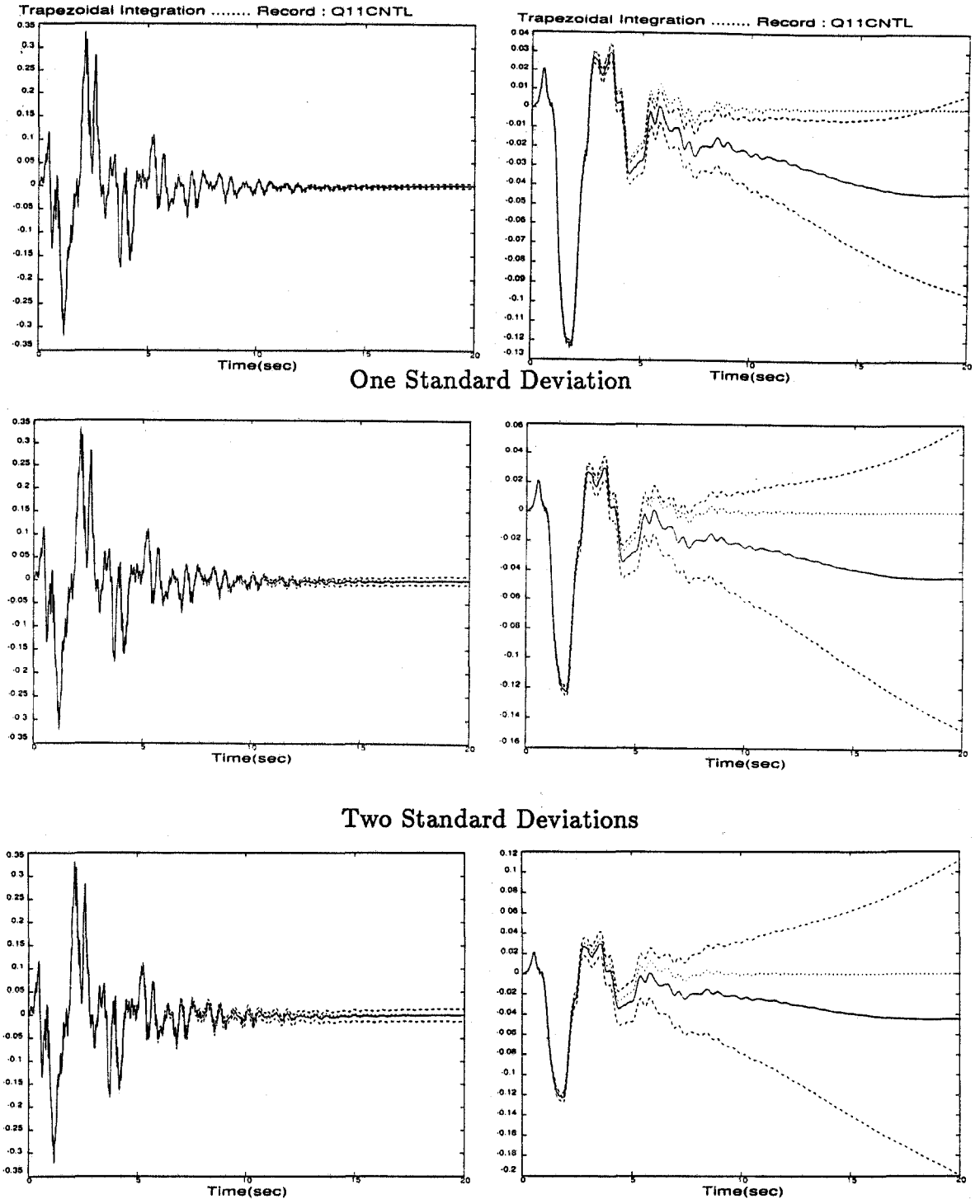

Figure 3-13. Reliability bounds for the time domain processing of synthetic signal Q11CNTL.
(____ most probable; . . . . . exact; - - - - - deviations).

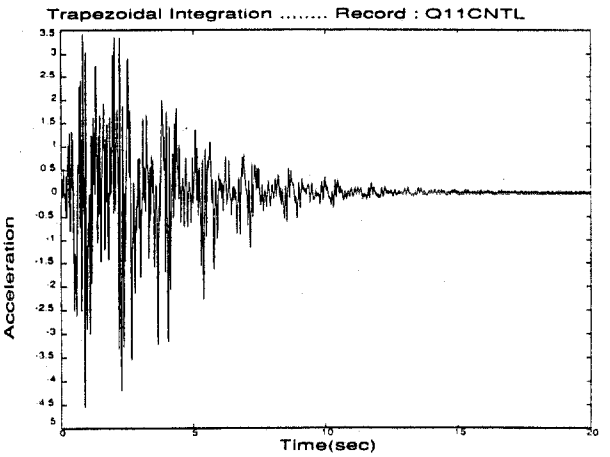

One Standard Deviation

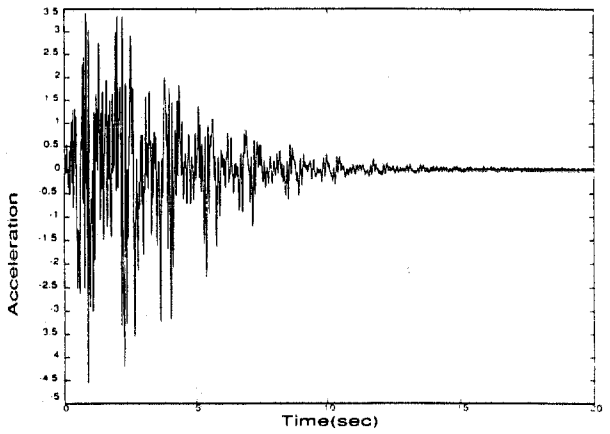

Two Standard Deviations

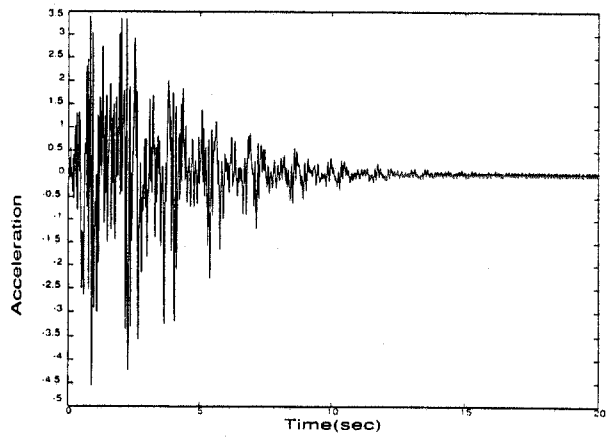

Three Standard Deviations

Figure 3-14. Reliability bounds for the most probable acceleration of synthetic signal Q11CNTL.
(____ most probable; . . . . . exact; - - - - - deviations).

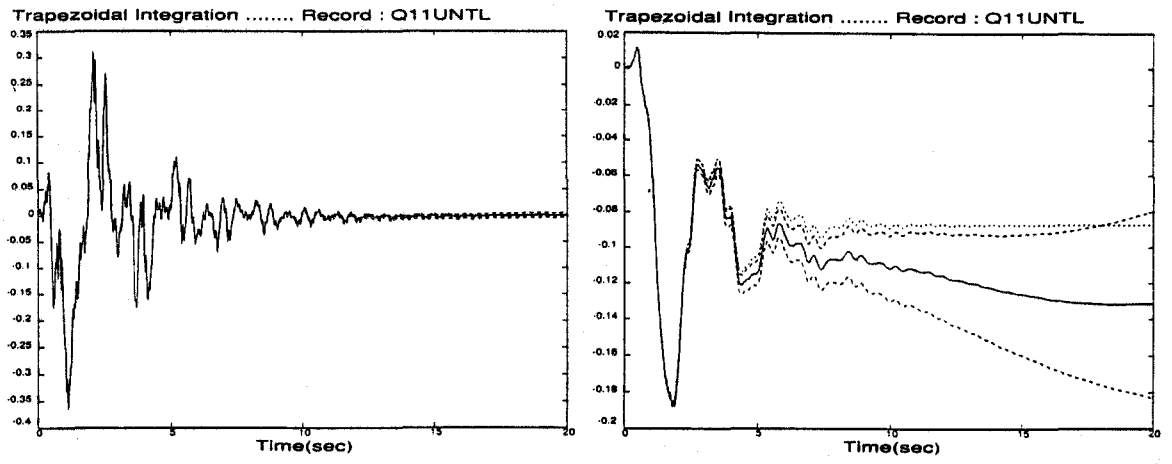

One Standard Deviation

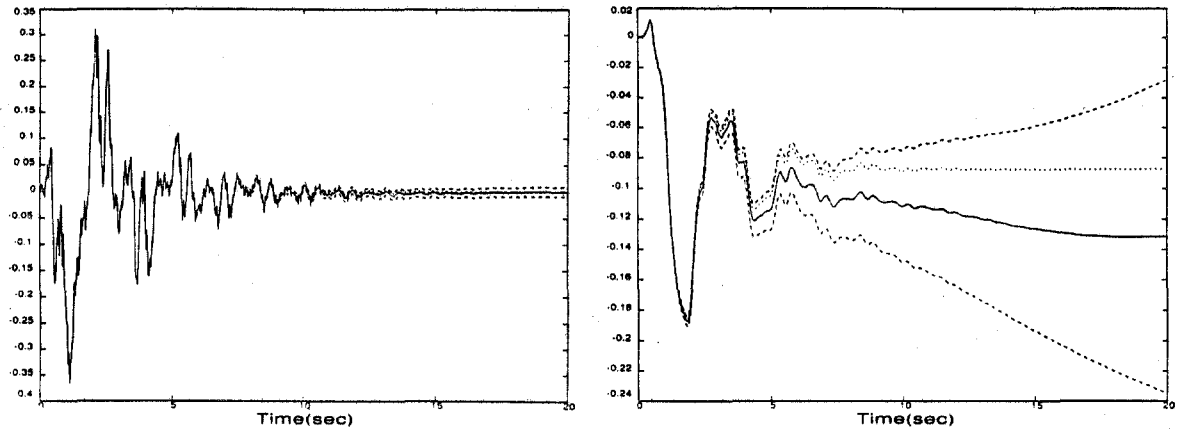

Two Standard Deviations

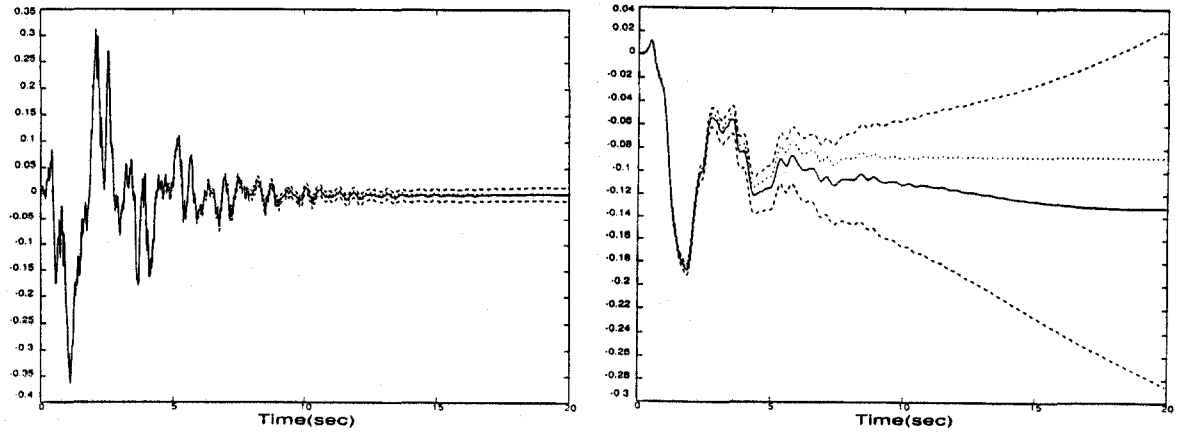

Three Standard Deviations

VELOCITY DISPLACEMENT

Figure 3-15. Reliability bounds for the time domain processing of synthetic signal Q11UNTL.
(____ most probable; . . . . . exact; - - - - - deviations).

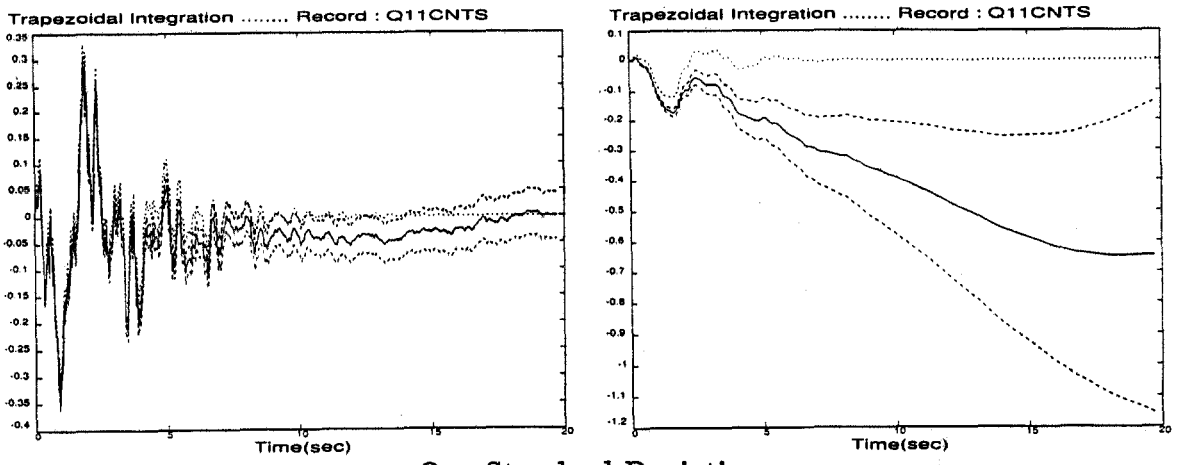

One Standard Deviation

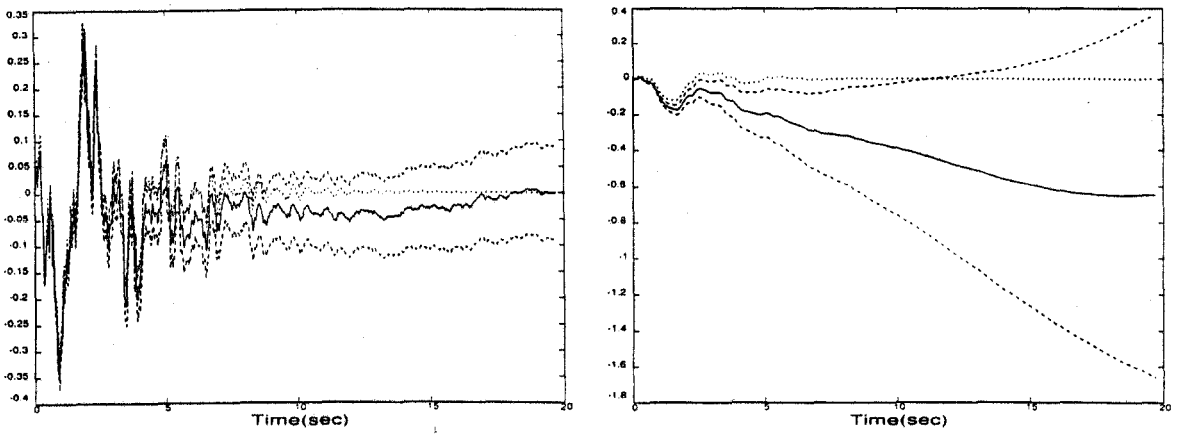

Two Standard Deviations

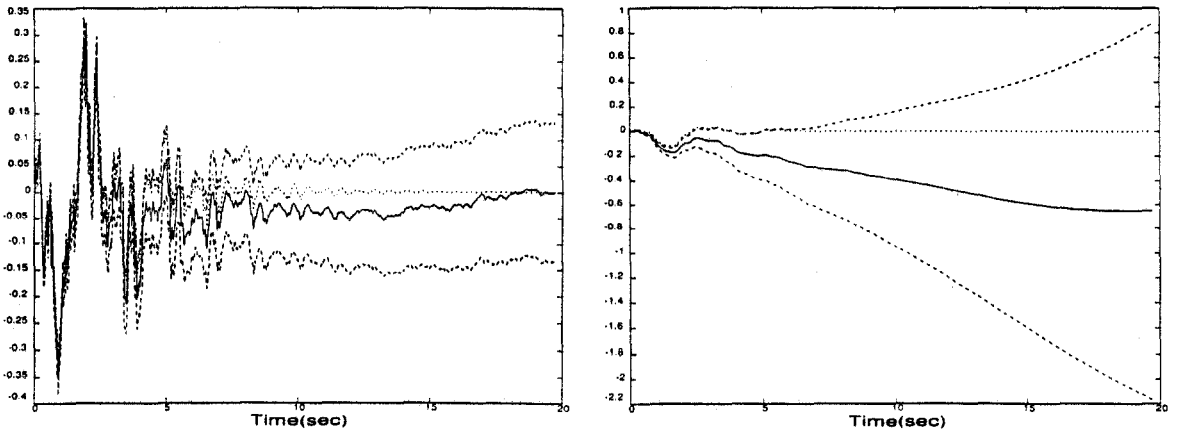

Three Standard Deviations

VELOCITY DISPLACEMENT

Figure 3-16. Reliability bounds for the time domain processing of synthetic signal Q11CNTS.
(____ most probable; . . . . . exact; - - - - - deviations).

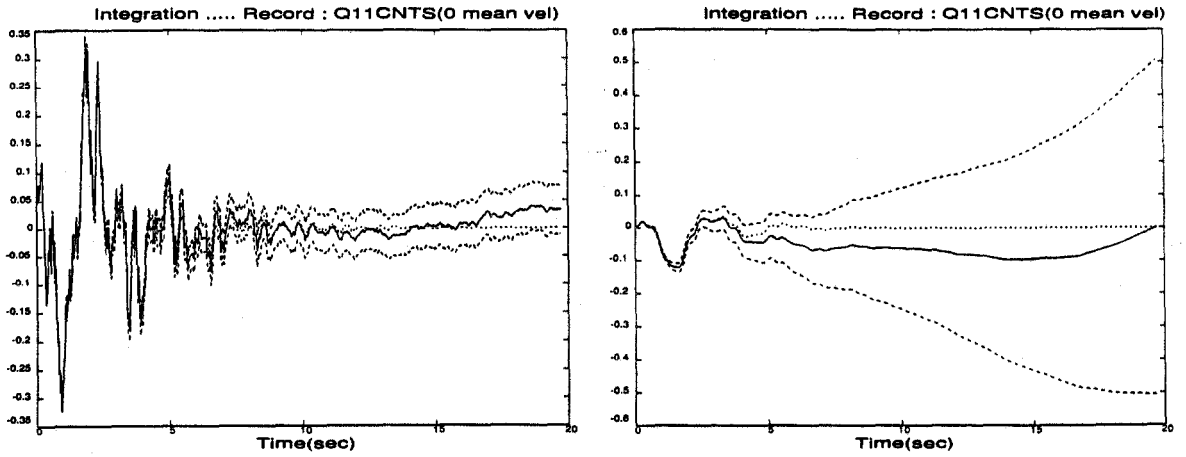

One Standard Deviation

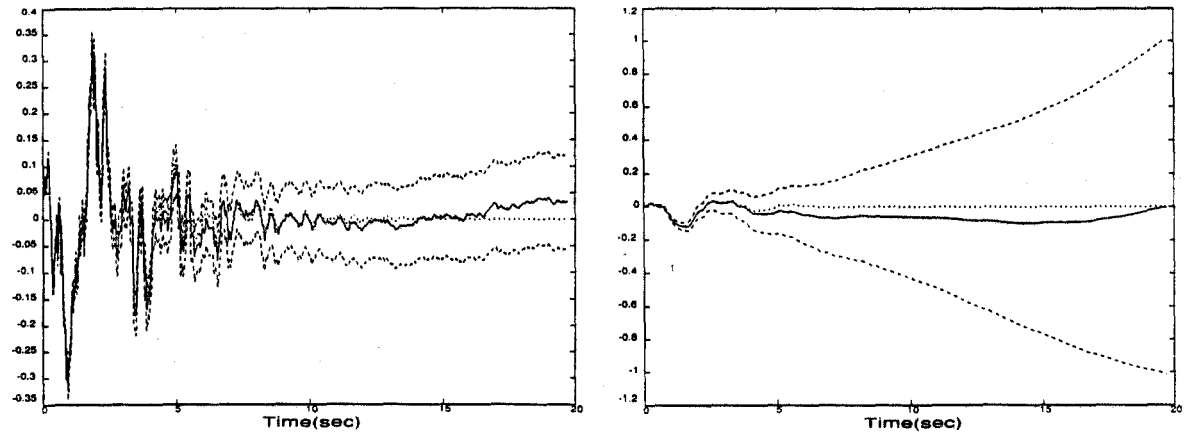

Two Standard Deviations

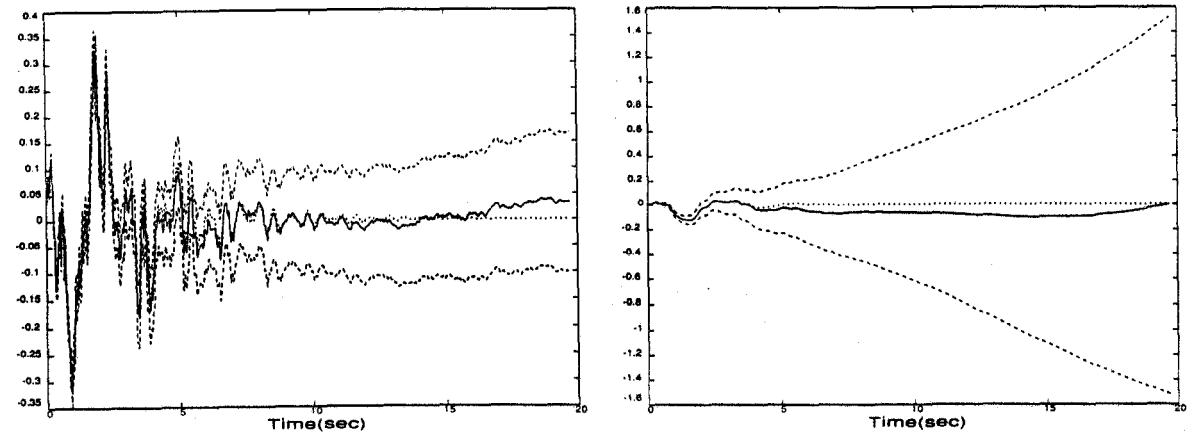

Three Standard Deviations

VELOCITY DISPLACEMENT

Figure 3-17. Reliability bounds for the time domain processing of synthetic signal Q11CNTS, with zero mean velocity.
(____ most probable; . . . . . exact; - - - - - deviations).

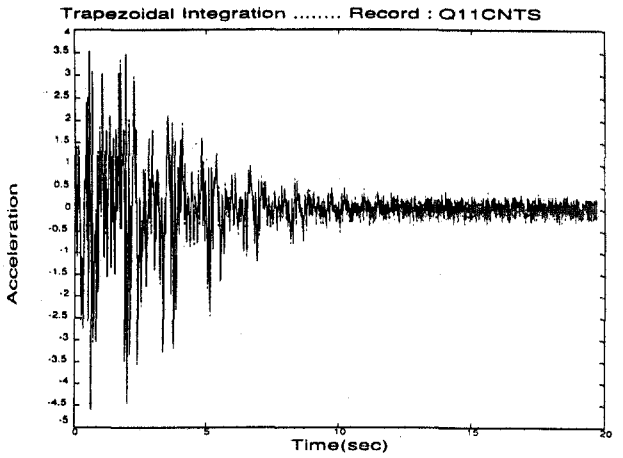

One Standard Deviation

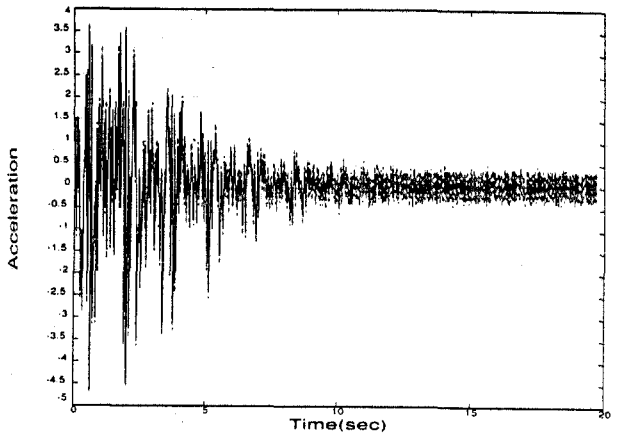

Two Standard Deviations

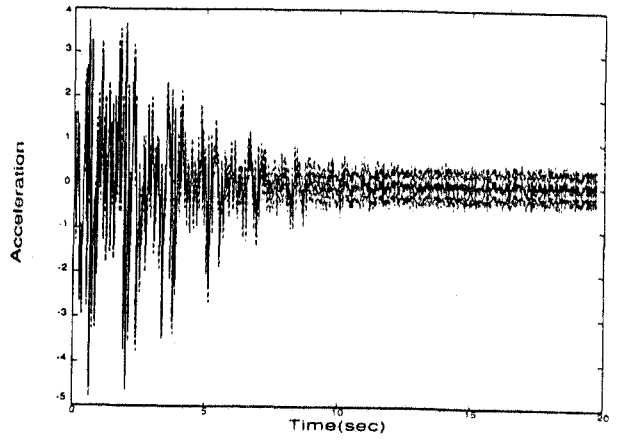

Three Standard Deviations

Figure 3-18. Reliability bounds for the most probable acceleration of synthetic signal Q11CNTS.
(____ most probable; . . . . . exact; - - - - - deviations).

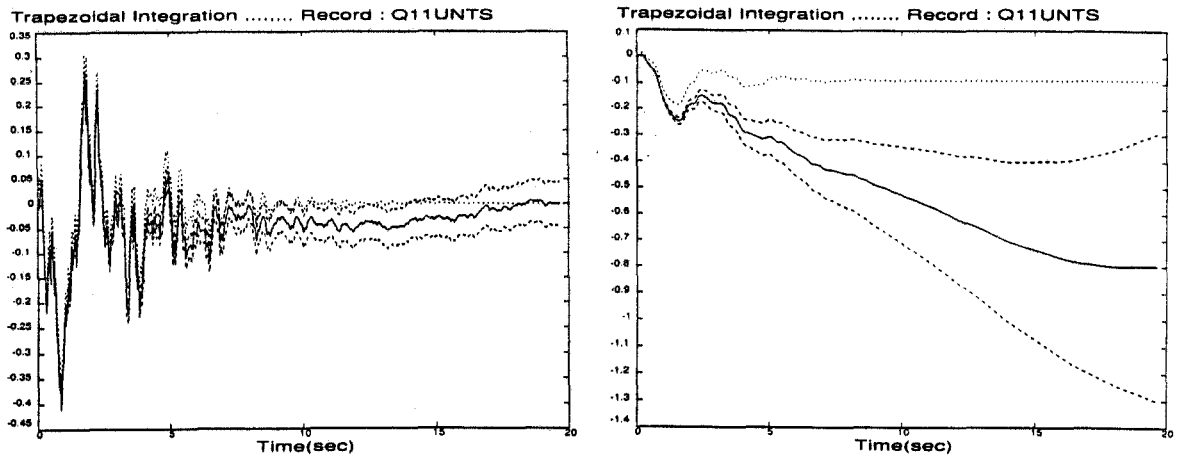

One Standard Deviation

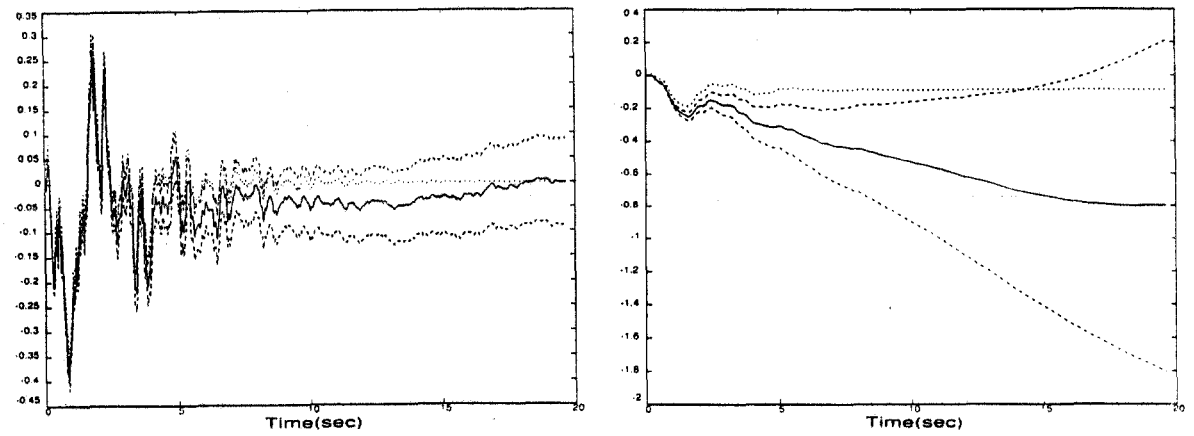

Two Standard Deviations

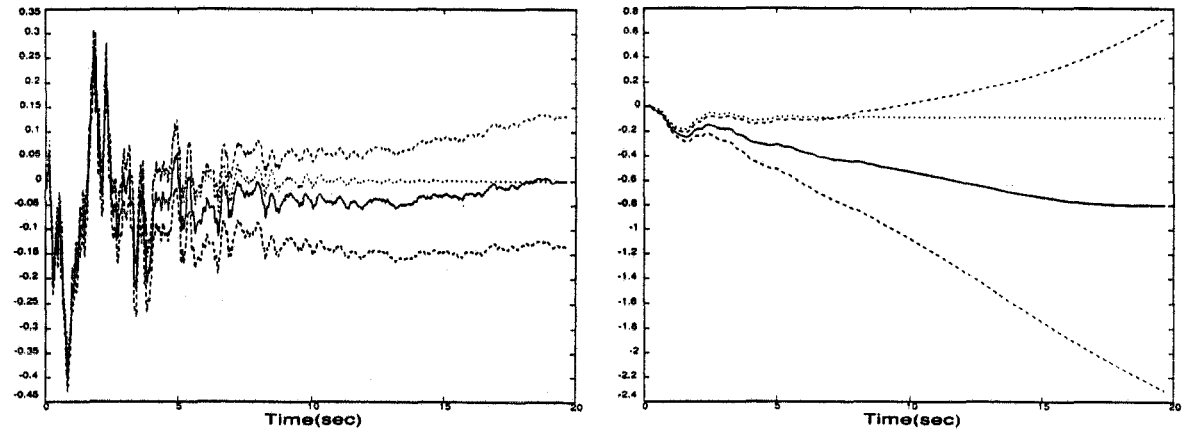

Three Standard Deviations

VELOCITY DISPLACEMENT

Figure 3-19. Reliability bounds for the time domain processing of synthetic signal Q11UNTS.
(____ most probable; . . . . . exact; - - - - - deviations).

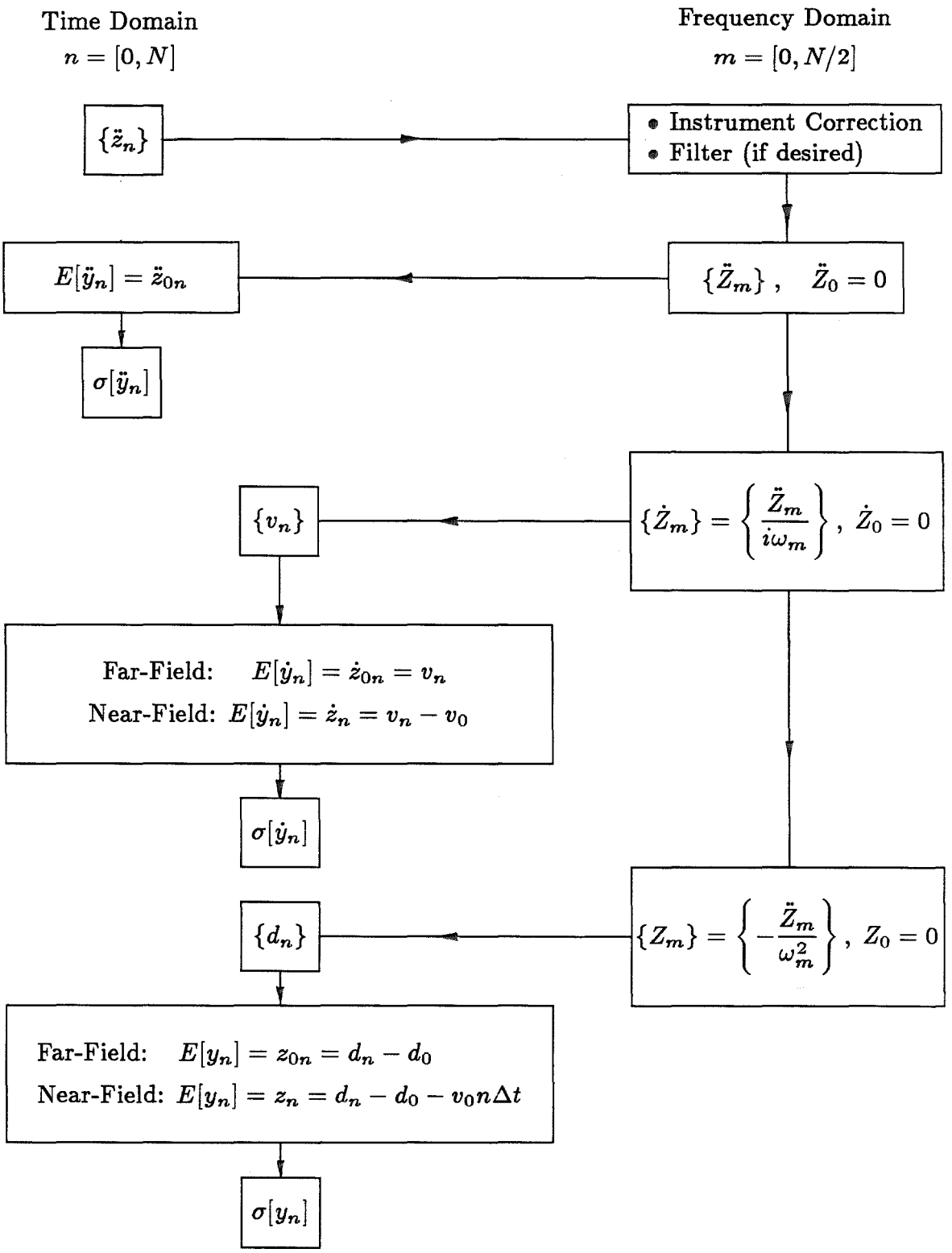

Figure 3-20. Flowchart of the probabilistic frequency domain processing method [implemented without the spectral substitution method (Ch.4)].

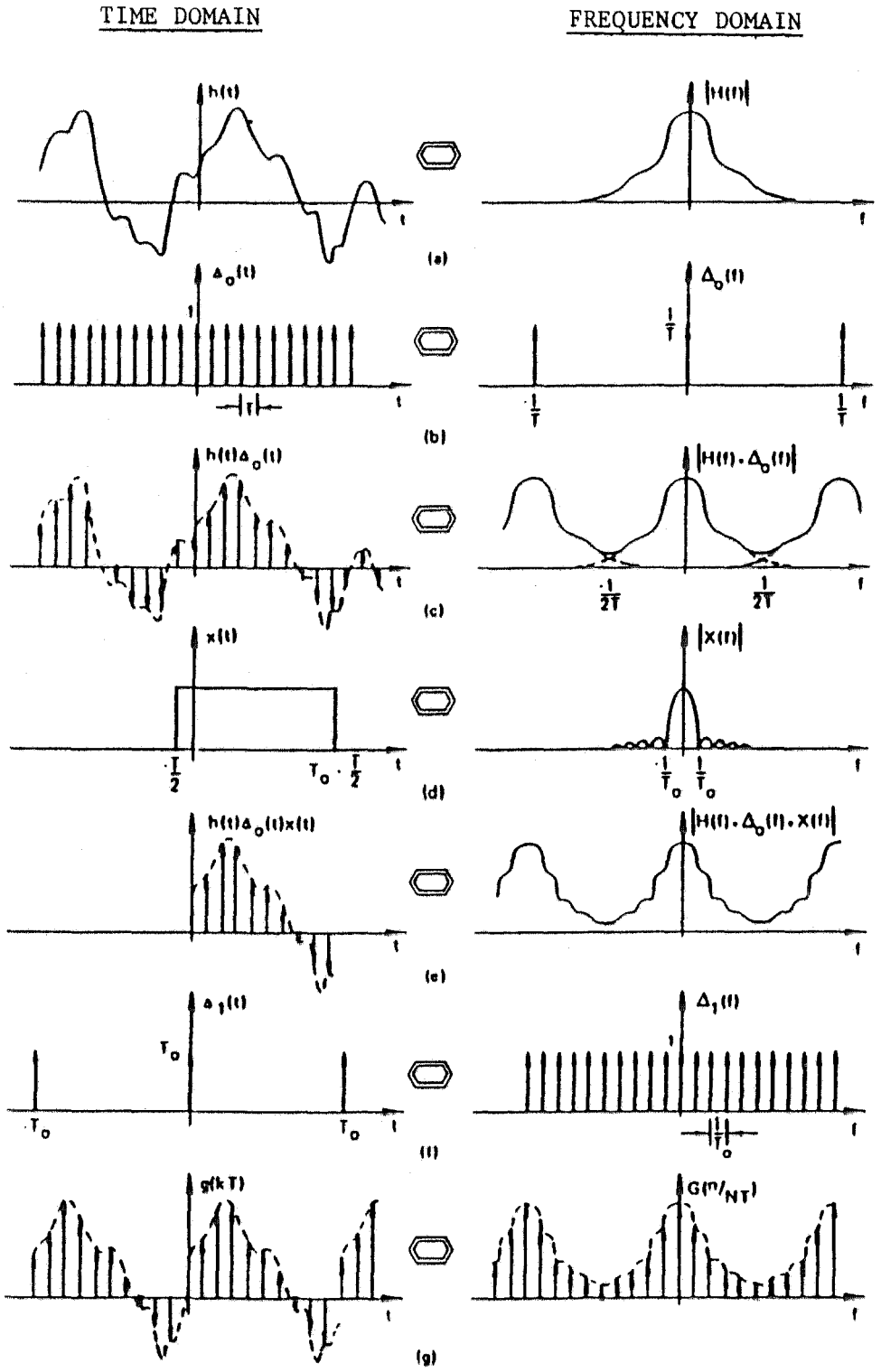

Figure 3-21. Discrete Fourier transform of a general waveform [Brigham, 1974] Description of main steps: (a) continuous signal; (b) sampling in time domain; (c) aliasing; (d) time windowing; (e) leakage; (f) sampling in frequency domain; and (g) discrete signal.

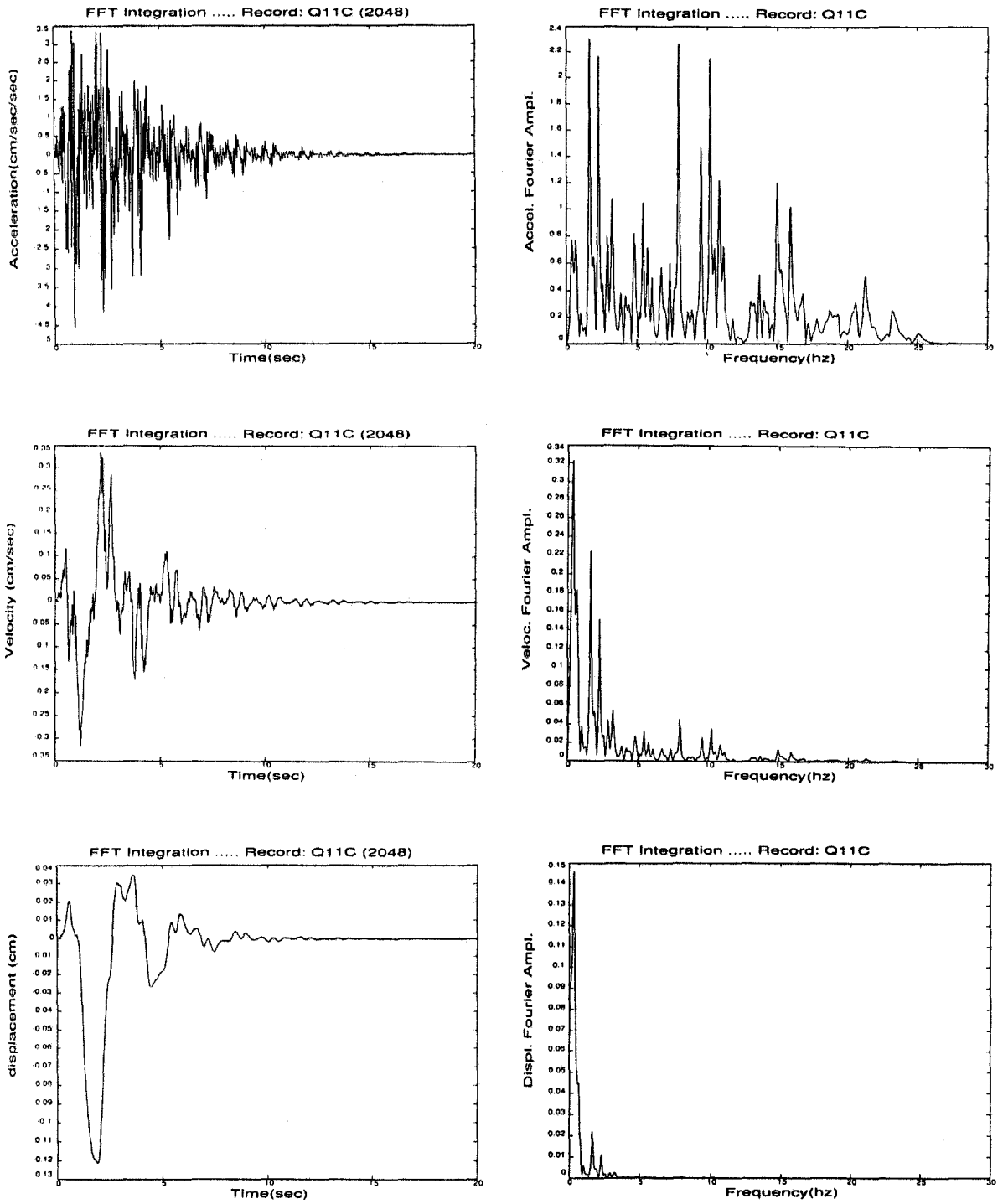

Figure 3-22. Time histories and Fourier amplitude spectra of the complete synthetic signal Q11C (200 harmonics between 0.015 Hz and 25 Hz; 2001 points at $\Delta t = 0.01$ sec) processed with the frequency domain method and 47 zeroes appended for FFT.

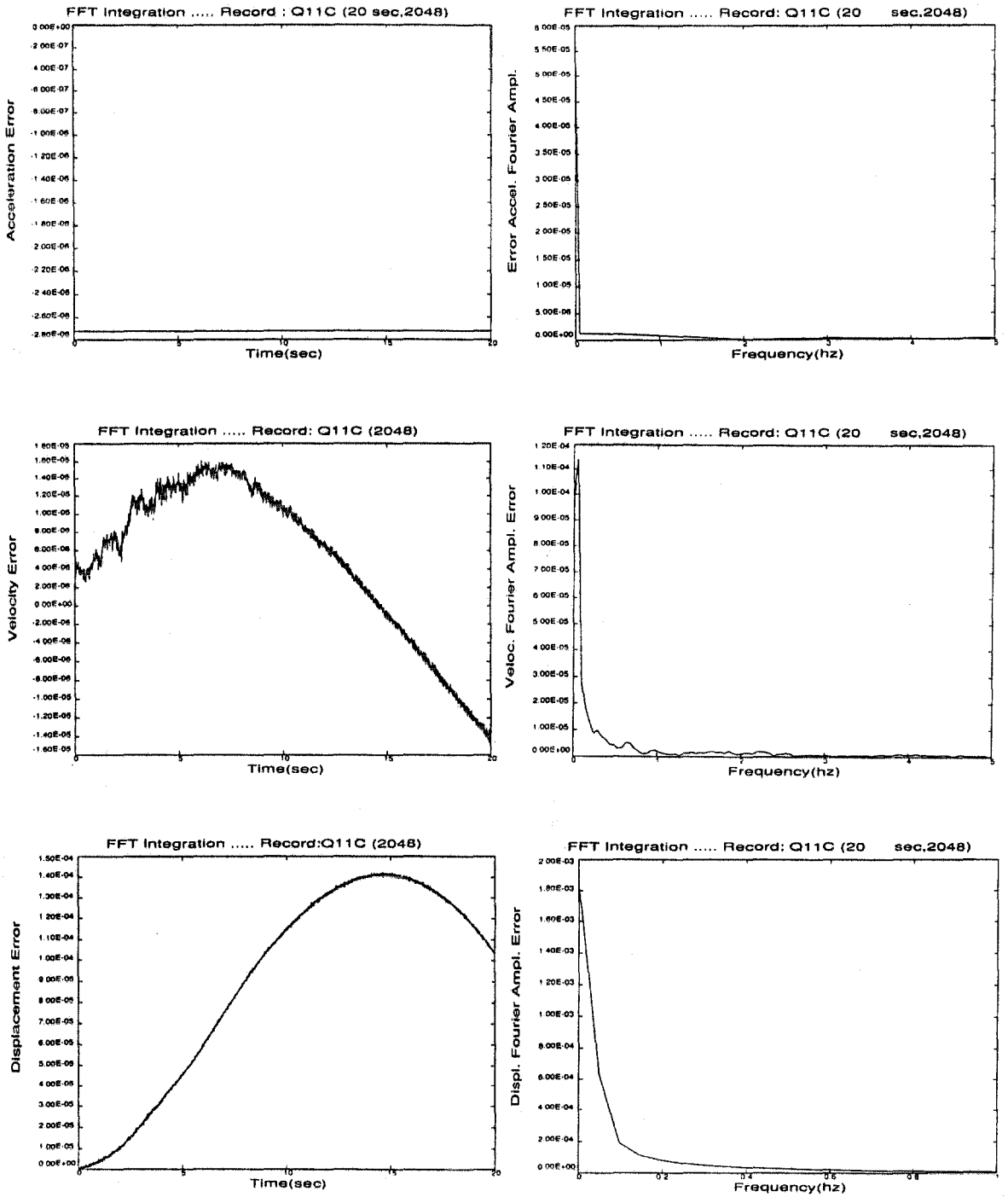

Figure 3-23. Time history errors and Fourier amplitude spectra errors in complete synthetic signal Q11C (2001 points at $\Delta t = 0.01$ sec) processed with the frequency domain method and 47 zeroes appended for FFT. Error = Exact (2001 points + 47 zeroes) − Processed (2001 points + 47 zeroes).

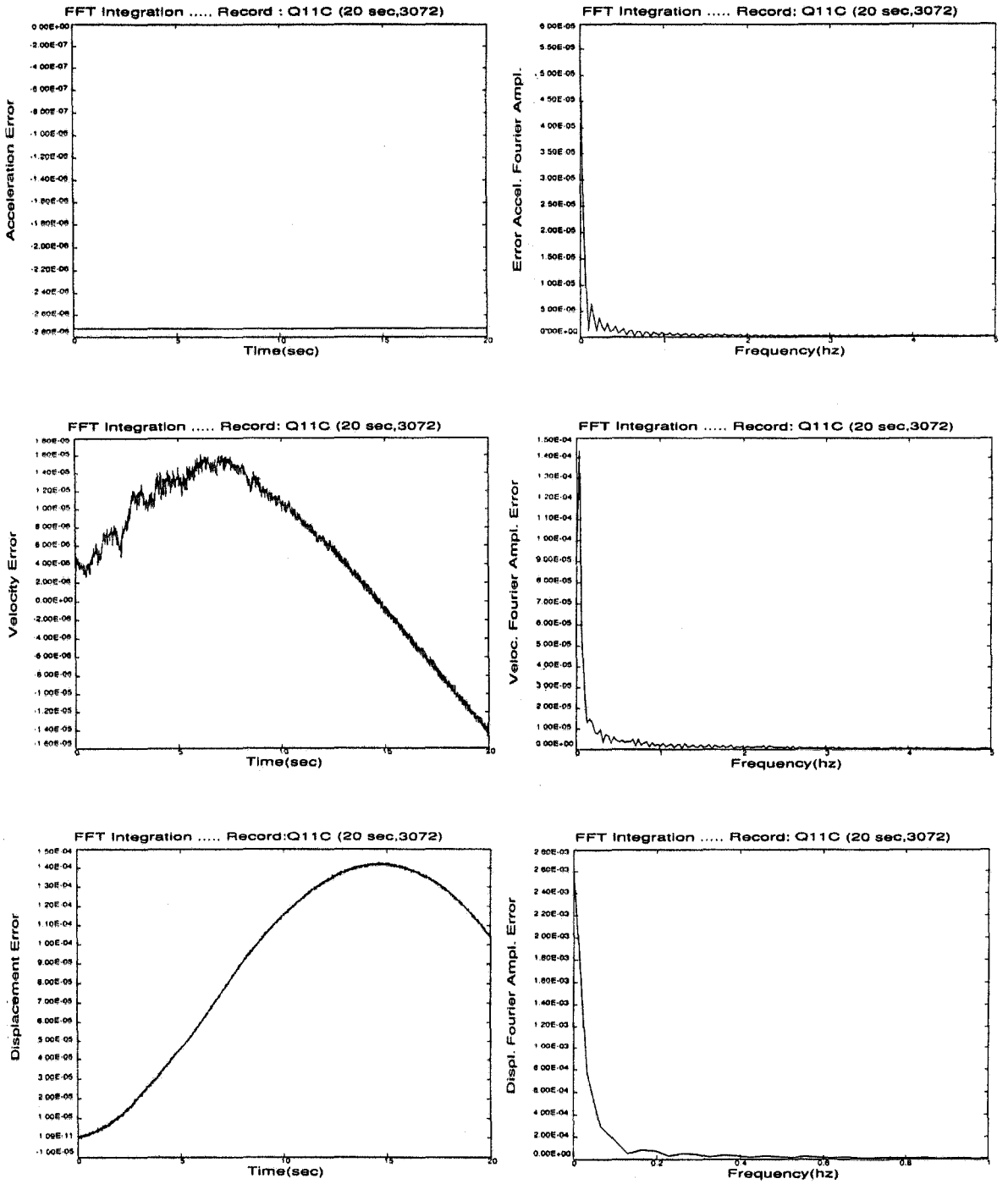

Figure 3-24. Time history errors and Fourier amplitude spectrum errors in complete synthetic signal Q11C (2001 points at $\Delta t = 0.01$ sec) processed with the frequency domain method and 1023 zeroes appended for FFT. Error = Exact (2001 points + 1023 zeroes) – Processed (2001 points + 1023 zeroes).

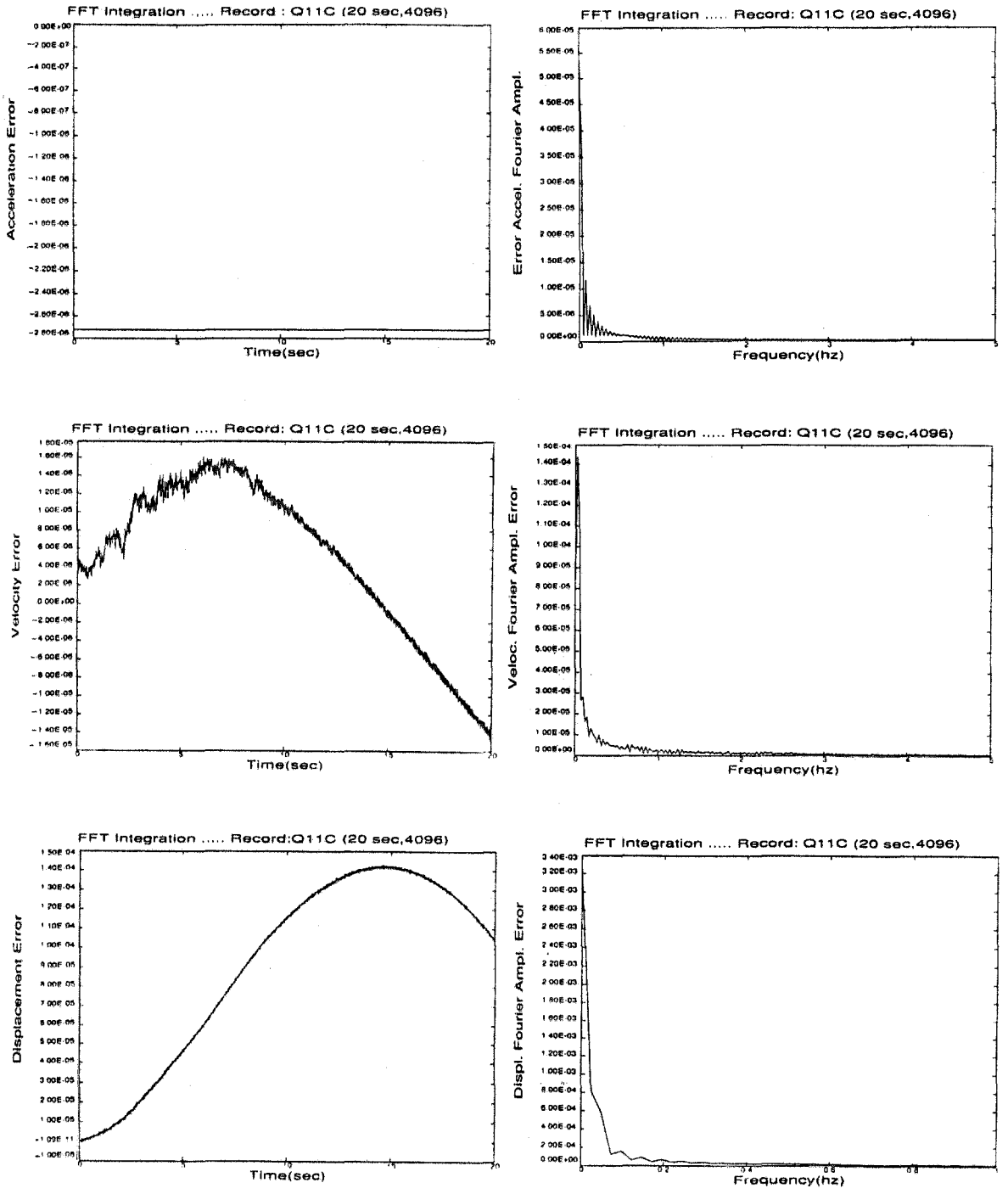

Figure 3-25. Time history errors and Fourier amplitude spectrum errors in complete synthetic signal Q11C (2001 points at $\Delta t = 0.01$ sec) processed with the frequency domain method and 2047 zeroes appended for FFT. Error = Exact (2001 points + 2047 zeroes) – Processed (2001 points + 2047 zeroes).

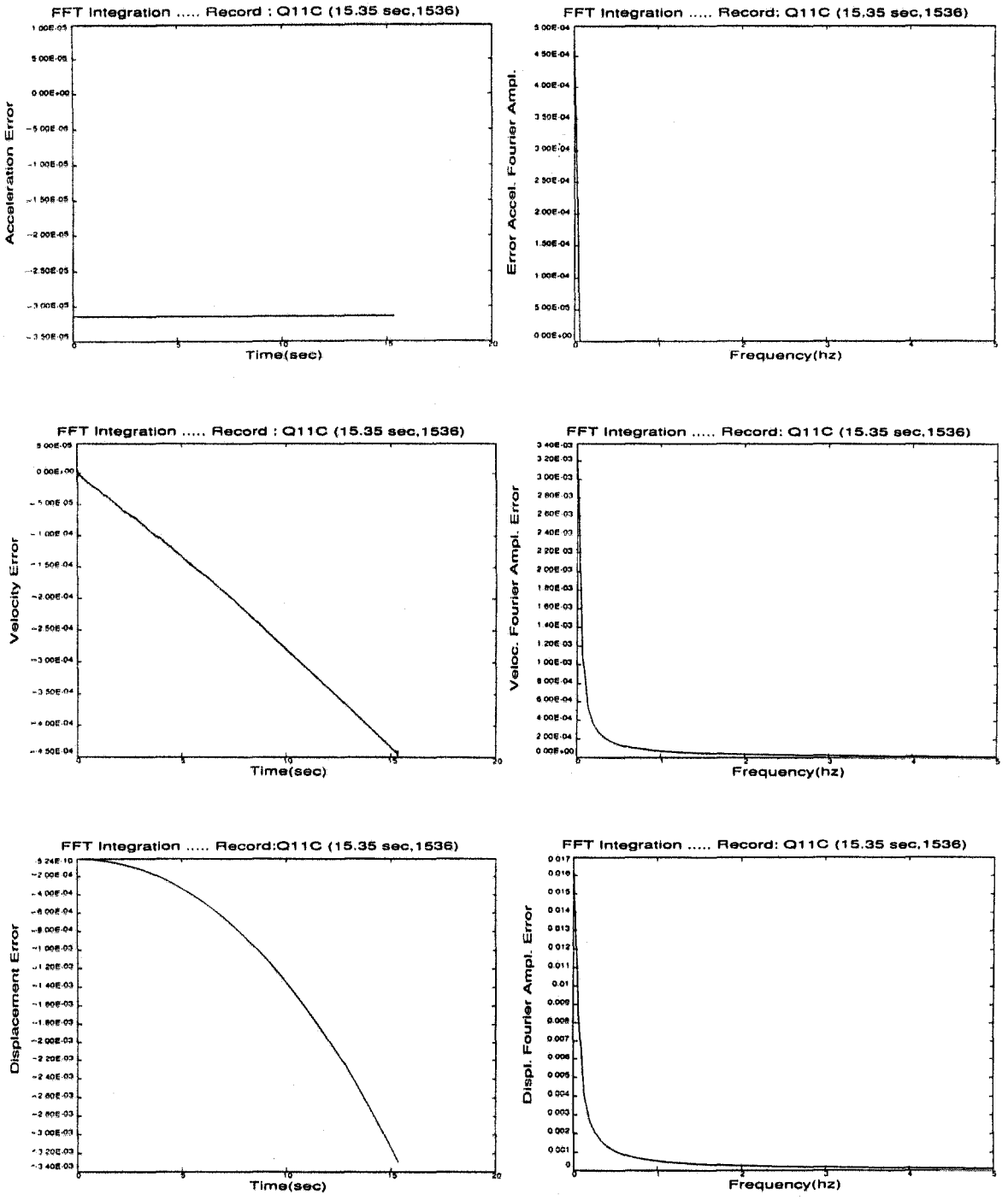

Figure 3-26. Time history errors and Fourier amplitude spectrum errors in truncated signal Q11C (1536 points at $\Delta t = 0.01$ sec) processed with the frequency domain method and 0 zeroes appended for FFT. Error = Exact (1536 points + 0 zeroes) – Processed (1536 points + 0 zeroes).

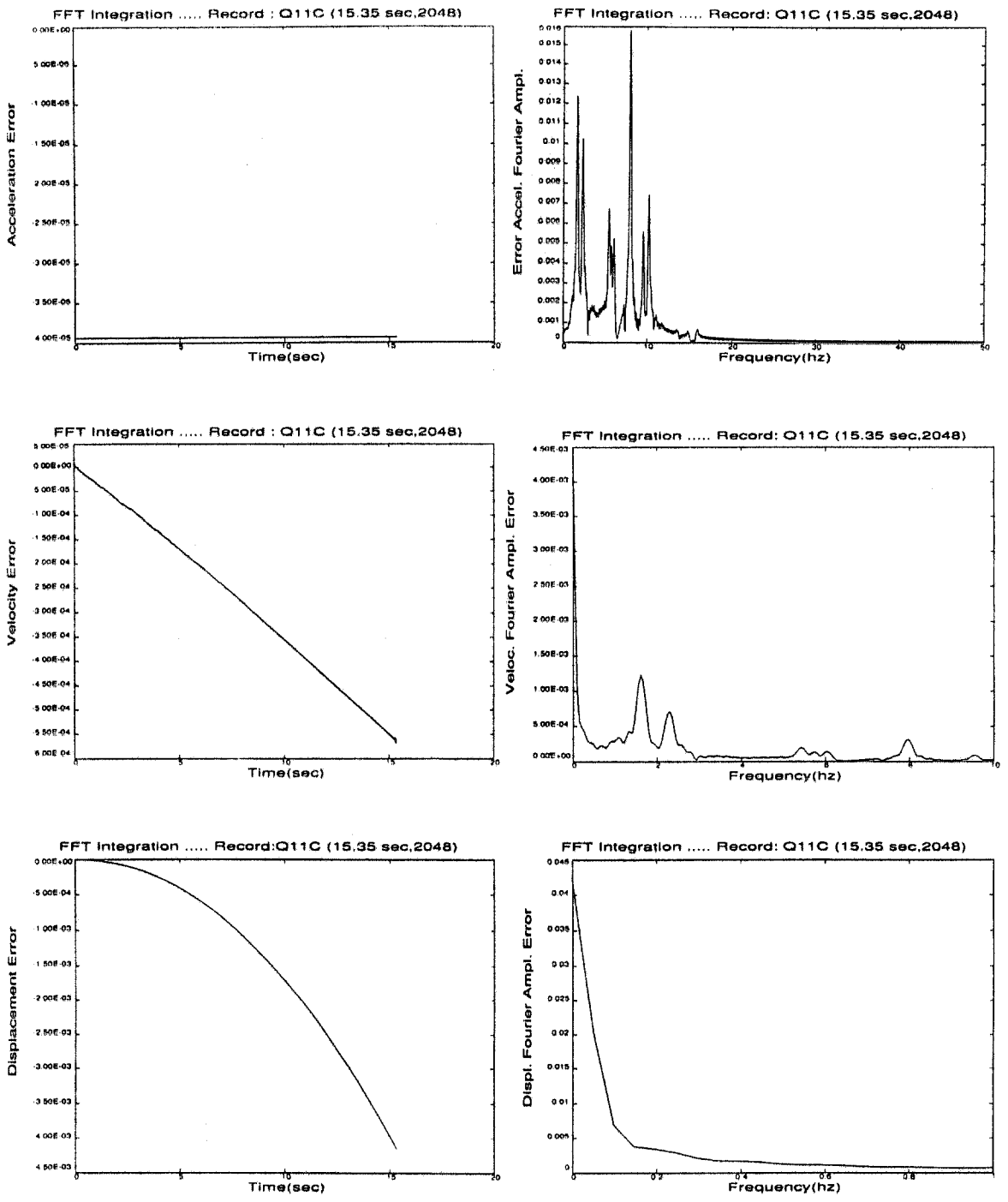

Figure 3-27. Time history errors and Fourier amplitude spectrum errors in truncated signal Q11C (1536 points at $\Delta t = 0.01$ sec) processed with the frequency domain method and 512 zeroes appended for FFT. Error = Exact (2001 points + 47 zeroes) − Processed (1536 points + 512 zeroes).

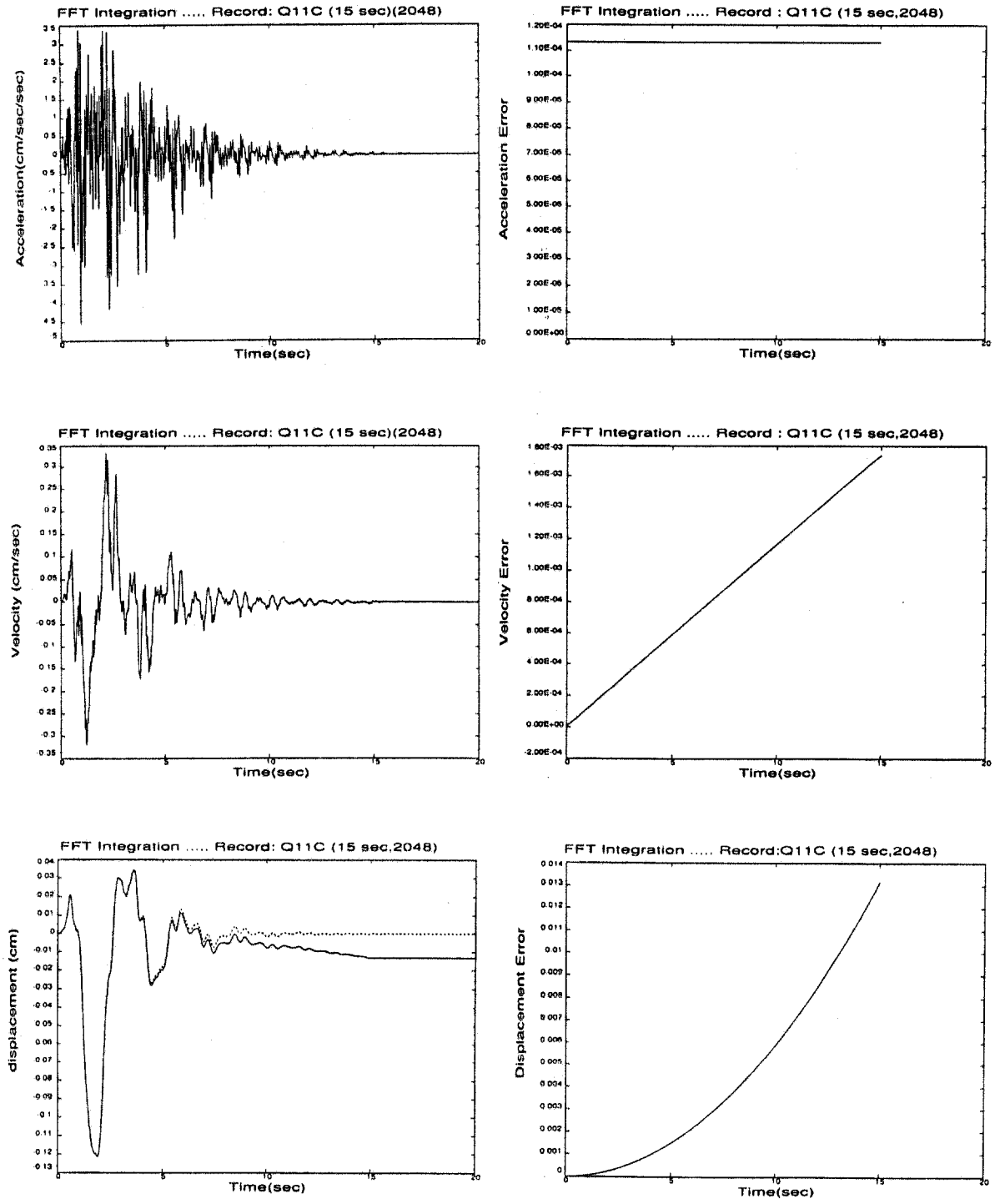

— Processed - - - Exact Error = Exact (2001 pts) – Processed (1501 pts)

Figure 3-28. Time histories and errors of the end truncated signal Q11C (15 sec) processed with the frequency domain method.

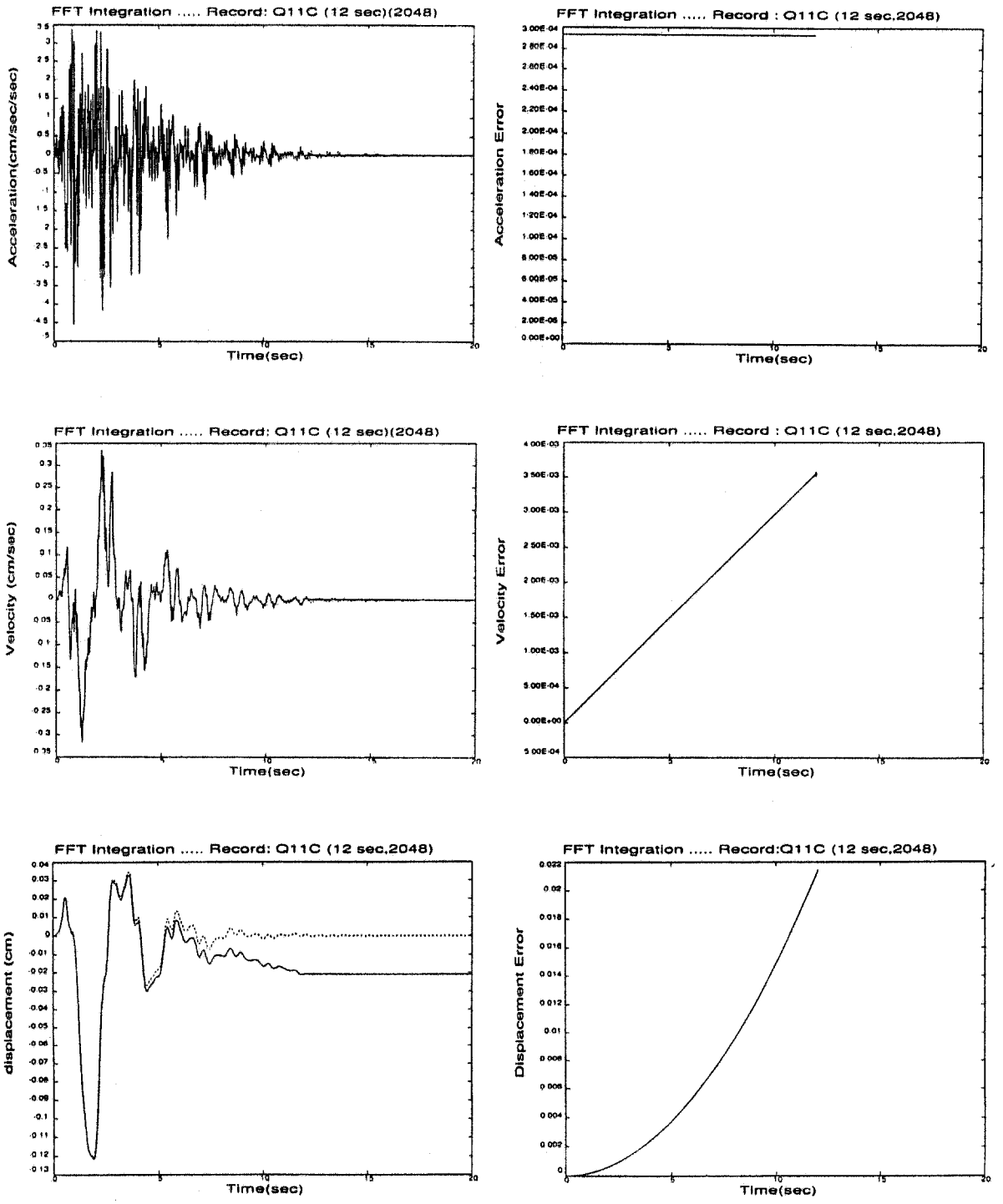

Figure 3-29. Time histories and errors of the end truncated signal Q11C (12 sec) processed with the frequency domain method.

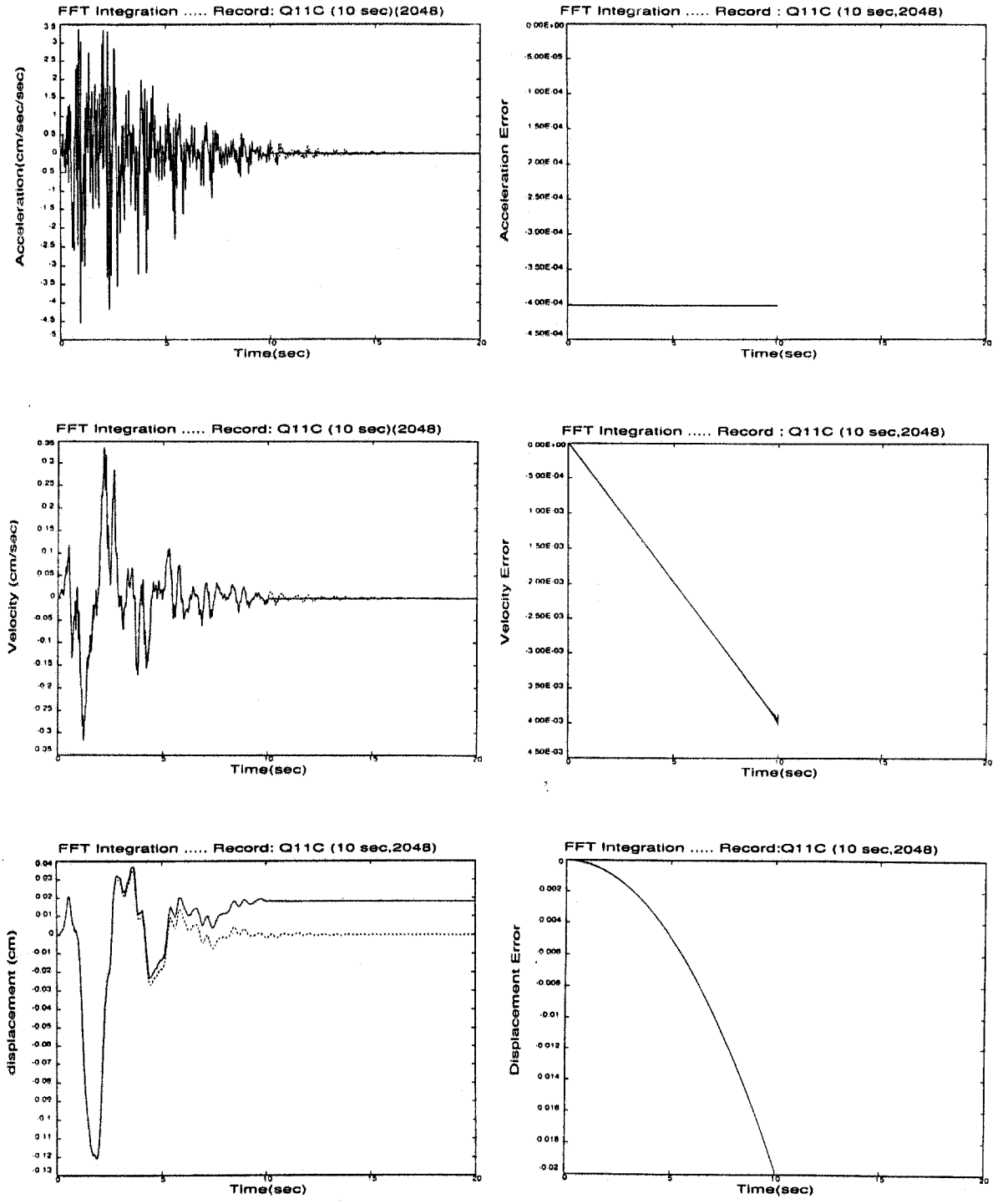

— Processed - - - Exact Error = Exact (2001 pts) – Processed (1001 pts)

Figure 3-30. Time histories and errors of the end truncated signal Q11C (10 sec) processed with the frequency domain method.

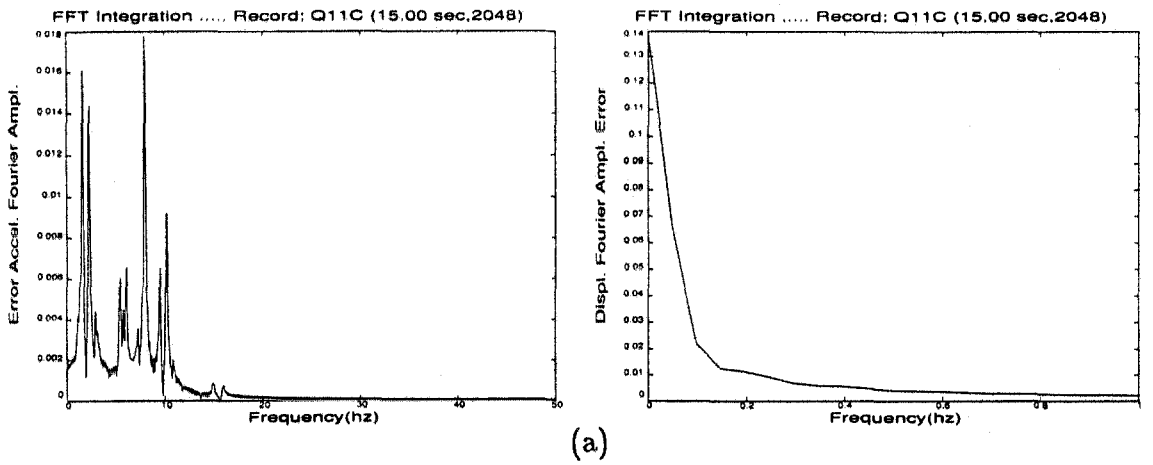

(a)

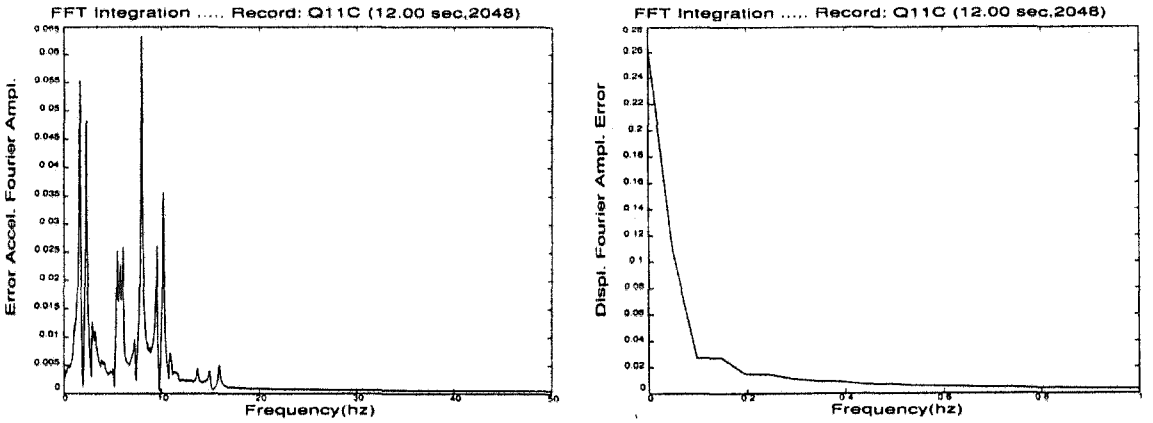

(b)

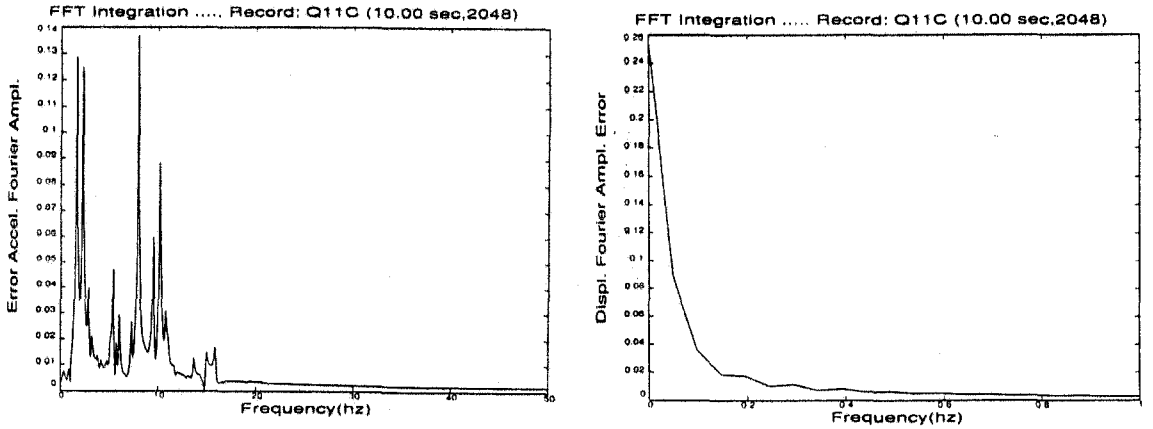

(c)

Figure 3-31. Acceleration and displacement Fourier amplitude spectrum errors for end truncated signal Q11C processed with the frequency domain method. (a) 15 sec (Fig. 3.28); (b) 12 sec (Fig. 3.29); (a) 10 sec (Fig. 3.30).

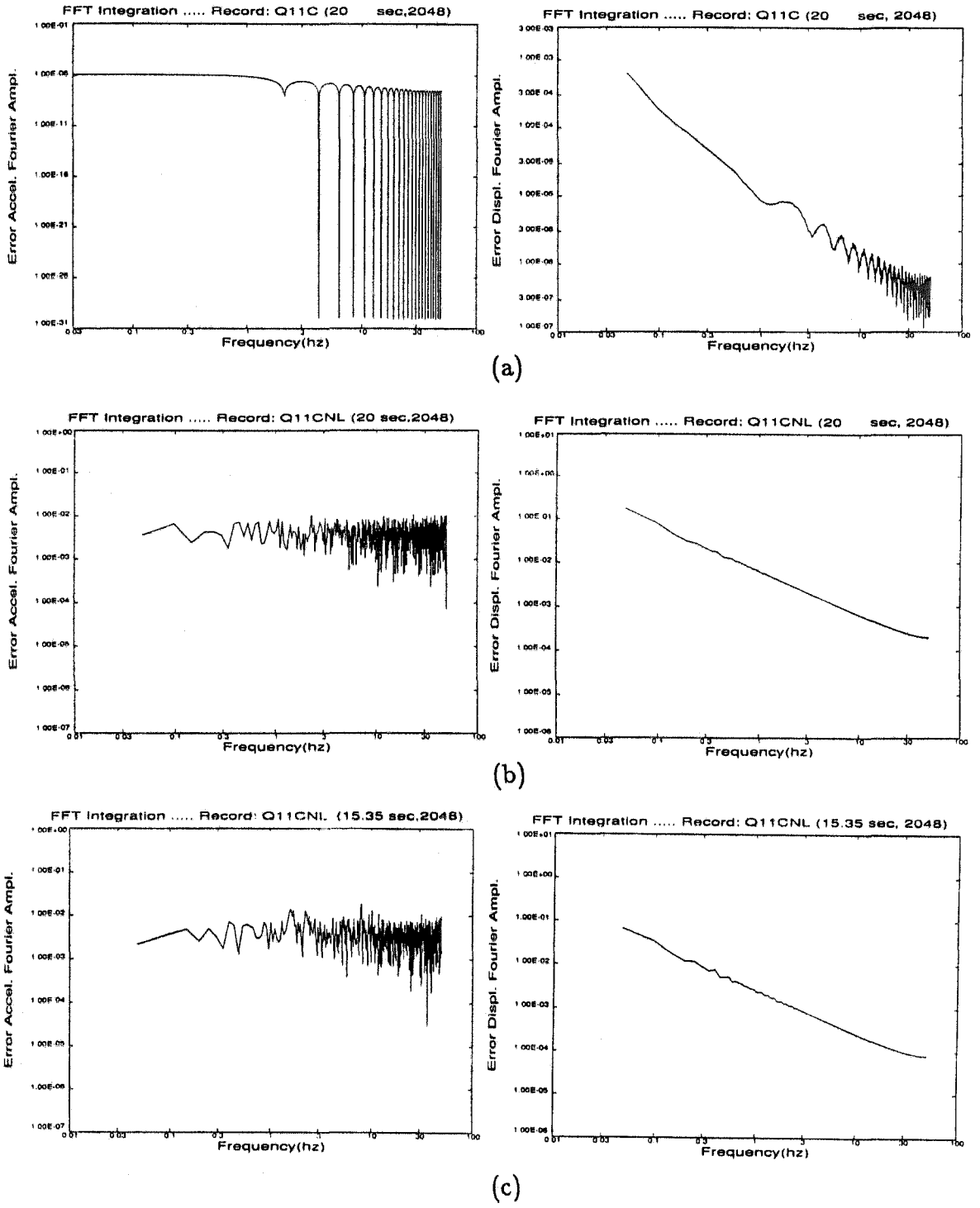

Figure 3-32. Errors in the acceleration and displacement Fourier amplitude spectra (log-log scale) from the frequency domain processing method for (a) uncontaminated and complete synthetic signal Q11C (2001 points + 47 zeroes); (b) noise contaminated synthetic signal Q11CNL (2001 points + 47 zeroes); (c) noise contaminated and truncated synthetic signal Q11CNL (1536 points + 512 zeroes).

Chapter 4

ERROR REDUCTION BY OPTIMAL METHODS

4.1 Introduction

So far we have presented a new probabilistic approach to earthquake accelerogram processing which performs integration in either the time domain or the frequency domain, and uses no filter to remove possible errors at the high and low frequency ends of the signal. Assumptions were made on the values of either the initial motion at start-up time, or the total mean of the signal, thus producing the most probable time histories given those assumptions. The variances of the start-up and noise levels were used to compute the confidence intervals about the most probable value of the signal. It was shown that the standard deviations of the acceleration and the velocity produce only slight departures from the most probable signals, but that the error levels associated with the displacement time histories were so large as to make these signals almost unusable. These large displacement errors, due to long-period drifts, are the main motivation behind the myriad of correction methods, all involving classical digital band-pass filters, that have been proposed. However, it was shown in Ch. 2 that these filters not only discard recording and digitization noise outside the cut-off bands, along with other information of possible physical importance, but they may also induce additional error in the signal due to poor internal performance. These methods usually produce "good" looking displacement signals which are often not a close representation of the actual motion at the recording site. Recovering these exact displacements may unfortunately be an impossible task, but the purpose of this chapter is to propose a better method to correct for the long-period errors.

The sources of the error in recorded accelerograms were shown to be due to both the digitization noise and the unknown offset in the acceleration which can arise

from missing data at the beginning as well as at the end of the event (e.g., analog accelerograph), or from a drift in the zero baseline (e.g., digital accelerograph). The missing data leads to uncertainties in the acceleration *d.c.* which would be zero if the complete time history was available. The digitizing and recording noise affect each harmonic of the spectrum including *d.c.*, but the signal-to-noise level is worse at the low- and high-frequency ends of the spectrum. In most recorded earthquake accelerograms obtained from analog instruments, the error at and near *d.c.* resulting from the uncertainty in the temporal mean is much larger than the error due to the digitization noise.

The following two approaches will attempt to correct each of these sources of error separately. The first one, referred to as the Wiener optimal noise filter, finds the signal-dependent filter which attempts to remove only the noise, and not the signal, throughout the whole frequency range as a function of the signal-to-noise ratio. It will be shown that if based on the information available from the recorded accelerogram, such an optimal filter would always have a transfer function equal to unity. This implies that the approach proposed in Ch. 3, which does not use any filtering, is consistent as being the optimal way to process the signal based on the information in the data, but of course this does not help to solve the long-period drift problem in the displacement. Also, hybrid versions of the Wiener noise filters, which are no longer optimal, are tested and presented. The second method proposed in this chapter corrects the error-corrupted ends of the signal's spectrum, especially near *d.c.* where baseline errors are predominant, by using other information in addition to the data. It is based on the optimization of earthquake spectral models for free-field records and structural spectral models for in-structure records. The intent is to replace the spurious frequency components by their most probable value as defined by the optimization scheme. The advantages of this second approach include the substantial reduction of the low-frequency error due to shifts in the acceleration baseline, the possible recovery of any nonzero final displacements, and identification of important seismological and structural parameters.

4.2 Noise Filters

4.2.1 Wiener Optimal Noise Filter

The topic of retrieving a signal from noise-contaminated data is one that has been of great concern to electrical and communication engineers for many years [Whalen, 1971]. However, their problems and their needs are somewhat different than the ones faced in the processing of strong-motion records.

Wiener [1950] first suggested the notion of *optimal linear filter*, $\phi(t)$, which can be used to decrease the noise level in measured data. The objective of his approach is to find a linear transformation which provides the best estimate $\tilde{y}(t)$ of a stationary infinite continuous stochastic process $y(t)$ (i.e., the true signal) in terms of some known statistics of $y(t)$ and of a measured stationary process $z(t)$ related to $y(t)$ [Papoulis, 1965]. Equivalently, this optimal filter $\phi(t)$ has an impulse response function which minimizes the mean-square error ϵ:

$$\epsilon = E\left[\left|\tilde{y}(t) - y(t)\right|^2\right] , \tag{4.2.1}$$

where ,

$$\tilde{y}(t) = \int_{-\infty}^{+\infty} z(t-\tau)\phi(\tau)d\tau . \tag{4.2.2}$$

E is the expectation operator involving the prior joint probability distribution of $y(t)$ and $z(t)$. In its most general form, the solution to Eqs. 4.2.1 and 4.2.2 leads to the Weiner-Hopf equation, which for zero-mean processes implies that the filter has a transfer function of the form:

$$\Phi(f) = \frac{S_{yz}(f)}{S_{zz}(f)} , \tag{4.2.3}$$

where S_{zz} is the power spectrum of the process $z(t)$, and S_{yz} is the cross-spectrum of processes $y(t)$ and $z(t)$. Here, the cross-spectrum is defined as the Fourier transform of the cross-correlation function R_{yz}, where:

$$R_{yz}(\tau) = E\left[y(t)z(t-\tau)\right] \quad \text{and} \quad S_{yz}(f) = \int_{-\infty}^{+\infty} R_{yz}(\tau)e^{-i2\pi f\tau}d\tau . \tag{4.2.4}$$

Hence, obtaining the best estimate $\tilde{y}(t)$ of the true signal $y(t)$ from another process $z(t)$, only requires the knowledge of either the auto- and cross-correlation functions or the auto- and cross-power spectra of the two processes.

In many signal-processing applications, $y_n = y(n\Delta t)$ is a discrete-time Gaussian process with known autocorrelation function or power spectral density, which is contaminated with uncorrelated zero-mean white noise δ_n, and $z_n = y_n + \delta_n$ [Press *et al.*, 1986]. For such cases, the discrete optimal filter is given at the discrete frequencies ω_m by:

$$\Phi_m = \frac{E\left[|Y_m|^2\right]}{E\left[|Y_m|^2\right] + E\left[|\Delta_m|^2\right]} \ , \tag{4.2.5}$$

where Y_m, Z_m and Δ_m are the discrete Fourier transform of y_n, z_n and δ_n respectively. This expression for Φ_m assumes that the power spectra of the true signal and of the noise are known. The denominator of Eq. 4.2.5 is the power spectral density of the stochastic process z_n which is to be measured.

When the signal to be measured is obtained from a linear transformation of the true signal (e.g., signal measured at the output of a transducer), so that:

$$Z_m = H_m \cdot Y_m + \Delta_m \ . \tag{4.2.6}$$

where H_m is the discrete transfer function of the linear system and H_m^* its complex conjugate, then the best estimate $\tilde{Y}_m$ of the true signal Y_m is obtained for the optimal filter Φ_m such that:

$$\Phi_m = \frac{H_m^* \cdot E\left[|Y_m|^2\right]}{|H_m|^2 \cdot E\left[|Y_m|^2 + E\left[|\Delta_m|^2\right]\right.} \ , \tag{4.2.7}$$

According to Eq. 4.2.5, the optimal noise filter in this case is always positive and real. This implies that the best estimate $\tilde{Y}_m$ of the true signal involves no phase change in the noise reduction process. Also, the value of Φ_m, which always lies between zero and unity, is a function of the signal-to-noise ratio at any given spectral point. Indeed, as the noise dominates the signal, or equivalently as the signal-to-noise ratio becomes small, the optimal filter Φ_m approaches zero. Inversely, as the signal-to-noise increases, Φ_m approaches unity.

The above derivation assumes a prior and complete knowledge of the power spectrum of the true signal. In the case of earthquake ground-motion accelerograms, Brune's spectrum [Brune, 1970] could provide a model for the spectral amplitude of the true signal. However, Brune's source spectrum is only valid at low frequencies, and cannot properly represent effects such as propagation and local site response. Even if Brune's spectrum were a valid model over the whole frequency range, the optimal filter approach of Eq. 4.2.5 would also require the knowledge of all the parameters defining the spectrum such as the corner frequency and the seismic moment. In practice, this knowledge is not always available. An approach using Brune's model which does not have this deficiency is introduced later.

The above analysis applies to a situation where the optimality is based on information prior to the use of the measured data, so $\Phi(f)$ in Eq. 4.2.3 would best be called the "prior optimal linear filter." For optimality based on the measured data $\ddot{z}(t)$ as well, the expectation operator E in Eq. 4.2.1 should involve the conditional probability distribution of the $\ddot{y}(t)$ given $\ddot{z}(t)$. In this case, applying Wiener's concept of finding the best approximation $\tilde{Y}(f)$ to a true earthquake signal, the optimal filter is still defined by Eq. 4.2.3, but this now leads to the result that the optimal $\Phi(f)$ is equal to unity throughout the whole spectrum. This implies that for discretized earthquake accelerograms, the best approximation $\tilde{\ddot{y}}_n$ is given by the measured, baseline-corrected and unfiltered data $\ddot{z}_n$. This is consistent with the approach adopted in Ch. 3, by which the most probable motions based on the data are defined to be the ones that are actually measured.

4.2.2 Hybrid Noise Filters

Noise filters which decrease the amplitude of the spectrum at points where the signal-to-noise ratio is low can be constructed using a formula analogous to the results of Wiener's approach. However, these filters are no longer optimal in the statistical sense. To avoid phase changes in the signal, such filters should have positive real transfer function. Also, these must have amplitudes in the range of zero to one which increase as a function of the signal-to-noise ratio. Several possibilities are suggested below, and tested on the noise-contaminated synthetic signals for their correction effectiveness.

A modified version of Wiener's optimal noise filter is defined by the transfer function:

$$\Phi_m = \frac{|\ddot{Z}_m|^2}{|\ddot{Z}_m|^2 + E\left[|\Delta_m|^2\right]} , \qquad m \in [0, \frac{N}{2}] , \tag{4.2.8}$$

where the frequency range is *d.c.* to the Nyquist frequency corresponding to the discrete time signal, and where $|\ddot{Z}_m|$ is the Fourier amplitude spectrum of the measured data assuming instrument correction is not required, similar to Eq. 4.2.5. If the measured data needs to be instrument-corrected, the noise filter should have a transfer function similar to Eq. 4.2.7, where H_m is the instrument transfer function. The power spectral density of the noise, $E[|\Delta_m|^2]$, is that of the digitization and recording error. As has been previously discussed in Chs. 2 and 3, such noise can be assumed to be Gaussian-distributed white noise with most probable value zero and standard deviation a, usually of the order of 0.001 g for analog accelerographs. It can be shown that the power spectral density of the noise is then constant over the whole frequency range of the spectrum and is defined by:

$$E\left[|\Delta_m|^2\right] = \frac{a^2}{N} , \tag{4.2.9}$$

where N is the number of data points in the discrete time signal.

Alternatively, the power spectral density of the noise can be extracted from the spectrum of the measured data. Typically, accelerograms are discretized at intervals of 0.01 sec, giving a Nyquist frequency of 50 Hz, but analog accelerographs have natural frequencies of about 25 Hz beyond which their response decreases sharply. Also, ground motion spectra are usually very small above 25 Hz. Hence, it can be argued that between 25 Hz and 50 Hz the spectrum of the measured data primarily reflects the digitizing and recording noise. Since Gaussian white noise has a constant power spectral density, the average value of the power spectrum between 25 Hz and 50 Hz could be defined to be the proper estimate for $E[|\Delta_m|^2]$ through out the whole frequency range of the data between *d.c.* and 50 Hz. Thus,

$$E\left[|\Delta_m|^2\right] = \frac{1}{P} \sum_{p=N/2-P+1}^{N/2} |\ddot{Z}_p|^2 , \qquad \forall m \in [1, N/2] , \tag{4.2.10}$$

where ω_P is approximately 25 Hz.

The correction effectiveness of the modified Wiener noise filter is tested on signal *Q11CNS*, which is the noise-corrupted version of synthetic signal *Q11C* scaled as a small earthquake (i.e., the level of noise is large with respect to the signal). No other sources of error exist in the signal to be processed. This signal is composed of 200 modulated frequencies between 0.05 Hz and 25 Hz, and hence all frequency content in the spectrum of the noise-contaminated signal between 25 Hz and 50 Hz is due primarily to the added Gaussian white noise. Eq. 4.2.10 is used to estimate the power spectral density function of the noise. The value of the noise variance a^2 inferred by equating Eq. 4.2.9 and Eq. 4.2.10 is almost identical to the one used to generate the noise in the uncorrupted synthetic signal. Hence, under the assumption that the noise is Gaussian and white, then Eq. 4.2.10 can provide good estimates of the power spectral density function of the noise.

The normalized measure-of-error J is used to examine how well the modified Wiener filter reduces the noise in the signal, where:

$$J = \frac{\sum_{i=1}^{N}(z_i - y_i)^2}{\sum_{i=1}^{N} y_i^2} \,. \tag{4.2.11}$$

In this equation, z_i is the noise-contaminated and filtered acceleration, velocity or displacement, and y_i is the exact counterpart. Although in the following discussion J is computed using the time-domain results, because of Parseval's identity, Eq. 4.2.11 could be equally viewed as comparing the change in the noise level in the frequency domain.

The values of J for the error in the acceleration, velocity and displacement, in the cases where no filter or the modified Wiener filter are implemented, are summarized in Table 4.2.1. These results indicate that the modified Wiener filter is capable of reducing the error in the acceleration by 35%, in the velocity by 60%, and in the displacement also by 60%. The differences in the time histories between the unfiltered and the filtered cases can be observed in Figs. 3.4 and 4.2.1 respectively. The plots of the error in the acceleration between the exact and the processed signals (top-right figure), show that the Wiener filter reduced the level of the white noise throughout the time history. Similarly, although the shape of the error in the velocity and the displacement have not changed much after implementation of the

noise filter, they have significantly decreased in amplitude. In particular, the drift in the displacement has decreased by 40%. The improvement in the displacement accuracy is primarily due to the low-frequency correction of the modified Weiner filter. The changes made elsewhere in the frequency domain where the filter varies erratically have little effect. Hence, the modified Wiener filter is capable of reducing the noise level in the time histories without affecting the predominant harmonics of the signal. The long-period errors primarily due to the shift in the acceleration temporal mean are still present, but have decreased in amplitude.

The modified Wiener filter obtained for signal *Q11CNS* is illustrated in Fig. 4.2.2.a. It is not a traditional type of filter, in the sense that it depends on the signal-to-noise ratio of the spectrum, and hence will be highly erratic in the frequency domain and different from one signal to the next. However, this figure illustrates the concept that the transfer function is close to unity in the region where the signal-to-noise ratio is large (i.e., below 25 Hz), and is close to zero in the region where the ratio is small (i.e., above 25 Hz). In particular, the filter decreases the high-frequency noise above 25 Hz by an average of 60%. Although the transfer function of the filter has an unusual form, the time-domain results (Figs. 3.4 and 4.2.1) prove that such a filter does reduce the error level.

Using the philosophy behind the modified Wiener noise filter, another class of noise filters can be defined. These are called exponential noise filters and are of the form:

$$\Phi_m(\alpha,\beta) = \exp\left[-\alpha\left(\frac{E\left[|\Delta_m|^2\right]}{|\ddot{Z}_m|^2}\right)^{\beta}\right], \qquad \forall m \in [1, N/2]\,. \tag{4.2.12}$$

Just like the modified Wiener filter defined in Eq. 4.2.8, the exponential noise filters are signal-dependent, and decrease the noise as a function of the signal-to-noise ratio. However, they differ in that they approach zero faster as the ratio decreases, and approach unity faster as the ratio increases. The rate at which these filters approach zero or unity is controlled by the parameters α and β.

For comparison, the exponential noise filters were also tested on synthetic signal *Q11CNS* for different values of α and β. The values of the measure-of-error J for

the acceleration, velocity and displacement, and for different combinations of α and β are listed in Table 4.2.1. It must first be noted that for most combinations of α and β listed in this table, J has substantially decreased from the case where no noise filter is implemented; there is up to 60% improvement in the acceleration, 86% in the velocity and 93% in the displacement. In general, the exponential filters were more effective than the modified Wiener filter in decreasing the error levels in the time histories.

Table 4.2.1 indicates that there is a trade-off between the role of α and β and their effect on the measures-of-error. For a constant value of α and increasing values of β, the measure-of-error J in the displacement decreases and that in the acceleration increases. Conversely, for a constant value of β and increasing values of α, the measures-of-error in the acceleration, velocity and displacement seem to decrease initially before increasing again. The relationship between the variations in α and β, and in the J's, does not appear to be a simple one, but it can be noticed that as β becomes large the value of the J's remains more or less constant regardless of the value assigned to α. More insight into the interaction between α and β can be gained by examining the transfer functions of the exponential noise filter obtained with *Q11CNS* for some of the cases listed in Table 4.2.1 and Fig. 4.2.2. The transfer function of the exponential noise filter for $\alpha = 1$ and $\beta = 1$ (Fig. 4.2.2.b) is very similar to that of the Wiener filter (Fig. 4.2.2.a), with the exception that the exponential filter decreases on the average more of the high-frequency noise, as corroborated by the slight drop in the J's. For $\alpha = 10$ and $\beta = 1$ (Fig. 4.2.2.e), most of the harmonics which have a high proportion of noise are removed, and in the process the amplitude of the harmonics where the signal-to-noise ratio is average are also significantly decreased. This alters the shape of the time histories and creates errors, as is reflected in the large values of J in Table 4.2.1. Conversely, for $\alpha = 1$ and $\beta = 10$ (Fig. 4.2.2.d), the filter has a transfer function that is equal to unity almost everywhere except at the harmonics which have a very small signal-to- noise ratio, in which cases it is equal to zero.

In effect, increasing α significantly decreases the amplitudes of all of the harmonics which do not have a very high signal-to-noise ratio. Whereas, increasing β

selectively removes all the harmonics which have an extremely small signal-to-noise ratio, and leaves all other harmonics unchanged although they may be contaminated by noise. A parametric study of the J's has shown that the combination $\alpha = 2$ and $\beta = 4$ offers the best compromise between the two effects. The transfer function of this case is illustrated in Fig. 4.2.2.e for synthetic signal *Q11CNS*. Compared to the transfer function of the Wiener filter (Fig. 4.2.2.a), the chosen exponential filter retains more of the spectrum below 25 Hz, in the range where the signal predominates, but removes on the average about the same amount of the high-frequency noise above 25 Hz. This is also reflected in the changes in J listed in Table 4.2.1. The measure-of-error in the acceleration is approximately the same for both types of noise filters, yet the error in the displacement from the exponential filter dropped by an extra 80%. Hence, when the proper combination for α and β is selected, the exponential noise filter significantly improves the correction effectiveness of the frequency-domain accelerogram processing method. In particular, for *Q11CNS* it decreases the noise-induced error in the acceleration by 25%, in the velocity by 85% and in the displacement by 90%.

The time histories for *Q11CNS* produced by implementation of the exponential filter with $\alpha = 2$ and $\beta = 4$ are shown in Fig. 4.2.3. Compared to the corresponding results obtained when no noise filter is implemented (Fig. 3.4), and when the modified Wiener filter is used (Fig. 4.2.1), the exponential noise filter considerably decreases the error in the processed time histories. However, according to the plots depicting the error between the noise-contaminated filtered signal and the exact signal, the exponential filter does not thoroughly remove the noise in the acceleration, which along with the shift in the temporal mean, still contributes to significant long-period errors in the displacement.

In the above, the noise filters are signal-dependent. Thus, the improvement in the correction effectiveness of the filter is in direct relation to the signal-to-noise ratio of the signal. For small events, in which the signal-to-noise ratio is relatively small, the noise filters have just shown to be useful in significantly decreasing the noise-induced errors. However, when large events are tested with the noise filters, the correction effectiveness of the processing procedure shows very little improvement.

This is expected for large events, since in this case the processing and digitization errors have a minimal effect on the time histories, and the transfer function of the noise filter is approximately unity. For instance, the measures-of-error J for the unfiltered large event simulation *Q11CNL* contaminated with noise are two orders of magnitude smaller than the values listed for the unfiltered signal *Q11CNS* in Table 4.2.1. Hence, there is very little room for improvement.

In the next section, a different and complementary approach to filtering is investigated. It will be shown to correct the long-period drifts in the time histories without affecting the harmonics that have a reasonable signal-to-noise ratio. If such an approach is adopted, then the noise filters presented in this section would only be useful in correcting the high-frequency errors which are prevalent mainly in the acceleration time histories. The high-frequency errors induced by digitization and processing are mostly of concern for small seismic events, and are not greatly reduced by the noise filters for large seismic events. Under such conditions, the noise filters described in this section are not part of the standard probabilistic frequency-domain processing method, but they could be implemented as an option if desired.

4.3 Spectral Substitution Method

4.3.1 Motivation and Methodology

It has been shown that the unknown offset in the acceleration, because of missing initial and final data points or baseline drift, together with digitization errors, is the largest source of long-period error in the velocity and displacement signals. In the frequency domain, this appears as unusually high values of the signal spectra at low frequencies. Indeed, the low-frequency error due to the unknown acceleration offset is expected to behave as the spectrum of the integrated boxcar function, centered at *d.c.*, as explained in Sec. 3.3. Also, the signal is particularly affected by the digitization noise at high frequencies, where the amplitude is small. The signal-to-noise ratio remains good in the intermediate frequency range, as has been shown in the previous section, so spectral correction is only necessary at low and high frequencies.

Standard earthquake accelerogram filtering and processing methods in use to date deal with the error-contaminated regions of the spectra by simply removing them. However, spectral models have been developed from extensive studies performed on earthquake ground and structural response, and this information could be used to process accelerograms. The following correction method proposes to optimize models of source and structural spectra in the reliable frequency range of the signal, in order to extrapolate estimates for the regions where noise and error prevail. In other words, the upper and lower frequency bands where the recorded data proves to be unreliable are reconstructed according to the optimized model.

Using an output-error approach [Beck, 1989] the model amplitude spectrum, $\left|\ddot{B}(\omega, \underline{\theta})\right|$, as a function of the parameters $\underline{\theta}$, is fitted to the instrument-corrected amplitude spectrum of the measured data $\left|\ddot{Z}(\omega)\right|$ where ω ranges over the discrete FFT frequencies. One approach would be to make the assumption that the uncertain error γ_n in the model spectrum is additive and is described by a Gaussian distribution, that is:

$$\left|\ddot{Z}(\omega_n)\right| = \left|\ddot{B}(\omega_n, \underline{\theta})\right| + \gamma_n \,, \tag{4.3.1}$$

for each FFT frequency ω_n. One problem with this approach is that the right-hand side has a nonzero probability of becoming negative, but the left-hand side is always nonnegative. However, ignoring this difficulty for the moment, then according to a Bayesian probability approach [Beck, 1989], the most probable set of variables $\hat{\underline{\theta}}$ is the one that optimizes the output-error function:

$$J(\underline{\theta}) = \frac{1}{N} \sum_{n=1}^{N} \left[\left|\ddot{Z}(\omega_n)\right| - \left|\ddot{B}(\omega_n, \underline{\theta})\right| \right]^2 . \tag{4.3.2}$$

Testing of this procedure on real earthquake records proved that these assumptions led to convergence problems and poor fits of the model to the data. These problems mainly occured because such a formulation produces shallow valleys for the error function within which nonlinear optimization schemes cannot easily converge. Thus, the additive-error assumption suffers from several problems and is not a good approach to use.

Another approach is to assume that the uncertain output error is multiplicative and is described by a Log-Normal distribution, i.e., the logarithm of the error has a

Gaussian distribution with zero mean and variance σ^2, say. Thus the output-error equation is given by:

$$\text{Log}\left|\ddot{Z}(\omega_n)\right| = \text{Log}\left|\ddot{B}(\omega_n, \underline{\theta})\right| + \epsilon_n \ , \tag{4.3.3}$$

where ϵ_n is the logarithm of the uncertain multiplicative error at frequency ω_n, and the logarithm to base e is used. The most probable set of variables $\underline{\hat{\theta}}$ is now the one that minimizes the following output-error function:

$$JL(\underline{\theta}) = \frac{1}{N}\sum_{n=1}^{N}\left[\text{Log}\left|\ddot{Z}(\omega_n)\right| - \text{Log}\left|\ddot{B}(\omega_n, \underline{\theta})\right|\right]^2 . \tag{4.3.4}$$

This approach does not suffer from the problems arising when using an additive error. Indeed, it is observed to converge fast and to give model spectra which are good fits to the data.

The value $JL(\underline{\hat{\theta}})$ can be shown to be the most probable estimate of the variance $\hat{\sigma}^2$ of the uncertain output error ϵ_n defined in Eq. 4.3.3 [Beck, 1989]. If $\hat{\epsilon}_n$ is defined as the departure of the recorded spectrum from its most probable value at each frequency ω_n based on the spectral model:

$$\hat{\epsilon}_n = \text{Log}\left|\ddot{Z}(\omega_n)\right| - \text{Log}\left|\ddot{B}(\omega_n, \underline{\hat{\theta}})\right| \ , \tag{4.3.5}$$

then comparison of $\hat{\epsilon}_n$ to $\hat{\sigma} = \sqrt{JL(\underline{\hat{\theta}})}$ provides a measure of the reliability of the data at frequency ω_n. For instance, according to the error distribution, there is a 84.1% probability that the logarithm of the data amplitude spectrum will not exceed $\hat{\sigma}$ about the most probable value of the logarithm of the model spectrum. Hence, if $\hat{\epsilon}_n$ is greater than $\hat{\sigma}$, then it is very likely that the measured $\left|\ddot{Z}(\omega_n)\right|$ is being controlled by noise. At that frequency, the amplitude of the measured data, $\left|\ddot{Z}(\omega_n)\right|$, could be replaced by the most probable value of the amplitude, $\left|\ddot{B}(\omega_n, \underline{\hat{\theta}})\right|$, obtained from the optimization. Since the model does not provide an estimate of the true phases at the noise-contaminated harmonics, only the amplitudes are substituted at the noise-controlled frequencies while the phases are kept at their original values.

Through this approach, it is no longer necessary to guess which harmonics must be discarded because of a small signal-to-noise ratio. The proposed statistical methodology provides both a measure for the reliability of the recorded data spectrum as well as a most probable estimate for the amplitude of the spectrum at each harmonic which is dominated by noise.

The purpose of this correction method is mainly to obtain a better estimate of the spectral shape near *d.c.* and above the natural frequency of the instrument, which are the regions where recording and digitizing noise are dominant. The models used for the optimization are defined accordingly, as explained in more detail in the following sections. Within the intermediate frequency band, typically between about 1 Hz and 25 Hz, it is assumed that the effect of digitizing and processing noise are minimal. Although in the intermediate frequency range the model provides a description of the spectral shape which is good on the average, it cannot reproduce the contributions from phenomena other than the source mechanism at low frequencies and the decay rate at high frequencies, since only the variables that adequately describe the high and low frequency behavior of the spectra are used to perform the optimizations. Thus, it is suggested that no corrections be made in the intermediate range up to the instrument's natural frequency, and so only the harmonics at the two extreme regions of the spectra are altered following the methodology described above.

The low frequency cut-off is selected as the first data point for which the magnitude of the difference between the measured and the most probable model spectrum is less than one standard deviation, as given by Eq. 4.3.5. Testing of this procedure on recorded accelerograms demonstrated that the cut-off frequency is usually below 0.06 Hz. Other criteria for the low frequency cut-off levels can be chosen, if desired, such as two or three standard deviations. However, it must be taken into account that the value given for the variance after minimization is relatively high since the fit of the spectral model in the intermediate frequency range between 1 Hz and 20 Hz is only approximate. The variance, which is described by parameter $\hat{\sigma}$, will decrease as the model becomes a closer representation of the measured spectrum throughout the whole frequency range. This, however, implies that the spectral

model needs to be described by more variables. Although such a model could easily be implemented, the extra variables would mainly affect the fit within the intermediate frequency band without providing significantly better estimates for the upper and lower ranges. It would also unnecessarily make the convergence to the minimum more difficult, and significantly increase the computing time. Identification of these extra parameters remains outside the scope of this study.

The nonlinear minimization scheme utilized is a combination of the steepest descent method and Newton's method [Gill *et al.*, 1981]. The first method exhibits fast convergence to the neighborhood of the minimum, but the second method provides a better convergence rate once the neighborhood of the minimum is found. In the minimization algorithm, the two methods are alternatively used until the minimum is reached. The user must provide initial estimates for the variables which should be in the region of the global minimum to ensure proper convergence.

Testing using the recorded accelerograms showed that the convergence rate also improved as the model provided a better description throughout the whole spectrum, and as less of the noise-corrupted data at the extremes of the spectrum were used in Eq. 4.3.4. Thus, to improve the convergence rate and the spectral fit, several models are proposed depending on the nature of the recorded motions. Also, from the conclusions reached in Sec. 3.3, the following rule of thumb is used to select the bandwidth within which the minimization is performed, and where the signal-to-noise ratio is thought to be relatively large. If the accelerogram has been digitized up to T_0 sec, then the portion of the measured data used for minimization is selected between the next harmonic after frequency T_0^{-1} Hz up to the instrument's natural frequency. This choice of the bandwidth for the minimization is based on the fact that the largest long-period error is due to the unknown shift in the acceleration. As has been studied in Sec. 3.3, after processing and double integration of the acceleration, this error shows up the most at T_0^{-1} Hz. Although many zeroes are often required to be padded onto the digitized accelerogram to use the FFT algorithm, which artificially increases the length of the record, the extra information it provides for the first harmonic of the spectrum is not reliable. Hence, the proper

record length T_0 to consider is the one corresponding to the number of digitized points, and not the one obtained after zeroes have been padded.

If not enough points are digitized from the accelerogram, then there is not a sufficient spectral resolution at low frequencies for the minimization scheme to converge properly. To allow proper convergence of the correction scheme, it is imperative to digitize the accelerogram up to the time of the instrument's automatic shut-off. This also provides smaller estimates for the standard deviation of the time histories, as described in Ch. 3.

4.3.2 Spectral Models

As for any model optimization problem, the results are strongly dependent on how well the data is represented by the model. In the case of strong-motion earthquake accelerogram spectra, the problem of defining a proper model is a complex one. Many seismologists have tackled this problem [Brune, 1970; Hanks, 1982; Papageorgiou, 1988]. All agree that the recorded strong-motion displacement amplitude spectra $B(f)$, which mainly reflects the body wave behavior, can be described by the following decomposition [Joyner&Boore, 1988]:

$$B(f) = C\,S(f)\,A(f)\,D(f)\,. \tag{4.3.6}$$

C is a scaling constant which depends on the radiation pattern, the free surface effects, the geometric spreading, and the medium density and shear velocity. $S(f)$ is the source spectrum. Its effect typically dominates the low-frequency portion of the accelerogram below 1 Hz, and is given for far-field body waves by Brune [1970] to be

$$S(f) = \frac{M_0}{\left[1 + \left(\frac{f}{f_0}\right)^2\right]}\,, \tag{4.3.7}$$

where M_0 is the seismic moment, and f_0 is the corner frequency which can be defined as a function of the body wave velocity, the stress drop along the fault and the seismic moment. Alternatively, f_0 can be infered from information on the fault dimensions. Other expressions for $S(f)$ have been proposed [Papageorgiou & Aki, 1983; Joyner & Boore, 1988], but these are more complex and require more

parameters. It will be shown for "far-field" records that Eq. 4.3.7. provides an adequate representation of the low-frequency behavior of the spectrum with a minimum number of parameters, and that a more complicated model is not necessary for accelerogram correction purposes. However a correction should be made for "near-field" records as described later. $A(f)$ is the amplification factor, it describes the frequency-dependent wave propagation effects as a function of the surrounding medium properties both at the source and at the recording site. The main contribution of $A(f)$ in the accelerogram spectrum is to provide a better description of the motions at intermediate frequencies, typically within the 1 Hz to 15 Hz range. Since the recorded motions in that frequency band are fairly accurate because of the high signal-to-noise ratio, no model corrections are necessary and so expressions for $A(f)$ will not be incorporated in the equation for the model.

$D(f)$ is called the diminution factor. It describes the frequency-dependent attenuation as a function of the hypocentral distance. There is still debate as to what a proper form for $D(f)$ should be [Papageorgiou, 1988; Hanks, 1982], especially regarding the high-frequency decay rate beyond 25 Hz, but it is generally given as a function of the "material" attenuation $Q(f)$, the hypocentral distance r, the S-wave propagation velocity β, and the frequency f_H at which the spectrum sharply decreases [Hanks, 1982; Joyner & Boore, 1988]. Anderson and Hough [1984] suggested an expression of the form:

$$D(f) = \exp\left[-\frac{\pi f r}{Q(f)\beta}\right] \cdot \exp\left[-\frac{f}{f_H}\right] . \tag{4.3.8}$$

According to this last equation, the high-frequency decay can be separated into two exponential terms. The first one is a function of distance, and $Q(f)$ is often taken as a constant. The second one is a function of frequency f_H which controls the high-frequency decay. An instrument-correction term is often added to Eq. 4.3.6. However, since the model spectrum is fitted to the instrument-corrected amplitude spectrum of the measured data such a term is not necessary in this case.

From the above discussion, the model for the acceleration amplitude spectrum of strong ground motions can be simplified to the following expression:

$$\ddot{B}(\omega) = \frac{D_0 \omega_0^2 \omega^2}{\left[\omega_0^2 + \omega^2\right]} \cdot R(\omega) \cdot \exp\left[-\frac{\omega}{\omega_H}\right] . \tag{4.3.9}$$

According to Eq. 4.3.6 and 4.3.7, the constant D_0 incorporates into a single parameter the seismic moment, the stress drop, the radiation pattern, the medium density and shear velocity in the region of the source, as well as local site amplifications to some degree. The expression for $R(\omega)$, which does not involve parameters, depends on whether the record to be processed is obtained in the near-field or in the far-field, as will be discussed in the following sections. Thus, the optimization of the model spectrum for ground acceleration correction can be reduced to the identification of only 3 variables: D_0, the *d.c.* value of the displacement spectrum, ω_0, the corner frequency and ω_H, a high-frequency decay parameter.

So far only ground motions have been discussed, however accelerograms are also obtained for structural motions. The same approach can be applied to correct structural records, and Eq. 4.3.9 can be used to define an appropriate model spectrum for structural response, as will be discussed in Sec. 4.3.2.3.

4.3.2.1 Far-field Ground Motions

Far-field ground motions (i.e., those that are far enough away from the fault that there is no permanent displacement from tectonic deformation produced by the earthquake) are the most common type of accelerogram records obtained during seismic events. It is known that unless there are substantial local site effects which produce permanent displacements, such as soil liquefaction or subsidence, the recorded spectrum should on the average behave as described schematically by Fig. 4.3.1. The acceleration amplitude spectrum increases as ω^2 up to the corner frequency ω_0, where it levels off until it reaches ω_H and starts decaying exponentially. Equivalently, the corresponding displacement spectrum is flat and equal to constant D_0 until it reaches the corner frequency ω_0. Such a model is described by Eq. 4.3.9 provided that the distance function R is set to unity. Hence, the acceleration amplitude spectrum model for far-field ground motions is defined to be:

$$\ddot{B}(\omega) = \frac{D_0 \omega_0^2 \omega^2}{[\omega_0^2 + \omega^2]} \cdot \exp\left[-\frac{\omega}{\omega_H}\right] . \tag{4.3.10}$$

The spectral model defined in Eq. 4.3.10 is optimized for the set of variables:

$$\underline{\theta} = (D_0, \omega_0, \omega_H) . \tag{4.3.11}$$

Eq. 4.3.10 implies that the temporal mean of the complete acceleration and velocity histories is zero, since the *d.c.* of the acceleration and velocity amplitude spectra of the model are zero. Also, D_0 represents the *d.c.* value of the displacement, and can be related to the temporal mean of the complete displacement time history of the event. Since the temporal mean in the velocity is zero, and the displacement time history starts at zero in theory, the far-field spectral model given in Eq. 4.3.10 implies that the final value of the complete displacement time history is zero. This is the behavior which is theoretically expected. However, in practice the recorded time histories are not complete, because of missing data at the beginning and at the end. Thus, certain corrections are necessary to obtain the far-field records (Secs. 3.3 and 4.3.3).

4.3.2.2 Near-field Ground Motions

In the near-field, the displacement time history is expected to have a nonzero final offset, thus implying that the velocity has a nonzero temporal mean. In fact, it is easy to show that the value of the final displacement is equal to the product of the duration and the temporal mean of the velocity, under the assumption that the initial displacement is zero. In the frequency domain, there will be a finite nonzero value for the *d.c.* component of the velocity spectrum, but an infinite value for the *d.c.* component of the displacement spectrum. Eq 4.3.9 can be used in the near-field by taking:

$$R(\omega) = \frac{1}{\omega} \,. \tag{4.3.12}$$

Hence, the model for the acceleration amplitude spectrum of near-field ground motions is defined by:

$$\ddot{B}(\omega) = \frac{D_0 \omega_0^2 \omega}{\left[\omega_0^2 + \omega^2\right]} \cdot \exp\left[-\frac{\omega}{\omega_H}\right] \,, \tag{4.3.13}$$

where the set of variables $\underline{\theta}$ used for the optimization of the model is the same as that defined for the far-field case in Eq. 4.3.11. For all the altered harmonics, the amplitude is given by the optimized spectral model, but no correction is performed on the value of the corresponding phase. The estimated value of D_0 gives the amplitude of the spectral component of the complete velocity history at *d.c.*, which

also turns out to be the value of the absolute final displacement offset. However, this does not provide information for the sign of the *d.c.*, and it is important to know whether the *d.c.* value of the velocity is $+D_0$ or $-D_0$, or, equivalently, if the final displacement offset is $+D_0$ or $-D_0$ respectively. Such information can be obtained , for example, from geomorphological studies of the fault's rupture pattern. For instance, along a strike-slip fault it should be easy to determine which of the records in the direction of the fault's strike should have a positive or negative final displacement.

The near-field ground spectrum described by Eq. 4.3.13 is consistent with the theory of crack propagation and stress relaxation along a finite length fault, for which the final dislocation is related to the fault geometry and the stress drop [Aki & Richards, 1980]. Theoretical derivation of the problem also demonstrates that the far-field motions are obtained by differentiation of the near-field equations, which is the reason for the choice of $R(\omega)$ in Eq. 4.3.12.

4.3.2.3 Structural Response Motions

The measured structural data $\ddot{x}_j(t)$, as recorded on strong-motion accelerograms, represents the absolute acceleration of the structure at location j. It can be decomposed as the sum of the input ground acceleration $\ddot{z}(t)$, and the relative acceleration of the structure at that location $\ddot{y}_j(t)$, under the assumption of planar motion:

$$\ddot{x}_j(t) = \ddot{z}(t) + \ddot{y}_j(t) \ . \tag{4.3.14}$$

The relative acceleration of the structure, modelled as a linear multi-degree-of-freedom oscillator, can itself be decomposed into a linear combination of the modal accelerations $\ddot{\gamma}_r(t)$ over all contributing modes r, and where $\ddot{\gamma}_r(t)$ is subject to the equation of motion of the r^{th} mode:

$$\ddot{\gamma}_r(t) + 2\zeta_r\omega_r\dot{\gamma}_r(t) + \omega_r^2\gamma_r(t) = -\alpha_r\ddot{z}(t) \ , \tag{4.3.15}$$

ζ_r is the modal damping, ω_r is the modal frequency and α_r is the modal participation factor.

In the frequency domain, Eq. 4.3.15 is equivalent to:

$$\ddot{\Gamma}_r(\omega) = \frac{\alpha_r \omega^2 \ddot{Z}(\omega)}{\left[(\omega_r^2 - \omega^2) + 2i\zeta_r\omega_r\omega\right]} \,. \tag{4.3.16}$$

The relative response at the location j is given by:

$$\ddot{Y}_j(\omega) = \sum_{r=1}^{N} \ddot{\Gamma}_r(\omega)\phi_{rj} \,, \tag{4.3.17}$$

where N is the number of modes contributing substantially to $\ddot{y}_j$, and ϕ_{rj} is the mode shape component of the r^{th} mode at the location j.

Combining Eqs. 4.3.14, 4.3.16, and 4.3.17, the absolute response of the structure in the frequency domain, at any location j, is given by:

$$\ddot{X}_j(\omega) = \left[1 + \sum_{r=1}^{N} \frac{\alpha_r \phi_{rj} \omega^2}{(\omega_r^2 - \omega^2) + 2i\zeta_r\omega_r\omega}\right] \cdot \ddot{Z}(\omega) \,. \tag{4.3.18}$$

Thus the absolute acceleration of the structure at location j can be expressed by the product of the ground motion spectrum, as defined in either Secs. 4.3.2.1 for the far-field, or 4.3.2.2 for the near-field, and a structural response term as a function of the modal properties of the structure.

The purpose of this derivation is to find an appropriate model to fit to the measured structural data in order to replace the noise-contaminated portions of the spectrum near *d.c.* and at high frequencies by their most probable values. As was the case for the models proposed for the ground-motion spectra, it is not of concern to model exactly the intermediate-frequency range of the spectrum. The dominant structural response term in Eq. 4.3.18 is usually the absolute acceleration contribution of the first mode. Under the assumption that

$$\sum_{r=1}^{N} \alpha_r \phi_{rj} \simeq 1 \,,$$

the equation for the spectral model of the absolute acceleration of the structure could be simplified to:

$$\left|\ddot{X}_j(\omega)\right| \simeq \left|\ddot{Z}(\omega)\right| \cdot \left|\alpha_1\phi_{1j}\right| \cdot \frac{\left[\omega_1^4 + (2\zeta\omega_1\omega)^2\right]^{1/2}}{\left[(\omega_1^2 - \omega^2)^2 + (2\zeta\omega_1\omega)^2\right]^{1/2}} \,. \tag{4.3.19}$$

The model of Eq. 4.3.19 assumes that the building responds in its first mode only, and does not allow higher mode contributions. By incorporating the variable $\alpha_1\phi_{1j}$ into the variable D_0 describing the behavior of the ground spectrum at *d.c.* (Eq. 4.3.10 or 4.3.13), the model as defined in 4.3.19 can be described by the following five variables forming the set $\underline{\theta}$:

$$\underline{\theta} = (D_0, \omega_0, \omega_H, \omega_1, 2\zeta\omega_1) \; . \tag{4.3.20}$$

The minimization scheme displayed serious convergence problems when it was tested on recorded structural data using Eq. 4.3.19 as the model and Eq. 4.3.20 as the set of variables. The principal problem was that it could not converge on a proper value for the high-frequency decay variable as defined by ω_H. Hence, the ω_H term is unnecessary for structural records. Furthermore, the model described by Eq. 4.3.19 only includes the first mode effects. Hence, the decay due to higher-frequency modes is impossible to observe correctly, which may partly explain the observed convergence problems for the structural damping term $2\zeta\omega_1$. Also, this variable representing the first mode damping effects, appears both in the numerator and denominator of Eq. 4.3.19. Hence, the model may not be flexible enough to allow for contributions from other modes, especially regarding the high-frequency decay as mentioned above. In view of these comments, an alternate expression for the far-field structural spectrum is proposed:

$$\left|\ddot{X}_j(\omega)\right| = \frac{D_0\omega_0^2\omega^2}{(\omega_0^2+\omega^2)} \cdot \frac{\omega_1^2 + c\omega}{(\omega_1-\omega)^2 + d\omega} \; , \tag{4.3.21}$$

with corresponding set of variables:

$$\underline{\theta} = (D_0, \omega_0, \omega_1, c, d) \; . \tag{4.3.22}$$

Eq. 4.3.21 does not include the exponential ω_H decay term, and allows more flexibility in identifying the decay behavior due to structural damping. The variables c and d do not represent any particular physical quantity, other than maybe a general description of the damping and of the higher mode effects. At low frequencies, where the spectral substitution is implemented, the absolute displacement of the

structure is governed by the ground motion, as expected. A trial-and-error approach was used to obtain this equation for the structural model. It was found to provide the best convergence and fit when tested on strong-motion records obtained at different buildings.

Eq. 4.3.21 is valid for far-field structural motions, but it can be adjusted for near-field records by dividing by ω (Eq. 4.3.12). Although in practice it is rare to find instrumented structures built very near a significant fault, the ω^{-1} correction term might still be necessary to observe nonzero final ground displacements. However, Eq. 4.3.21 may not be appropriate to observe in-structure permanent offsets.

4.3.3 Processing Procedure

The processing procedure for the spectral substitution method is very similar to that described for the frequency-domain approach presented in Sec. 3.3.1. Typically, for analog accelerograms, the uncorrected digitized accelerogram is linearly interpolated to Δt =0.01 sec. For digital records, Δt may be even smaller. The temporal mean of the N digitized points is forced to zero. The data is then padded with zeroes at the end, so that there is the necessary number of points, NT, to perform the Fourier transform with the FFT algorithm. The data is then instrument-corrected in the frequency domain. The appropriate spectral model (Eq. 4.3.10, 4.3.13 or 4.3.21) is then fitted to the logarithm of the acceleration spectrum of the measured data.

In the cases where judgement is not sufficient to determine which of the near-field or far-field spectral models is appropriate, the answer is usually given by the minimization algorithm itself. Indeed, application to recorded ground motion accelerograms has shown that the minimization algorithm does not converge when the spectral model is not proper. The goodness-of-fit and the speed of convergence are also a measure of how well the spectral model represents the measured data. Once the minimization is performed and a most probable model is found, the error between the logarithm of the measured data spectrum and the logarithm of the model spectrum is then computed according to Eq. 4.3.5. The last low-frequency point whose error is more than the one standard deviation defined by $\pm\hat{\sigma}$ (from Eq. 4.3.4

with the optimal parameter $\hat{\underline{\theta}}$), is selected as the cut-off for the low-frequency correction. All points of the spectrum below, and including the cut-off frequency, are substituted by the amplitudes provided by the optimized spectrum, but the phases are not changed. The high-frequency cut-off is less critical since it mainly affects the acceleration time histories for which the signal-to-noise ratio is usually high. Thus, this cut-off can be set to any reasonable value, but could also be selected according to the same criteria as for the low-frequency cut-off. The amplitudes above the high-frequency cut-off are then substituted by the optimized values of the model, and the phases are kept unchanged. All points of the accelerogram spectrum from, but not including, the low-frequency cut-off up to the high-frequency cut-off are not altered. This spectral correction produces accelerograms which are consistent with the physics of the underlying motions and for which changes have been made only in those parts of the spectrum where truncation error and noise are dominant.

The most probable acceleration time history $\ddot{z}_{0n}$ with zero temporal mean is obtained by inverting the corrected Fourier spectrum. The acceleration spectrum is also divided by $i\omega$ and $-\omega^2$ to obtain the velocity and displacement spectra, except for their *d.c.* values which are set to zero. The procedure to obtain the velocity and the displacement time histories are slightly different depending on the nature of the record, as described in Ch. 3, and illustrated in Fig. 3.20. Implementation of the spectral substitution method changes the processing procedure in the following way.

In Eq. 4.3.10, for far-field records, the variable D_0 represents the *d.c.* value of the complete displacement. D_0 does not affect the *d.c.* of the velocity or the acceleration, although it controls the substituted amplitude of the spectra at the corrected frequencies. Hence, the spectral substitution method has changed the inverse Fourier transforms of the signals $\ddot{z}_n$, v_n and d_n (Fig. 3.20), but the most probable acceleration and velocity time histories in the far-field remain those that have zero temporal mean and are defined by $\ddot{z}_{0n}$ and $\dot{z}_{0n}$.

In theory, the identification of the *d.c.* of the signal could be used to set the temporal mean of the displacement time history to its most probable value, and to correct the errors in the displacement induced by the uncertain initial velocity

or the uncertain temporal mean of the truncated velocity time history. However, this requires that the earthquake be recorded and digitized in most of its entirety. Because in practice many data points are missing at the beginning or at the end of the record, it is impossible to estimate the temporal mean of the truncated displacement time history. Thus, for far-field records, it is still more accurate to impose a zero initial value for the displacement than it is to impose a *d.c.* value of D_0. Although the estimated parameter D_0 is of no help in resetting the proper temporal mean of the truncated displacement time histories in the far-field, it is instrumental in defining the amplitudes of the low frequency harmonics that need to be substituted (Eqs. 4.3.10 and 4.3.21). The most probable displacement time history for far-field records corrected with the spectral substitution method is defined by z_{0n} (Fig. 3.20), and it has zero initial and final value (since it corresponds to the zero velocity temporal mean condition).

As was mentioned in Sec. 3.3, imposing a zero temporal mean velocity condition on a severely truncated record, may create unrealistic shifts in the initial portion of the velocity time history. In such cases, it may be advisable to produce the most probable velocity time history on the basis of a zero initial velocity condition $\dot{z}_n$, since it is a more realistic assumption. The corresponding displacement is then z_n as defined in Fig. 3.20, but it usually exhibits large and unrealistic drifts. However, instances where $\dot{z}_n$ and z_n were more appropriate rarely occurred when the spectral substitution method was tested on analog records, as will be seen in the next section.

In summary, for records where no final displacements are expected (i.e., far-field or undamaged structure) the most probable set of time histories from the spectral substitution method are given by $\ddot{z}_{0n}$, the acceleration with zero temporal mean, $\dot{z}_{0n}$ the velocity with zero temporal mean, and z_{0n} the displacement with zero initial condition obtained from $\dot{z}_{0n}$. For far-field records processed with the spectral substitution method, the equations presented in Fig. 3.20 still apply.

In the near-field, the *d.c.* corresponding to the complete velocity time history is theoretically given by the estimated value of the variable D_0 in Eq. 4.3.13. Altering the *d.c.* of the velocity does not alter the acceleration time history in any way. Hence, the most probable acceleration time history for near-field records remains

the one with zero temporal mean $\ddot{z}_{0n}$, as in the far-field case, but now $\dot{Z}(0) = D_0$ (Fig. 3.20).

Inversion of the velocity spectrum with a *d.c.* value D_0 produces the velocity time history $\dot{z}_{0n}$. However, as for the far-field case, D_0 which is the *d.c.* corresponding to the complete velocity time history, may induce shifts in the initial portion of the truncated velocity time history which are not compatible with seismic motions. In this case, it may be preferable to use the velocity time history with zero initial value $\dot{z}_n$, as defined in Fig 3.20, although application of the spectral substitution method to analog accelerograms obtained in the near-field has not found this to be necessary so far.

In the previous section, it was shown that for near-field records D_0 represented both the *d.c.* of the velocity spectrum, and the final value of the complete displacement time history. Fault motions are expected to approach the final displacement offset value soon after the onset of the rupture, and hence D_0 should be a good approximation of the final displacement even for near-field records which suffered significant end truncation. In the near-field, the most probable value of the initial displacement is still assumed to be zero. To account for the D_0 *d.c.* value of the velocity, a linear correction term must be added to the displacement time history d_n, which is obtained after spectral substitution for $Z(0) = 0$ and produced after Fourier inversion (Fig. 3.20):

$$z_{0n} = d_n - d_0 + \frac{D_0}{NT} n \,, \qquad n = 1, \ldots, N \tag{4.3.23}$$

Hence, for near-field records processed with the spectral substitution method, the definition of the time history z_{0n} differs from the one given in Fig. 3.20.

As was the case for far-field records, a near-field displacement signal z_n could be obtained to correspond to the zero initial velocity condition, in instances where imposing a D_0 *d.c* in the velocity creates unrealistic large shifts in the initial portion of the severly truncated velocity time history. However, as will be seen in the next section, such cases seldomly seem to occur when the spectral substitution method is used. Also, the displacement time histories z_n, corresponding to the zero initial velocity condition, both in the far-field and the near-field, usually display large drifts

which are unrealistic. Hence, there is a trade-off between the two assumptions, and employing the zero temporal mean velocity in the far-field, or D_0 temporal mean velocity in the near-field, instead of zero initial velocity, remains the better option.

To summarize, the set of records which should best describe the event in the near-field for which final displacement offsets are expected, is given by $\ddot{z}_{0n}$, the acceleration time history with zero temporal mean; $\dot{z}_{0n}$, the velocity time history with *d.c.* value D_0, and z_{0n}, the displacement time history with zero initial value corresponding to a value D_0 for the *d.c.* of the velocity. When processing near-field records with the spectral substitution method, the flowchart of the algorithm in Fig. 3.20 must be modified such that $\dot{Z}(0) = D_0$, and z_{0n} is given by Eq. 4.3.23.

4.3.4 Application to Ground Motion Records: 1979 Imperial Valley Earthquake

The synthetic accelerogram formulation presented in Sec. 2.2 cannot be used to test the performance of the spectral substitution method described in Secs. 4.3.1 and 4.3.2, since the synthetic record formulation does not explicitly behave according to Brune's spectrum at low frequencies, and does not have an exponential decay for high frequencies. Hence, the minimization algorithm would probably not converge when applied to the synthetic records.

However, accelerogram correction using the spectral substitution method has been tested on a large number of records obtained from a strong-motion array triggered by the Imperial Valley earthquake of October 15, 1979 ($M_L = 6.6$). Both the Imperial fault and the Brawley fault ruptured during this event. The Imperial fault is a strike-slip fault which ruptured over a 30.5 km length with right lateral motions. Geological surveys performed just after the event reported maximum surface offsets across the fault of about 60 cm at a distance of 5 to 10 km north-west of the epicenter [Sharp *et al.*, 1982]. The amount of displacement offset decreased moving north-west along the fault. In the vicinity where the strong-motion array crosses the Imperial fault, right lateral offsets of the order of 30 cm were reported (Fig. 4.3.2.). The Brawley fault runs north-south and is located to the north-east of the Imperial fault. The Brawley fault is primarily a normal fault, which ruptured over a 13 km extent during the event, with downward surface offsets of up to 17 cm

west of the fault. In the vicinity where the Brawley fault intersects with the Imperial fault, the survey also reports a number of surface breaks along secondary faults with both normal and right or left lateral strike-slip features.

The crustal structure of the Imperial valley was extensively studied by Fuis *et al.* [1982]. They reported a sedimentary layer of depth 4 km to 5 km; the linear P wave velocity gradient increases from approximately 2 km/sec at the surface, to 5 km/sec at the bottom of the sedimentary layer. Hartzell and Helmberger [1982] inferred an S-wave velocity gradient which increases from 1 km/sec at the surface up to 3 km/sec at the bottom of the layer. Using a shear beam model, under the simplifying assumptions that the velocity structure of the sedimentary layer, of average depth 4.5 km, is constant, with average S-wave velocity 2 km/sec, and that the lateral boundary effects can be neglected, the predominant period of the valley excited by the vertically incident SH-waves is approximately 9 sec (it could be greater because of the softer surface layer). Similarly, that due to the P-waves is approximately 5 sec, based on an average velocity of 3.5 km/sec.

Thirteen analog strong motion instruments, operated by the U.S. Geological Survey, are installed symmetrically across the Imperial fault in an array perpendicular to the its direction (Fig. 4.3.2). The triaxial instruments are SMA-1T's; they record the strong motions in three directions (clockwise from the north): 140^o, which is parallel to the strike, up, and 230^o, which is perpendicular to the strike. Because the Imperial fault has a strike-slip rupture mechanism, the records obtained for the 230^o component (i.e., perpendicular to the fault) should be dominated by SH wave motions, whereas the vertical and the 140^o components should be dominated by the P and SV wave motions [Hartzell and Helmberger, 1982]. The array is located approximately 27 km away from the epicenter, and in the vicinity of the intersection between the Imperial and the Brawley faults, as shown in Fig. 4.3.2 [Brady *et al.*, 1980; Porcella *et al.*, 1979]. Because of the close proximity of each of the instruments in the array, neighboring records can be corrected with the spectral substitution method and compared to verify the consistency of the results. Records have also been obtained near the epicenter and along the fault line. These provide an excellent opportunity to test whether the near-field model of the spectral

substitution method can provide an adequate static and dynamic description of the event and if it can approximately predict final offsets in the displacement time history. The intent of this section is to test the processing method and to prove that it yields physically plausible results. It is not the purpose here to provide an in-depth analysis and description of the static and dynamic behavior of the Imperial Valley earthquake of October 15, 1979, although such an analysis using the records processed with the spectral substitution method would be a useful follow-up study.

A selection of far-field and near-field records from the Imperial Valley strong motion array that have been processed with the spectral substitution method is now presented.

4.3.4.1 Far-field Records: Stations 2 and 3

Records in all three directions at Station 2 (Keystone Rd.) and Station 3 (Pine Union School) are processed according to the procedure for far-field records described in Sec. 4.3.3 and the results are shown for comparison. These two stations are less than 3 km away from each other. In particular, this analysis will show that the ground motion time histories from both stations in the same direction exhibit similar features suggesting that the spectral substitution method is capable of producing consistent results for the time histories. Stations 2 and 3 are located respectively at a distance of 16 km and 13 km away from the fault and about 30 km from the epicenter. These stations can be considered to be located in the far-field, so Eq. 4.3.10 is used as the model for the earthquake spectrum.

The 230^o component of Station 2 was only digitized up to 39.63 sec, although the motions have not significantly decayed by that time (Fig. 4.3.4). This comment also applies to all subsequent records discussed herein. The data, which is linearly interpolated to intervals of 0.01 sec, is padded with zeroes up to 40.95 sec (i.e., 4096 data points) to have the correct number of points to perform the FFT. The resulting discrete spectrum is provided at frequency intervals of 0.0244 Hz, between *d.c.* and the Nyquist frequency 50 Hz. Spectral optimization using the far-field model (Eq. 4.3.10) converged to the following values for the variables:

$$D_0 = 138.0 \text{ cm.sec} , \quad f_0 = 0.101 \text{ Hz} , \quad f_H = 8.37 \text{ Hz} .$$

Fig. 4.3.3 represents the spectral fit of the optimization model for the 230° component of Station 2. The optimized spectrum is plotted as a dashed line in Fig. 4.3.3(a) and (b) for the acceleration spectrum and the displacement spectrum respectively, using a log-log scale. In these two plots the solid lines represent the spectra of the measured data, and it can be seen that the model fit is relatively good at high and low frequencies, but it is only average within the intermediate frequency range (0.5 Hz-10 Hz). This is expected since, as was mentioned in Sec. 4.3.2, the model spectrum is simplified only to represent the contributions of the high and low-frequency behaviors of the event, and it is not formulated to include effects such as local site conditions that mainly alter the spectrum at intermediate frequencies. In Fig. 4.3.3(c) the solid line represents the most probable error $\hat{\epsilon}_n$ as defined by Eq. 4.3.5, and the dashed lines represent from bottom to top $+1\hat{\sigma}$, $+2\hat{\sigma}$, and $+3\hat{\sigma}$ as given by Eq. 4.3.4, where $\hat{\sigma}$ is the standard deviation about the most probable value of the error between the log-acceleration of the optimized model spectrum and the measured spectrum. Because the logarithm of the acceleration spectrum is used for the minimization, $\hat{\sigma}$ is the same for either the acceleration or displacement fit since the "integration" terms $\log(\omega^2)$ cancel out in Eq. 4.3.4. The error plot of Fig. 4.3.3(c) shows that only the first spectral amplitude, excluding *d.c.*, is above the one standard deviation level. Hence, both *d.c.* and the first harmonic are substituted by the amplitudes of the optimized spectral model. The fit at high frequencies becomes poor above 35 Hz. Thus, for this record the low-frequency cut-off is selected as 0.0244 Hz and the high-frequency cut-off is 35 Hz.

The time histories obtained after using the spectral substitution method on the 230° component of Station 2 for the 4096 point accelerogram are shown in Figs. 4.3.4 through 4.3.7 for substitutions from *d.c.* up to 0.0732 Hz respectively. In these figures, and in all the subsequent ones representing time histories, the top figure, labeled "*acceleration*," represents the most probable corrected acceleration $\ddot{z}_{0n}$. In the middle row, the figure to the left, labeled "*velocity*," represents the velocity time history $\dot{z}_n$ which has zero initial value (Fig. 3.20), and to the right is the velocity time history $\dot{z}_{0n}$, labeled "*zero mean velocity*" or "D_0 *mean velocity*," which has zero temporal mean for far-field records or D_0 velocity *d.c.* for near-field records. In the bottom row are shown the displacement time histories with zero

initial value; the record to the left, z_n, labeled "*displacement*," corresponds to the zero initial velocity condition, and the one to the right, z_{0n}, labeled "*displacement[0 mean vel]*" or "*displacement[D_0 mean vel]*," corresponds to a zero velocity *d.c.* in the far-field (Fig. 3.20) or to a D_0 velocity *d.c.* in the near-field (Eq. 4.3.23). From the arguments presented in the previous section the most probable set of records is shown in the plots on the right of the figures. The other plots to the left of the figures correspond to the zero intial velocity condition, and are provided for comparison.

Fig. 4.3.4 represents the time histories obtained when no spectral substitution is performed. In other words, these are the "uncorrected" time histories. The most probable acceleration $\ddot{z}_{0n}$ does not show any particular problem. However, the most probable velocity $\dot{z}_{0n}$, with zero temporal mean has a large initial value which is unrealistic. Also, the most probable displacement z_{0n}, obtained by removing the temporal mean from the velocity, exhibits a very large long-period error. This parabolic shape is a result of imposing a zero temporal mean in the velocity which forces the displacement with zero initial condition to also end at zero. In this case, it is clear from the velocity time histories that the record has been truncated before the end of the event, although the acceleration time history is quite small. In theory, the temporal mean velocity of the complete record should be zero, but missing data at the beginning and at the end of the record will create a shift in the temporal mean of the acceleration and the velocity. The error in the initial value of the most probable velocity and in the time history of the most probable displacement will become greater as more data is missing from the digitized record. When the zero initial velocity criteria is used, the velocity time history $\dot{z}_n$ behaves more properly in the beginning, but the displacement z_n drifts parabolically with time, as shown on the left-hand plots of Fig. 4.3.4.

According to the error plot shown in Fig. 4.3.3(c), the amplitude of the first harmonic at 0.0244 Hz is unreliable and should be substituted by the corresponding amplitude of the optimized far-field model, shown in Fig. 4.3.3(a) for the acceleration spectrum or Fig. 4.3.3(b) for the displacement spectrum. This is referred to as a "1-point" correction, and the resulting time histories are illustrated in Fig. 4.3.5.

There is little perceptible change in the most probable acceleration $\ddot{z}_{0n}$ between the uncorrected and the 1-point corrected records. Indeed, the values of the peak accelerations are almost identical in both cases. The most probable velocity $\dot{z}_{0n}$ has been shifted down by about 5 cm/sec, but still displays a dominant 8-second period. The greatest change occurs in the most probable displacement z_{0n}, in which the large parabolic error has virtually disappeared after the 1-point substitution. The displacement signal now shows that the valley initially moved with a strong 8-second pulse, and then resonated with a long-period motion.

Although the error plot (Fig. 4.3.3(c)) indicates that only the first point should be substituted, it can be argued that the standard deviation is abnormally high in these records because the simple spectral model used for the optimization is not capable of capturing the complex behavior of the local site effects in the Imperial Valley at the intermediate frequencies. Thus, the large value of the standard deviation in this case is more representative of the poor fit at intermediate frequencies, than it is at low frequencies. Hence, the standard deviation of the digitizing and recording noise alone would be smaller if did not include the model error in the intermediate frequency range. This would imply that more than one point in the data spectrum should be substituted.

The advantage of the spectral correction method is that increasing the value of the cut-off frequency does not completely remove all contributions from the harmonics located below. It only resets the amplitudes of the harmonics below the cut-off frequency to their most probable value as defined by the optimization results. As the substituted amplitude of the measured spectrum becomes closer to the most probable amplitude of the model spectrum, the changes in the resulting time histories due to the correction become smaller. However, since the model spectrum does not properly represent the behavior of the signal at intermediate frequencies, and to avoid introducing processing error into the signal, the cut-off frequency should not be increased beyond the estimated value of the corner frequency f_0, above which the optimal model is less reliable. Thus, increasing the cut-off frequency up to the corner frequency should not alter the predominant low-frequency features of the time histories that conform to the source-spectrum model.

In Fig. 4.3.6, the 230° component of Station 2 is processed with a 2-point substitution for which the cut-off frequency is 0.0488 Hz. This point is located right below the level defining one standard deviation, but because of the arguments presented above, substituting this amplitude may be justified. Again, compared to the uncorrected and the 1-point corrected signals, there is no significant change in the most probable acceleration time history. The most probable velocity with zero temporal mean, $\dot{z}_{0n}$ illustrated on the right of the figure, now starts near zero and is approximately flat over the first 3 sec. This behavior is the one that is normally expected from far-field velocity time histories. Although there is a slight decrease in the maximum velocity time history, the peak-to-peak amplitude remains the same. The displacement time history now shows a dominant 8-second period wave through out the whole record, and the most probable displacement z_{0n} is initially flat and does not drift, as expected in the far-field. The 2-point substitution yields results for the time histories which seem to be the proper representation of the motions at the recording site.

The displacement time history of the 230° component of Station 2 corrected with a 2-point spectral substitution is compared to the displacement time history processed by *USGS* with an improved version of Volume II and which is band-pass filtered between 0.17 Hz and 23 Hz. (Fig. 4.3.7). The peaks of both displacement records are perfectly in phase, and the underlying features are very similar. However, the *USGS* record has a dubious initial behavior, whereas the displacement record obtained with the spectral substitution method is flat as expected. Also, because of the repeated linear trend removal in Volume II, the *USGS* displacement record is evenly balanced about the zero baseline. In comparison, the displacement time history obtained with the 2-point spectral substitution is skewed to one side, which could be physically possible. Finally, because the spectral substitution method does not remove the low frequency components of the records, as does Volume II, longer-period motions are observable in the displacement time history corrected the spectral substitution method, than with the Volume II method.

The same accelerogram is also processed with a 3-point substitution, for which the cut-off frequency is 0.0732 Hz, and the error (Fig. 4.3.3(c)) is close to, but above,

−1 standard deviation. The time histories defining the most probable acceleration, velocity and displacement for the 3-point substitution are almost identical to the 2-point substitution results. In particular, the displacement still features the dominant 8-second period wave. The time histories are still approximately the same when the cut-off is increased up to 0.0976 Hz for the 4-point correction. This could have been expected since for this record the amplitude of the measured data coincides almost exactly with the optimal model at 0.0976 Hz (i.e., the error is almost zero at this frequency (Fig. 4.3.3(c)). However, when the cut-off is increased up to the next increment at 0.1221 Hz, which is beyond the minimized value of the corner frequency ($f_0 = 0.101$ Hz), the corrected time histories show significant changes (Fig. 4.3.8). In particular the "most probable" velocity $\dot{z}_{0n}$ now starts off with a dubious looking 7-second period wave, and seems to be drifting away near the end. Also, it appears that the velocity is now mainly composed of a smaller period wave of 3 to 4 sec. The "most probable" displacement z_{0n} has also changed significantly after this correction, and no longer seems to be representative of the kind of behavior expected from a seismic displacement time history. Thus, the processing of this record confirms that as long as the cut-off frequency is selected between the frequency obtained from the probabilistic criterion and the corner frequency, the corrected time histories are not sensitive to the precise cut-off.

To prove that zero padding does not influence the minimization and correction method results, the same record (Station 2, 230° component) is now tested by padding more zeroes at the end of the accelerogram. The total record length is increased from the previous 4096 data points to 6144 data points. Thus, the spectrum is now discretized at intervals of 0.0163 Hz compared with the previous interval of 0.0244 Hz. Since the frequency increments are smaller, there are more points in the low-frequency portion of the measured spectrum (Fig. 4.39) to identify the spectral behavior during the minimization and substitution steps. But the spectrum itself has not altered much, and the frequencies that coincide with the previous case still have the same amplitudes.

This longer version of the record is processed in exactly the same way as was done previously. The minimization results using the far-field spectral model are:

$$D_0 = 126.7 \text{ cm.sec} , \quad f_0 = 0.114 \text{ Hz} , \quad f_H = 7.54 \text{ Hz} .$$

Although these values are slightly different from the ones obtained previously, comparison of the plotted spectral fits for the 40.95 sec case (Fig. 4.3.3) and the 61.43 sec case (Fig. 4.3.9) shows very little difference. According to the correction criteria, the plot of the error shows that 2 points should be substituted with a cut-off frequency of 0.0326 Hz (Fig. 4.3.9(c)). The first point that does not require substitution at low frequencies is the harmonic at 0.0488 Hz. This coincides exactly with the results obtained when the data was padded with zeroes only up to 40.95 sec.

Fig. 4.3.10 shows the "uncorrected" time histories of the extended 61.43 sec record. Increasing the length of the record by padding the accelerogram with zeroes alters the temporal mean of the velocity, the effect of which is observable in the uncorrected time histories (Fig. 4.3.10). The time histories of the longer record only differ slightly from those of the shorter record (Fig. 4.3.4) in the signals from which a temporal mean correction is applied (i.e., $\ddot{z}_{0n}$, $\dot{z}_{0n}$ and z_{0n}). The difference is the greatest in the displacement, but is negligible for the acceleration and velocity time histories. However, the signals that are obtained with the zero initial value assumption are identical (i.e., $\dot{z}_n$ and z_n).

In Fig. 4.3.11, the record which is padded with zeroes up to 61.43 sec is processed with a 2-point spectral substitution. This corresponds to the optimal low-frequency cut-off of 0.0326 Hz as dictated by the standard deviation level in the error plot (Fig. 4.3.9). The results for the most probable time histories are almost identical to those obtained for the shorter signal at its optimal cut-off frequency of 0.0244 Hz (Fig. 4.3.5), except for a 1% to 2% error in the peak values and a different behavior at the end of z_{0n} due to the imposed correction in the temporal mean velocity. Similarly, if a 3-point spectral substitution had been done, the most probable time histories would have been almost identical to the results shown in Fig 4.3.6. Hence, the spectral correction method seems to be consistent in choosing an optimal low frequency cut-off and produces similar processed time histories regardless of the number of zeroes padded to the accelerogram.

The next point to investigate is whether the spectral substitution method is consistent and effective in its removal of the low-frequency noise. This can be examined by verifying that records obtained at adjacent sites can produce comparable time histories. In particular, the predominant long periods composing the velocity and displacement records should be the same at both sites. For this purpose, the results of the previous record (Station 2, 230°) are compared to those of Station 3 (230°). These two records are aligned, at a direction perpendicular to the fault, and are less than 3 km apart. Hence, the corrected time histories should in theory exhibit the same predominant features of the outgoing *SH*-wave.

The accelerogram of Station 3 (230°) was originally digitized up to 39.63 sec, as was the 230° component of Station 2, so it was padded with zeroes up to 40.95 sec. It was processed in exactly the same manner as the 230° component of Station 2 using a far-field spectral model. The minimization results are illustrated in Fig. 4.3.12. The optimal parameters are:

$$D_0 = 172.2 \text{ cm.sec} , \quad f_0 = 0.086 \text{ Hz} , \quad f = 7.29 \text{ Hz} .$$

These values are close to the ones obtained for the Station 2 record. The fit at intermediate frequencies appears to be better than for Station 2, and may be due to a lesser amount of local site response at Station 3.

The error plot (Fig. 4.3.12(c)) shows that only the two first points lie outside the one standard deviation interval, and hence the optimal low-frequency cut-off is 0.0488 Hz. Fig. 4.3.13 shows the time histories of the uncorrected record, and Fig. 4.3.14 those of the 2-point corrected record with the optimal cut-off. In this case, the substitution of the first harmonic has not altered the signal much from the uncorrected time histories. As is shown in the error plot, this is because the point which is substituted at 0.0488 Hz is very close to the one standard deviation level, i.e., it is believable in the statistical sense.

The most probable time histories for the 230° component of Stations 2 and 3 (Figs. 4.3.6 and 4.3.14) can be compared. These records are processed with the spectral substitution method at their optimal low-frequency cut-off. The most probable accelerations have different behaviors, especially between 8 and 10 sec, as

expected, since they are dominated by high frequencies which will not propagate coherently over 2 to 3 kms. However, the most probable velocity and displacement exhibit very similar characteristics, especially in the initial portion of the records. In particular, the most probable displacement at both recording sites display the same initial rise, followed by a large 8-second pulse and by similar long-period waves. The difference in the peak values is expected since Station 3 is closer to the fault than Station 2.

So far it has been shown that the spectral optimization method produces time histories with similar features for two components in the same direction from adjacent sites. For instance, the processing of the displacement time histories showed that in the direction perpendicular to the fault the motions are very similar and the valley appears to be excited with a dominant period of around 8 sec.

The accelerogram of the 140° component of Station 2 is digitized up to 39.64 sec at intervals of 0.01 sec, so it was padded with zeroes for a total record length of 4096 data points. Fig. 4.3.15 illustrates the results for the spectral fit of this record. Both the acceleration and displacement fits are good, as shown in Fig. 4.3.15(a) and (b) respectively. The parameters of the optimized model are:

$$D_0 = 93.58 \text{ cm.sec} , \quad f_0 = 0.129 \text{ Hz} , \quad f_H = 7.59 \text{ Hz} .$$

The error plot in Fig. 4.3.15(c) indicates that only the amplitude at 0.0244 Hz needs to be substituted by the model. The time history results of the 1-point substitution for the 140° component of Station 2 are shown in Fig. 4.3.16.

Similarly, the data of the 140° component of Station 3 is digitized up to 39.62 sec at intervals of 0.01 sec, so it was also padded with zeroes for a total record length of 4096 points. Fig. 4.3.17 illustrates the spectral fit of this record, for which the parameter of the minimized model are:

$$D_0 = 107.8 \text{ cm.sec} , \quad f_0 = 0.121 \text{ Hz} , \quad f_H = 7.05 \text{ Hz} .$$

The error plot indicates that only one point at 0.0244 Hz lies above the one standard deviation level and needs to be substituted. The time history results of this 1-point substitution for the 140° component of Station 3 are given in Fig. 4.3.18.

Comparison of the corrected time histories for the 140° components of Station 2 and 3 shows again that the acceleration for both sites are similar, except between 8 and 12 sec. In this range, the peaks are much higher for Station 2, perhaps because of a greater contribution of local site conditions (Figs. 4.3.16 and 4.3.18). Nevertheless, the most probable velocity and displacement time histories at both stations display very similar features. In particular, the predominant period in the most probable displacement is approximately 8 sec for both the 230° and the 140° components, as expected if the valley was amplifying the motions at this period. Note also that the components in the same direction from Stations 2 and 3 are more similar than the 140° and 230° component obtained at each station.

The vertical (up) components of Stations 2 and 3 have also been processed and corrected with the spectral substitution method. These records have been digitized up to 39.54 sec and 39.59 sec respectively, at intervals of 0.01 sec. They are both padded with zeroes for a total record length of 40.95 sec. The spectral fits and error plots for the vertical records of Stations 2 and 3 are shown in Figs. 4.3.19 and 4.3.21 respectively. In both cases, the far-field model provides a good fit to the data except at very low frequencies. The poor fit in the spectral amplitudes near *d.c.* is attributed to the large error in the temporal mean of the measured acceleration due to the large amount of missing data from instrument trigger at the beginning and to premature digitization cut-off at the end, as is shown in the acceleration time histories of Figs. 4.3.20 and 4.3.22. For Station 2, the values of the parameters for the optimized model are:

$$D_0 = 71.54 \text{ cm.sec} , \quad f_0 = 0.081 \text{ Hz} , \quad f_H = 23.5 \text{ Hz} .$$

and for Station 3 :

$$D_0 = 49.28 \text{ cm.sec} , \quad f_0 = 0.106 \text{ Hz} , \quad f_H = 15.56 \text{ Hz} .$$

The error plots show that the most probable set of time histories for Stations 2 and 3 are obtained by a 2-point spectral substitution up to 0.0488 Hz (Figs. 4.3.19(c) and 4.3.21(c)). The corresponding time histories are presented in Figs. 4.3.20 and 4.3.22 respectively. Comparison of these figures shows that once again the records

at both sites display the same prevailing features, but are very much different from the time histories obtained for the 230° and 140° components, as expected since the latter are horizontal motions. In particular, the predominant period for the vertical motions is approximately 4 sec, whereas that for the 230° and the 140° components were 8 sec. The most probable vertical displacement time histories, obtained by removing the temporal mean of the velocity, also seem to be composed of a longer 20- to 30-second period wave. Because of the large amount of missing data points, this long period behavior is more likely to be attributed to an error in the estimate of the acceleration mean than to be a representation of the ground motions. Nevertheless, these displacement time histories remain the most probable ones in the absence of information about the true value of the missing data.

The preceding examples demonstrate that the spectral substitution method is capable of producing similar types of records for accelerograms obtained at adjoining sites in the far-field. It is thus consistent and effective in correcting the noise introduced in the spectrum by the recording and digitization processes at low frequencies, without removing the characteristics expected from an earthquake signal. It was also demonstrated that the low-frequency cut-off is not a sensitive parameter as long as the harmonics below the cut-off are represented in the processed signal according to the most probable value of the model's spectral amplitude. It was also shown that the Imperial Valley responded strongly with a 8-second period in the horizontal directions, and a 4-second period in the vertical direction. These dominant periods are assumed to be properties of the whole valley, since they are consistent with the results inferred from the velocity structure, as explained at the beginning of this section. The 8-second period would not be noticed in the strong-motion records processed with current correction methods because high-pass filters remove all contributions from harmonics below the cut-off frequency, which for this particular event was chosen by USGS as 0.17 Hz (6 sec) [Brady, Perez & Mork, 1982].

4.3.4.2 Near-field Records: Stations 6 and 7, and Bond's Corner

The spectral substitution method is next tested on near-field records, for which the model to be optimized is given by Eq. 4.3.13. In this case, the variable

D_0 represents the most probable mean in the velocity. Since the most probable displacement time history z_{0n} is produced under the assumption that the initial displacement is zero, D_0 also represents the final displacement offset. When using far-field records it was shown that D_0 represented the temporal mean in the displacement. It was also previously mentioned that either the initial value at trigger or the temporal mean of the motion could be prescribed, but imposing a condition on both the initial value and the temporal mean at the same time is not feasible mathematically if only constant offsets are allowed. Because the most probable displacement time histories are generated under the assumption that the initial value is zero, this automatically forces a corresponding *d.c.* value for the far-field displacement spectrum. For near-field records, the most probable displacement time histories z_{0n} are produced by the velocity time history $\dot{z}_{0n}$ with a prescribed temporal mean D_0. Hence, for near-field records, making a substitution at the *d.c.* of the velocity spectrum only, while keeping all higher spectral amplitudes unchanged, will produce a correction in the displacement signal according to Eq. 4.3.23. The sign of the velocity temporal mean correction is chosen to be consistent with the fault's displacement pattern, as explained in Sec. 4.3.1. For near-field records, substitution of the velocity spectrum at *d.c.* alone is referred to as a "*d.c.* correction."

To illustrate the correction of near-field ground motions, two of the records obtained from the Imperial Valley earthquake of October 15, 1979, are used. The first example is the 140° component of Station 7 from the strong-motion array (Fig. 4.3.2). This station is located just 1 km west of the fault, but at a distance of 27 km from the epicenter. The 140° component, which is parallel to the strike of the fault, should display final displacement offsets. According to geologic surveys performed just after the event, right-lateral dislocations of the order of 30 cm were measured in this region of the fault [Sharp *et al.*, 1982]. Because Station 7 is located on the west side of the fault and the 140° component is directed southeastward along the strike, final displacement offsets consistent with right-lateral fault motions should be obtained for a negative value of the velocity temporal mean. The results of the spectral optimization with the near-field model (Eq. 4.3.13) for the 140° component of Station 7 are shown in Fig. 4.3.23. These figures show that the near-field spectral model can provide an adequate fit through most of the spectrum,

but that at low frequencies, the *d.c.* and the first three harmonics need to be substituted. The values of the estimated parameters are:

$$D_0 = -64.91 \text{ cm} , \quad f_0 = 0.53 \text{ Hz} , \quad f_H = 23.76 \text{ Hz} .$$

Compared to the results obtained at Stations 2 and 3 for the same 140° component, the identified value of f_H for the near-field record is 3 times larger. As the body waves travel away from the epicenter, the higher frequencies decay faster, thus making f_H decrease to smaller frequencies. The change in f_0 from 0.12 Hz to 0.5 Hz suggests that this parameter is not exclusively a source property. The most probable time histories obtained by performing a 3-point spectral substitution with negative final displacement offset are shown in Fig. 4.3.24. The velocity time history with D_0 temporal mean, $\dot{z}_{0n}$, starts-off flat, as expected, although the initial value is shifted by a large amount. As was mentioned in Sec. 4.3.2, this could be an indication of severe data truncation in the processed accelerogram, for which the estimated temporal mean of the complete velocity time history, D_0, is not a good approximation. The most probable displacement z_{0n} behaves statically and dynamically as could be expected from a near-field record: initially, the ground slips along with the fault before oscillating about the final offset value. However, because of the large uncertainty caused by the missing data in the accelerogram, the value of the final displacement offset, as given by the processing method, should not be assigned a high reliability. Nevertheless, given the available information, these time histories are the most probable ones, and the standard deviations defined in Ch. 3 are expected to provide conservative bounds for their reliability, regardless of the error in the displacement, as will be seen in Ch. 5.

To verify that the spectral substitution method produces final displacement offsets consistent with the measured 30 cm total right-lateral dislocation, the 140° component of Station 6 is also processed. This station is located just across the fault from the previous Station 7, and in the vicinity of the intersection with the Brawley fault. Site inspections have shown that in this general area the geology is complex. Many smaller faults were triggered by the earthquake, some of which exhibited reverse left-lateral and normal motions. Under these conditions it is difficult to

make an estimate for the proper sign of the final displacement offset. The results of the spectral optimization with the near-field model are illustrated in Fig. 4.3.25. The values of the estimated parameters for the 140^0 component of Station 6 are:

$$D_0 = 31.47 \text{ cm} , \quad f_0 = 1.15 \text{ Hz} , \quad f_H = 35.23 \text{ Hz} .$$

The fit of the model to the measured spectrum is "good," and only the *d.c.* must be substituted. The record is first processed under the assumption that the final displacement at that location is *positive* to be consistent with right-lateral dislocations along the Imperial fault. This is illustrated in Fig. 4.3.26. The most probable displacement time history does not behave statically as would be expected from a dislocating fault. In particular, it is somewhat unlikely that halfway during the event the static motions reverse from a negative direction to a positive one. Hence, assuming that the *d.c.* is positive may not be correct. The same record is thus processed with a spectral substitution at *d.c* for *negative* final displacements, as shown in Fig. 4.3.27. There is no difference in the most probable acceleration $\ddot{z}_{0n}$. The most probable velocity $\dot{z}_{0n}$ with $-D_0$ temporal mean now starts off flat with initial values close to zero, which is the expected behavior. The most probable displacement z_{0n} now appears to behave statically as expected from a dislocating strike-slip fault. Hence, the assumption of a negative final displacement does indeed appear to be the better solution. A left-lateral dislocation at Station 6 may be possible, since the recording site is located at the intersection of the Imperial and Brawley faults, where field explorations performed just after the event showed very complex sub-faulting patterns [Sharp, *et al.*, 1982]. Thus, in cases where the fault mechanism is uncertain, the proper sign of the velocity *d.c.* for near-field models may sometimes be determined by inspection of the behavior of the displacement time history after correction. Also, near-field records which are expected to generate displacement offsets have a large signal-to-noise ratio. Hence, if the accelerogram is digitized up to the time of instrument shut-off, the static behavior of the displacement processed with no temporal mean velocity correction, z_n, should be reliable enough to properly indicate the direction of the final displacement offset, and the sign of the spectral substitution at *d.c.*

Comparison of the most probable final displacement offsets at the 140° components of Station 7 (Fig. 4.3.24) and Station 6 (Fig. 4.3.27) indicates that the overall dislocation across this section of the fault is right-lateral with a relative offset of the order of 20 cm. This result agrees with the results of the on-site measurements of 30 cm, demonstrating that the spectral substitution processing method is capable of giving a reasonable estimate for the displacement offset from near-field analog records. In particular, it might be concluded that both sites on either side of the fault moved northward. Since Station 6 is located at the intersection of the Brawley and Imperial faults, where the ground is highly fractured, it is physically possible that the motions at this site were northward and in the opposite direction expected from a right-lateral fault rupture. Also, according to the processed time histories, the absolute dislocation at Station 7, on the west side, was of the order of 50 cm, whereas that at Station 6 on the east side was only 30 cm.

The 140° component at Bond's Corner (Fig. 4.3.2) was processed next with the spectral substitution method for near-field records. This site is located to the east of the fault at an epicentral distance of only 6 km. When using the near-field model given by Eq. 4.3.13, the optimization algorithm could not converge on a value for the cut-off of the high-frequency exponential decay. For sites located very near the epicenter, it is expected that the high-frequency content of the earthquake has not significantly decreased, and hence an exponential decay behavior may not be appropriate. To conform to the high-frequency behavior of records obtained very close to the epicenter, the near-field model of Eq. 4.3.13 is used, but f_H is fixed at an arbitrarily large value, and the optimization is only performed on the two variables D_0 and f_0. The minimization results of this model for the 140° component at Bond's Corner, in which f_H is fixed at an arbitrarily large value of 10^7 Hz, are illustrated in Fig. 4.3.28. These figures show that the two variables are sufficient to provide an adequate description of the acceleration and displacement spectrum throughout the whole frequency range, and that only the *d.c.* and the first harmonic at 0.0244 Hz need to be spectrally substituted. The values of the estimated parameters are:

$$D_0 = 34.99 \text{ cm.sec} , \quad f_0 = 1.113 \text{ Hz} .$$

The value of the identified corner frequency f_0 is very close to the value obtained for the 140° component of Station 6 located 1 km away from the fault. Hence, the optimization algorithm has produced consistent results although the high-frequency behavior at the two sites was quite different.

The most probable time histories for the 140° component of Bond's Corner obtained for a 1-point substitution up to 0.0244 Hz are shown in Fig. 4.3.29. Because this recording site is located to the east of the fault, right-lateral motions should yield a positive value for the final displacement offset. The static and dynamic behavior shown in the plot of the most probable displacement time history is consistent with the motions in the near-field in the direction of the strike of the fault. In this area, geologic surveys have measured total dislocation along the fault of 60 to 70 cm [Sharp *et al.*, 1982]. Although Bond's Corner is approximately 6 km away from the rupture of the fault, nonzero dislocations are still expected. The most probable displacement time history, z_{0n}, for a D_0 temporal mean velocity indicates that the final offset after the event may be of the order of 30 cm, which could be physically possible. The corresponding most probable velocity, $\dot{z}_{0n}$, also appears to behave correctly, although the initial values are slightly higher than expected. This may be an indication that the accelerogram has been truncated prematurely, and that D_0 overestimates the temporal mean of the truncated velocity time history. Under these conditions, the final displacement offset in z_{0n} might be slightly overestimated as well, and should not be assigned a high reliability. However, the spectral substitution method generates time histories which are the best estimate of the motion given the information available, and uncertainties due to digitization and recording errors are conservatively accounted for by the reliability bounds.

Application of the correction method to recorded earthquake accelerograms and the tests of the synthetic accelerograms have demonstrated that a significant source of long-period error is the offset in the temporal mean of the accelerogram due to missing and undigitized data. This source of long-period error is unnecessarily aggravated by the previous practice of sometimes not providing the fully digitized records up to the time of instrument shut-off. However, the spectral substitution method has just proven to be particularly useful in partially recovering the most

probable static and long-period ground motions within the portion of the spectrum which is the most affected by the end truncation. This correction method produces most probable time histories which appear to be compatible with local static and dynamic ground behavior due to earthquakes. Because long-period motions are not removed with the spectral substitution method, strong-motion ground accelerograms, even from analog accelerographs, can now be used to perform more complete studies of source mechanisms and local site response. This is believed to be the first time that reasonable permanent displacement offsets have been determined from records from analog accelerographs. Iwan *et al.* [1984] have previously done this for digital accelerograph records.

4.3.5 Application to Structural Records: 1979 Imperial Valley Earthquake

The spectral substitution method is now used to correct structural records. The following example uses two of the accelerograms obtained at the Imperial County Services building during the Imperial Valley earthquake of October 15, 1979 (Fig. 4.3.2). At the time of the event, the building was instrumented with an analog 13-channel central recording accelerograph system (CRA-1). The structure is a six-story reinforced concrete building with discontinuous shear walls at the first story along the north-south (i.e., transverse) directions. It is located approximately 8 km southwest of the Imperial fault trace, and 27 km away from the earthquake's epicenter. The first floor columns at the east end of the building suffered severe damage during the event, and were shortened by 23 cm. The instrumentation and the behavior of the building during the earthquake have been greatly reported and studied [for example, Rojahn & Mork, 1982]. During the event, the building's natural period in the east-west (i.e., longitudinal) direction is reported to have increased from approximately 1.0 sec up to 1.7 sec. The dominant period in the recorded motions for the north-south direction elongated from 0.6 sec up to 0.8 sec at the west end of the building, and up to 1.2 sec at the east end where the columns failed.

Spectral substitution is performed on the record which measured the transverse north-south motions of the building along the west end of the roof (trace 3). The

corresponding record obtained at the ground floor (trace 11) is also spectrally corrected for comparison. These records are linearly interpolated at 0.01 sec intervals up to 58.08 sec, and are obtained from FBA-1 accelerometers which have natural frequencies of about 55 Hz. Hence, no high-frequency correction is necessary. The low frequencies are corrected according to the spectral substitution method. Zeroes are padded up to 61.43 sec for the implementation of the discrete Fourier transform algorithm, and the spectral model used in the minimization process is given by Eq. 4.3.21. Because the epicenter and the fault are a fair distance away, the far-field spectrum is used as the model for the input ground motion. The spectral fit and error for the roof record are shown in Fig. 4.3.30. The 5 optimized variables describing the model spectra of absolute structural motions are:

$$D_0 = 68.68 \text{ cm.sec} , \quad f_0 = 0.150 \text{ Hz} ,$$

$$f_n = 2.00 \text{ Hz} , \quad d = 4.44 , \quad c = 3.14 .$$

The error plot (Fig. 4.3.30) indicates that $d.c.$ and the 2 points up to 0.0326 Hz need to be spectrally substituted. The corrected time histories are shown in Fig. 4.3.31.

The most probable displacement record shows that at the west end of the building the absolute motion at the roof was dominanted by an 8-second period. An apparent 18-second period occurs approximately 20 sec after the beginning of the event, however, there is no evidence of this period in the spectra (Fig. 4.3.30). A much smaller period of about 0.8 sec is superimposed on these. According to the studies performed on the structure, this 0.8-second period is the fundamental north-south period of the building during the larger amplitude motions.

The north-south record at the west end ground floor is also spectrally corrected (Fig. 4.3.32). The optimization results for the 5 parameter structural model are:

$$D_0 = 69.17 \text{ cm.sec} , \quad f_0 = 0.137 \text{ Hz} ,$$

$$f_n = 3.42 \text{ Hz} , \quad d = 12.42 \quad c = -0.735 .$$

The parameters D_0 and f_0 are approximately the same at the roof and at the ground floor. However, the parameters f_n, d and c, have changed. At the roof

level, these parameters reflect the dominant fundamental behavior of the building, where $f_n = 2.00$ Hz (0.5 sec) corresponds approximately to the natural period in the early stages of the earthquake, whereas at the ground level, these parameters are probably controlled by the ground motion and not by the dynamics of the structural system. In fact, since this is a ground floor record, it is strictly neither structural nor free-field motion. However, all three classes of models (structural, far-field and near-field) were tested, and the structural model gave by far the better fit to the data.

According to the error plot (Fig. 4.3.32(c)), the ground floor record should be spectrally corrected from *d.c.* up to 0.0651 Hz, for a 4-point spectral substitution. The corrected time histories are presented in Fig. 4.3.33. It is interesting to note that the most probable displacements at the roof (Fig. 4.3.31) and at the ground floor display very similar motions. In particular, for both sets of processed time histories, the most probable velocity $\dot{z}_{0n}$ starts off flat with initial value approximately zero. The corresponding displacements z_{0n}, which are overlaid in Fig. 4.3.34 for better comparison, are both skewed in the same direction with a small offset of the order of 2 cm. This might be due to residual dislocation from the Imperial fault, or to a local ground failure, or to an error from noise and truncation. Also, both sets of displacement records are in phase and are mainly composed of an 8-second wave. Of course, the ground floor displacement does not show much of the structural 0.8 sec fundamental period.

Hence, the processing of these two records produced consistent results. Presumably, the 8-second period motion observed in both the roof and the ground floor processed time histories are due to the valley amplification observed in the free-field records described previously. These long-period motions could not be properly observed in the CDMG versions using the standard filtering process with a band-pass range of 0.17 Hz up to 23 Hz [Porter, 1982]. The spectral substitution method should thus prove to be a useful tool for the study of long-period soil-foundation-structure response motions.

NOISE FILTER ϕ_m		MEASURE-OF-ERROR, J		
		Acceleration	Velocity	Displacement
None		0.0200	0.1525	101.65
Modified Wiener		0.0132	0.0621	41.06
Exponential				
α	β			
1	1	0.0125	0.0414	25.57
1	2	0.0140	0.0231	9.77
1	4	0.0155	0.0207	7.32
1	10	0.0167	0.0207	7.31
2	1	0.0117	0.0451	28.98
4	1	0.0139	0.0722	49.19
10	1	0.0257	0.1430	96.90
2	4	0.0147	0.0208	7.37
5	10	0.0159	0.0207	7.30
10	10	0.0155	0.0207	7.25
10	20	0.0165	0.0208	7.37
20	20	0.0163	0.0208	7.38

Table 4.2.1 Comparison of the acceleration, velocity and displacement measure-of-error J for no filter, the modified Weiner noise filter, and the exponential noise filter as a function of α and β.

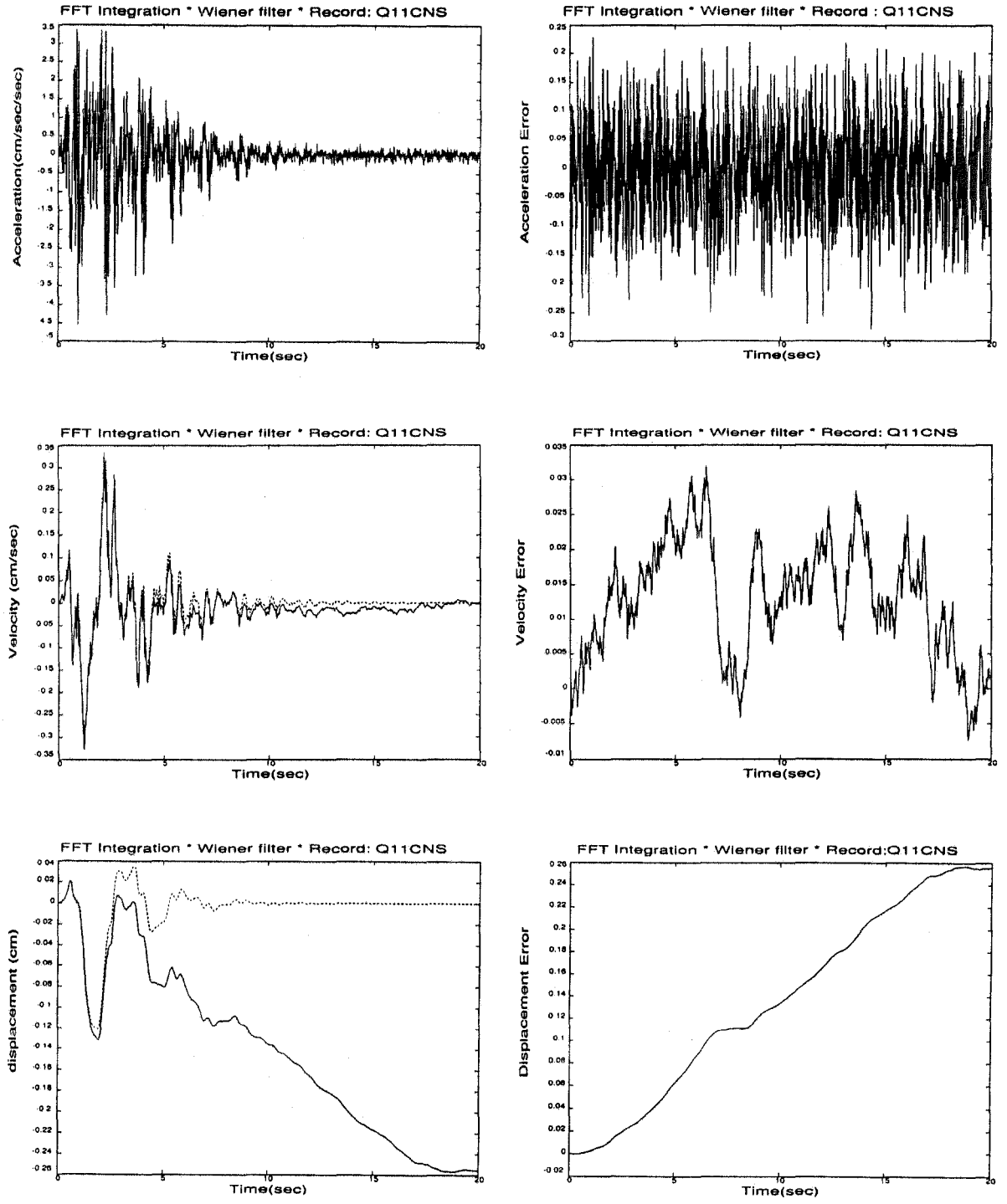

Figure 4-2-1. Synthetic signal Q11CNS processed with frequency-domain method and the modified Wiener noise filter.

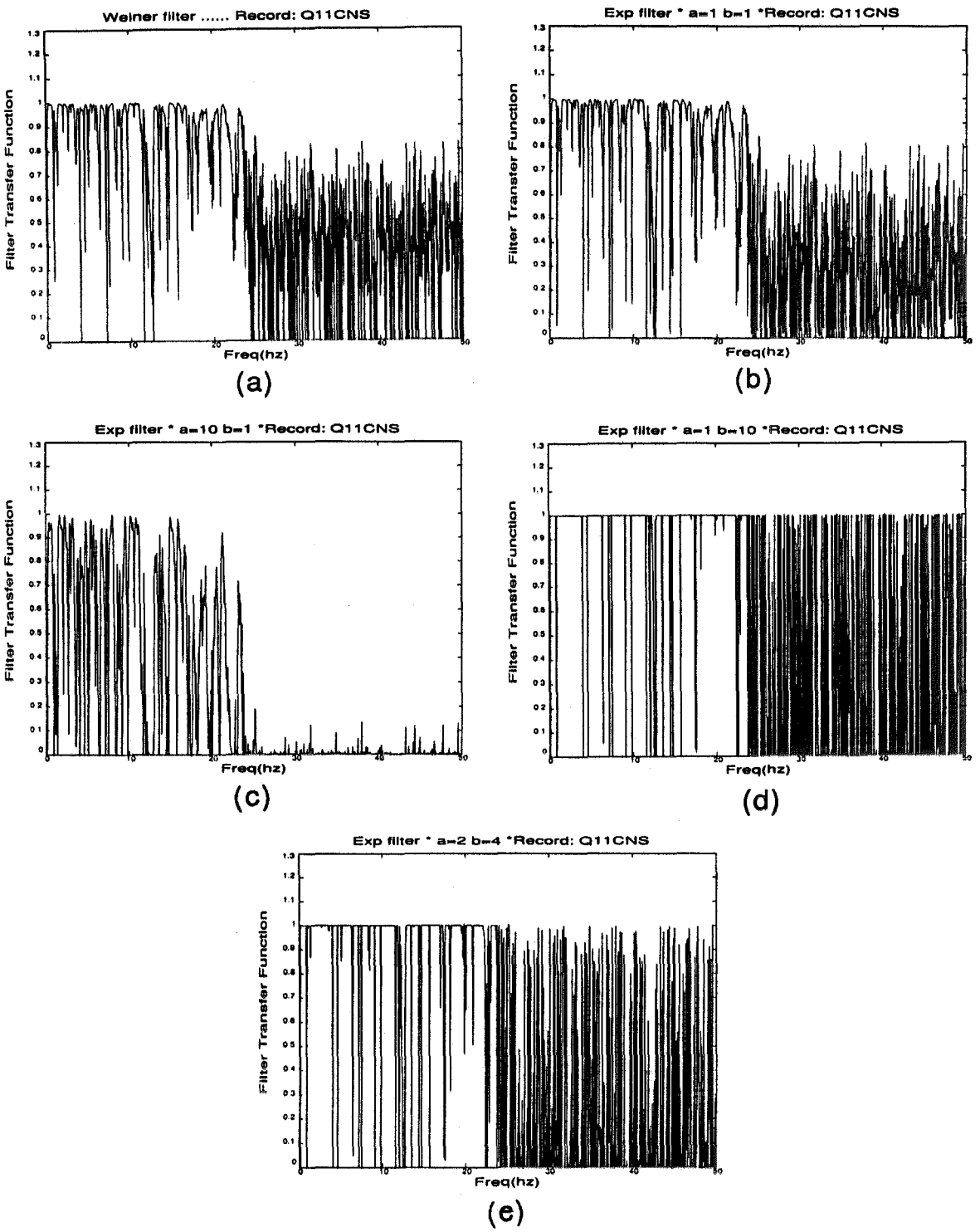

Figure 4-2-2. Transfer function of the noise filters for Q11CNS: (a) modified Wiener filter; (b) exponential noise filter ($\alpha = 1, \beta = 1$); (c) exponential noise filter ($\alpha = 10, \beta = 1$); (d) exponential noise filter ($\alpha = 1, \beta = 10$); (e) exponential noise filter ($\alpha = 2, \beta = 4$).

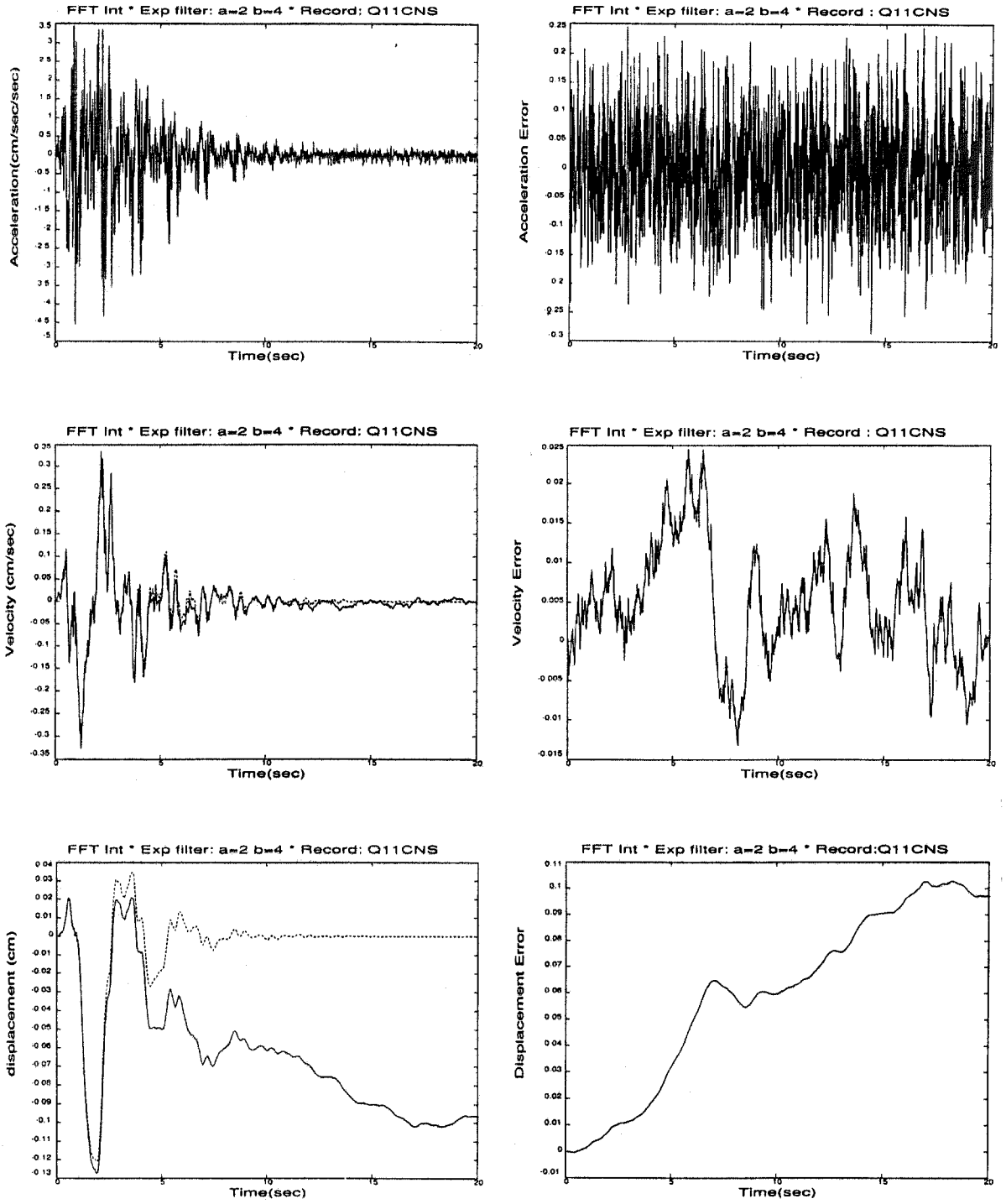

(— Processed, - - - Exact)

Figure 4-2-3. Synthetic signal Q11CNS processed with the frequency domain method and the exponential noise filter $(\alpha = 2, \beta = 4)$.

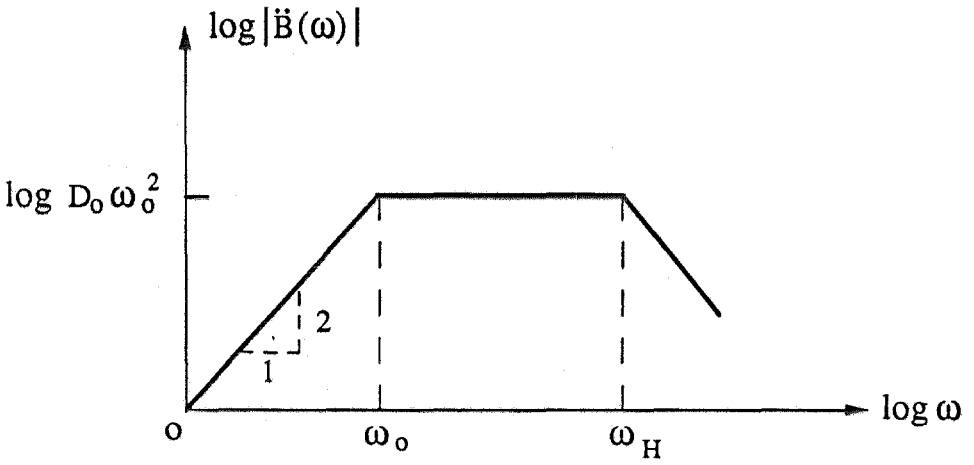

a) Acceleration spectrum

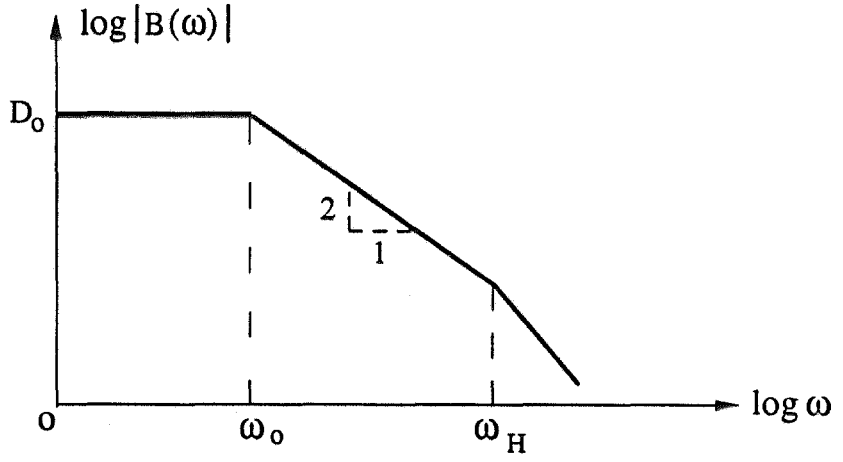

b) Displacement spectrum

Figure 4-3-1. Schematic representation of the acceleration and displacement spectra for far-field ground motions.

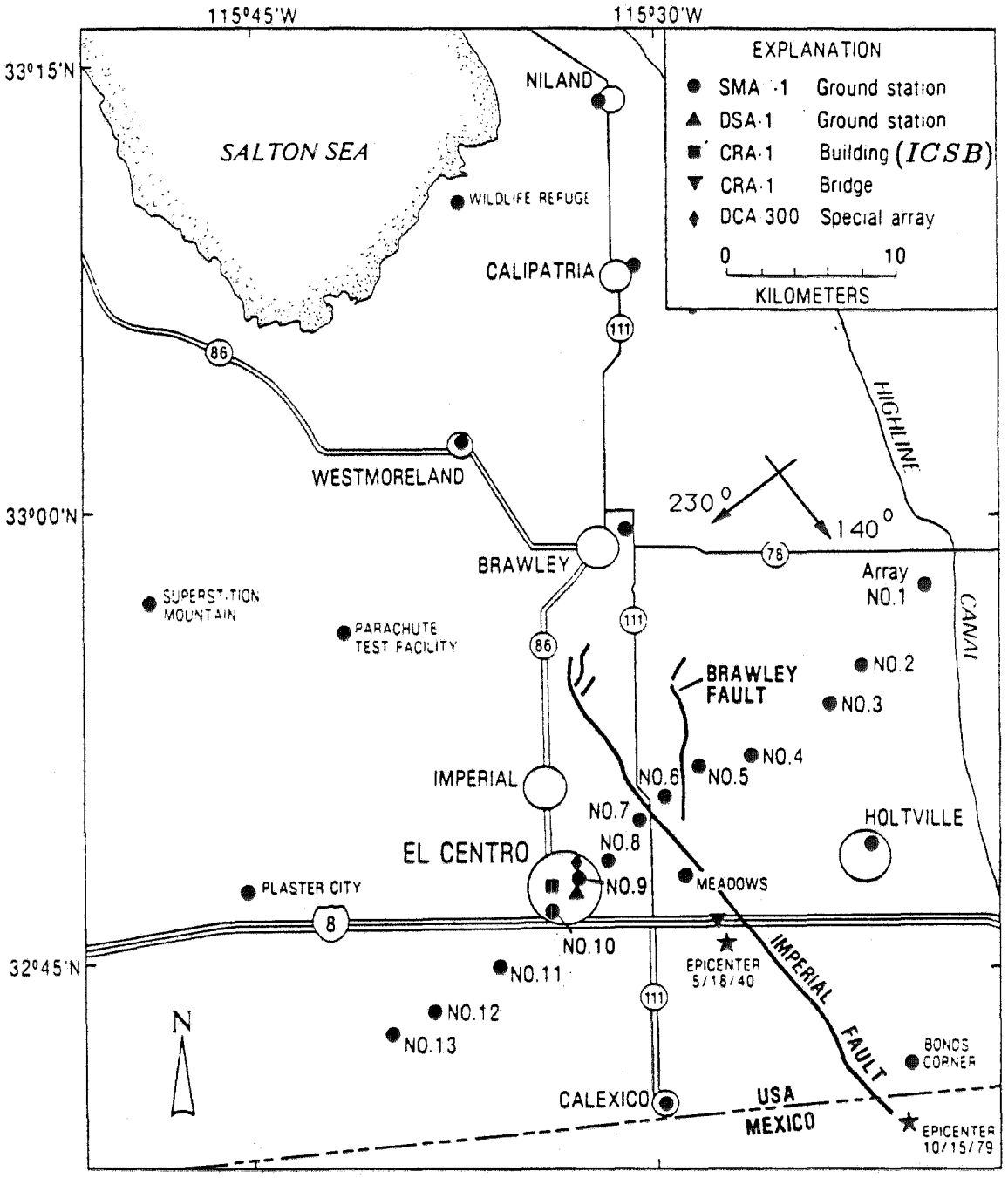

Figure 4-3-2. Strong-motion stations in the Imperial Valley, California [Porcella and Matthiesen, 1979].

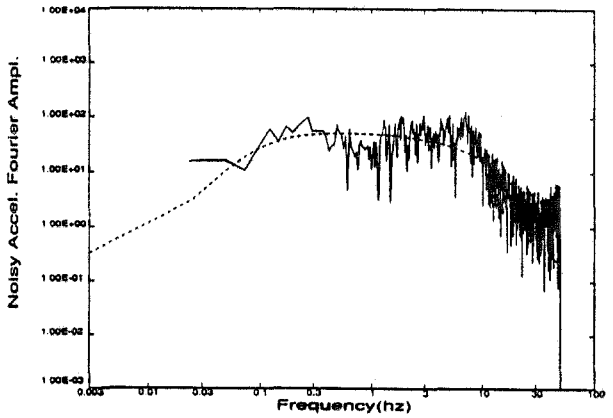

(a)

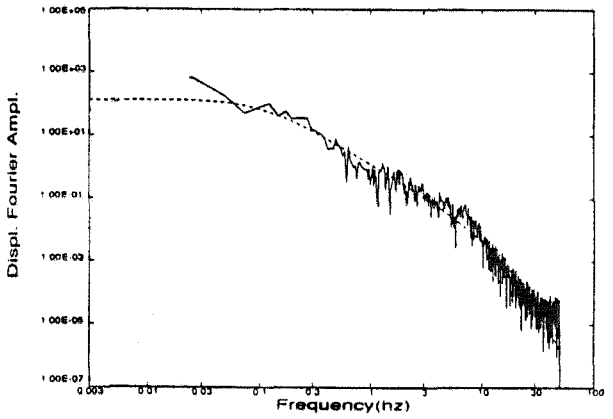

(b)

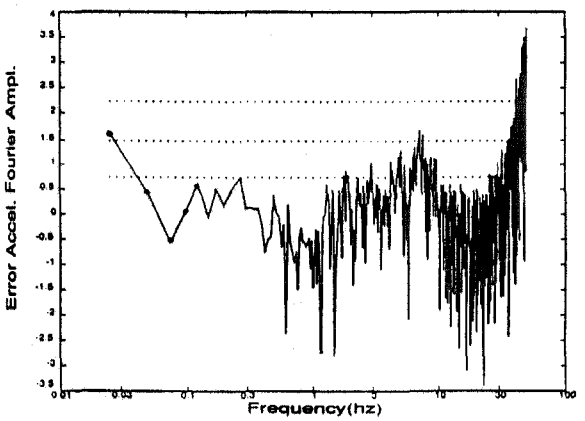

(c)

Figure 4-3-3. Imperial Valley earthquake (10/15/79). Station 2 (230°) extended to 4096 points. Spectral minimization results with the far-field model: $D_0 = 138.0$ cm.sec, $f_0 = 0.101$ Hz, $f_H = 8.37$ Hz.

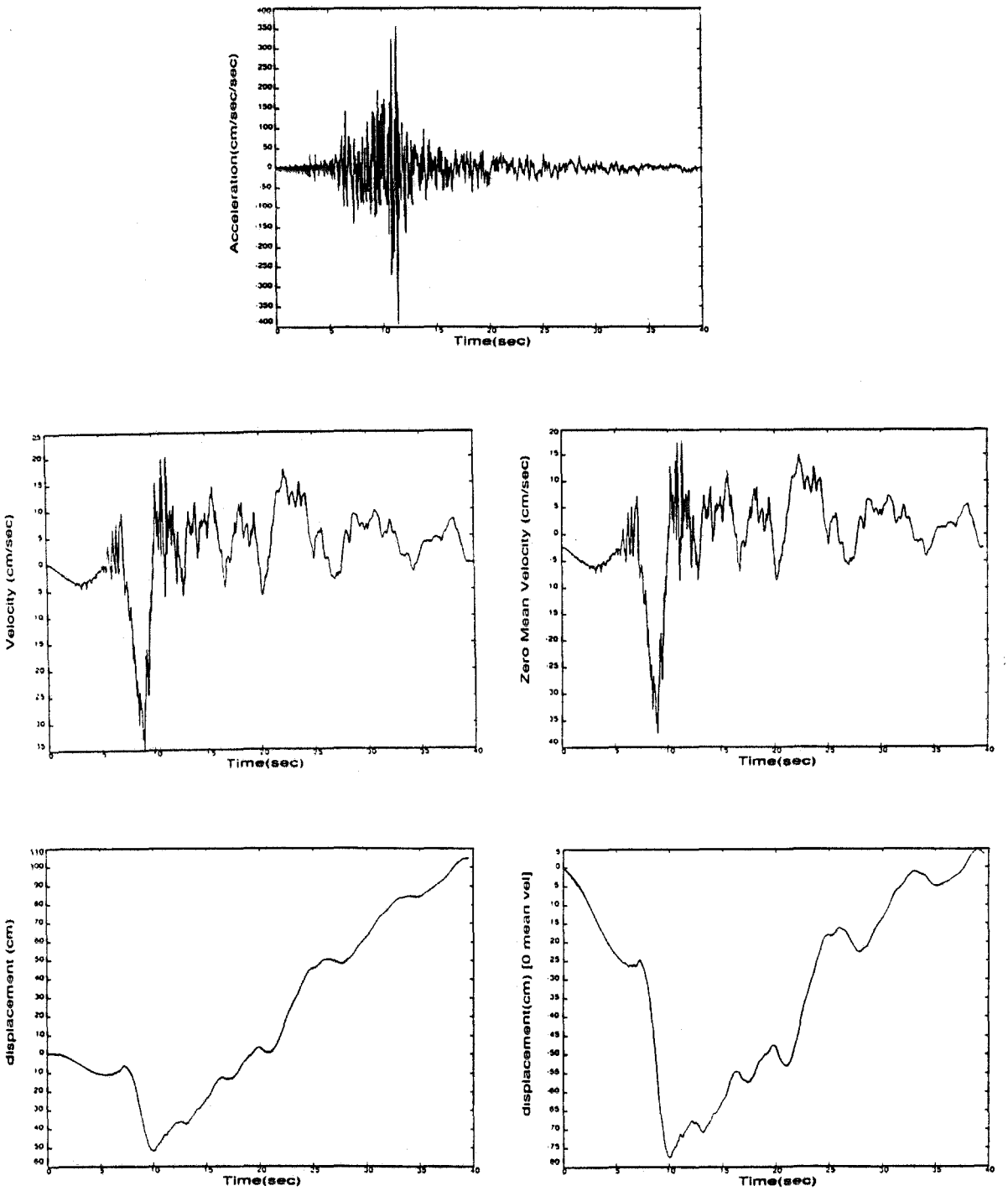

Figure 4-3-4. Imperial Valley earthquake (10/15/79). Station 2 (230°) extended to 4096 points. Far-field model processed with no spectral substitution (0 point).

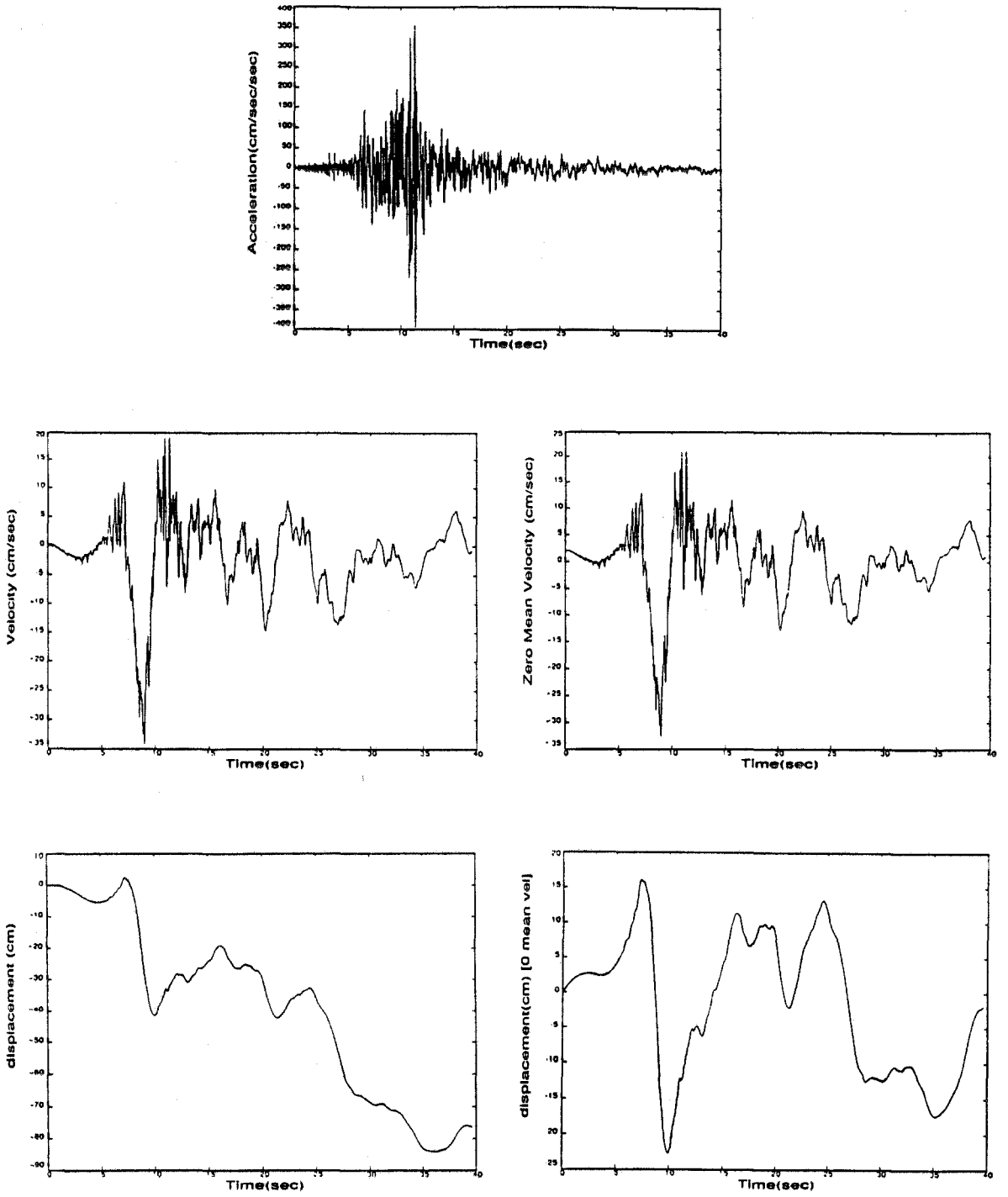

Figure 4-3-5. Imperial Valley earthquake (10/15/79). Station 2 (230°) extended to 4096 points. Far-field model processed with spectral substitution up to 0.0244 Hz (1 point).

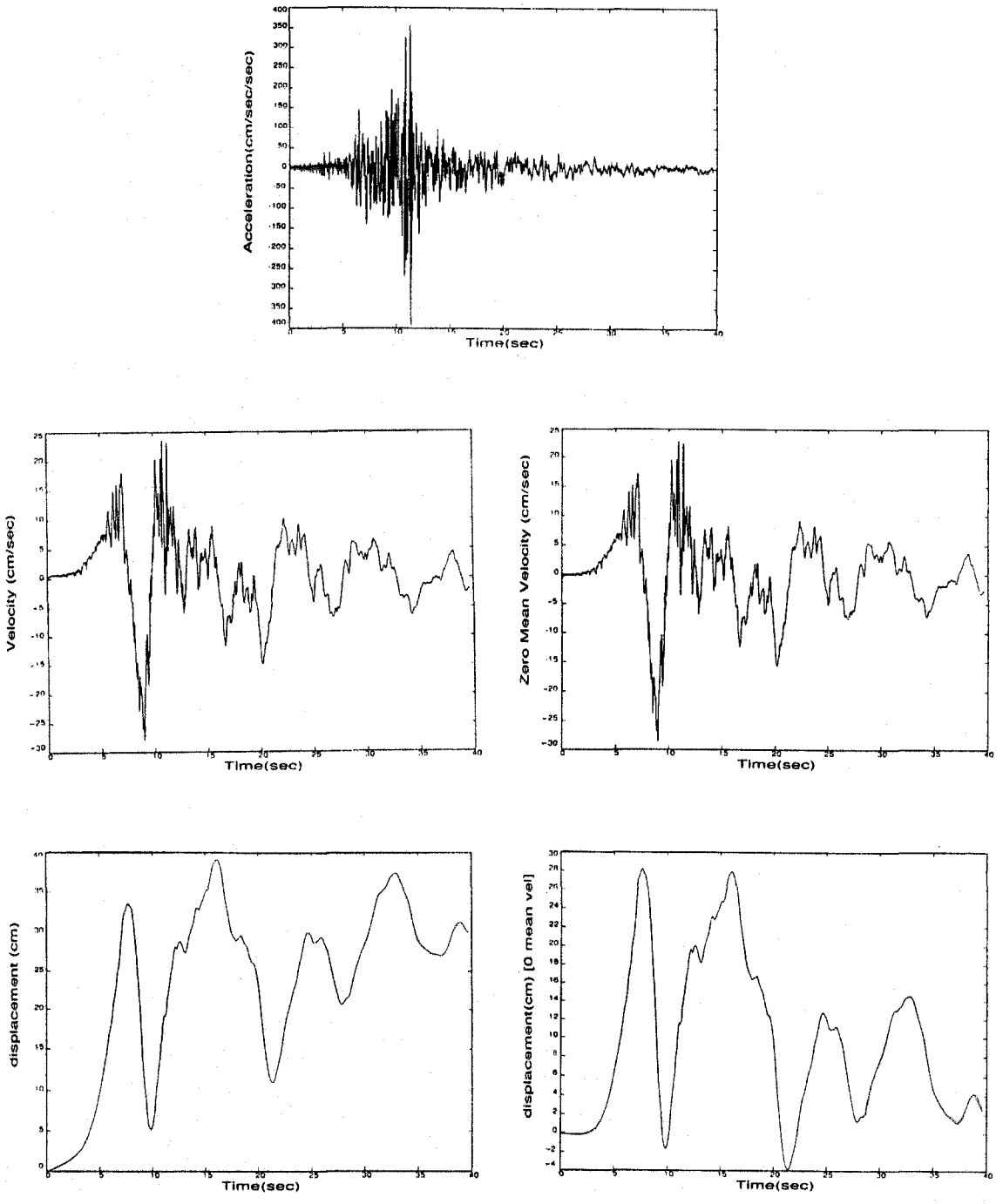

Figure 4-3-6. Imperial Valley earthquake (10/15/79). Station 2 (230°) extended to 4096 points. Far-field model processed with spectral substitution up to 0.0488 Hz (2 points).

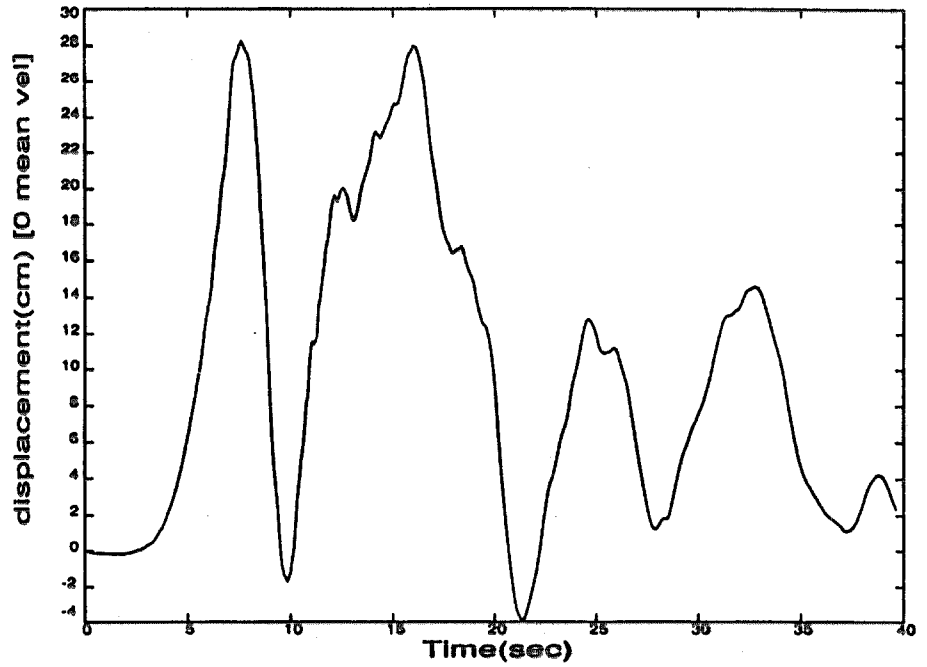

(a) 2-point spectral substitution (0.0488 Hz)

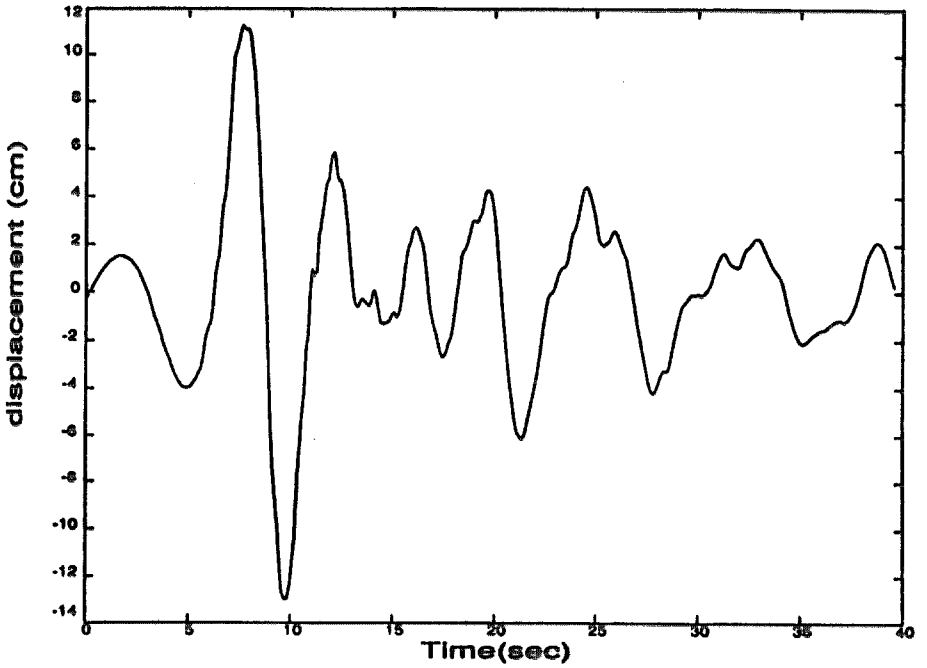

(b) USGS: filter 0.03-0.17 Hz and 23-25 Hz

Figure 4-3-7. Imperial Valley earthquake (10/15/79). Station 2 (230°). Displacement records corrected with the spectral substitution and USGS methods.

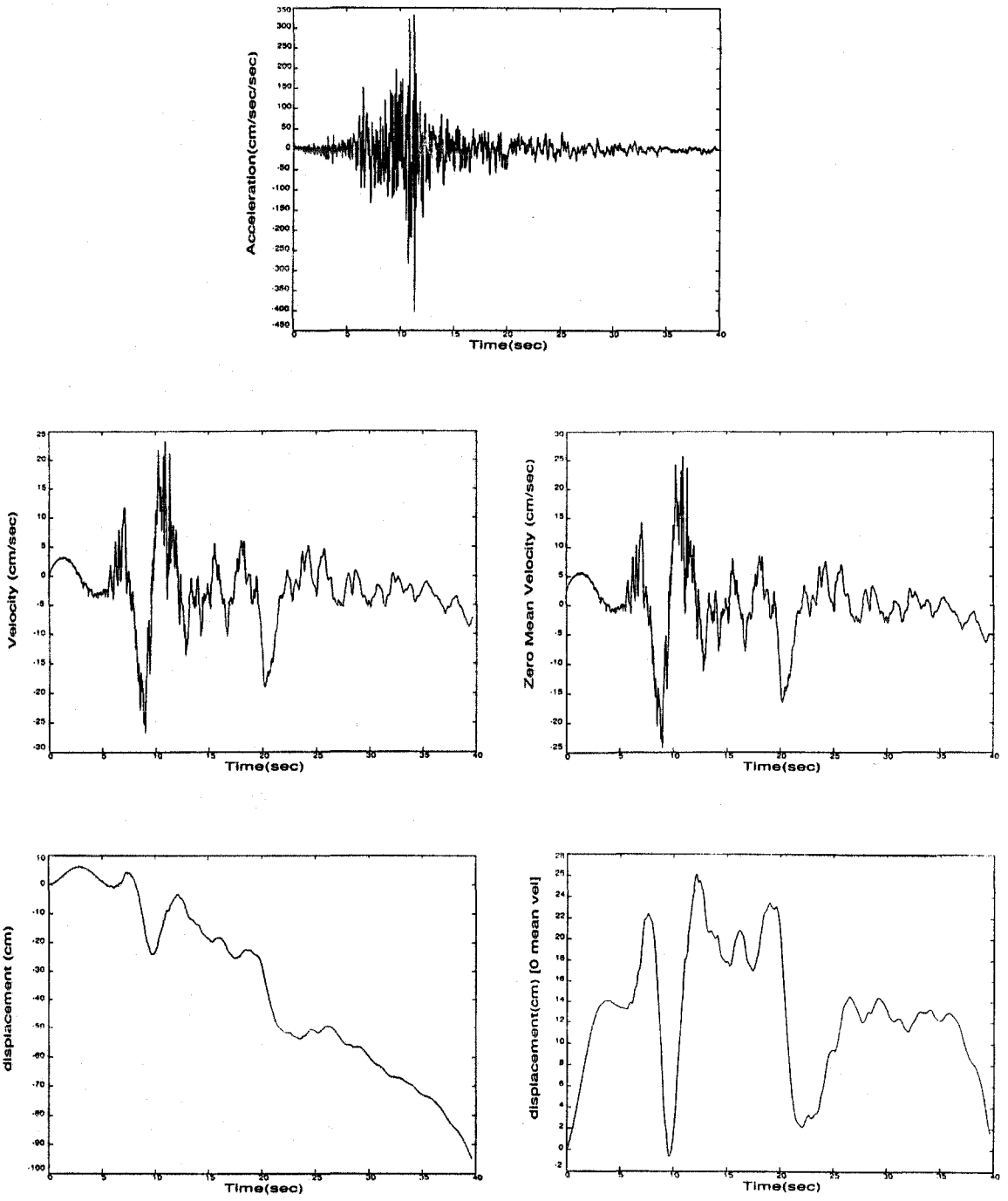

Figure 4-3-8. Imperial Valley earthquake (10/15/79). Station 2 (230°) extended to 4096 points. Far-field model processed with spectral substitution up to 0.122 Hz (5 points).

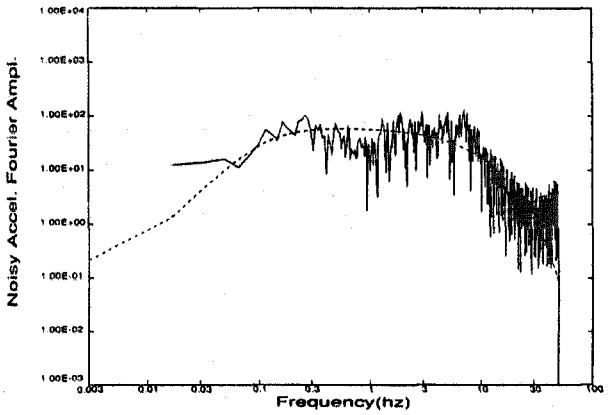

(a)

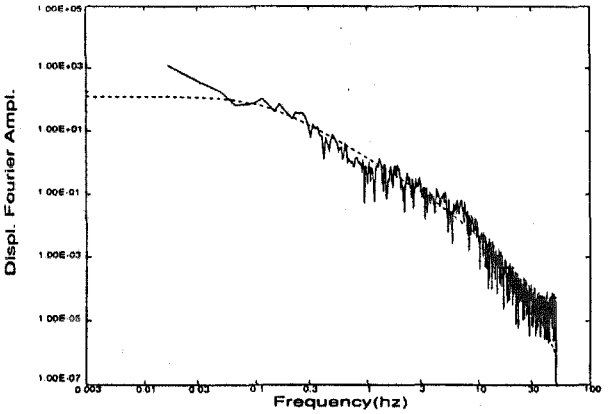

(b)

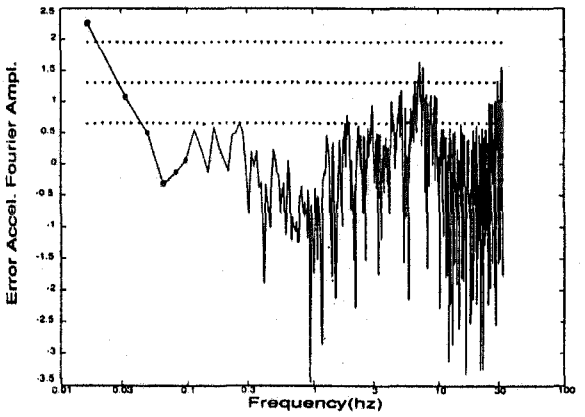

(c)

Figure 4-3-9. Imperial Valley earthquake (10/15/79). Station 2 (230°) extended to 6144 points. Spectral minimization results with the far-field model: $D_0 = 126.7$ cm.sec, $f_0 = 0.114$ Hz, $f_H = 7.54$ Hz.

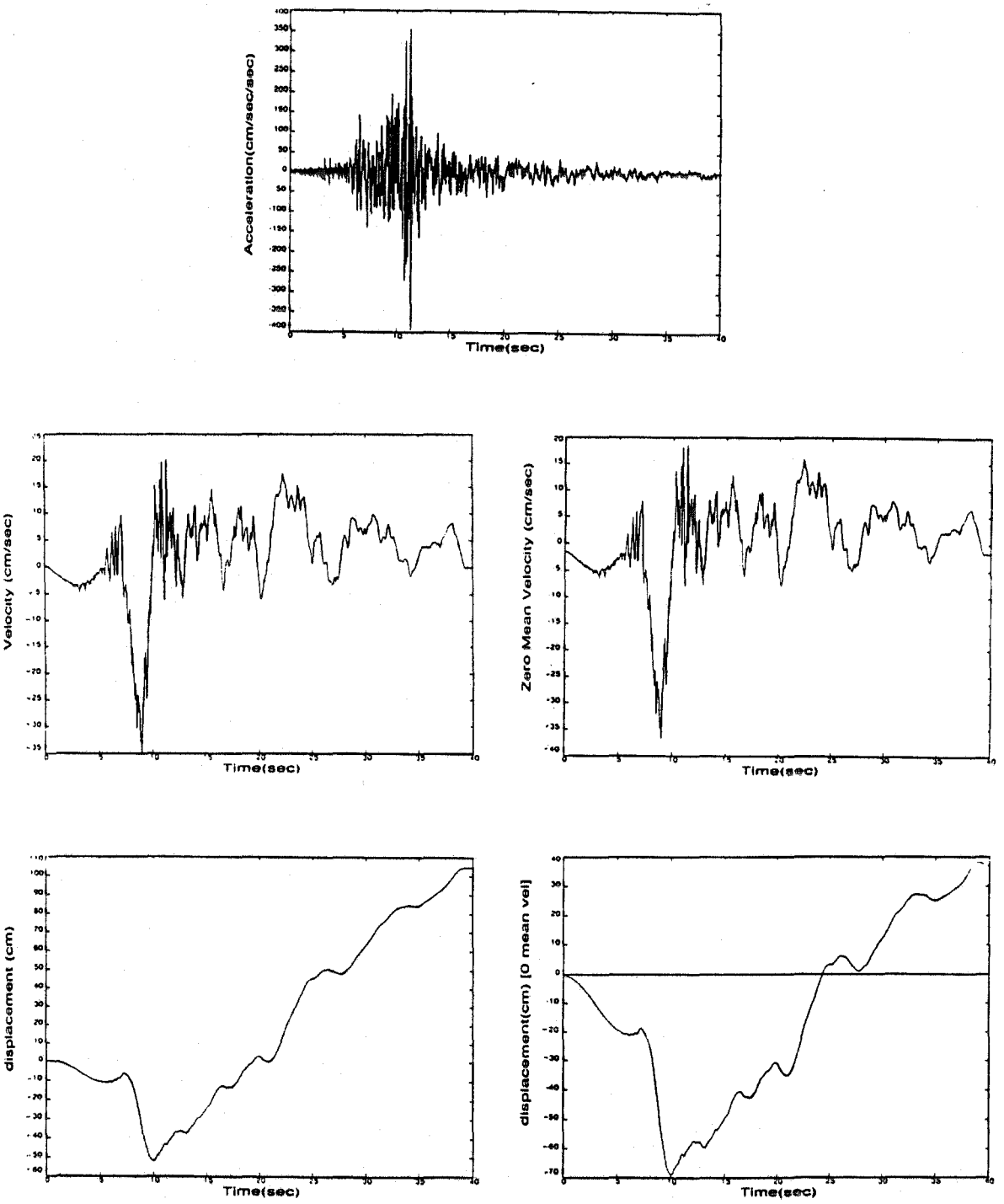

Figure 4-3-10. Imperial Valley earthquake (10/15/79). Station 2 (230°) extended to 6144 points. Far-field model processed with no spectral substitution (0 point).

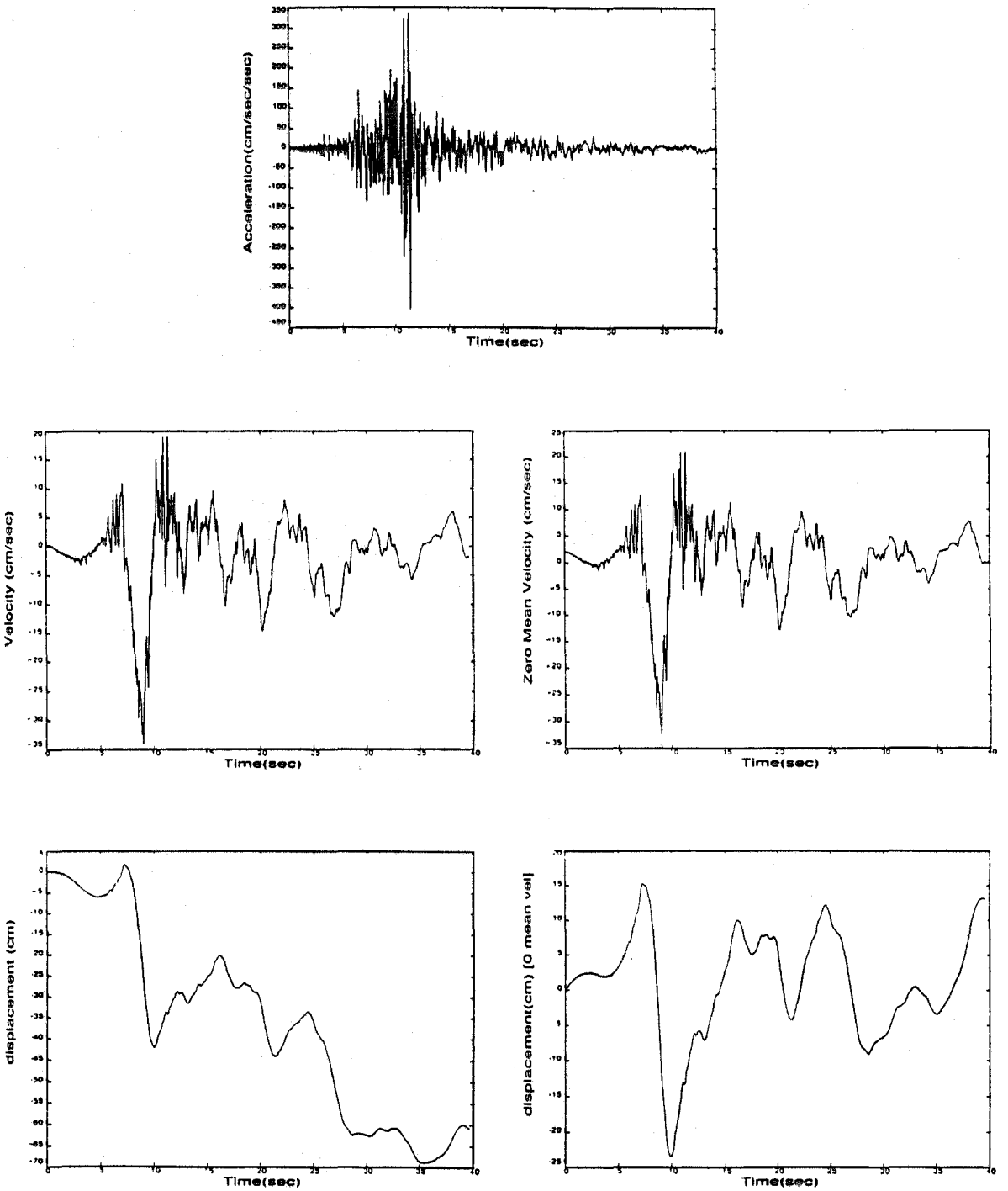

Figure 4-3-11. Imperial Valley earthquake (10/15/79). Station 2 (230°) extended to 6144 points. Far-field model processed with spectral substitution up to 0.0326 Hz (2 points).

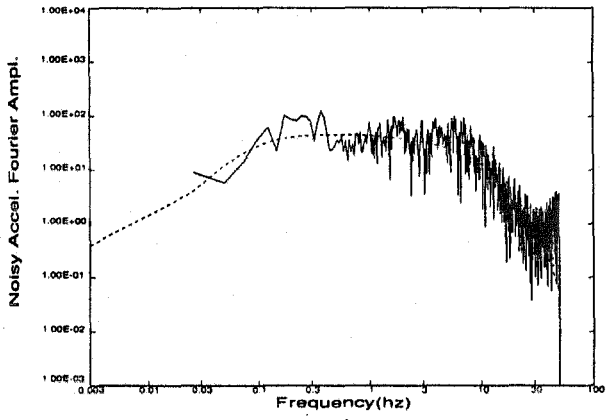

(a)

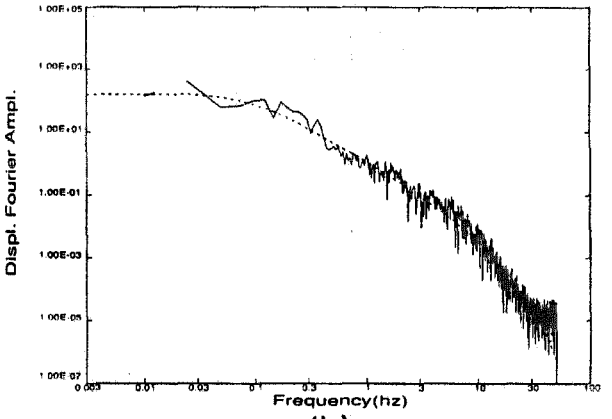

(b)

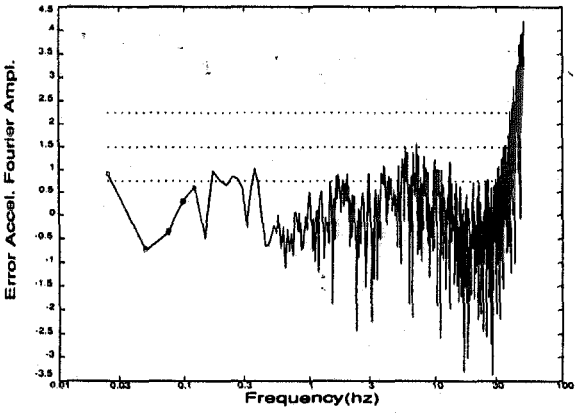

(c)

Figure 4-3-12. Imperial Valley earthquake (10/15/79). Station 3 (230°) extended to 4094 points. Spectral minimization results with the far-field model: $D_0 = 172.2$ cm.sec, $f_0 = 0.086$ Hz, $f_H = 7.29$ Hz.

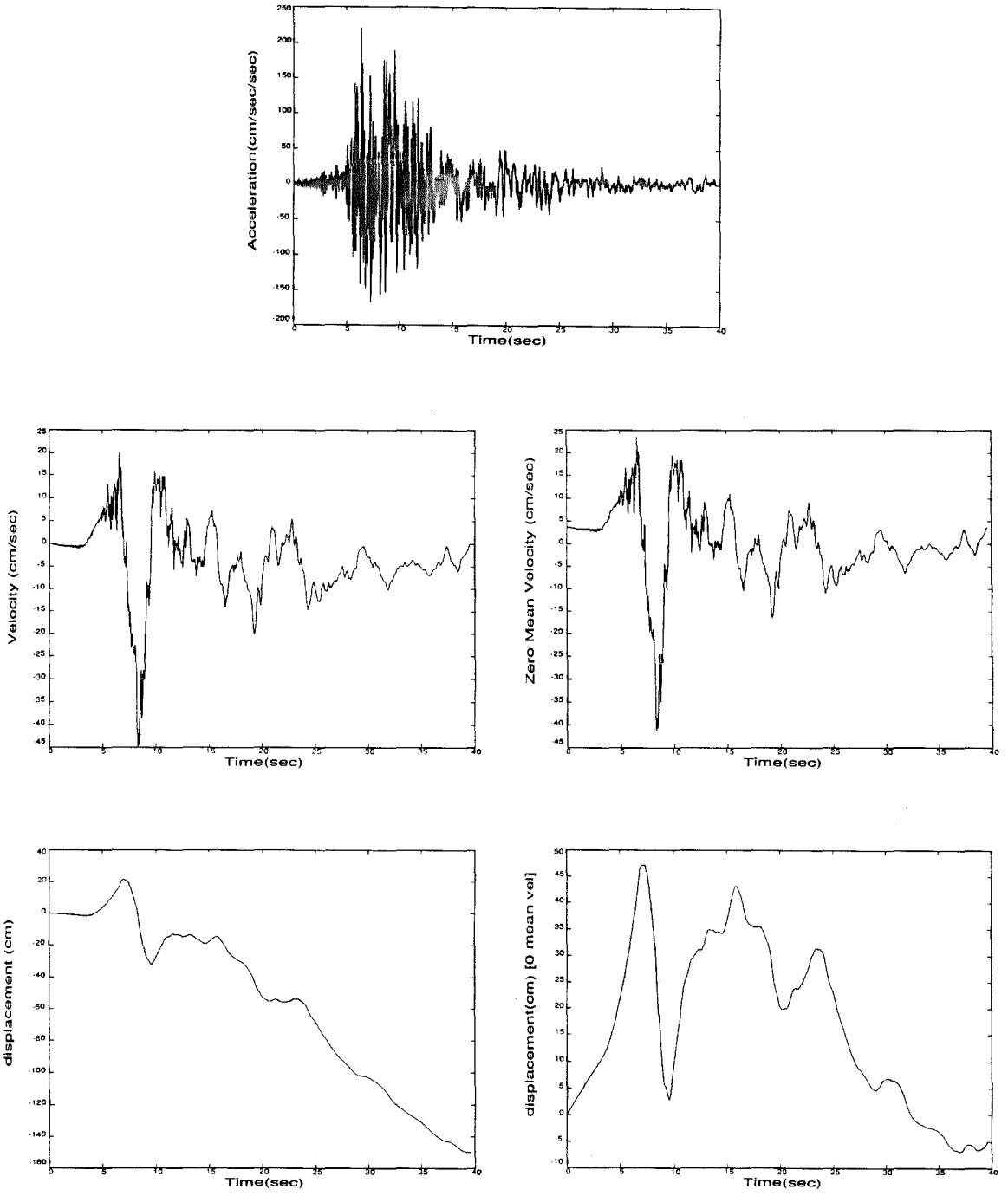

Figure 4-3-13. Imperial Valley earthquake (10/15/79). Station 3 (230°) extended to 4096 points. Far-field model processed with no spectral substitution (0 point).

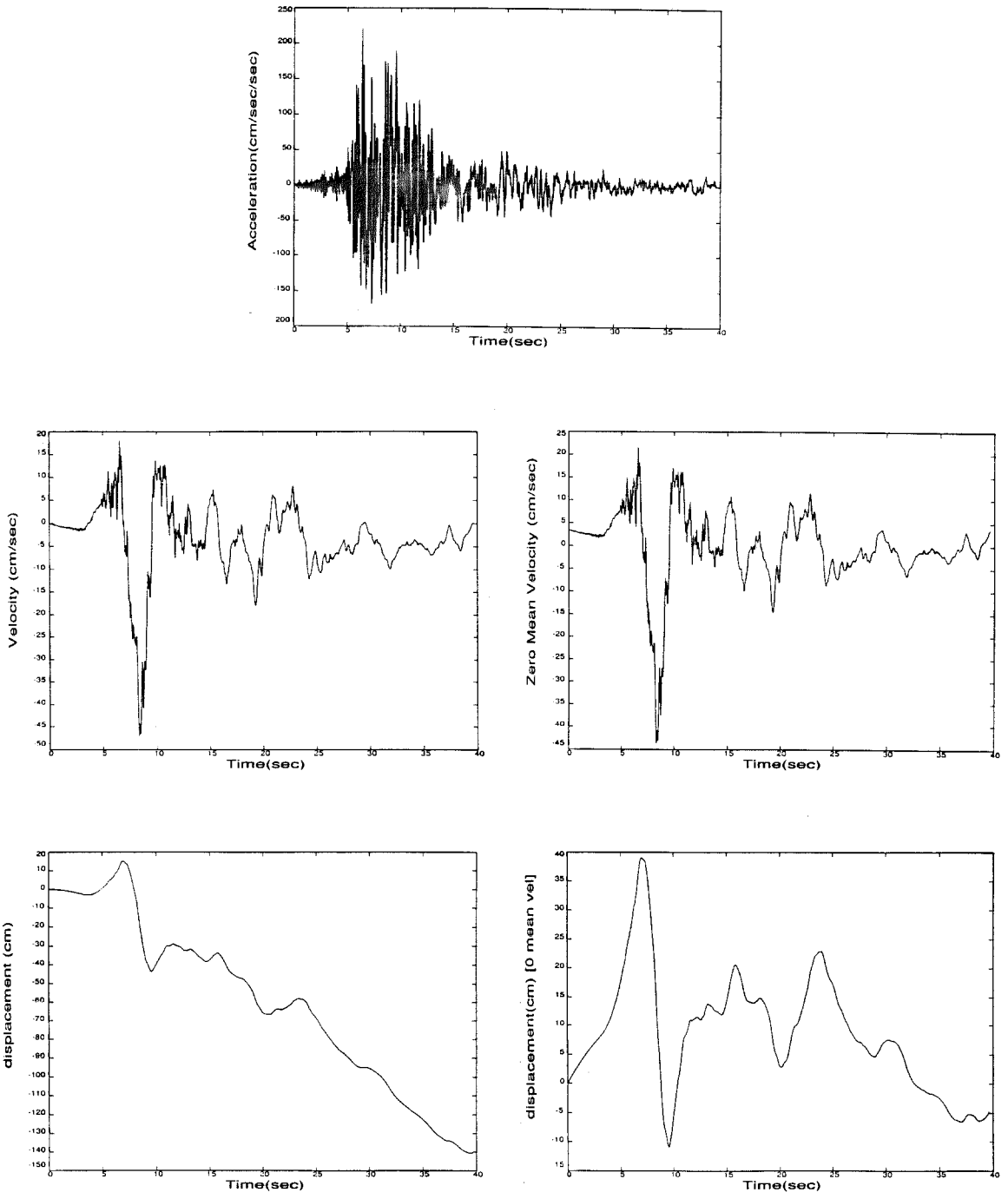

Figure 4-3-14. Imperial Valley earthquake (10/15/79). Station 3 (230°) extended to 4096 points. Far-field model processed with spectral substitution up to 0.0488 Hz (2 points).

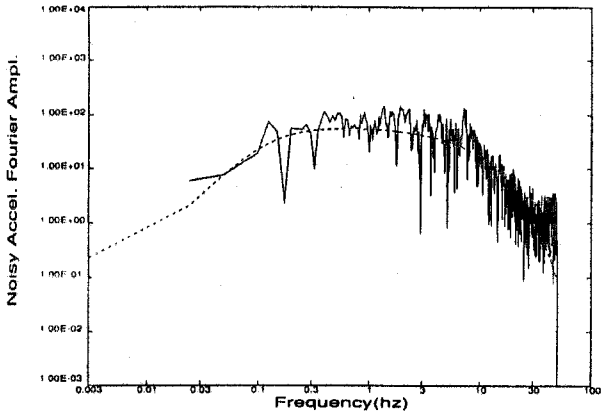

(a)

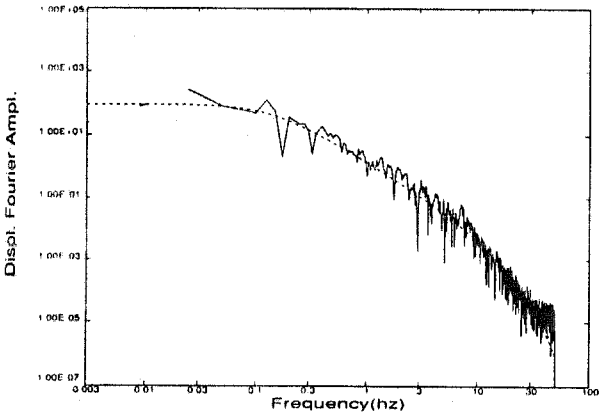

(b)

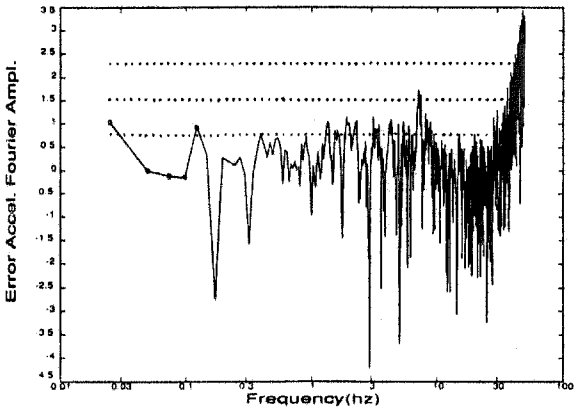

(c)

Figure 4-3-15. Imperial Valley earthquake (10/15/79). Station 2 (140°) extended to 4096 points. Spectral minimization results with the far-field model: $D_0 = 93.58$ cm.sec, $f_0 = 0.129$ Hz, $f_H = 7.59$ Hz.

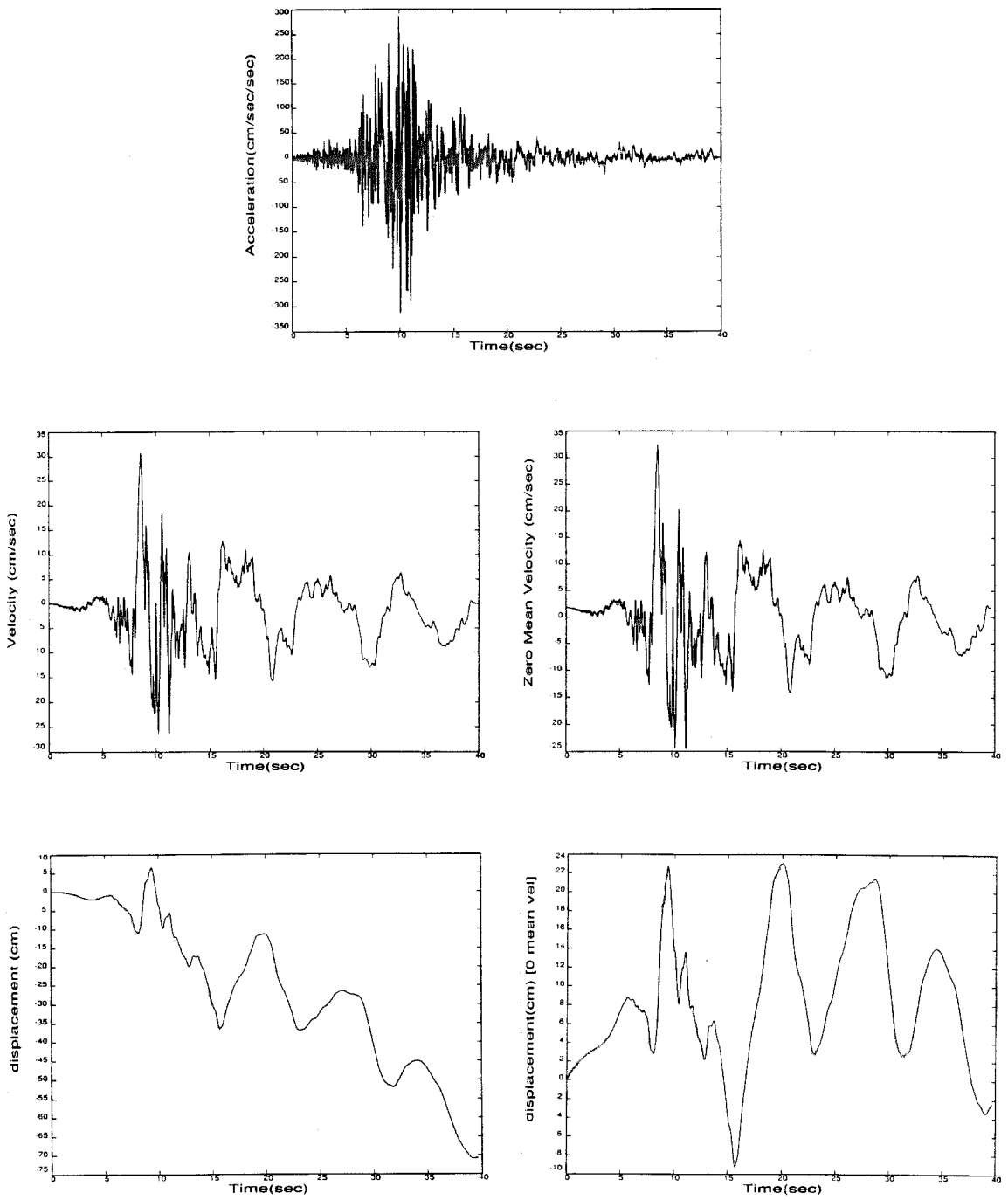

Figure 4-3-16. Imperial Valley earthquake (10/15/79). Station 2 (140°) extended to 4096 points. Far-field model processed with spectral substitution up to 0.0244 Hz (1 point).

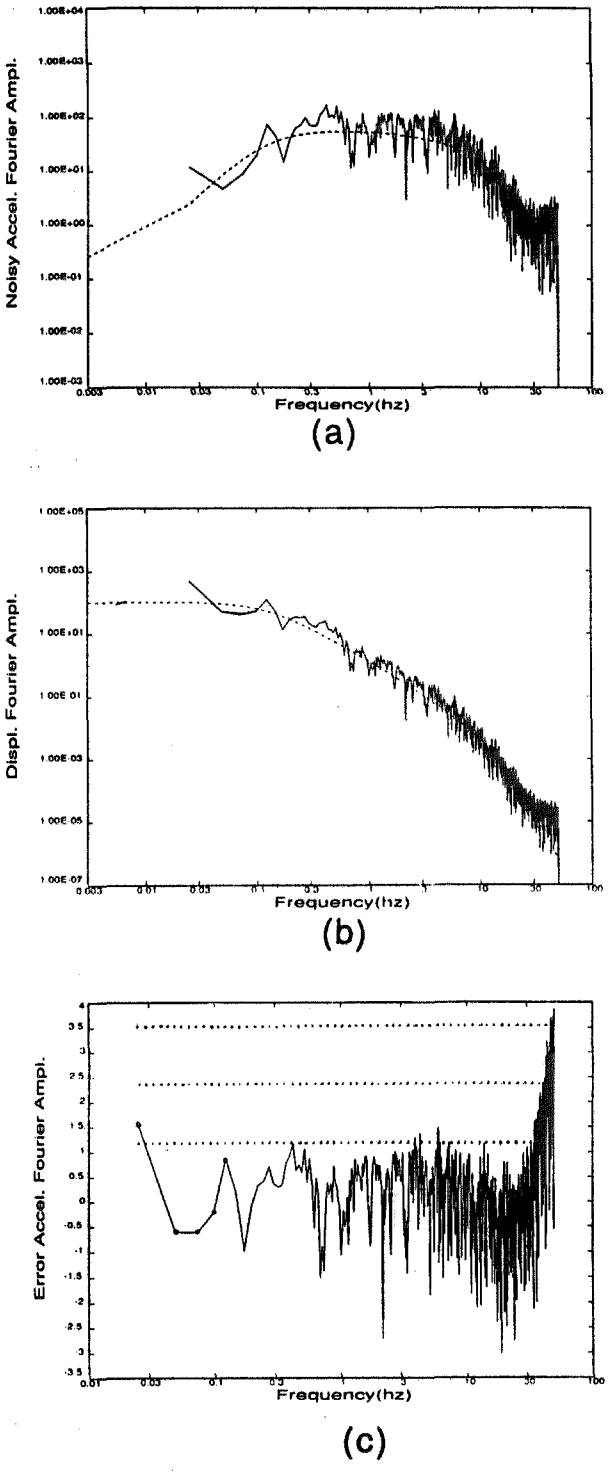

Figure 4-3-17. Imperial Valley earthquake (10/15/79). Station 3 (140°) extended to 4096 points. Spectral minimization results with the far-field model: $D_0 = 107.8$ cm.sec, $f_0 = 0.121$ Hz, $f_H = 7.05$ Hz.

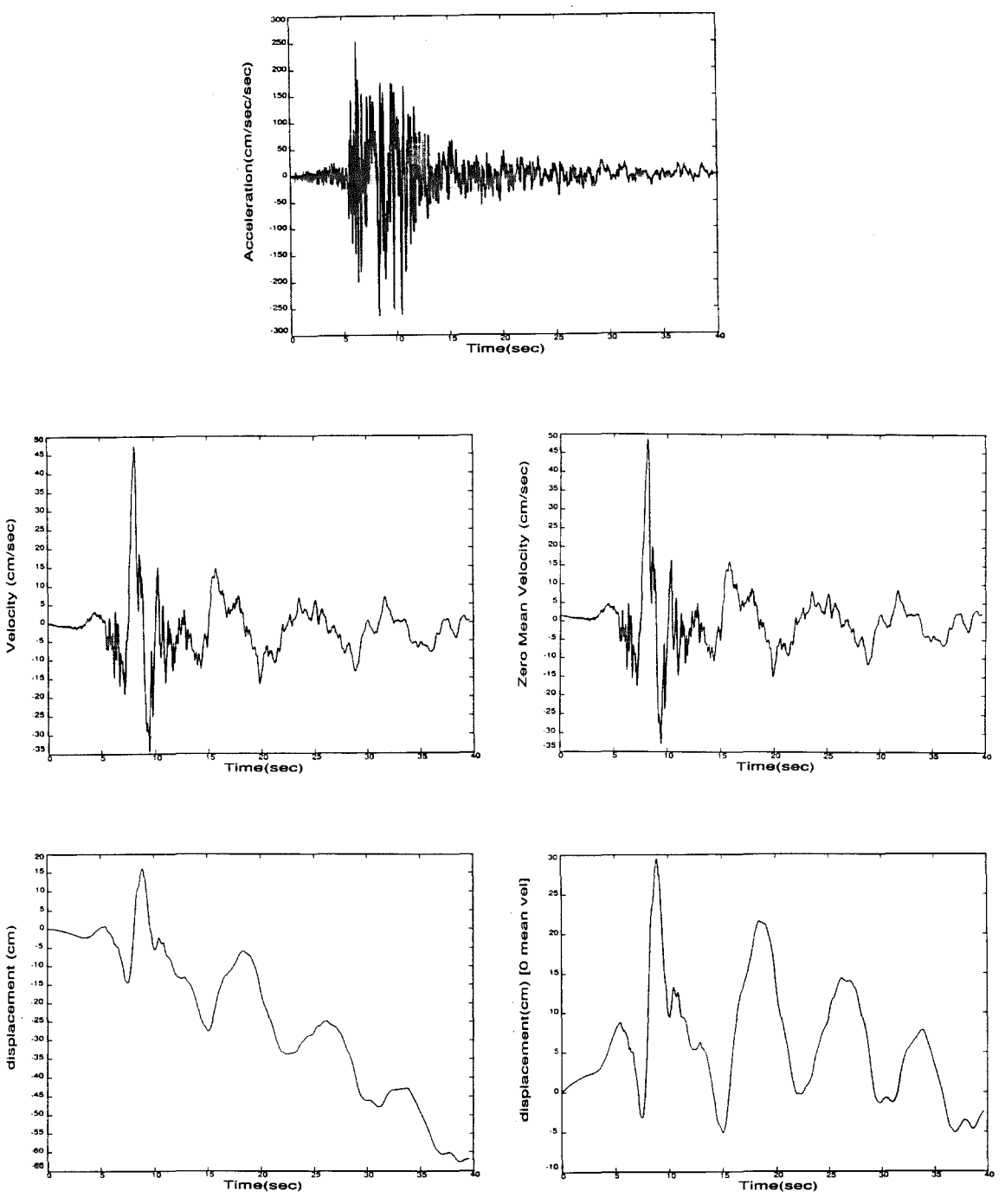

Figure 4-3-18. Imperial Valley earthquake (10/15/79). Station 3 (140°) extended to 4096 points. Far-field model processed with spectral substitution up to 0.0244 Hz (1 point).

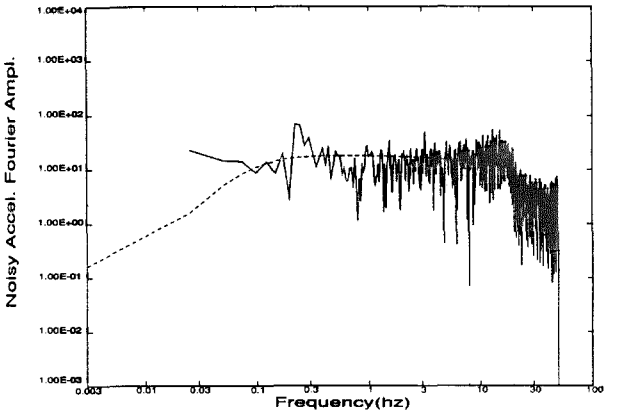

(a)

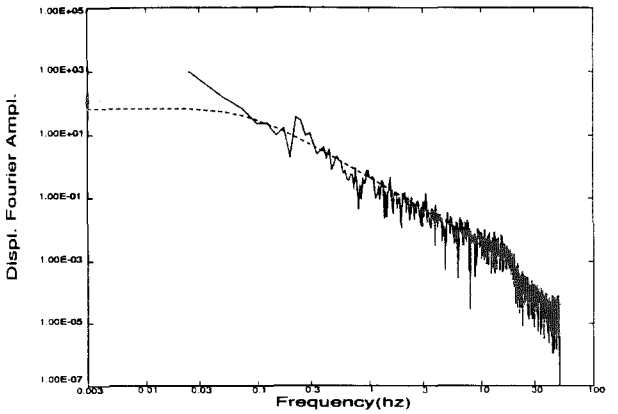

(b)

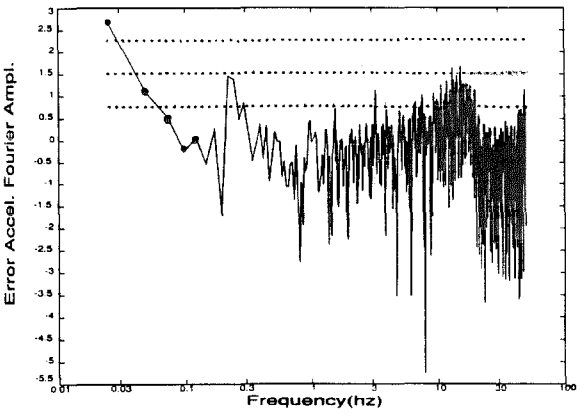

(c)

Figure 4-3-19. Imperial Valley earthquake (10/15/79). Station 2 (up) extended to 4096 points. Spectral minimization results with the far-field model: $D_0 = 71.54$ cm•sec, $f_0 = 0.081$ Hz, $f_H = 23.5$ Hz.

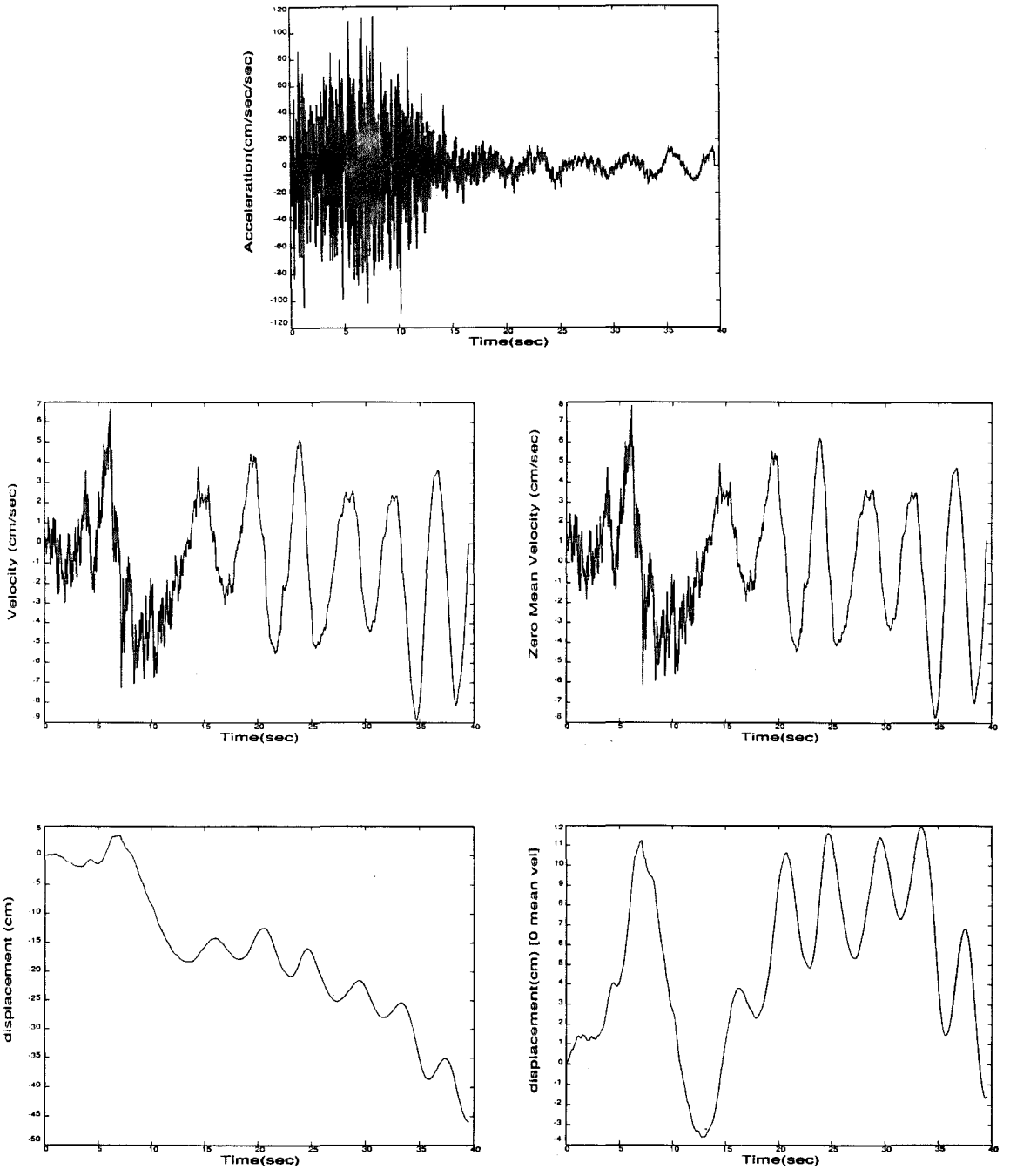

Figure 4-3-20. Imperial Valley earthquake (10/15/79). Station 2 (up) extended to 4096 points. Far-field model processed with spectral substitution up to 0.0488 Hz (2 points).

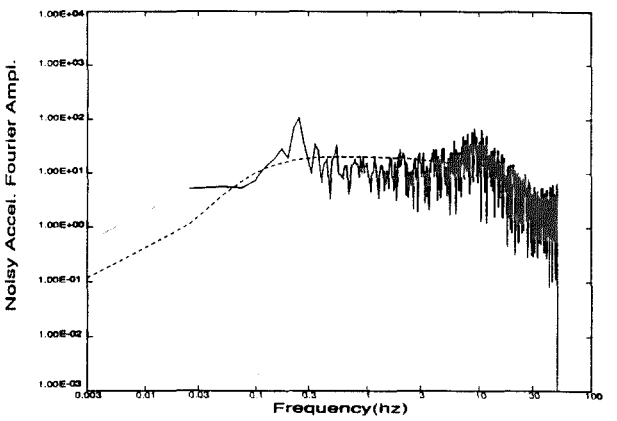

(a)

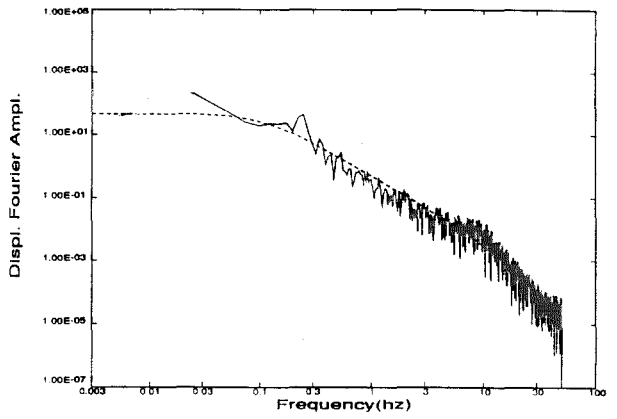

(b)

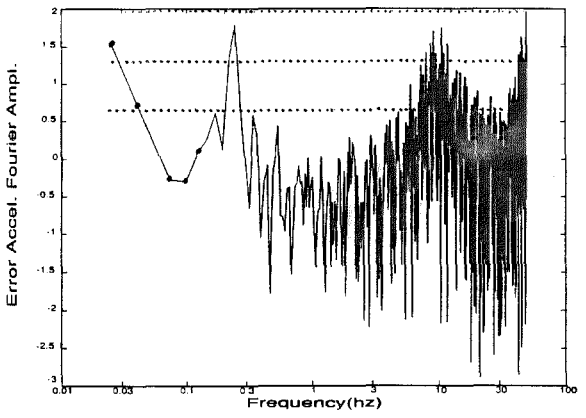

(c)

Figure 4-3-21. Imperial Valley earthquake (10/15/79). Station 3 (up) extended to 4096 points. Spectral minimization results with the far-field model: $D_0 = 49.28$ cm,sec, $f_0 = 0.106$ Hz, $f_H = 15.56$ Hz.

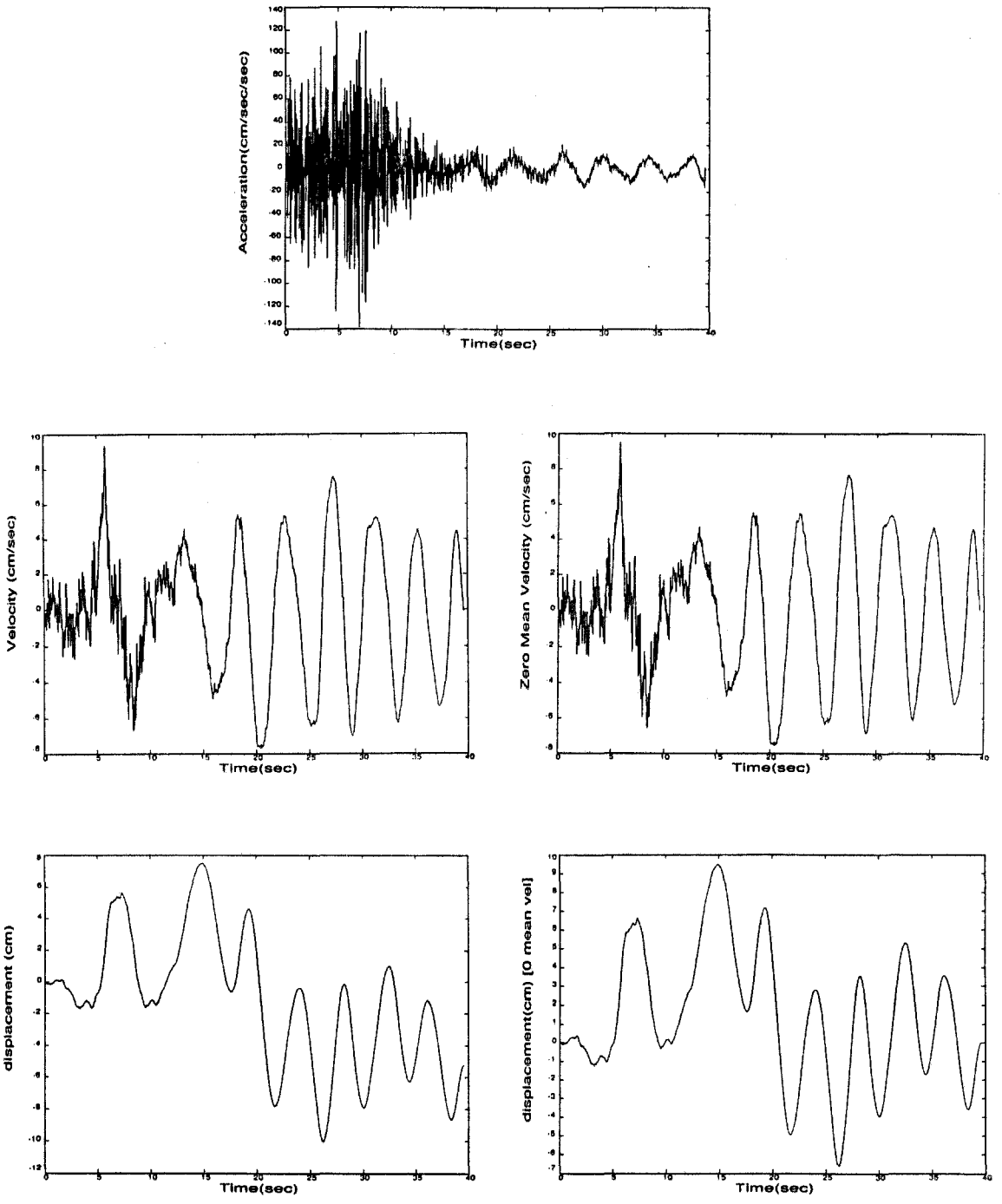

Figure 4-3-22. Imperial Valley earthquake (10/15/79). Station 3 (up) extended to 4096 points. Far-field model processed with spectral substitution up to 0.0488 Hz (2 points).

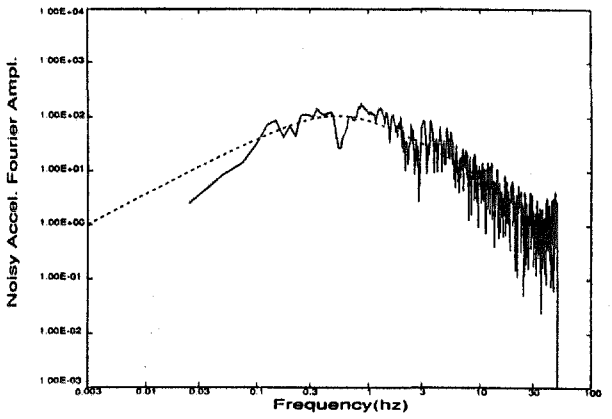

(a)

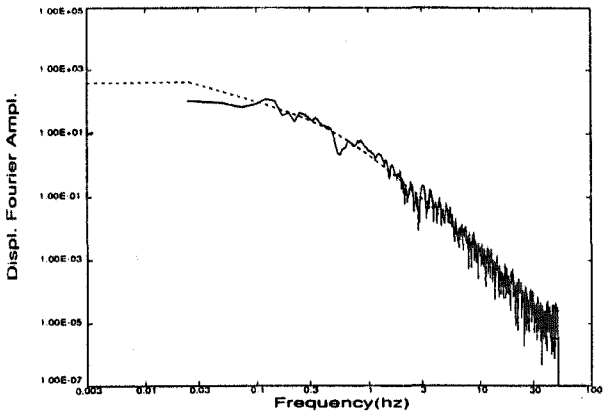

(b)

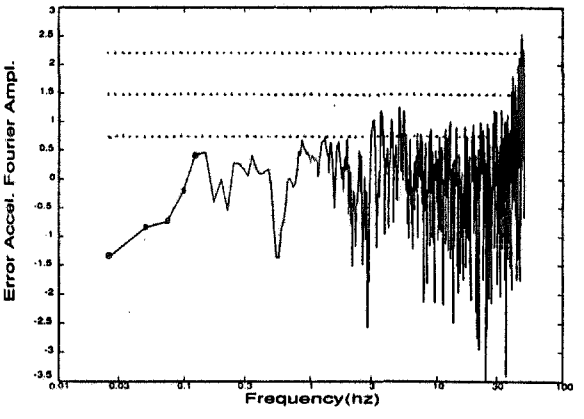

(c)

Figure 4-3-23. Imperial Valley earthquake (10/15/79). Station 7 (140°) extended to 4096 points. Spectral minimization results with the near-field model: $D_0 = 64.91$ cm, $f_0 = 0.530$ Hz, $f_H = 23.76$ Hz.

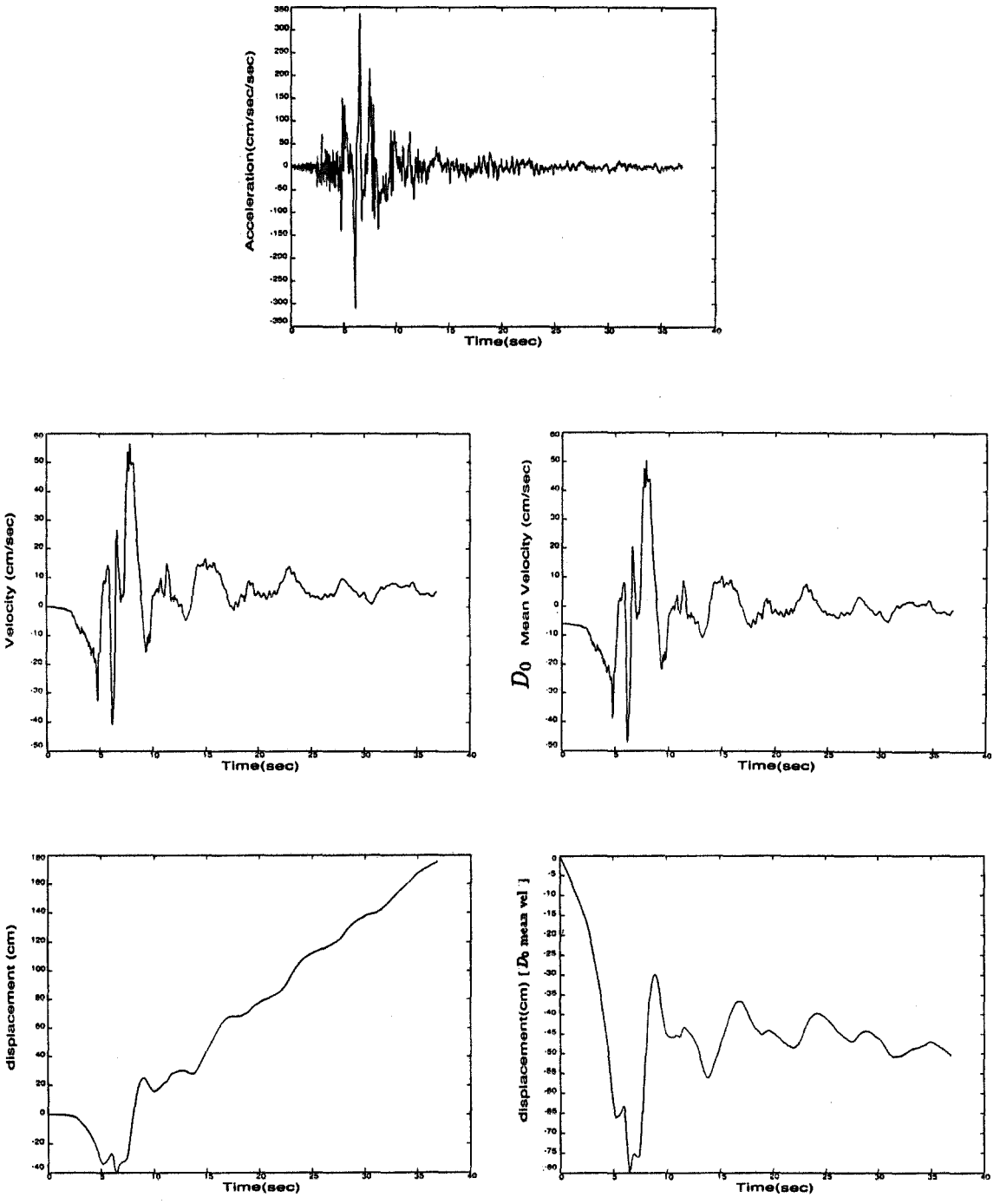

Figure 4-3-24. Imperial Valley earthquake (10/15/79). Station 7 (140°) extended to 4096 points. Near-field model processed with spectral substitution up to 0.0732 Hz with negative final displacement offset (3 points).

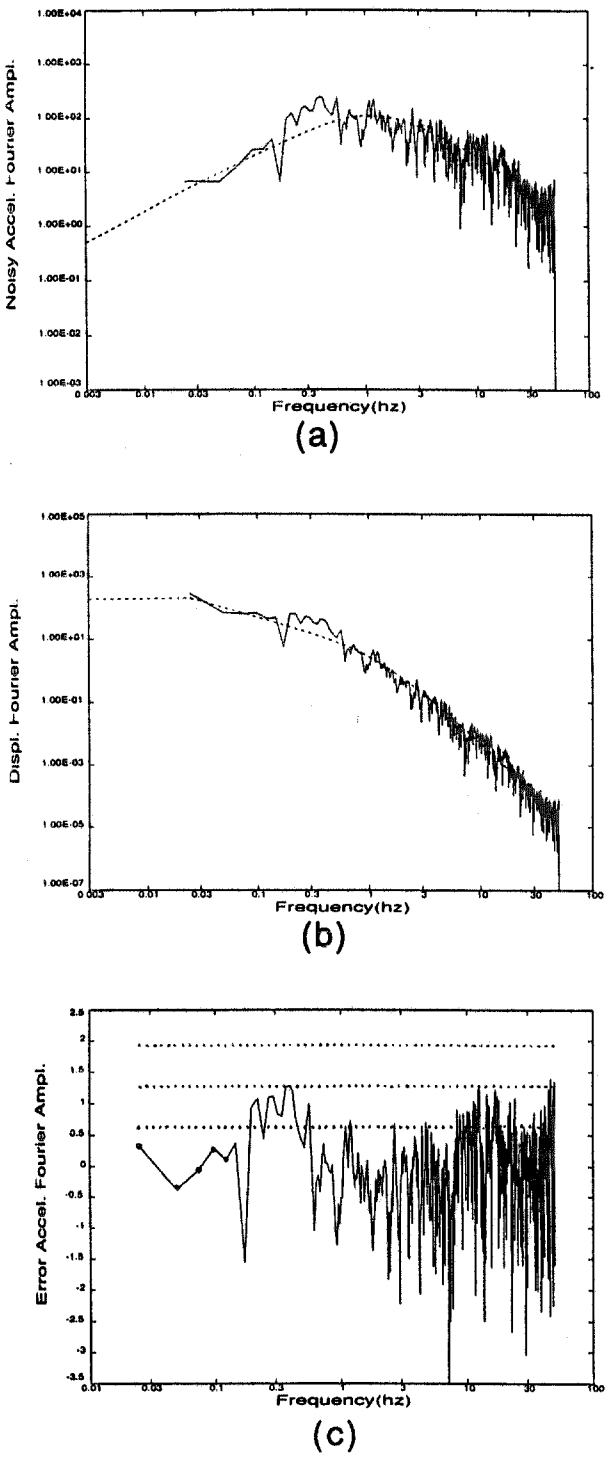

Figure 4-3-25. Imperial Valley earthquake (10/15/79). Station 6 (140°) extended to 4096 points. Spectral minimization results with the near-field model: $D_0 = 31.47$ cm, $f_0 = 1.149$ Hz, $f_H = 35.23$ Hz.

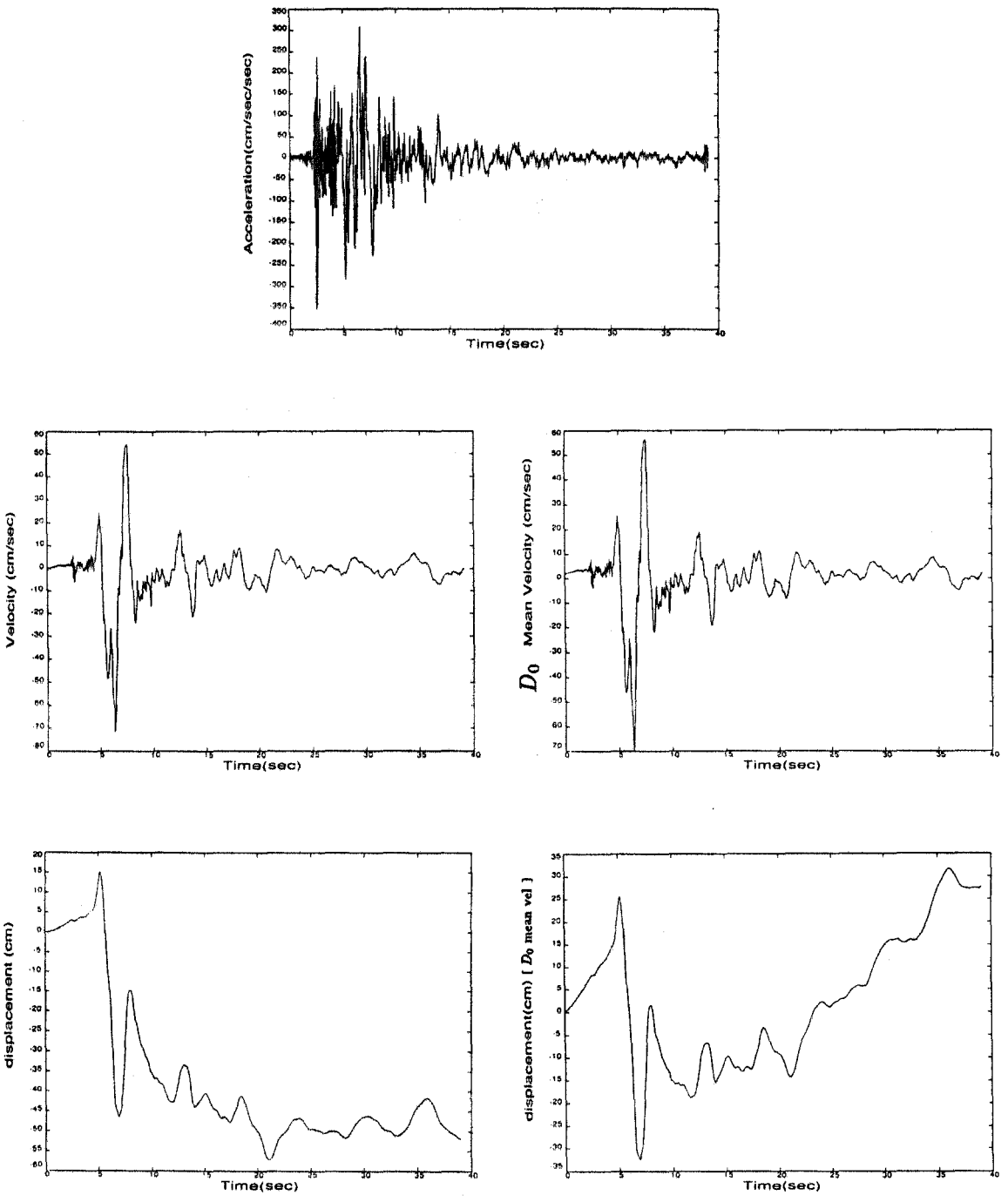

Figure 4-3-26. Imperial Valley earthquake (10/15/79). Station 6 (140°) extended to 4096 points. Near-field model processed with spectral substitution at d.c. for positive final displacement offset (0 point).

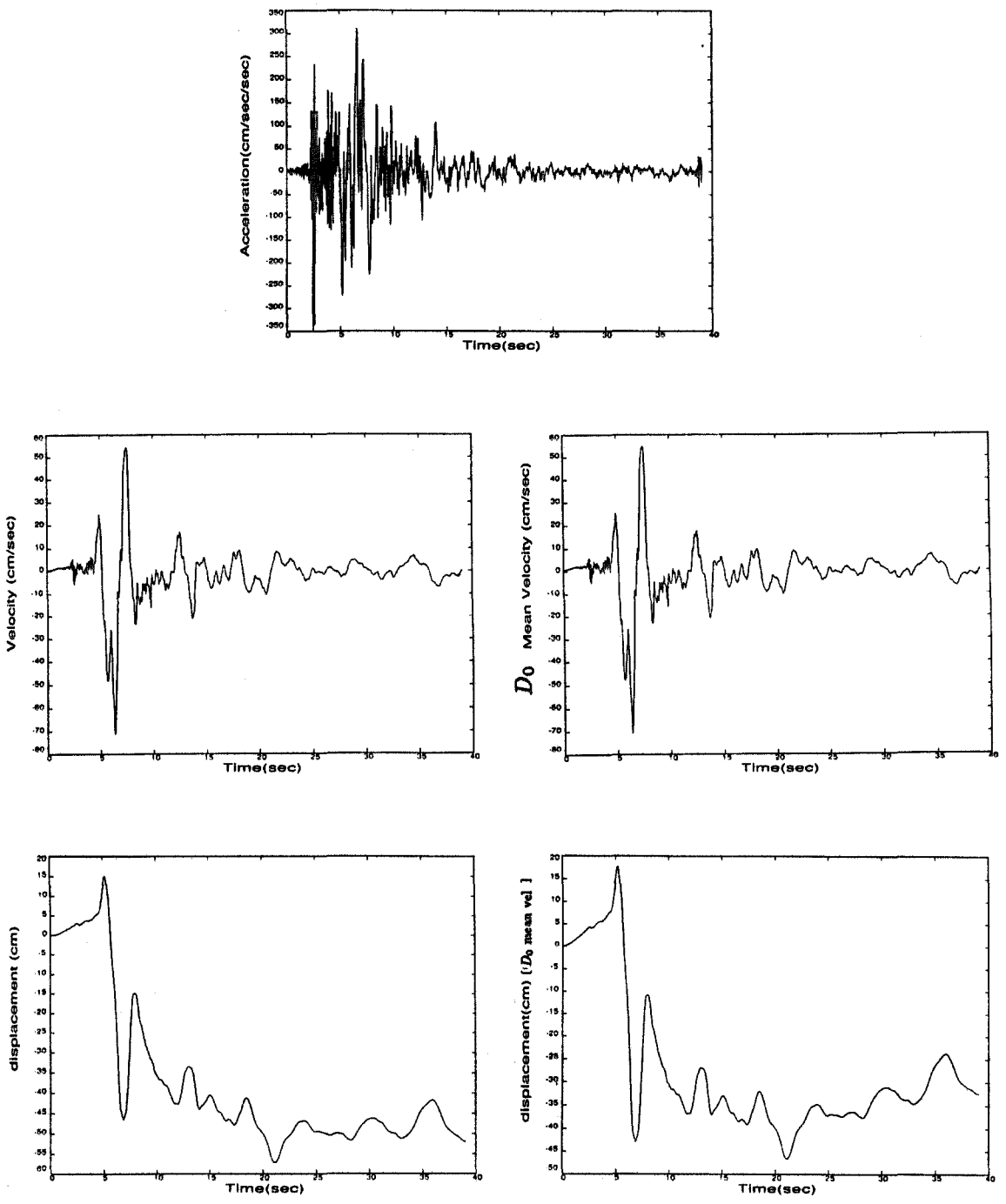

Figure 4-3-27. Imperial Valley earthquake (10/15/79). Station 6 (140°) extended to 4096 points. Near-field model processed with spectral substitution at d.c. for negative final displacement offset (0 point).

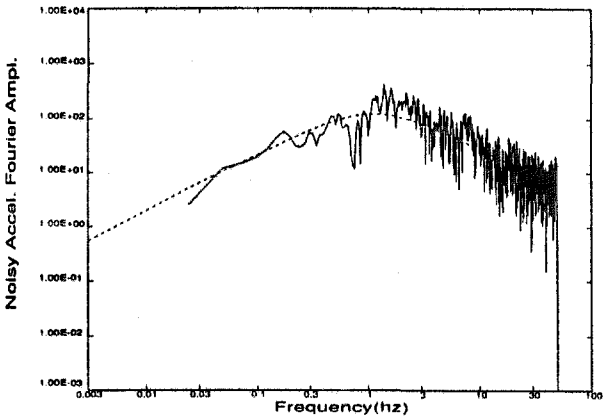

(a)

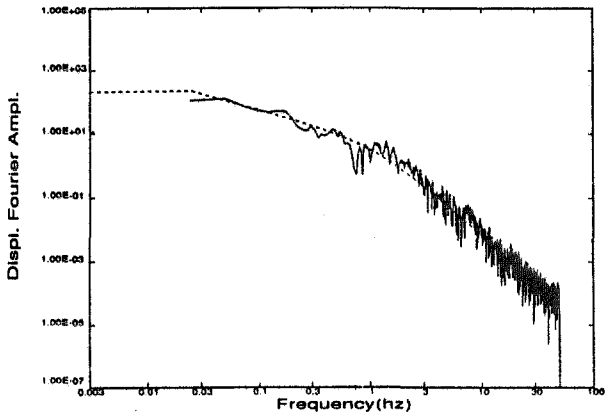

(b)

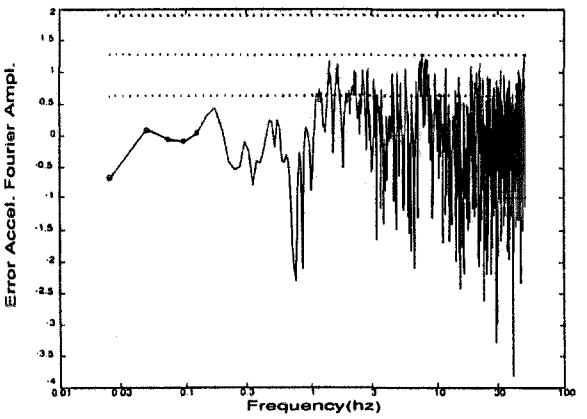

(c)

Figure 4-3-28. Imperial Valley earthquake (10/15/79). Bond's Corner (140°) extended to 4096 points. Spectral minimization results with the near-field model: $D_0 = 34.99$ cm, $f_0 = 1.113$ Hz, $f_H = 10^7$ Hz.

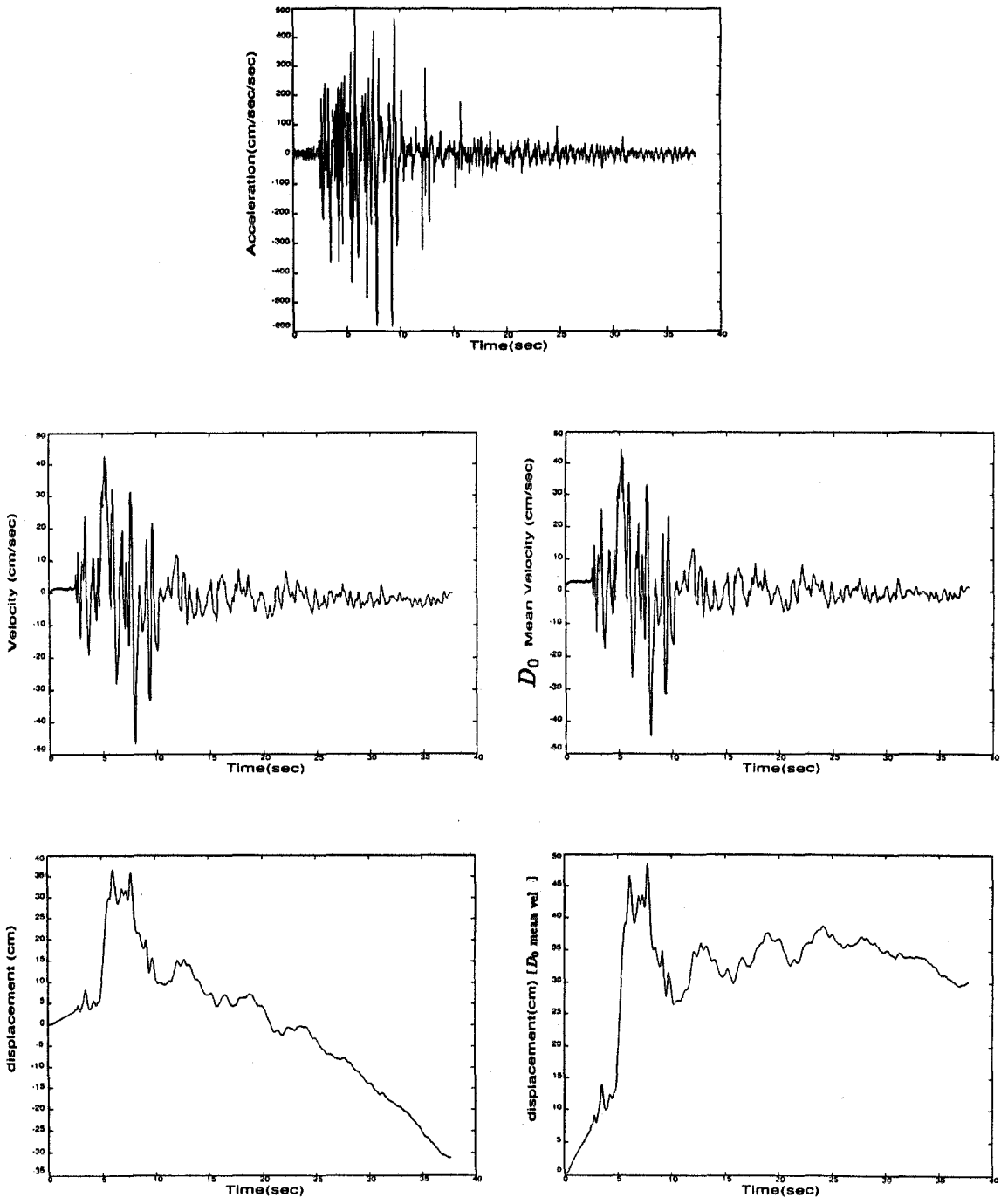

Figure 4-3-29. Imperial Valley earthquake (10/15/79). Bond's Corner (140°) extended to 4096 points. Near-field model processed with spectral substitution up to 0.0244 Hz for positive final displacement offset (1 point).

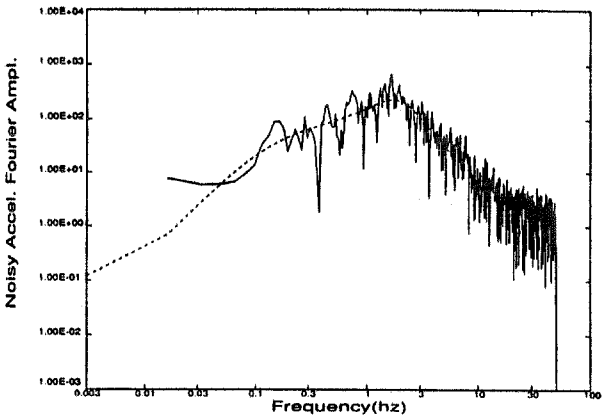

(a)

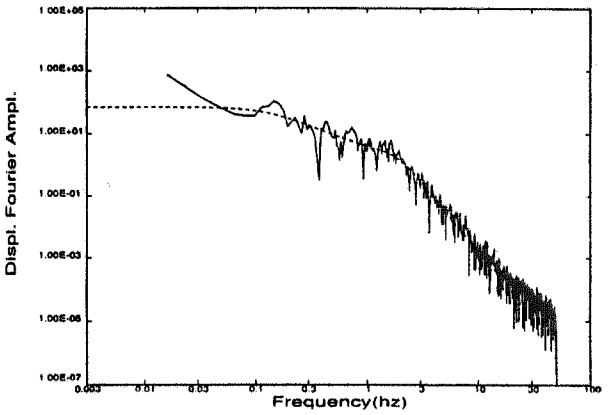

(b)

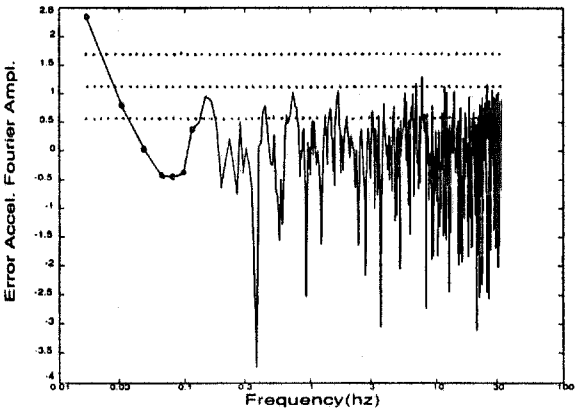

(c)

Figure 4-3-30. Imperial Valley earthquake (10/15/79). Imperial County Services building (north component, roof/W. end). Spectral minimization results with structural model: $D_0 = 68.68$ cm.sec, $f_0 = 0.15$ Hz, $f_n = 2.00$ Hz, $d = 4.44$, $c = 3.14$.

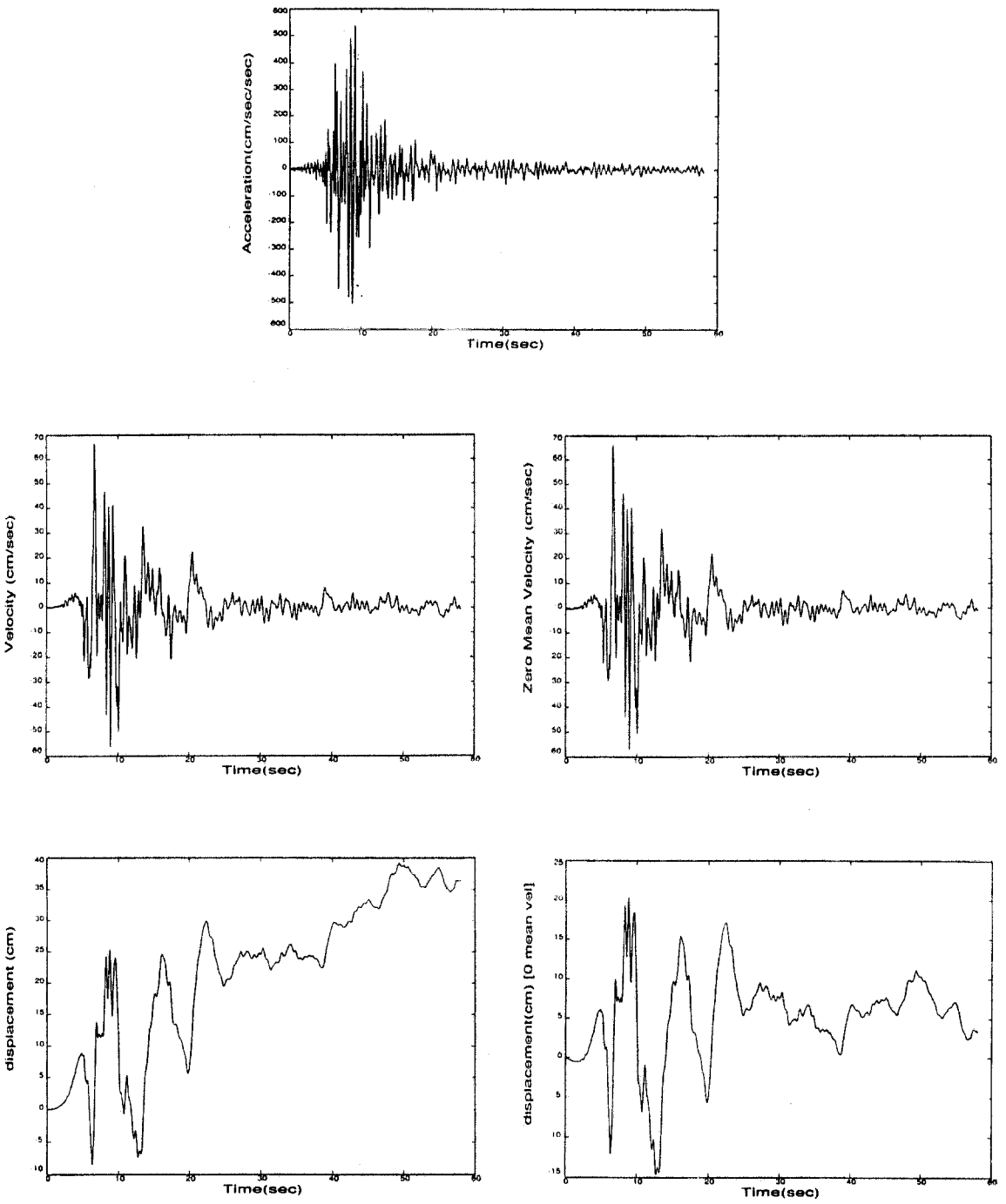

Figure 4-3-31. Imperial Valley earthquake (10/15/79). Imperial County Services building (north component, roof/W. end). Structural model processed with spectral substitution up to 0.0326 Hz (2 points).

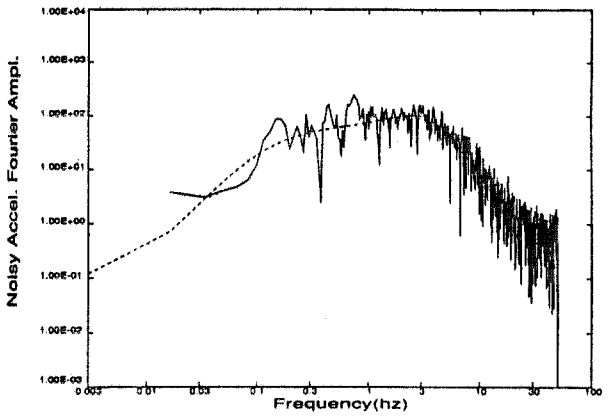

(a)

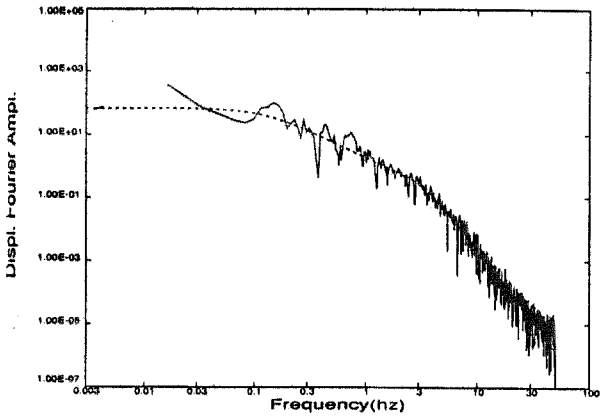

(b)

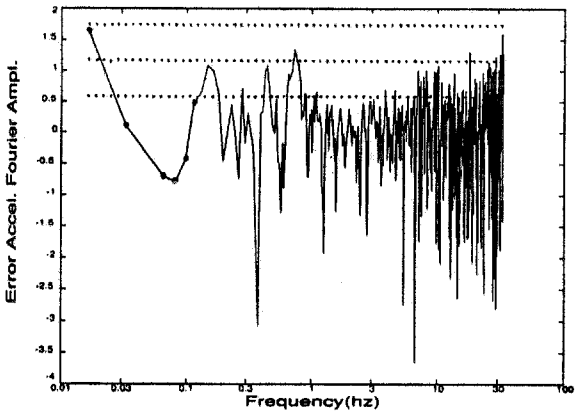

(c)

Figure 4-3-32. Imperial Valley earthquake (10/15/79). Imperial County Services building (north component, 1st floor/W. end). Spectral minimization results with structural model: $D_0 = 69.17$ cm.sec, $f_0 = 0.137$ Hz, $f_n = 3.42$ Hz, $d = 12.42$, $c = 0.735$.

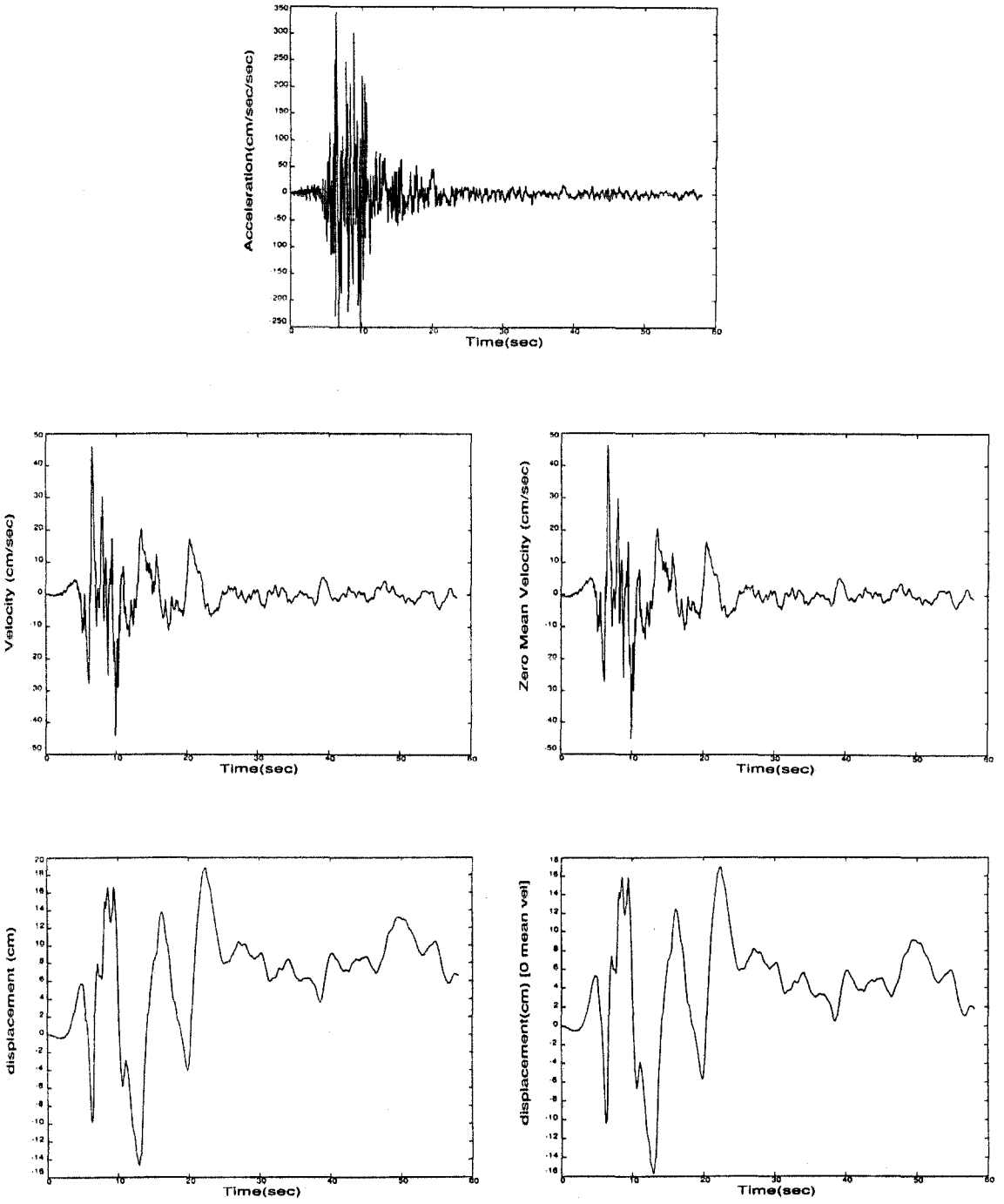

Figure 4-3-33. Imperial Valley earthquake (10/15/79). Imperial County Services building (north component, 1st floor/W. end). Structural model processed with spectral substitution up to 0.0651 Hz (4 points).

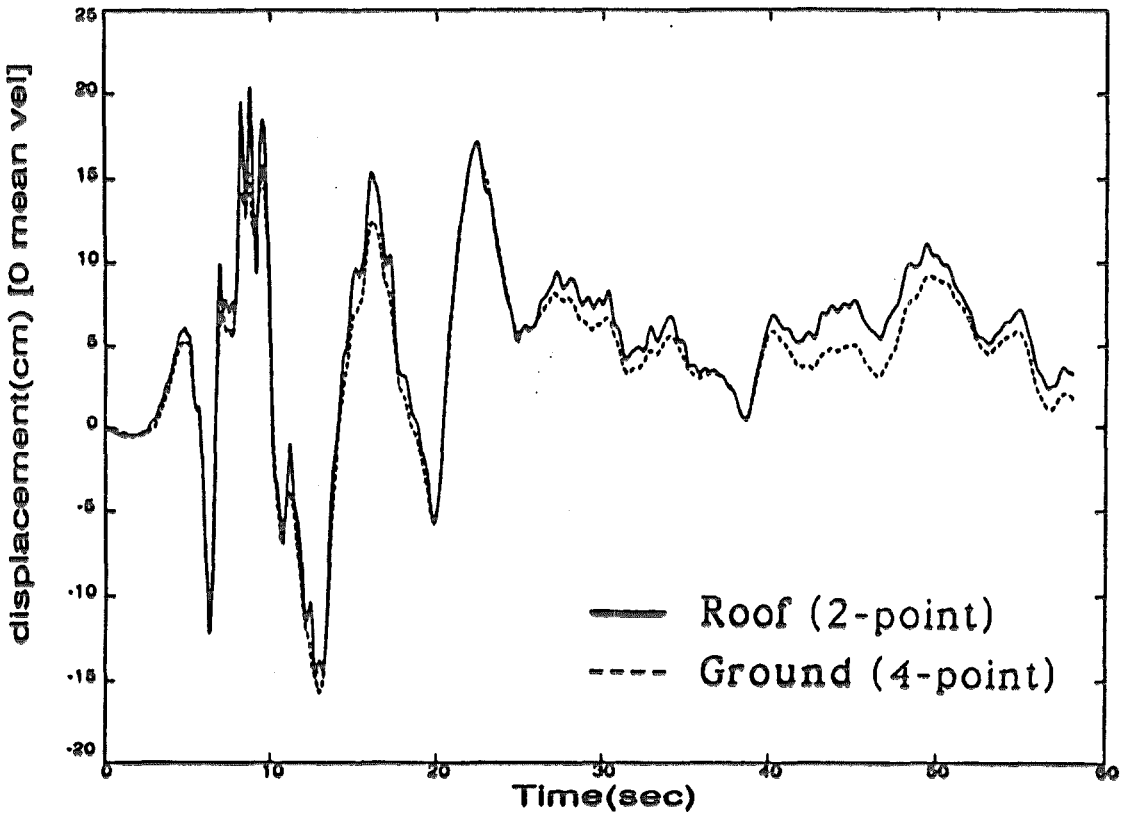

Figure 4-3-34. Ground and roof absolute displacement records corrected with the spectral substitution method. Imperial County Services Building, N./ W. end (10/15/79).

Chapter 5

CASE STUDY: FULL PROCESSING OF AN ACCELEROGRAM

In this chapter, a selected accelerogram is fully processed with the probabilistic frequency-domain approach described in Ch. 3, and corrected according to the spectral substitution method described in Sec. 4.3. The time histories obtained from this processing method are then compared to those provided by a conventional processing method.

The processing procedure is illustrated in the flowchart of Fig. 3.20. In summary, the uncorrected accelerogram is first linearly interpolated to equal time steps of 0.01 sec. The temporal mean of this record is then removed in the time domain. To use the fast Fourier transform algorithm, zeroes are then added at the end of the signal to give a power of 2, or 3 times that, whichever is smaller. In the frequency domain, if necessary, the signal is instrument-corrected according to the information provided concerning the instrument's natural period and damping.

The Fourier amplitude spectrum of the acceleration is then used to perform the optimization step of the spectral substitution method with the appropriate spectral model (near-field, far-field or structural), as described in Sec. 4.3.2. The optimal parameters describing the model are obtained, and the standard deviation of the error between the logarithm of the optimal spectral model and the logarithm of the amplitude spectrum of the measured data is computed. Overlaid plots of the optimal model spectrum and the accelerogram displacement amplitude spectrum are produced for visual inspection, as well as the error plot with the standard deviation levels. From the low-frequency portion of the error plot, the last data point to fall above the one standard deviation level is selected as the cut-off for the spectral substitution. All points of the acceleration amplitude spectrum between *d.c.* and the cut-off frequency inclusive are replaced by the amplitude spectrum of

the optimized model; the phases are left unchanged. The same procedure is used for the high-frequency correction, for which the cut-off can be selected with the above probabilistic criterion or imposed based on the instrument's natural frequency.

As an alternative to the spectral substitution method, the acceleration amplitude spectrum could be corrected with one of the noise filters described in Sec. 4.2, which reduce the level of noise throughout the whole spectrum. The signal could also be corrected with any standard band-pass filter (i.e., Ormsby, Butterworth, etc.) by multiplying the acceleration spectrum by the filter's transfer function. The signal may also be processed without implementing any of the "filter" methods; such signals will be referred to as "uncorrected" although they are possibly instrument-corrected, and will be shown later for comparison purposes. In general, the user must decide which correction method option to choose. In the software which has been developed, the default option produces both the uncorrected time histories, as well as those obtained with the spectral substitution method.

The acceleration Fourier spectra of the uncorrected and spectrally-corrected signals are then converted into the velocity and the displacement spectra, by dividing by $i\omega$ and $-\omega^2$ respectively. At *d.c.*, for all but the near-field records corrected with the spectral substitution method, the acceleration, velocity and displacement spectra are set to zero. For near-field records corrected with the spectral substitution method, the *d.c.* of the velocity spectrum is set to the estimated value D_0. The correction for the temporal mean or initial value of the signals is performed later on in the time domain.

The spectra of the uncorrected spectrally-corrected signals are then converted back into the time domain using the inverse fast Fourier transform. For far-field records, this yields time histories which have zero temporal mean. According to the developments presented in Ch. 3, the most probable acceleration and velocity have zero temporal mean, and the most probable displacement has zero initial value and is obtained from the zero temporal mean velocity. Hence, after inverse Fourier transformation, no further correction is necessary to produce the most probable acceleration or velocity. The most probable displacement is obtained by subtracting the initial value of the inverse transformed displacement time history from each

point. For near-field records corrected with the spectral substitution method, the most probable velocity has temporal mean D_0 after inverse Fourier transformation, and no other correction is then necessary. However, the most probable displacement time history must be adjusted for the D_0 temporal mean of the velocity (Eq. 4.3.23).

Once the most probable time histories are obtained, their respective standard deviations are computed according to the Eq. 3.15 for the acceleration, Eq. 3.21 for the velocity and Eq. 3.24 for the displacement. The variances for the digitization and processing noise a^2, the start-up truncation b^2, and the end truncation c^2 are assigned by the operator. Finally, plots of the uncorrected and corrected time histories are produced, and are presented bounded by one, two or three standard deviations.

The accelerogram chosen as an example is one of the structural records obtained during the Imperial Valley earthquake of October 15, 1979, at the Imperial County Services building. Description of the seismic event and of the building are given in Secs. 4.3.4 and 4.3.5. This particular accelerogram recorded the north-south motions at the west end of the roof. It has already been used in Sec. 4.3.5 as an illustration of the spectral substitution method applied to structural records.

The accelerogram was originally digitized up to 58.04 sec at unequal time increments. The record is linearly interpolated to equal time increments of 0.01 sec, and is padded at the end with 339 zeroes for a total record length of 61.43 sec. After Fourier transformation into the frequency domain, the record is instrument-corrected using the instrument's natural frequency of 55.55 Hz and damping factor of 0.66. Optimization of the five-parameter structural model (Eq. 4.3.21) is performed on the Fourier amplitude spectrum of the instrument-corrected acceleration. The estimated ground motion parameters are:

$$D_0 = 68.68 \text{ cm.sec}, \quad f_0 = 0.15 \text{ Hz},$$

and the estimated structural parameters are:

$$f_n = 2.00 \text{ Hz}, \quad d = 4.44, \quad c = 3.14.$$

Rojahn & Mork [1982] reported that the fundamental period at the west end of the building in the north-south direction elongated from 0.5 sec, at the beginning of the earthquake, to 0.8 sec after the earthquake where the structure was in a

damaged condition. This corresponds approximately to the value estimated for f_n by the optimization scheme.

Overlaid plots of the measured and the minimized model amplitude spectra for the acceleration and the displacement are presented in Fig. 4.3.30(a) and (b) respectively. The error plot of Fig. 4.3.30(c) indicates that a 2-point correction at low frequencies up to 0.0326 Hz is necessary. The error plot also shows that at high frequencies the measured data conforms well to the optimal model, and that no correction for the digitization and processing noise is necessary at that end of the spectrum. Hence, the record is only corrected at low frequencies.

According to the arguments presented in Chs. 2 and 3, the time history standard deviations are computed on the basis that for the digitization noise $a = 0.001$g, and for the start-up truncation $b = 0.033$g. It was also argued in Sec. 3.2 that the errors induced by the end truncation could be neglected as long as the accelerogram is fully digitized up to the time of instrument shut-off. Unfortunately, this has not been a common practice for older records. In particular, for the present record, the motions are still significant at 58.04 sec; at that time the accelerations are approximately ten times larger than in the initial portion just after triggering occurred. In the absence of any other information, the standard deviation c for the end truncation is tentatively set equal to ten times that of the instrument start-up b. If the probabilistic method is implemented as part of a standard accelerogram processing method, only fully digitized records should be used to avoid these unnecessary uncertainties.

The most probable uncorrected acceleration $\ddot{z}_{0n}$, velocity $\dot{z}_{0n}$, and displacement z_{0n} are far-field records computed according to the flowchart of Fig 3.20. These time histories are obtained without any filtering, and are only altered in the time domain to obtain zero initial displacement. Hence, they represent the structural motion given by the data as recorded and measured. The most probable time histories (solid line) are presented bounded by one, two, and three standard deviations (dotted lines) in Figs. 5.1, 5.2, 5.3 respectively. The most probable acceleration and velocity time histories appear to behave properly and the plots show that the associated uncertainties are very low even at the three standard deviation

level. The most probable uncorrected displacement time history on the other hand displays an unrealistic long-period component, so that it would be doubtful that the true displacement would be bounded by the three standard deviation uncertainty level. It has been shown in Chs. 3 and 4 that this long-period error is dominantly due to the premature end truncation of the digitization process which creates a large shift in the temporal mean of the acceleration and velocity. It was observed that in the frequency domain, this created large errors in the estimate of the first few components of the spectrum. Relative to the size of the measured spectrum, these errors remain minimal for the acceleration, and are acceptable for the velocity, but become clearly predominant for the displacement after double integration. Such a source of displacement error could be greatly reduced if the full length of the recorded and digitized accelerogram was provided. As it stands, the time histories that are presented in Figs. 5.1 through 5.3 remain the most probable, although it is certain that better estimates could be achieved if the full length of the accelerogram could be used in the processing procedure.

The values used for a^2 and b^2 are based on laboratory tests and measurements, and should be representative. It was also shown in Ch. 3 that these values provided proper bounds to the noise-corrupted and start-up truncated synthetic accelerograms. Hence, the fact that the three standard deviation level does not appear to provide sufficient bounds for the most probable uncorrected displacement is indicative that the variance c^2 assigned to the uncertainty in the acceleration from end truncation is still not large enough. This is quite surprising since the value used for c^2 is 100 times larger than b^2 for the instrument trigger, and is 1000 times larger than a^2 for the digitization and processing noise. Apparently for this accelerogram, the source of error of greatest concern is not the digitization and processing noise, nor the missing initial points, but the error in the acceleration temporal mean due to undigitized data at the end of the original analog record. Fortunately, this source of error is well corrected for by the spectral substitution method.

The most probable acceleration, velocity and displacement corrected with a 2-point spectral substitution up to 0.0326 Hz are presented by the solid line in Figs. 5.4, 5.5., 5.6 and are bounded respectively by one, two and three standard

deviations represented by the dotted lines. There are practically no changes in the most probable acceleration and velocity compared to the uncorrected results, and the standard deviations still appear to provide small but proper bounds. However, the most probable displacement obtained after spectral substitution no longer displays the long-period error observed in the uncorrected time history. The displacement standard deviations that bound these records are still computed with the same assumptions on c^2 as given for the uncorrected results. It would now appear that this is too conservative an assumption since only one standard deviation seems to provide sufficient bounds about the most probable displacement, whereas for the three standard deviation level the uncertainty at the end of the displacement signal is almost three times larger than the peak value. This is expected, since the spectral substitution method removes some of the error-dominated harmonics at low frequencies which govern the errors in the displacement time histories. Hence, when using the spectral substitution method, the standard deviations should be decreased. However, in the absence of any further information concerning the undigitized data at the end of the accelerogram and of a more elaborate approach which incorporates the error-reduction from the spectral substitution method, the standard deviations can only be roughly estimated.

Next the time histories obtained by the 2-point spectral substitution method up to 0.0326 Hz are compared to the those provided by the California Divisions of Mines and Geology (CDMG) in Volume II. The records from the Imperial Valley earthquake of October 15, 1979 obtained at the Imperial County Services building were processed by using a standardized package maintained at the Lawrence Berkeley Laboratory of the University of California. The processing method is similar to the one used in the late seventies by the *USGS* and is an improved version of the time-domain processing method presented in Sec. 2.5. The high-pass and low-pass Ormsby filters had transition bandwidths of 0.03-0.17 Hz and 23.0-25.0 Hz [Porter, 1982]. Hence, only the signal in the 0.17-23.0 Hz range should be unchanged from the measured data. This is observable in Fig. 5.7 which represents the overlaid plots of the Fourier amplitude spectrum of the processed displacements with the 2-point spectral substitution as a solid line and the CDMG Volume II method as a dashed line. There is a significant difference between the two processing method

at low frequencies below 0.17 Hz. The amplitudes near *d.c.* are 100 times smaller with Volume II, and are still quite small up to approximately 0.1 Hz. The spectral substitution method provides information on periods in the time histories above 6 sec without creating any long-period drift in the displacement.

At high frequencies, Volume II uses the Ormsby filter to remove all contributions above 25 Hz. The probabilistic method indicated that no correction is required, so none was implemented. But surprisingly enough Fig. 5.7 shows that the time history obtained with the spectral substitution method with no high-frequency correction has significantly less high-frequency content, by two orders of magnitude, above 10 Hz than does the one obtained with Volume II which implements a high-frequency filter. Furthermore, the fall-off at high-frequencies in the most probable displacement appears to have a reasonable behavior [Anderson & Hough, 1984]. As has been studied in Ch. 2, part of this high-frequency error found in the Volume II processing could be attributed to the trapezoidal integration rule, and the repeated filtering of the acceleration, velocity and displacement with the Ormsby filter. The inference is that the frequency-domain processing method provides better estimates for the high-frequency behavior of the recorded accelerogram than does the standard Volume II method.

Comparison of the time history results for the two methods is presented in Fig. 5.8, on the left of which are overlaid plots of the processed acceleration, velocity, and displacement where the solid line is the spectrally-substituted signal, and the dotted line is the Volume II corrected signal. On the right of Fig. 5.8 are plots representing the difference between the respective time histories. The difference in the acceleration time histories is barely visible, but the plot of the difference shows the two methods disagree mainly at high frequencies for the reasons explained in the previous paragraph and illustrated in Fig. 5.7. The difference in the treatment of the high-frequency portion of the spectrum leads to disagreements in the acceleration of the order of 10% of the peak. The velocity time histories also only differ slightly, and the dominant difference is an 8-second period representing amplitudes of about 10% of the peak. From the analysis performed in Ch. 4 on the free-field records, it was seen that 8 sec may correspond to a resonant period of the Imperial

Valley. This 8-second period cannot be observed in the time histories processed with Volume II, since it filters out all frequencies below 0.17 Hz. This difference at the 8-second period is emphasized in the displacement time histories and is responsible for differences in the peaks of close to 50% in the strong shaking portion of the record, although the overall motions are in phase and follow the same trends. Although it has no physical justification, Volume II forces the displacement time histories to have zero temporal mean. This can be observed in Fig. 5.8 where the Volume II displacement oscillates about the zero baseline. The displacement obtained with the 2-point spectral substitution method has a bias towards positive displacements due to a non-zero temporal mean, which is expected in theory. This same behavior was observed in the corresponding first-floor record (Fig. 4.3.33), and can be attributed to the influence of the source mechanism on the ground motion.

The comparison of the processed time histories obtained with these two methods shows among other things that there can be large differences due to the nature of the correction procedure. The frequency-domain processing method, in conjunction with the spectral substitution correction at low frequencies, has shown to produce satisfactory results with only a minimal amount of correction. This method has the advantage of preserving most of the recorded accelerogram unaltered. The low-frequency harmonics that are statistically determined to have a small signal-to-noise ratio are not discarded, but simply set back to their most probable value. The corrected acceleration, velocity and displacement are presented bounded by several levels of standard deviations to depict the uncertainties associated with each of the time histories due to digitization and processing noise, as well as errors in the estimate of the acceleration temporal mean from missing data at the beginning and the end of the record. The frequency-domain method, in conjunction with the spectral substitution method, is a better option for processing of accelerograms.

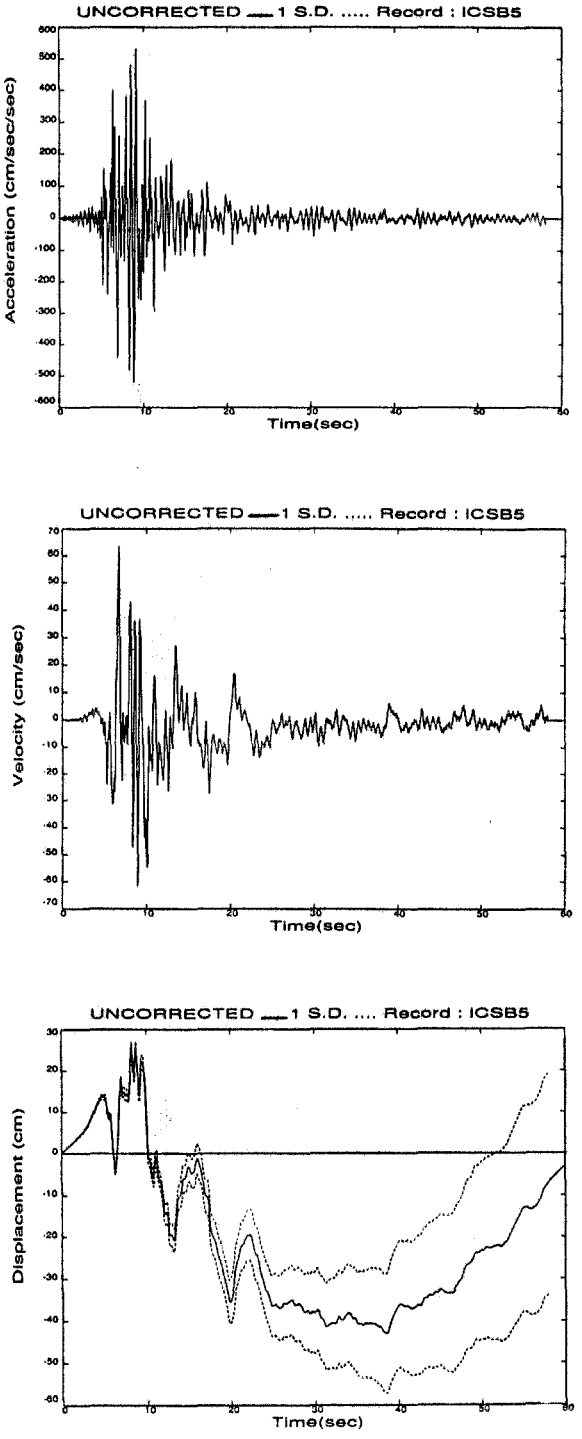

Figure 5-1. Imperial Valley earthquake (10/15/79). Imperial County Services building (north component, roof/W. end). Processed with the frequency domain method for 1 standard deviation reliability bound and no spectral substitution.

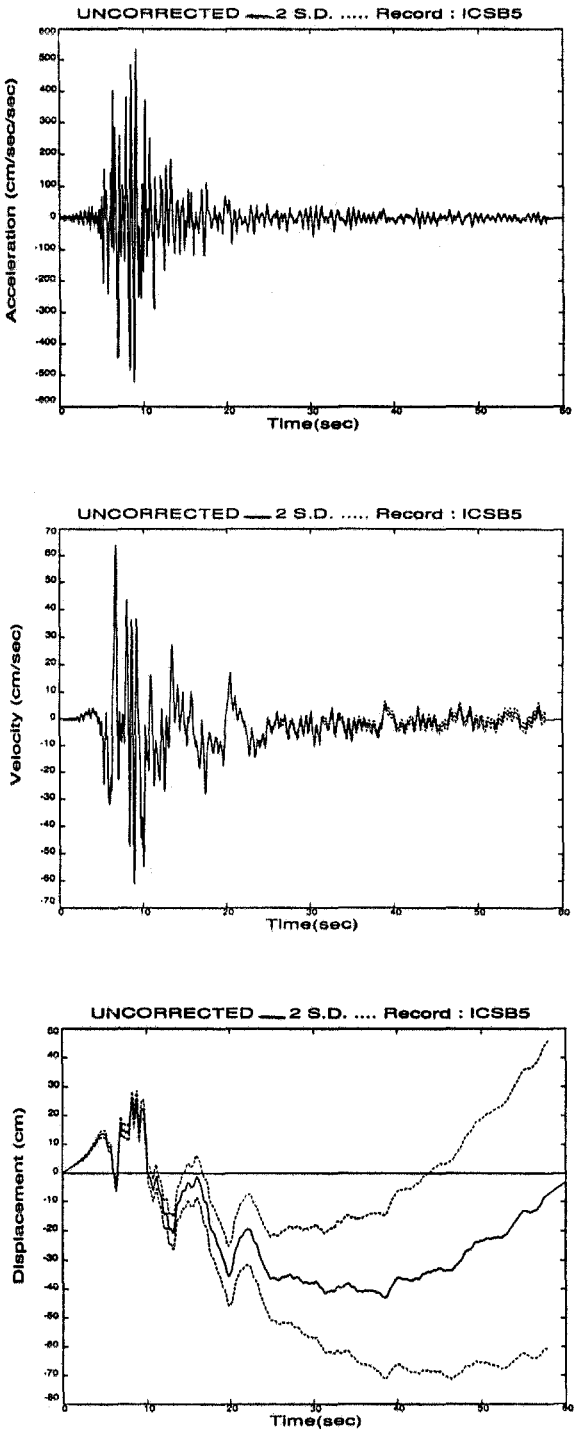

Figure 5-2. Imperial Valley earthquake (10/15/79). Imperial County Services building (north component, roof/W. end). Processed with the frequency domain method for 2 standard deviation reliability bound and no spectral substitution.

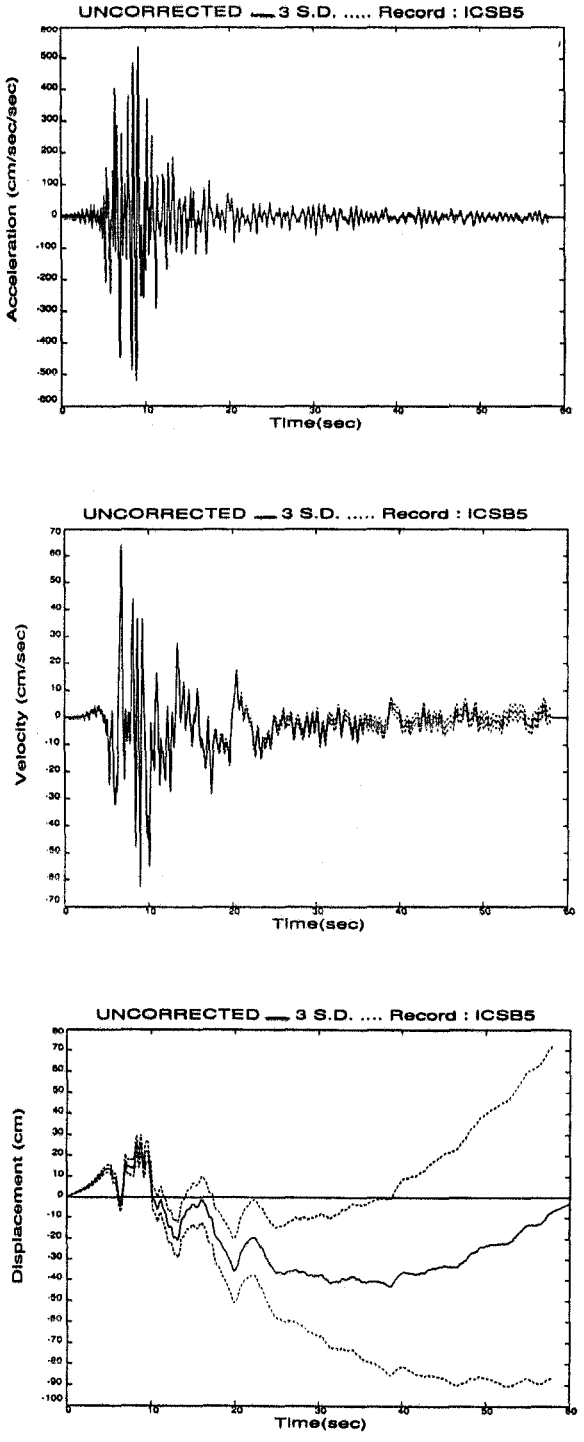

Figure 5-3. Imperial Valley earthquake (10/15/79). Imperial County Services building (north component, roof/W. end). Processed with the frequency domain method for 3 standard deviation reliability bound and no spectral substitution.

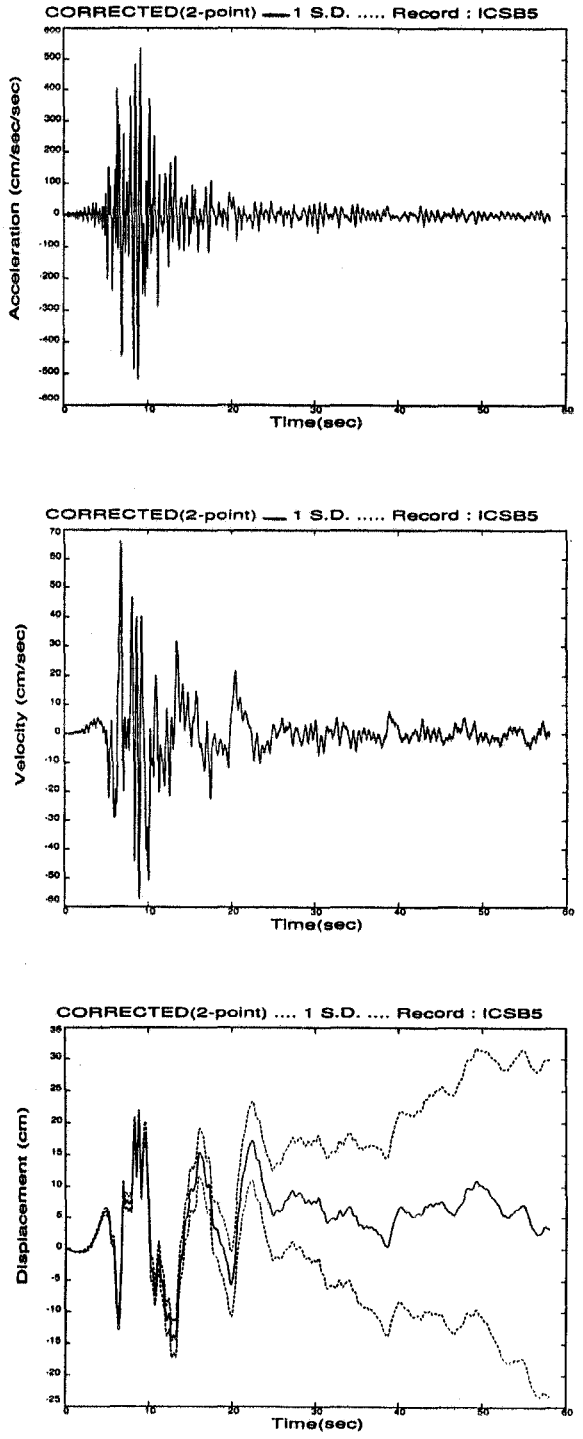

Figure 5-4. Imperial Valley earthquake (10/15/79). Imperial County Services building (north component, roof/W. end). Processed with the frequency domain method for 1 standard deviation reliability bound and 2-point spectral substitution.

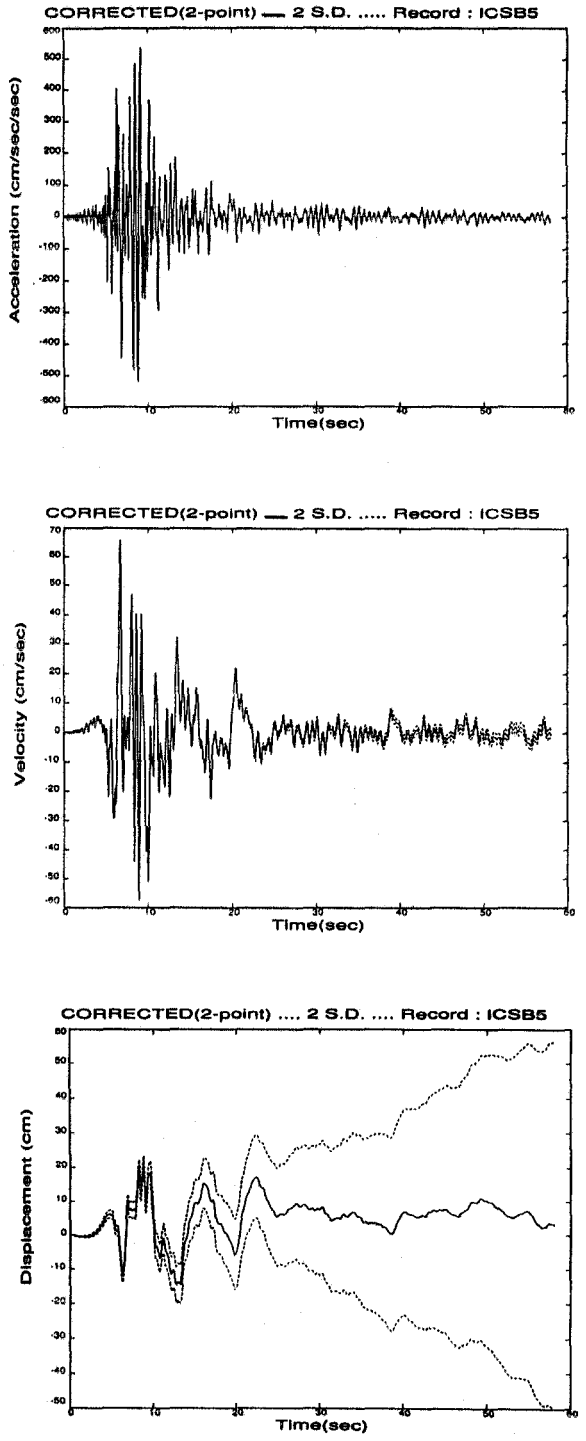

Figure 5-5. Imperial Valley earthquake (10/15/79). Imperial County Services building (north component, roof/W. end). Processed with the frequency domain method for 2 standard deviation reliability bound and 2-point spectral substitution.

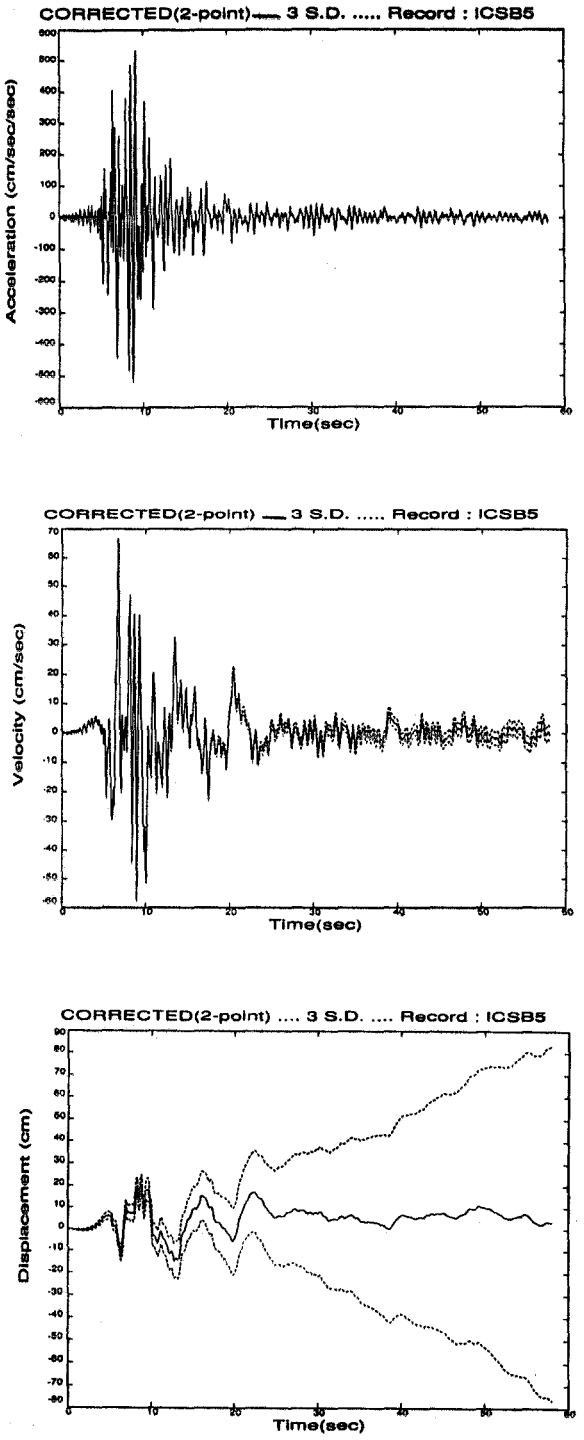

Figure 5-6. Imperial Valley earthquake (10/15/79). Imperial County Services building (north component, roof/W. end). Processed with the frequency domain method for 3 standard deviation reliability bound and 2-point spectral substitution.

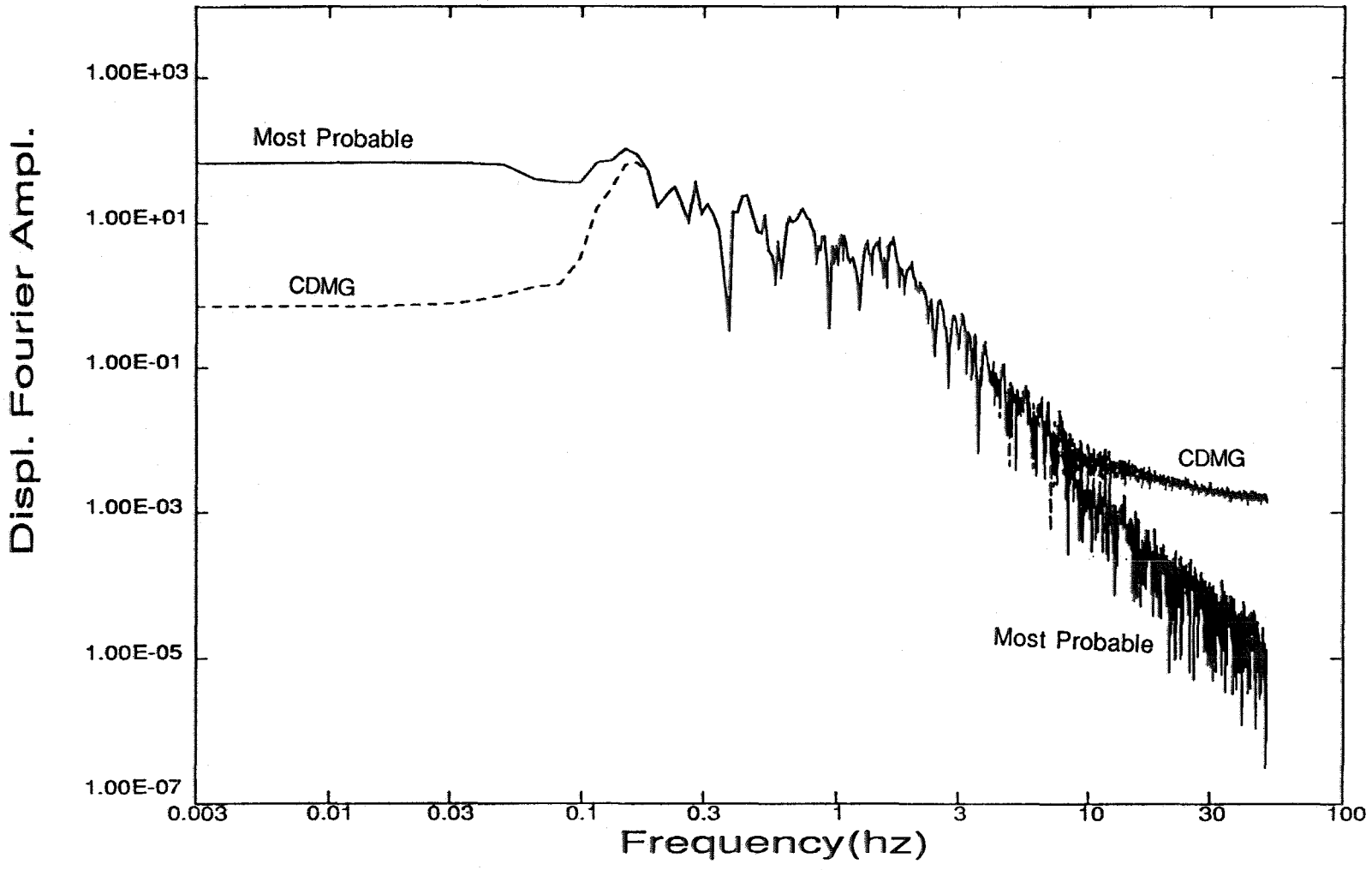

Figure 5-7. Imperial Valley earthquake (10/15/79). Imperial County Services building (north component, roof/W. end). Displacement Fourier amplitude spectrum (cm·sec).

(___ : 2-point spectral substitution up to 0.0326 Hz
- - - : Volume II correction, filter 0.03–0.17 — 23.0–25.0 Hz)

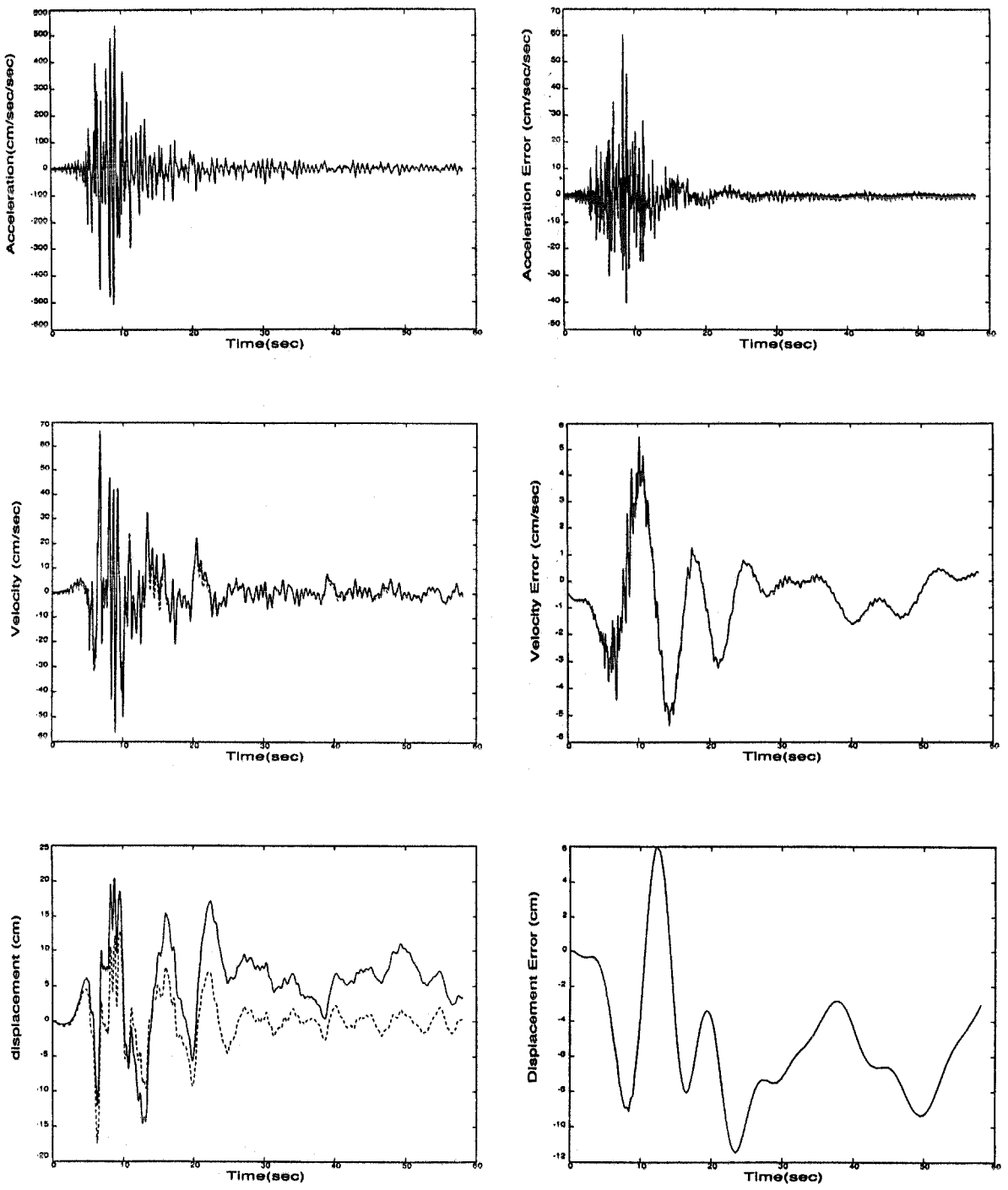

Figure 5-8. Imperial Valley earthquake (10/15/79). Imperial County Services building (north component, roof/W. end). Corrected time histories and errors.

(___ : 2-point spectral substitution up to 0.0326 Hz
- - - : Volume II correction, filter: 0.03–0.17 — 23.0–25.0 Hz)

Chapter 6

CONCLUSIONS AND RECOMMENDATIONS

In Ch. 2 a systematic approach to the study of errors found in processed accelerograms was proposed. This method used synthetic accelerograms generated by closed-form expressions for the accelerations, which could be exactly integrated to produce the corresponding velocities, displacements and spectra. The proposed analytical expression of the acceleration did not attempt to reproduce exactly the motion of a specific earthquake, but has proven to be general enough to capture most of the features expected from strong-motion records. The equation for the synthetic acceleration called for parameters which were randomly chosen within pre-specified bounds. This allowed the generation of a multitude of earthquake-like acceleration signals. These synthetic accelerograms were also contaminated with added Gaussian white noise to simulate processing and digitization noise, and were truncated at the beginning and at the end of the record to simulate instrument trigger and shut-off mechanisms. These effects were scaled to model accelerograms of large events (i.e., 50% g) or of small events (i.e., 5% g).

The testing methodology is applicable to a wide variety of processing methods for either digital or analog accelerograms. It was shown that the study of the errors found in processed accelerograms could be separated into the study of the *internal performance* and that of the *correction effectiveness*. The first judges how much error or distortion the correction method adds into a noise-free continuous-time input signal and its integrals. The latter is a measure of how well the processing method can correct the errors in a corrupted input signal, which are often of an uncertain nature. The versatility of the synthetic records proved to be a valuable tool which permitted an in-depth study of the internal performance and the correction effectiveness of processing methods by comparing the exact analytical time history to its processed and noise-corrupted counterpart.

The original Volume II processing method was used to illustrate the testing methodology. It was first shown how the internal performance could be assessed by analytically deriving the equivalent transfer functions of each of the steps of the processing routine, which may sometimes be a nontrivial problem. Although this approach proved to be somewhat useful in identifying the sources of the processing errors, it required lengthy and tedious numerical computations, careful bookkeeping, and in practice, could mainly be applied to simple sinusoidal signals composed of a few harmonics. It was shown that such disadvantages did not exist when noise-free synthetic accelerograms are used to study the processing method's internal performance. It was demonstrated that the sources of errors within the processing routine could be isolated by either bypassing certain steps of the program or by processing synthetic signals which did not contain harmonics within certain frequency ranges. In this manner, it was possible to identify the type and amount of error induced by each of the steps of the processing routine.

Testing of the correction effectiveness of a processing method requires that the processed input signal be corrupted by the type of error most likely to occur. In the case of earthquake accelerograms, these errors are of an uncertain nature (e.g., missing data and digitization noise), and analytical methods cannot be used to verify how well the processing method corrects them. But it was shown that these errors could be modelled and incorporated in the synthetic records by simulations, which could then be used to test the correction effectiveness of the processing method. This was achieved by fixing the processing and filtering parameters of the accelerogram processing program, and by isolating or combining each of the input errors for different earthquake sizes. A large number of error-contaminated synthetic accelerograms were tested, and comparison of the processed output signals enabled an evaluation of how well the errors had been corrected on the average.

It was concluded that in general the Volume II processed and corrected acceleration time histories exhibited a very low output-error level regardless of the added error in the input accelerogram, and hence could be used with confidence. However, the errors in the processed velocity were large enough to warrant caution, and those in the processed displacement could be so big as to make the signal unreliable. It

was shown that Volume II is not capable of greatly reducing digitization noise in the input accelerogram, nor can it properly estimate the true value of the signals at the time of trigger or recover existing final displacement offsets. Thus, it does not have good correction effectiveness. However, it can be deemed insensitive or consistent, in the sense that regardless of the amount or nature of the error in the input of a given record, it will always produce nearly the same output for a fixed set of Ormsby filter parameters. As the cut-off and roll-off frequencies of the filter are changed, so are the output errors and the shape of the processed time histories. The main sources of error within the original Volume II method were found to be the Ormsby filter used in the high-pass filtering, the time-domain integration with the trapezoidal rule, and the repeated filtering, decimation and mean removal of the acceleration, velocity and displacement. It was concluded that it is the poor internal performance of the Volume II processing method, and not the errors in the input accelerogram, which is the dominant factor controlling the amount of output error. Although some of these sources of errors have already been identified in the past, the novelty of this approach lies in the systematic way the internal performance and the correction effectiveness of the processing routine can be identified and tested for any source and type of errors, even those which are uncertain.

Only the original Volume II method has been tested [Trifunac & Lee, 1973]. However, the same methodology should be applied to any of the improved and more recent processing methods to assess their internal performance and correction effectiveness. Because of the uncertainties involved in the recording and digitization process (i.e., missing data, added noise), it is clear that it is impossible to retrieve the exact signal from the measured accelerogram. A deterministic solution to this problem does not exist. However, from laboratory experiments, it is feasible to determine the range of possible values that the uncertain parameters can take, and assign a probability distribution to each of them. In Ch. 3, a method for obtaining the most probable acceleration, velocity and displacement, as well as their respective levels of uncertainty, has been proposed by describing the true signal and the error statistically. Such an approach makes it possible to obtain the accelerations, velocities and displacements which are the most likely to have

occurred during the seismic event based on the measured accelerogram and the most probable instrument truncation and digitization noise levels.

The proposed probabilistic processing method can apply equally well to analog or digital accelerograms. In Ch. 3, the processing method is first described in the time domain, using the trapezoidal rule as the integration scheme. It was shown that the true signal could be written as a function of the measured accelerogram data, the uncertain missing data, and the digitization noise. These errors are the source of the uncertain shift in the acceleration baseline, and are responsible for the long-period displacement errors. The accelerograms are corrected and integrated under the assumption that the most probable temporal mean acceleration is zero, and that only one point with most probable value zero is missing at the beginning of the record due to trigger start-up. For cases where final displacement offsets are expected, such as in the near-field along a fault, or in a damaged structure, the most probable initial velocity and displacement were also assumed to be zero. For far-field or small event records, which are not expected to produce final displacement offsets, the temporal mean velocity is assumed to be zero, and the corresponding displacement time history is integrated for zero initial value. These were shown to be reasonable assumptions. The standard deviations of the acceleration, velocity and displacement were then derived as a function of the standard deviation of the digitization noise, a, of the missing initial acceleration point, b, and of the missing end data, c. Values for a, b, and c can be found from laboratory experiments or judgement. It was shown that high-pass filters can be a major source of internal performance error, and in general do not contribute much to the overall correction effectiveness of the method. Thus, the new processing procedure described in Ch. 3 does not recommend the use of any high-pass filter. However, they could be easily implemented within the program's structure if necessary, and alternatives to traditional high-pass filtering methods are proposed in Ch. 4. Finally, the procedure produces plots which represents the most probable value of the processed signal, along with its uncertainty level of one, two or three standard deviations.

The time-domain probabilistic processing method is tested with the synthetic signals for its internal performance and its correction effectiveness. It was shown

that the method has good internal performance, in the sense that the only significant source of output error is introduced at high frequencies by the trapezoidal rule. These errors mainly affected the velocity time history, and were shown to be small and negligible compared to the effects of digitization noise, even for simulations of large events. The probabilistic processing method does not remove the noise, and allows the integrated velocities and displacements to drift due to various sources of errors affecting the temporal means. However, the probabilistic processing method was shown to have good correction effectiveness, in the sense that the uncertainty bounds about the estimated most probable time histories did enclose the exact signal. Contrary to the conclusions reached after testing Volume II, the study of the probabilistic processing method showed that, as expected, the relative amount of processing error decreased as the size of the earthquake increased. This implies that the most probable estimates of the time histories, as provided by the processing method, also become more reliable as the size of the earthquake increases.

A frequency-domain probabilistic accelerogram processing method was also proposed. The assumptions to obtain the most probable time histories are the same as for the time-domain method. Integration is performed in the frequency domain with zero *d.c.*, and any necessary corrections to the initial value are performed in the time domain after inverse transformation. The expressions for the standard deviations corresponding to the most probable acceleration, velocity and displacement are the same as the ones derived in the time domain if no filtering is done. The synthetic signals are used to evaluate the internal performance of the frequency-domain method, which implements a fast Fourier transform algorithm to compute the discrete Fourier transform. It was shown that adding zeroes to a truncated accelerogram produces leakage, a convolutive error in the spectrum affecting the entire frequency range. However, leakage did not induce errors in the processed and integrated time histories, except for possible aliasing of higher frequency components created by the leakage. It was also shown that the baseline correction of the accelerogram creates an additive error in the spectrum which is dominant at lower frequencies. These long-period errors affect the time histories and are amplified by integration. Equivalently, testing of the internal performance of the time-domain processing method showed that shifts in the temporal mean,

such as those resulting from missing data, are almost exclusively responsible for long-period errors in the integrated time histories. The internal performance of the time-domain method proved to be worse because integration is performed with the trapezoidal rule, compared to integration in the frequency domain which reduced the error level in the processed time histories by about two orders of magnitude. It was also shown that both the frequency-domain method and the time-domain method had similar correction effectiveness. Since it reduces integration errors and may be more time efficient, as was discussed in Ch. 3, the frequency-domain method is a better approach, and is the method implemented in the proposed standard processing routine.

The study of the correction effectiveness of the probabilistic processing method, in either the time domain or the frequency domain, showed that the dominant sources of errors arose from the unknown offset in the accelerogram baseline, and the digitization noise. These errors have been shown to be properly accounted for by the reliability bounds. Nevertheless, the level of these errors can be reduced, and two new approaches to accelerogram correction are proposed in Ch. 4. The first approach is based on the Wiener optimal noise filter. It is signal-dependent, and attempts to estimate the best approximation to the true signal from noise-contaminated measured data. In effect, this filter reduces the noise throughout the whole spectrum as a function of the signal-to-noise ratio at each frequency of the record. The optimality of the filter requires the prior knowledge of the power spectral density of the true signal and of the noise. Applying Wiener's concept to cases where such prior information is not available (e.g., earthquake accelerograms), and only the signal itself can be used, led to the conclusion that such an optimal filter is equal to unity throughout the whole spectrum. Or in other words, it is best not to use a filter at all! However, noise filters which decrease the amplitude of the spectrum where the signal-to-noise ratio is low were proposed. Tests performed on noise-contaminated synthetic records showed that these noise filters are correction-effective for records of small events, since they are capable of partially reducing the low-frequency errors which result in linear and parabolic drifts in the time histories after integration. At high frequencies, the noise filters reduced the level of the error, although not significantly. For simulations of large events, the noise

filters proved to be less effective since the signal-to-noise is high throughout most of the spectrum. Such a noise-correction method is not included in the standard probabilistic frequency-domain processing routine, but could be implemented as an option if desired.

The second correction technique, called the spectral substitution method, corrects the error-corrupted ends of the accelerogram's spectrum, especially near *d.c.*. It is based on the optimization of spectral models for far-field or near-field earthquake ground motions, or for structural motions. The spectral models are formulated to adequately represent the behavior of the measured spectra at high and low frequencies where the error and noise prevail. However, these models are not intended to provide an accurate match at intermediate frequencies where the signal-to-noise ratio is high, and where no correction is necessary. D_0, one of the parameters which define the spectral models, is the *d.c.* value of the displacement spectrum in the far-field, and of the velocity spectrum in the near-field. Hence, for near-field records, D_0 is also an estimate of the final displacement offset. The error between the optimized model and the amplitude spectrum of the measured data is used as a statistical criterion for the spectral substitution. The low-frequency spectral amplitudes that lie outside one standard deviation about the most probable values are substituted by the amplitudes of the optimized model. The phases are kept unchanged. In this manner, the long-period motions in the measured accelerogram are not completely removed from the signal, they are simply replaced by their most probable value based on the data and the class of spectral models. The same correction technique can also be applied to the high-frequency end of the spectrum.

The spectral substitution method was applied to a set of analog accelerograms obtained during the October 15, 1979 Imperial Valley earthquake (M_L =6.6). The method was tested successfully on ground motion records obtained both in the near-field and in the far-field. It was found that the correction method produced consistent results for records obtained at adjacent sites for components along the same direction. It was thus concluded that the long-period motions that were observed in the processed and corrected time histories could be attributed to true ground response, and not just to errors in the digitization process. In particular,

it was found that the dominant horizontal period of motion of the Imperial Valley was 8 sec, and vertically the dominant period was of the order of 4 sec. Using a simplified shear-beam model of the Imperial Valley, it was shown that such periods could be possible in the valley. The corrected near-field displacement time histories also displayed final offsets that were reasonably consistent with those measured on-site after the seismic event. Because the low-frequency portion of the spectrum is not completely removed, contrary to current processing and correction methods which use standard filtering techniques, long-period motions beyond 8 sec and final displacement offsets were observed, for what is believed to be the first time, in time histories obtained from analog records.

When applied to accelerograms obtained during the same earthquake at the Imperial County Services building, the spectral substitution method implemented for structural models produced consistent results as well. For near-field and far-field records, the spectral models used for the optimization are consistent with the physics of earthquake source and propagation effects, and have shown to provide good matches to the measured data. Although it also provides good fits to the data, the spectral model that is used in the optimization of structural records was eventually obtained by trial and error. More research is desirable to explore this model and perhaps to suggest improved formulations.

In Ch. 5, one of the records obtained at the roof of the Imperial County Services building is used as an example of the complete processing procedure for the probabilistic frequency-domain method, with and without the spectral substitution method. Plots of the corresponding most probable time histories with their reliability bounds were provided. The standard deviations of the most probable time histories given in Ch. 3 are derived for records processed without spectral substitution. When using the spectral substitution method, the error levels should significantly decrease, especially in the displacement. Although still correct, the aforementioned reliability bounds are expected to be too conservative when the records are spectrally corrected. In future work, the effects of the spectral substitution correction on the statistical description of the error could be incorporated, in order to provide more adequate reliability bounds. The resulting time histories are also compared to

those processed by *CDMG* using a standard processing technique. The probabilisitic frequency-domain approach with low-frequency substitution produced satisfactory results with only a minimal amount of correction.

The frequency-domain method, in conjunction with the spectral substitution method, is felt to be a better option for processing of accelerograms. It tampers with the data much less than other processing methods, and does not completely remove the low-frequency portion of the accelerogram which could be of scientific interest, while still providing reasonable estimates for the time histories. Using the probabilistic framework, these time histories are the most probable ones based on the information available, and they can be assigned uncertainty levels to describe their reliability. As an extension to this work, probabilistic methods could also be applied to compute the response spectra. Also, since testing of this method on synthetic and true accelerograms has produced very satisfactory results, this accelerogram processing method could be used on a large number of existing strong-motion records to study the long-period dynamics of local geology and of structures, both in the near-field and in the far-field.

REFERENCES

1. Aki, K. and P. G. Richards (1980) "Quantative Seismology Theory and Methods," W. H. Freeman and Company, New York.

2. Anderson, J. G. and S. E. Hough (1984) "A Model for the Shape of the Fourier Amplitude Spectrum of Acceleration at High Frequencies," *Bulletin of the Seismological Society of America*, Vol. 74, pp. 1969–1993.

3. Basili, M. and G. Brady (1978) "Low Frequency Filtering and the Selection of Limits for Accelerogram Corrections," *Proceedings of the 6th European Conference on Earthquake Engineering*, Ljubljana, Vol. I, pp. 251–258.

4. Beck, J. L. (1989) "Statistical System Identification of Structures," *Proceedings of the 5th International Conference on Structural Safety and Reliability.*

5. Bendat, J. S. and A. G. Piersol (1986) "Random Data: Analysis and Measurement Procedures," 2nd Edition, John Wiley & Sons, New York.

6. Brady, A. G. and P. N. Mork (1984) "Synthetic Accelerograms for Testing Processing Proceedures," *Proceedings of the 8th World Conference on Earthquake Engineering*, pp. 127–134.

7. Brady, A. G., V. Perez and P. N. Mork (1980) "The Imperial Valley Earthquake, October 15, 1979. Digitization and Processing of Accelerograph Records," USGS Open-file Report 80-703.

8. Brady, A. G., V. Perez and P. N. Mork (1982) "Digitization and Processing of Main-Shock Ground Motion Data from the USGS Accelerograph Network," *U.S. Geological Survey Professional Paper 1254*, pp. 385–406.

9. Brigham, E. O. (1974) "The Fast Fourier Transform," Prentice-Hall, Inc., New Jersey.

10. Brune, J. N. (1970) "Tectonic Stress and the Spectra of Seismic Shear Waves from Earthquakes," *Journal Geophysics Research*, Vol. 75, pp. 4997–5009.

11. Converse, A. M., A. G. Brady and W. B. Joyner (1984) "Improvements in Strong-Motion Data Processing Procedures," *Proceedings of the 8th World Conference on Earthquake Engineering*, San Francisco, pp. 143–148.

12. Erdik, M. and J. Kubin (1984) "A Procedure for the Accelerogram Processing," *Proceedings of the 8th World Conference on Earthquake Engineering*, pp. 135–142.

13. Fletcher, J. B., A. G. Brady and T. C. Hanks (1980) "Strong-Motion Accelerograms of the Oroville, California Aftershocks: Data Processing and the Aftershock of 0350 August 6, 1975," *Bulletin of the Seismological Society of America*, Vol. 70, No. 1, pp. 243–267.

14. Fuis, G. S., W. D. Mooney, J. H. Healy, G. A. McMehan, and W. J. Lutter (1982) "Crustal Structure of the Imperial Valley Region," *U.S. Geological Survey Professional Paper 1254*, pp. 25–50.

15. Gill, P. E., W. Murray and M. H. Wright (1981) "Practical Optimization," Academic Press, Inc., New York.

16. Hall, J. F. (1982) "An FFT Algorithm for Structural Dynamics," *Earthquake Engineering and Structural Dynamics*, Vol. 10, pp. 797–811.

17. Hanks, T. C. (1982) "$f_{\max}$," *Bulletin of the Seismological Society of America*, Vol. 72, pp. 1867–1879.

18. Hanks, T. C. and R. K. McGuire (1981) "Tectonic Stress and the Spectra of Seismic Shear Waves from Earthquakes," *Journal of Geophysical Research*, Vol. 75, pp. 4997–5009.

19. Hartzell, S. and D. Helmberger (1982) "Strong-Motion Modeling of the Imperial Valley Earthquake of 1979," *Bulletin of the Seismological Society of America*, Vol. 72, pp. 571–596.

20. Hudson, D. E. (1979) "Reading and Interpreting Strong Motion Accelerograms," Monograph, Earthquake Engineering Research Institute, Berkeley, California.

21. Iwan, W. D., M. A. Moser and C. Y. Peng (1984) "Strong-Motion Earthquake Measurement using a Digital Accelerograph," California Institute of Technology, Earthquake Engineering Research Laboratory, Report No. EERL 84-02, Pasadena, California.

22. Joyner, W. B. and D. M. Boore (1988) "Measurement, Characterization, and Prediction of Strong Ground Motion," Earthquake Engineering and Soil Dynamics II—Recent Advances in Ground-Motion Evaluation, *Proceedings ASCE, Geotechnical Division*, Park City, Utah, pp. 43–102.

23. Kanamori, H. (1985) "Physics of Earthquakes," class notes, California Institute of Technology, Pasadena, California.

24. Khemici, O. and W. L. Chiang (1984) "Frequency Domain Corrections of Earthquake Accelerograms with Experimental Verifications," *Proceedings of the 8th World Conference on Earthquake Engineering*, pp. 103–110.

25. Lee, V. W. (1984) "Recent Developments in Data Processing of Strong-Motion Accelerograms," *Proceedings of the 8th World Conference on Earthquake Engineering*, pp. 119–126.

26. Oppenheim, A. V. and R. W. Schaffer (1975) "Digital Signal Processing," Prentice-Hall, Inc., New Jersey.

27. Papageorgiou, A. S. (1988) "On Two Characteristic Frequencies of Acceleration Spectra: Patch Corner Frequency and $f_{\max}$," *Bulletin of the Seismological Society of America*, Vol. 78, pp. 509–529.

28. Papageorgiou, A. S. and K. Aki (1983) "A Specific Barrier Model for the Quantitative Description of Inhomogeneous Faulting and the Prediction of Strong Ground Motion, I. Description of the Model," *Bulletin of the Seismological Society of America*, Vol. 73, pp. 693–722.

29. Papoulis, A. (1965) "Probability, Random Variables, and Stochastic Processes," McGraw-Hill Book Company, New York.

30. Porcella, R. L. and R. B. Matthiesen (1980) "Preliminary Summary of the U.S. Geological Survey Strong-Motion Records from the October 15, 1979 Imperial Valley Earthquake," USGS Open-file Report 79-1654.

31. Porter, L. D. (1982) "Data Processing for Main-Shock Motions Recorded by the California Divisions of Mines and Geology Strong-Motion Network," *U.S. Geological Survey Professional Paper 1254*, pp. 407–417.

32. Press, W. H., B. P. Flannery, S. A. Teukolsky and W. T. Vetterling (1986) "Numerical Recipes. The Art of Scientific Computing," Cambridge Univ. Press, Cambridge, Massachusetts.

33. Rabiner, L. R. and B. Gold (1975) "Theory and Application of Digital Signal Processing," Prentice-Hall, Inc., New Jersey.

34. Rojahn, C. and P. N. Mork (1982) "An Analysis of Strong-Motion Data from a Severly Damaged Structure—The Imperial County Services Building, El Centro, California," *U.S. Geological Survey Professional Paper 1254*, pp. 357–375.

35. Schiff, A. and J. L. Bogdanoff (1967) "Analysis of Current Methods for Interpreting Strong-Motion Accelerograms," *Bulletin of the Seismological Society of America*, Vol. 57, No. 5, pp. 857–874.

36. Shakal, A. F. and J. T. Ragsdale (1984) "Acceleration, Velocity and Displacement Noise Analysis for the CSMIP Accelerogram Digitization System," *Proceedings of the 8th World Conference on Earthquake Engineering*, pp. 111–118.

37. Sharp, R. V., et al. (1982) "Surface Faulting in Central Imperial Valley," *U.S. Geological Survey Professional Paper 1254*, pp. 119–144.

38. Stephens, J. E. and J. T. P. Yao (1985) "Data Processing of Earthquake Acceleration Records," *Structural Engineering*, CE-STR. 85-5.

39. Sunder, S. S. and J. J. Connor (1982) "A New Procedure for Processing Strong-Motion Earthquake Signals," *Bulletin of the Seismological Society of America*, Vol. 72, No. 2, pp. 643–661.

40. Trifunac, M. D. (1970) "Low Frequency Digitization Errors and a New Method for Zero Baseline Correction of Strong-Motion Accelerograms," California Institute of Technology, Earthquake Engineering Research Laboratory, Report No. EERL 70-07, Pasadena, California.

41. Trifunac, M. D. and V. W. Lee (1973) "Routine Processing of Strong-Motion Accelerograms," California Institute of Technology, Earthquake Engineering Research Laboratory, Report No. EERL 73-03, Pasadena, California.

42. Trifunac, M. D., F. E. Udwadia and A. G. Brady (1973) "Analysis of Errors in Digitized Strong-Motion Accelerograms," *Bulletin of the Seismological Society of America*, Vol. 63, pp. 157–187.

43. Trifunac, M.D. (1974) "Analysis of Strong Earthquake Ground Motion for Prediction of Response Spectra," *Earthquake Engineering and Structural Dynamics*, Vol. 2, pp. 59–69.

44. Whalen, A. D. (1971) "Detection of Signals in Noise," Academic Press, Inc., New York.

45. Wiener, N. (1950) "Extrapolation, Interpolation, and Smoothing of Stationary Time Series," M.I.T. and John Wiley & Sons, Inc., New York.

CALIFORNIA INSTITUTE OF TECHNOLOGY

Reports Published
by
Earthquake Engineering Research Laboratory (EERL)*
Dynamics Laboratory (DYNL)
Disaster Research Center (DRC)
Soil Mechanics Laboratory (SML)

Note: Numbers in parenthesis are Accession Numbers assigned by the National Technical Information Service; these reports may be ordered from the National Technical Information Service, 5285 Port Royal Road, Springfield, Virginia, 22161. Accession Numbers should be quoted on orders for reports (PB — —). Reports without this information either have not been submitted to NTIS or the information was not available at the time of printing. An N/A in parenthesis indicates that the report is no longer available at Caltech.

1. Alford, J.L., G.W. Housner and R.R. Martel, "Spectrum Analysis of Strong-Motion Earthquake," 1951. (Revised August 1964). (N/A)
2. Housner, G.W., "Intensity of Ground Motion During Strong Earthquakes," 1952. (N/A)
3. Hudson, D.E., J.L. Alford and G.W. Housner, "Response of a Structure to an Explosive Generated Ground Shock," 1952. (N/A)
4. Housner, G.W., "Analysis of the Taft Accelerogram of the Earthquake of 21 July 1952." (N/A)
5. Housner, G.W., "A Dislocation Theory of Earthquakes," 1953. (N/A)
6. Caughey, T.K. and D.E. Hudson, "An Electric Analog Type Response Spectrum," 1954. (N/A)
7. Hudson, D.E. and G.W. Housner, "Vibration Tests of a Steel-Frame Building," 1954. (N/A)
8. Housner, G.W., "Earthquake Pressures on Fluid Containers," 1954. (N/A)
9. Hudson, D.E., "The Wilmot Survey Type Strong-Motion Earthquake Recorder," 1958. (N/A)

---

* To order directly by phone, the number is (703) 487–4650.

10. Hudson, D.E. and W.D. Iwan, "The Wilmot Survey Type Strong-Motion Earthquake Recorder, Part II," 1960. (N/A)

11. Caughey, T.K., D.E. Hudson and R.V. Powell, "The CIT Mark II Electric Analog Type Response Spectrum Analyzer for Earthquake Excitation Studies," 1960. (N/A)

12. Keightley, W.O., G.W. Housner and D.E. Hudson, "Vibration Tests of the Encino Dam Intake Tower," 1961. (N/A)

13. Merchant, H.C., "Mode Superposition Methods Applied to Linear Mechanical Systems Under Earthquake Type Excitation," 1961. (N/A)

14. Iwan, W.D., "The Dynamic Response of Bilinear Hysteretic Systems," 1961. (N/A)

15. Hudson, D.E., "A New Vibration Exciter for Dynamic Test of Full-Scale Structures," 1961. (N/A)

16. Hudson, D.E., "Synchronized Vibration Generators for Dynamic Tests of Full-Scale Structures," 1962. (N/A)

17. Jennings, P.C., "Velocity Spectra of the Mexican Earthquakes of 11 May and 19 May 1962," 1962. (N/A)

18. Jennings, P.C., "Response of Simple Yielding Structures to Earthquake Excitation," 1963. (N/A)

19. Keightley, W.O., "Vibration Tests of Structures," 1963. (N/A)

20. Caughey, T.K. and M.E.J. O'Kelly, "General Theory of Vibration of Damped Linear Dynamic Systems," 1963. (N/A)

21. O'Kelly, M.E.J., "Vibration of Viscously Damped Linear Dynamic Systems," 1964. (N/A)

22. Nielsen, N.N., "Dynamic Response of Multistory Buildings," 1964. (N/A)

23. Tso, W.K., "Dynamics of Thin-Walled Beams of Open Section," 1964. (N/A)

24. Keightley, W.O., "A Dynamic Investigation of Bouquet Canyon Dam," 1964. (N/A)

25. Malhotra, R.K., "Free and Forced Oscillations of a Class of Self-Excited Oscillators," 1964.

26. Hanson, R.D., "Post-Elastic Response of Mild Steel Structures," 1965.

27. Masri, S.F., "Analytical and Experimental Studies of Impact Dampers," 1965.

28. Hanson, R.D., "Static and Dynamic Tests of a Full-Scale Steel-Frame Structures," 1965.

29. Cronin, D.L., "Response of Linear, Viscous Damped Systems to Excitations Having Time-Varying Frequency," 1965.

30. Hu, P.Y.-F., "Analytical and Experimental Studies of Random Vibration," 1965.

31. Crede, C.E., "Research on Failure of Equipment when Subject to Vibration," 1965.

32. Lutes, L.D., "Numerical Response Characteristics of a Uniform Beam Carrying One Discrete Load," 1965. (N/A)

33. Rocke, R.D., "Transmission Matrices and Lumped Parameter Models for Continuous Systems," 1966. (N/A)

34. Brady, A.G., "Studies of Response to Earthquake Ground Motion," 1966. (N/A)

35. Atkinson, J.D., "Spectral Density of First Order Piecewise Linear Systems Excited by White Noise," 1967. (N/A)

36. Dickerson, J.R., "Stability of Parametrically Excited Differential Equations," 1967. (N/A)

37. Giberson, M.F., "The Response of Nonlinear Multi-Story Structures Subjected to Earthquake Excitation," 1967. (N/A)

38. Hallanger, L.W., "The Dynamic Stability of an Unbalanced Mass Exciter," 1967.

39. Husid, R., "Gravity Effects on the Earthquake Response of Yielding Structures," 1967. (N/A)

40. Kuroiwa, J.H., "Vibration Test of a Multistory Building," 1967. (N/A)

41. Lutes, L.D., "Stationary Random Response of Bilinear Hysteretic Systems," 1967.

42. Nigam, N.C., "Inelastic Interactions in the Dynamic Response of Structures," 1967.

43. Nigam, N.C. and P.C. Jennings, "Digital Calculation of Response Spectra from Strong-Motion Earthquake Records," 1968.

44. Spencer, R.A., "The Nonlinear Response of Some Multistory Reinforced and Prestressed Concrete Structures Subjected to Earthquake Excitation," 1968. (N/A)

45. Jennings, P.C., G.W. Housner and N.C. Tsai, "Simulated Earthquake Motions," 1968.

46. "Strong-Motion Instrumental Data on the Borrego Mountain Earthquake of 9 April 1968," (USGS and EERL Joint Report), 1968.

47. Peters, R.B., "Strong Motion Accelerograph Evaluation," 1969.

48. Heitner, K.L., "A Mathematical Model for Calculation of the Run-Up of Tsunamis," 1969.

49. Trifunac, M.D., "Investigation of Strong Earthquake Ground Motion," 1969. (N/A)

50. Tsai, N.C., "Influence of Local Geology on Earthquake Ground Motion," 1969. (N/A)

51. Trifunac, M.D., "Wind and Microtremor Induced Vibrations of a Twenty-Two Steel Frame Building," EERL 70–01, 1970.

52. Yang, I-M., "Stationary Random Response of Multidegree-of-Freedom Systems," DYNL–100, June 1970. (N/A)

53. Patula, E.J., "Equivalent Differential Equations for Non-linear Dynamic Systems," DYNL–101, June 1970.

54. Prelewicz, D.A., "Range of Validity of the Method of Averaging," DYNL–102, 1970.

55. Trifunac, M.D., "On the Statistics and Possible Triggering Mechanism of Earthquakes in Southern California," EERL 70–03, July 1970.

56. Heitner, K.L., "Additional Investigations on a Mathematical Model for Calculation of Run-Up of Tsunamis," July 1970.

57. Trifunac, M.D., "Ambient Vibration Tests of a Thirty-Nine Story Steel Frame Building," EERL 70–02, July 1970.

58. Trifunac, M.D. and D.E. Hudson, "Laboratory Evaluations and Instrument Corrections of Strong-Motion Accelerographs," EERL 70–04, August 1970. (N/A)

59. Trifunac, M.D., "Response Envelope Spectrum and Interpretation of Strong Earthquake Ground Motion," EERL 70–06, August 1970.

60. Keightley, W.O., "A Strong-Motion Accelerograph Array with Telephone Line Interconnections," EERL 70–05, September 1970.

61. Trifunac, M.D., "Low Frequency Digitization Errors and a New Method for Zero Baseline Correction of Strong-Motion Accelerograms," EERL 70–07, September 1970.

62. Vijayaraghavan, A., "Free and Forced Oscillations in a Class of Piecewise-Linear Dynamic Systems," DYNL–103, January 1971.

63. Jennings, P.C., R.B. Mathiesen and J.B. Hoerner, "Forced Vibrations of a 22–Story Steel Frame Building," EERL 71–01, February 1971. (N/A) (PB 205 161)

64. Jennings, P.C., "Engineering Features of the San Fernando Earthquake of February 9, 1971," EERL 71–02, June 1971. (PB 202 550)

65. Bielak, J., "Earthquake Response of Building-Foundation Systems," EERL 71–04, June 1971. (N/A) (PB 205 305)

66. Adu, R.A., "Response and Failure of Structures Under Stationary Random Excitation," EERL 71–03, June 1971. (N/A) (PB 205 304)

67. Skattum, K.S., "Dynamic Analysis of Coupled Shear Walls and Sandwich Beams," EERL 71–06, June 1971. (N/A) (PB 205 267)

68. Hoerner, J.B., "Model Coupling and Earthquake Response of Tall Buildings," EERL 71–07, June 1971. (N/A) (PB 207 635)

69. Stahl, K.J., "Dynamic Response of Circular Plates Subjected to Moving Massive Loads," DYNL–104, June 1971. (N/A)

70. Trifunac, M.D., F.E. Udwadia and A.G. Brady, "High Frequency Errors and Instrument Corrections of Strong-Motion Accelerograms," EERL 71–05, 1971. (PB 205 369)

71. Furuike, D.M., "Dynamic Response of Hysteretic Systems With Application to a System Containing Limited Slip," DYNL–105, September 1971. (N/A)

72. Hudson, D.E. (Editor), "Strong-Motion Instrumental Data on the San Fernando Earthquake of February 9, 1971," (Seismological Field Survey, NOAA, C.I.T. Joint Report), September 1971. (PB 204 198)

73. Jennings, P.C. and J. Bielak, "Dynamics of Building-Soil Interaction," EERL 72–01, April 1972. (PB 209 666)

74. Kim, B.-K., "Piecewise Linear Dynamic Systems with Time Delays," DYNL–106, April 1972.

75. Viano, D.C., "Wave Propagation in a Symmetrically Layered Elastic Plate," DYNL–107, May 1972.

76. Whitney, A.W., "On Insurance Settlements Incident to the 1906 San Francisco Fire," DRC 72–01, August 1972. (PB 213 256)

77. Udwadia, F.E., "Investigation of Earthquake and Microtremor Ground Motions," EERL 72–02, September 1972. (PB 212 853)

78. Wood, J.H., "Analysis of the Earthquake Response of a Nine-Story Steel Frame Building During the San Fernando Earthquake," EERL 72–04, October 1972. (PB 215 823)

79. Jennings, P.C., "Rapid Calculation of Selected Fourier Spectrum Ordinates," EERL 72–05, November 1972.

80. "Research Papers Submitted to Fifth World Conference on Earthquake Engineering, Rome, Italy, 25–29 June 1973," EERL 73–02, March 1973. (PB 220 431)

81. Udwadia, F.E. and M.D. Trifunac, "The Fourier Transform, Response Spectra and Their Relationship Through the Statistics of Oscillator Response," EERL 73–01, April 1973. (PB 220 458)

82. Housner, G.W., "Earthquake-Resistant Design of High-Rise Buildings," DRC 73–01, July 1973. (N/A)

83. "Earthquake and Insurance," Earthquake Research Affiliates Conference, 2–3 April, 1973, DRC 73–02, July 1973. (PB 223 033)

84. Wood, J.H., "Earthquake-Induced Soil Pressures on Structures," EERL 73–05, August 1973. (N/A)

85. Crouse, C.B., "Engineering Studies of the San Fernando Earthquake," EERL 73–04, March 1973. (N/A)

86. Irvine, H.M., "The Veracruz Earthquake of 28 August 1973," EERL 73–06, October 1973.

87. Iemura, H. and P.C. Jennings, "Hysteretic Response of a Nine-Story Reinforced Concrete Building During the San Fernando Earthquake," EERL 73–07, October 1973.

88. Trifunac, M.D. and V. Lee, "Routine Computer Processing of Strong-Motion Accelerograms," EERL 73–03, October 1973. (N/A) (PB 226 047/AS)

89. Moeller, T.L., "The Dynamics of a Spinning Elastic Disk with Massive Load," DYNL 73–01, October 1973.

90. Blevins, R.D., "Flow Induced Vibration of Bluff Structures," DYNL 74–01, February 1974.

91. Irvine, H.M., "Studies in the Statics and Dynamics of Simple Cable Systems," DYNL–108, January 1974.

92. Jephcott, D.K. and D.E. Hudson, "The Performance of Public School Plants During the San Fernando Earthquake," EERL 74–01, September 1974. (PB 240 000/AS)

93. Wong, H.L., "Dynamic Soil-Structure Interaction," EERL 75–01, May 1975. (N/A) (PB 247 233/AS)

94. Foutch, D.A., G.W. Housner and P.C. Jennings, "Dynamic Responses of Six Multistory Buildings During the San Fernando Earthquake," EERL 75–02, October 1975. (PB 248 144/AS)

95. Miller, R.K., "The Steady-State Response of Multidegree-of-Freedom Systems with a Spatially Localized Nonlinearity," EERL 75–03, October 1975. (PB 252 459/AS)

96. Abdel-Ghaffar, A.M., "Dynamic Analyses of Suspension Bridge Structures," EERL 76–01, May 1976. (PB 258 744/AS)

97. Foutch, D.A., "A Study of the Vibrational Characteristics of Two Multistory Buildings," EERL 76–03, September 1976. (PB 260 874/AS)

98. "Strong Motion Earthquake Accelerograms Index Volume," Earthquake Engineering Research Laboratory, EERL 76–02, August 1976. (PB 260 929/AS)

99. Spanos, P-T.D., "Linearization Techniques for Non-Linear Dynamical Systems," EERL 76–04, September 1976. (PB 266 083/AS)

100. Edwards, D.B., "Time Domain Analysis of Switching Regulators," DYNL 77–01, March 1977.

101. Abdel-Ghaffar, A.M., "Studies of the Effect of Differential Motions of Two Foundations upon the Response of the Superstructure of a Bridge," EERL 77–02, January 1977. (PB 271 095/AS)

102. Gates, N.C., "The Earthquake Response of Deteriorating Systems," EERL 77–03, March 1977. (PB 271 090/AS)

103. Daly, W., W. Judd and R. Meade, "Evaluation of Seismicity at U.S. Reservoirs," USCOLD, Committee on Earthquakes, May 1. (PB 270 036/AS)

104. Abdel-Ghaffer, A.M. and G.W. Housner, "An Analysis of the Dynamic Characteristics of a Suspension Bridge by Ambient Vibration Measurements," EERL 77–01, January 1977. (PB 275 063/AS)

105. Housner, G.W. and P.C. Jennings, "Earthquake Design Criteria for Structures," EERL 77–06, November 1977 (PB 276 502/AS)

106. Morrison, P., R. Maley, G. Brady and R. Porcella, "Earthquake Recordings on or Near Dams," USCOLD, Committee on Earthquakes, November 1977. (PB 285 867/AS)

107. Abdel-Ghaffar, A.M., "Engineering Data and Analyses of the Whittier, California Earthquake of January 1, 1976," EERL 77–05, November 1977. (PB 283 750/AS)

108. Beck, J.L., "Determining Models of Structures from Earthquake Records," EERL 78–01, June 1978 (PB 288 806/AS)

109. Psycharis, I., "The Salonica (Thessaloniki) Earthquake of June 20, 1978," EERL 78–03, October 1978. (PB 290 120/AS)

110. Abdel-Ghaffar, A.M. and R.F. Scott, "An Investigation of the Dynamic Characteristics of an Earth Dam," EERL 78–02, August 1978. (PB 288 878/AS)

111. Mason, A.B., Jr., "Some Observations on the Random Response of Linear and Nonlinear Dynamical Systems," EERL 79–01, January 1979. (PB 290 808/AS)

112. Helmberger, D.V. and P.C. Jennings (Organizers), "Strong Ground Motion: N.S.F. Seminar-Workshop," SL–EERL 79–02, February 1978.

113. Lee, D.M., P.C. Jennings and G.W. Housner, "A Selection of Important Strong Motion Earthquake Records," EERL 80–01, January 1980. (PB 80 169196)

114. McVerry, G.H., "Frequency Domain Identification of Structural Models from Earthquake Records," EERL 79–02, October 1979. (PB–80–194301)

115. Abdel-Ghaffar A.M., R.F.Scott and M.J.Craig, "Full-Scale Experimental Investigation of a Modern Earth Dam," EERL 80–02, February 1980. (PB–81–123788)

116. Rutenberg, A., P.C. Jennings and G.W. Housner, "The Response of Veterans Hospital Building 41 in the San Fernando Earthquake," EERL 80–03, May 1980. (PB–82–201377)

117. Haroun, M.A., "Dynamic Analyses of Liquid Storage Tanks," EERL 80–04, February 1980. (PB–81–123275)

118. Liu, W.K., "Development of Finite Element Procedures for Fluid-Structure Interaction," EERL 80–06, August 1980. (PB 184078)

119. Yoder, P.J., "A Strain-Space Plasticity Theory and Numerical Implementation," EERL 80–07, August 1980. (PB–82–201682)

120. Krousgrill, C.M., Jr., "A Linearization Technique for the Dynamic Response of Nonlinear Continua," EERL 80–08, September 1980. (PB–82–201823)

121. Cohen, M., "Silent Boundary Methods for Transient Wave Analysis," EERL 80–09, September 1980. (PB–82–201831)

122. Hall, S.A., "Vortex-Induced Vibrations of Structures," EERL 81–01, January 1981. (PB–82–201849)

123. Psycharis, I.N., "Dynamic Behavior of Rocking Structures Allowed to Uplift," EERL 81–02, August 1981. (PB–82–212945)

124. Shih, C.-F., "Failure of Liquid Storage Tanks Due to Earthquake Excitation," EERL 81–04, May 1981. (PB–82–215013)

125. Lin, A.N., "Experimental Observations of the Effect of Foundation Embedment on Structural Response," EERL 82–01, May 1982. (PB–84–163252)

126. Botelho, D.L.R., "An Empirical Model for Vortex-Induced Vibrations," EERL 82–02, August 1982. (PB–84–161157)

127. Ortiz, L.A., "Dynamic Centrifuge Testing of Cantilever Retaining Walls," SML 82–02, August 1982. (PB–84–162312)

128. Iwan, W.D. (Editor) "Proceedings of the U.S. National Workshop on Strong-Motion Earthquake Instrumentation, April 12–14, 1981, Santa Barbara, California," California Institute of Technology, Pasadena, California, 1981.

129. Rashed, A., "Dynamic Analysis of Fluid-Structure Systems, " EERL 82–03, July 1982. (PB–84–162916)

130. National Academy Press, "Earthquake Engineering Research—1982."

131. National Academy Press, "Earthquake Engineering Research—1982, Overview and Recommendations."

132. Jain, S.K., "Analytical Models for the Dynamics of Buildings," EERL 83–02, May 1983. (PB–84–161009)

133. Huang, M.-J., "Investigation of Local Geology Effects on Strong Earthquake Ground Motions," EERL 83–03, July 1983. (PB–84–161488)

134. McVerry, G.H. and J.L. Beck, "Structural Identification of JPL Building 180 Using Optimally Synchronized Earthquake Records." EERL 83–01, August 1983. (PB–84–162833)

135. Bardet, J.P., "Application of Plasticity Theory to Soil Behavior: A New Sand Model," SML 83–01, September 1983. (PB–84–162304)

136. Wilson, J.C., "Analysis of the Observed Earthquake Response of a Multiple Span Bridge," EERL 84–01, May 1984. (PB–85–240505/AS)

137. Hushmand, B., "Experimental Studies of Dynamic Response of Foundations," SML 83–02, November 1983. (PB–86–115383/A)

138. Cifuentes, A.O., "System Identification of Hysteretic Structures," EERL 84–04, 1984. (PB–240489/AS14)

139. Smith, K.S., "Stochastic Analysis of the Seismic Response of Secondary Systems," EERL 85–01, November 1984. (PB–85–240497/AS)

140. Maragakis, E., "A Model for the Rigid Body Motions of Skew Bridges," EERL 85–02, December 1984. (PB–85–248433/AS)

141. Jeong, G.D., "Cumulative Damage of Structures Subjected to Response Spectrum Consistent Random Process," EERL 85–03, January 1985. (PB–86–100807)

142. Chelvakumar, K., "A Simple Strain-Space Plasticity Model for Clays," EERL 85–05, 1985. (PB–87–234308/CC)

143. Pak, R.Y.S., "Dynamic Response of a Partially Embedded Bar Under Transverse Excitations," EERL 85–04, May 1985. (PB–87–232856/A06)

144. Tan, T.-S., "Two Phase Soil Study: A. Finite Strain Consolidation, B. Centrifuge Scaling Considerations," SML 85–01, August 1985. (PB–87–232864/CC)

145. Iwan, W.D., M.A. Moser and C.-Y. Peng, "Strong-Motion Earthquake Measurement Using a Digital Accelerograph," EERL 84–02, April 1984.

146. Beck, R.T. and J.L. Beck, "Comparison Between Transfer Function and Modal Minimization Methods for System Identification," EERL 85–06, November 1985. (PB–87–234688/A04)

147. Jones, N.P., "Flow-Induced Vibration of Long Structures," DYNL 86–01, May 1986. (PB–88–106646/A08)

148. Peek, R., "Analysis of Unanchored Liquid Storage Tanks Under Seismic Loads," EERL 86–01, April 1986. (PB–87–232872/A12)

149. Paparizos, L.G., "Some Observations on the Random Response of Hysteretic Systems," EERL 86–02. 1986. (PB–88235668/CC)

150. Moser, M.A., "The Response of Stick-Slip Systems to Random Seismic Excitation," EERL 86–03, September 1986. (PB–89–194427/AS)

151. Burridge, P.B., "Failure of Slopes," SML 87–01, March 1987. (PB–89–194401/AS)

152. Jayakumar, P., "Modeling and Identification in Structural Dynamics," EERL 87–01, May 1987. (PB–89–194146/AS)

153. Dowling, M.J., "Nonlinear Seismic Analysis of Arch Dams," EERL 87–03, September 1987. (PB–89–194443/AS)

154. Duron, Z.H., "Experimental and Finite Element Studies of a Large Arch Dam," EERL 87–02, September 1987. (PB–89–194435/AS)

155. Whirley, R.G., "Random Response of Nonlinear Continuous Systems," EERL 87–04, September 1987. (PB–89–194153/AS)

156. Peng, C.-Y., "Generalized Model Identification of Linear and Nonlinear Dynamic Systems," EERL 87–05, September 1987. (PB–89–194419/AS)

157. Levine, M.B., J.L. Beck, W.D. Iwan, P.C. Jennings and R. Relles, "Accelerograms Recorded at Caltech During the Whittier Narrows Earthquakes of October 1 and 4, 1987: A Preliminary Report," EERL 88–01, August 1988. PB–

158. Nowak, P.S., "Effect of Nonuniform Seismic Input on Arch Dams," EERL 88–03, September 1988. (PB–89–194450/AS)

159. El-Aidi, B., "Nonlinear Earthquake Response of Concrete Gravity Dam Systems," EERL 88–02, August 1988. (PB–89–193124/AS)

160. Smith, P.W., Jr., "Considerations for the Design of Gas-Lubricated Slider Bearings," DYNL 89–01, January 1988. PB–

161. Donlon, W.P., Jr., "Experimental Investigation of the Nonlinear Seismic Response of Concrete Gravity Dams," EERL 89–01, January 1989. PB–

162. Jensen, H.A., "Dynamic Response of Structures with Uncertain Parameters," EERL 89–02, September 1989. PB–

163. Thyagarajan, R.S., "Modeling and Analysis of Hysteretic Structural Behavior," EERL 89–03, October 1989. PB–

164. US–China Joint Project on Strong Ground Motion Measurements, "Digital Near Source Accelerograms Recorded by Instrumental Arrays in Tangshan, China," EERL 89–04. PB–

165. Tan, P., "Numerical Simulations of Two-Dimensional Saturated Granular Media," SML 90–02, October 1989. PB–

166. Allard, M.A., "Soil Stress Field Around Driven Piles," SML 90–01. PB–